DREAMERS

Design REsearch, implementation And Monitoring of Emerging technologies for a new generation of Resilient Steel buildings

Grant Agreement Number: 101034015 - RFCS 2020

Deliverable D6.3

INFORMATIVE BOOK

Authors:

Vincenzo Piluso (UNISA, Project Coordinator)

Massimo Latour, Rosario Montuori, Elide Nastri, Sabatino Di Benedetto (UNISA)

Marco Casazza, Fabrizio Barone (UNISA)

Mario D'Aniello, Raffaele Landolfo, Roberto Carlevaris (UNINA)

Antonello De Leo (Tiar Studio)

Tudor Golea, Jean-François Demonceau (ULG)

Ana Francisca Santos, Aldina Santiago, Helena Gervásio, Luis da Silva (UC)

José Humberto Matias de Paula Filho, Marina D'Antimo, Renata Obiala (ArcelorMittal)

Date: 25.06.2025

TABLE OF CONTENTS

LIST OF FIGURES

LIST OF TABLES

CHAPTER 1

Architectural Design of the Demonstration Building

1.1 INTRODUCTION

The DREAMERS project is a demonstration project concluding a series of three projects, namely FREEDAM, FREEDAM-PLUS and DREAMERS, funded by the European Commission within the framework of RFCS (Research Fund for Coal and Steel).

The project FREEDAM (RFSR-CT-2015-00022), recently accomplished, regarded the design and testing of innovative connections equipped with friction dampers able to withstand, without any damage, destructive seismic events. FREEDAM connections exhibited excellent performances as demonstrated by experimental tests on beam-to-column connections and by full-scale seismic tests on a two-storey steel building carried out through the pseudo-dynamic testing method in a laboratory environment.

The DREAMERS demonstration project (RFCS 2020 - GA n. 101034015) aims to show the applicability and the excellent performances obtained through the application of FREEDAM connections in a real-scale environment. The demonstration consists in the realization of a real building, the so-called C3 Building at Salerno University Campus. The project has a significant focus on the structural part, but the architectural components and the mechanical/electrical systems have also been designed considering the most advanced available standards and technologies. The construction of the C3 Building has been recently completed. It is the first building worldwide to exploit FREEDAM technology. Beam-to-column connections of the seismic-resistant system are equipped with friction dampers connected to the bottom flange of the beams. The non-structural elements are conceived considering the damage issues, adopting partition walls, false ceilings, and façades able to follow the structural horizontal displacements without damage.

The innovative technology for seismic-resistant steel buildings, which was proposed, developed and tested during the FREEDAM project, is now applied to a real building. An innovative structural system based on the substitution strategy is adopted. The innovation is based on the adoption of beam-to-column connections equipped with friction dampers. The design strategy is

defined substitution strategy because the traditional dissipative zones of moment-resisting steel frames, i.e. the plastic hinges developed at the member ends under the occurrence of destructive seismic events, are substituted by beam-to-column connections equipped with friction dampers connected to the bottom flange of the beam and to the column flange.

DREAMERS project is the last step of a wider cooperation activity promoted by the University of Salerno (Italy), in collaboration with several European academic institutions. In particular, the University of Coimbra (PT), the University of Liege (B) and the University of Naples "Federico II" provided their contribution since the early activities of the FREEDAM project and up to the realization of the DREAMERS demonstration building.

The steps performed for the architectural design of the demonstration building are presented in this Chapter. The architectural design of the demonstration building was carried out by the technical offices of Salerno University with the collaboration of TiarStudio, under the supervision and coordination of Prof. Vincenzo Piluso as European coordinator of the DREAMERS project and leader of the design team.

In particular, TiarStudio was formally appointed by the University of Salerno to design the building envelope (including volumetry, layout within the site, and façade strategy) as well as the external landscape arrangement. The studio's primary interlocutors were the staff of the Department of Engineering, involved in the DREAMERS project, and the university technical office. TiarStudio work was carefully coordinated to align with the broader goals of the DREAMERS research and demonstration initiative.

The narrative herein presented retraces the evolution of the architectural contribution to the DREAMERS project, from its earliest conceptual studies to its final executive stage, highlighting design decisions and technical refinements along the way.

Although TiarStudio was not responsible for the structural design of the FREEDAM system itself, the architectural work was strongly influenced by its presence. The DREAMERS building is not only a university facility but also a prototype - a physical testbed for the FREEDAM technology, developed by a consortium of European universities. This structural detail allows beams and columns to move relative to one another without damage during an earthquake. Its integration shaped architectural decisions regarding layout, façade design, and the need for accessibility and flexibility around structural joints.

1.2 GENESIS AND DEVELOPMENT OF THE ARCHITECTURAL PROJECT

1.2.1 Starting ideas and their refinement

The realization of the DREAMERS demonstration building was planned in the Salerno University Campus located in Fisciano (SA), Italy. It is the main Campus of Salerno University. The construction site of the building is located near the university canteen in a sloping area downstream from the university residences. This area is shown in Fig. 1.1 where it is pointed out with a red boundary line. The project began in July 2021 with a series of preliminary proposals.

Figure 1.1*: Main Campus of Salerno University with the construction site*

The initial phase of the architectural design focused on the topographical configuration of the available lot and its planimetric dimensions (Fig. 1.2).

The initial design phase focused mainly on the volumetric configuration of the building and on verifying compliance with the limitations imposed by the urban planning indices. In particular, the constraints concern the maximum buildable planimetric surface and the maximum buildable volume taking into account the urban planning implementation plan (Piano Urbanistico Attuativo - PUA) of the University of Salerno as approved by the Municipality of Fisciano (SA). The PUA is a detailed urban planning tool used to implement the provisions of the Municipal Operational Plan (Piano Operativo Comunale - POC) or other municipal programming acts.

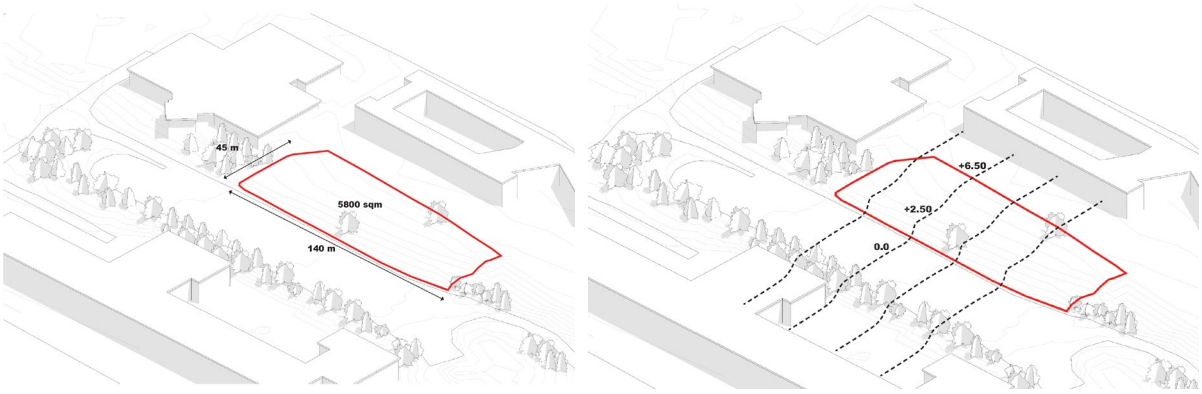

***Figure 1.2**: Available lot for the construction site*

They are particularly useful for complex projects that require a more specific definition of the urban insertion and the quality of public spaces. Accounting for buildable planimetric surface and the maximum buildable volume, three possible configurations were developed, each exploring different relationships with the sloped terrain of the site and offering various spatial arrangements. One proposal placed the building, composed of two parallelepiped-shaped blocks, in the upper part of the lot (Fig. 1.3), another adopted a more compact layout partially embedded in the slope (Fig. 1.4), and a third concerned an architectural layout characterized by two overlapping blocks in the shape of a parallelepiped, one arranged in a direction parallel to the road and the other in an orthogonal direction (Fig. 1.5). The second option - characterized by a semi-open ground floor, laboratories on the first floor, and offices above - was eventually chosen as the most suitable basis for further development.

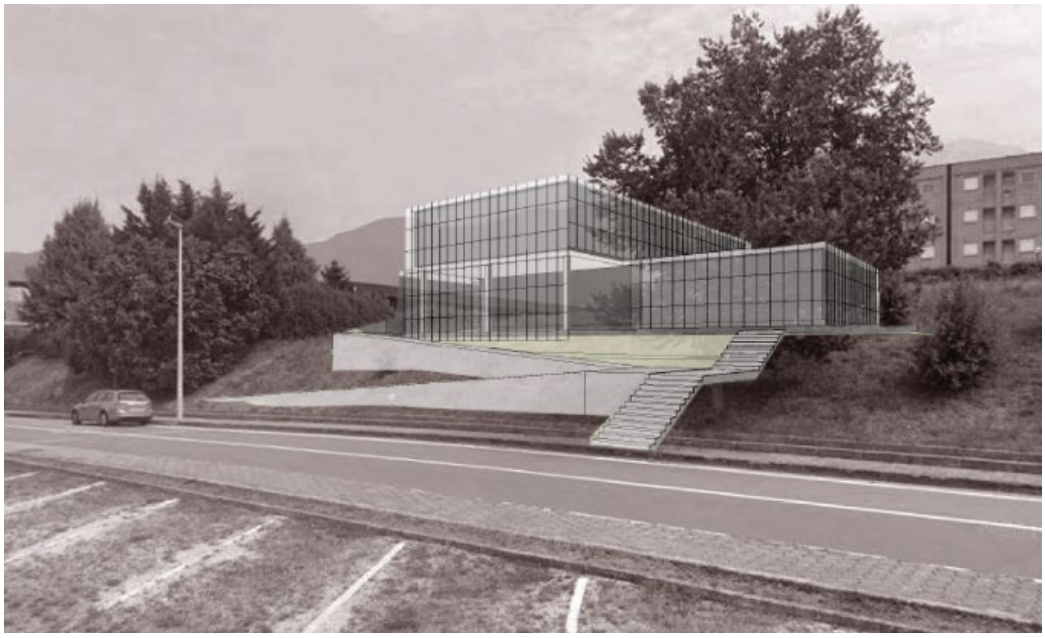

***Figure 1.3:** Preliminary proposals - two parallelepiped-shaped blocks in the upper part of the lot*

A few months later, in September 2021, the design began to take its final shape. The vertical circulation core was repositioned toward the back of the building, allowing the ground floor front to accommodate parking. Meanwhile, interior layouts were becoming clearer: the laboratory would occupy the first floor, while the offices, still conceived as open plan, would be located above. Attention also turned to the façade, and three options were proposed—each with a continuous glazed surface but different strategies for shading and visual expression, including vertical louvers, green mesh for climbing plants, and decorative perforated screens.

***Figure 1.4**: Preliminary proposals – a more compact layout partially embedded in the slope*

***Figure 1.5**: Preliminary proposals – two overlapping orthogonal blocks in the shape of a parallelepiped*

1.2.2 Technical Alignment

In January 2022, with the concept in place, discussions with the University's technical office led to a more defined internal organization. The building would consist of three main levels: a ground floor with the main entrance and technical rooms, a first floor housing the laboratory, and a top floor for offices.

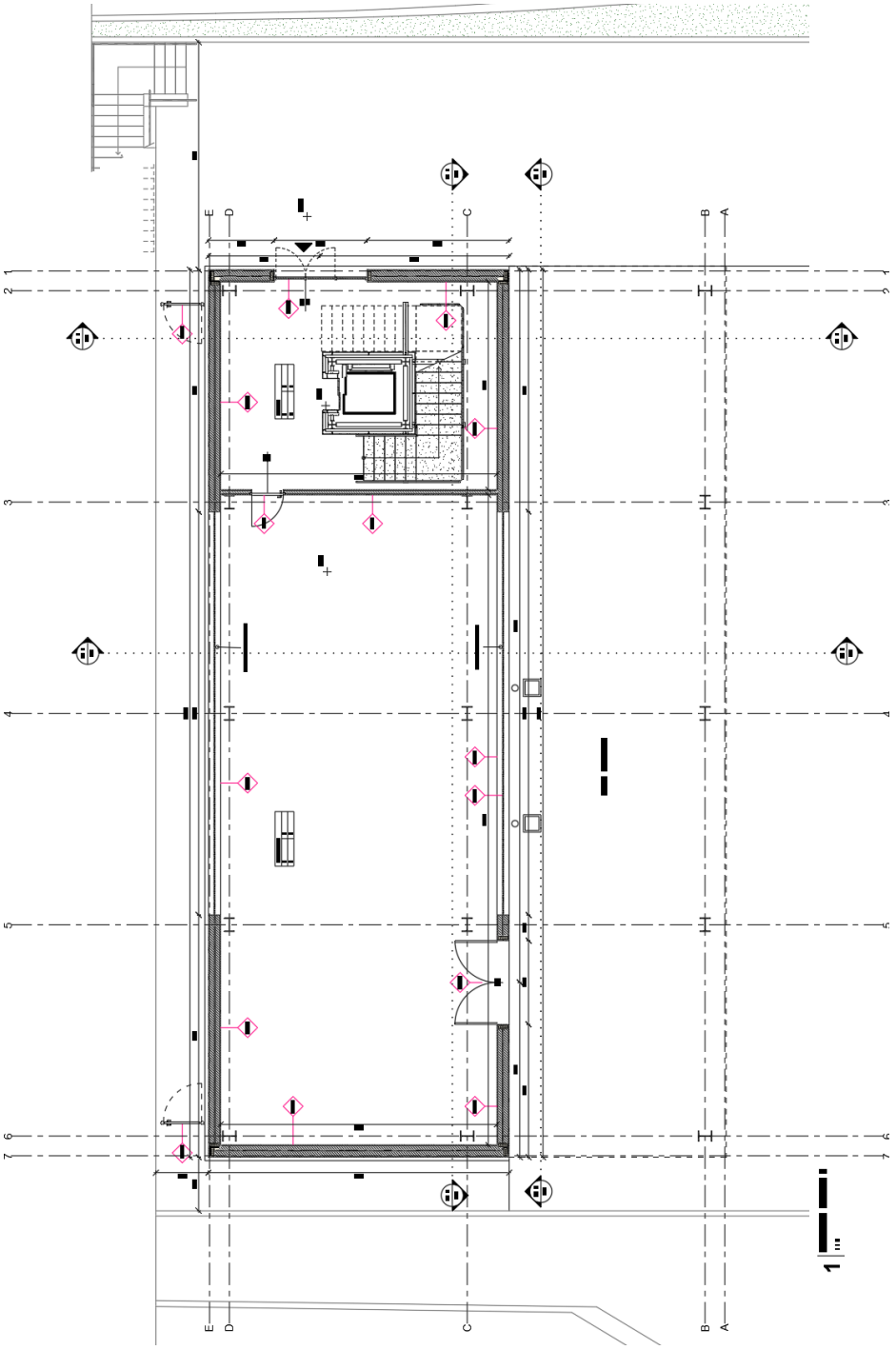

Figure 1.6: *Architectural design of the ground floor*

The primary destination of the C3 Building is the “Life Science Hub Laboratory”. The building has three floors with a covered area of about 376 sqm while the volume is about 4500 mc. The main dimensions of the building are 25.40 x14.80 m for a rectangular shape. The ground floor inter-storey height is 3.5 m, while the first and second floor have an inter-storey height equal to 4.20 m. The ground floor is partially open and arcaded to allow the parking of cars, while the covered part is devoted to host the main equipment of the technological center for thermal and electrical systems (Fig. 1.6). The first floor will host the laboratories so that all the rooms have been dimensioned to accommodate the instrumentations (Fig. 1.7).

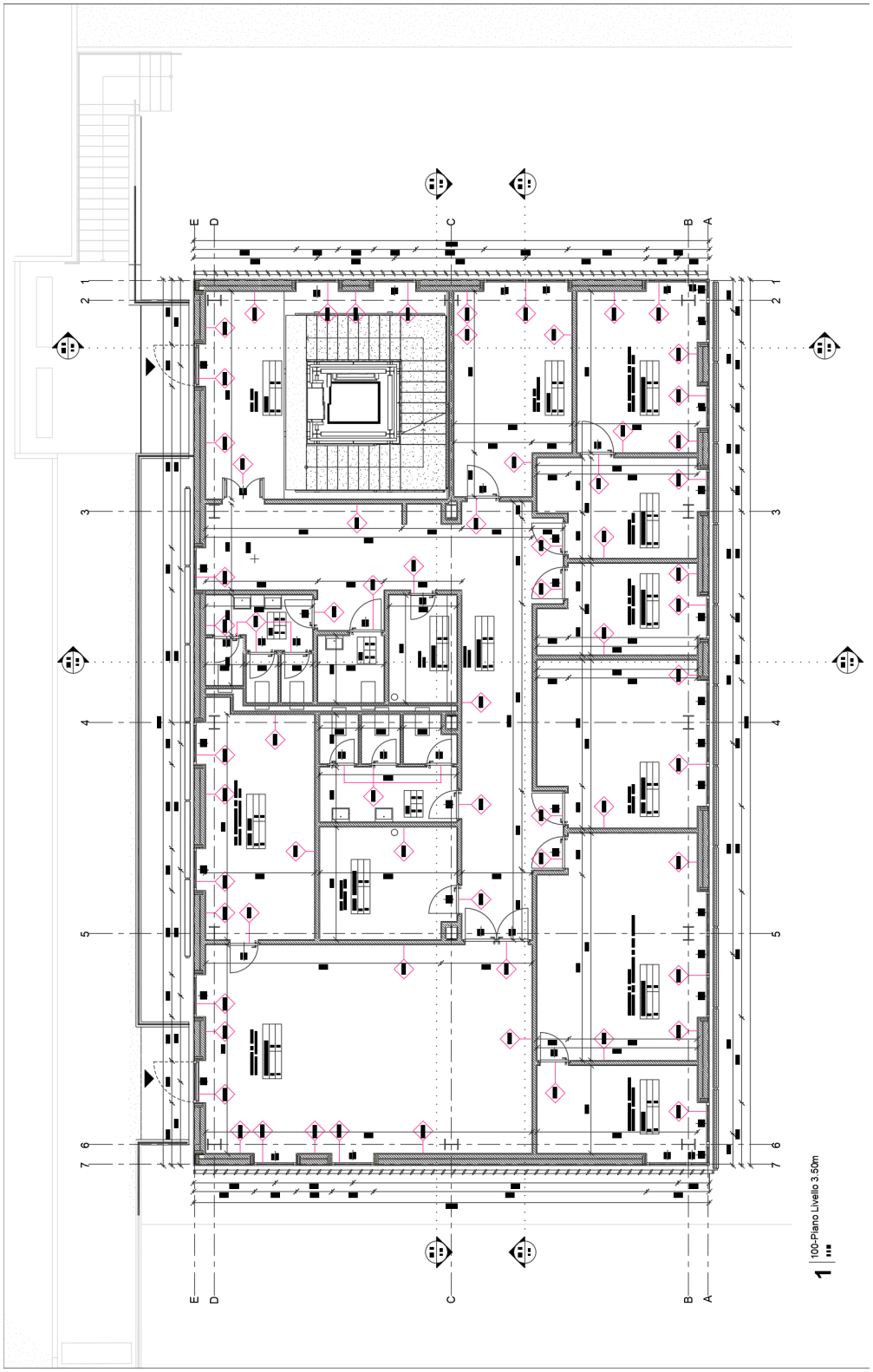

Figure 1.7: *Architectural design of the first floor*

The second floor is devoted to offices; in particular, seven office rooms, one meeting room and a storage room are located at this floor (Fig. 1.8). At the first and second floor there are also toilets for ladies, gentlemen and handicapped.

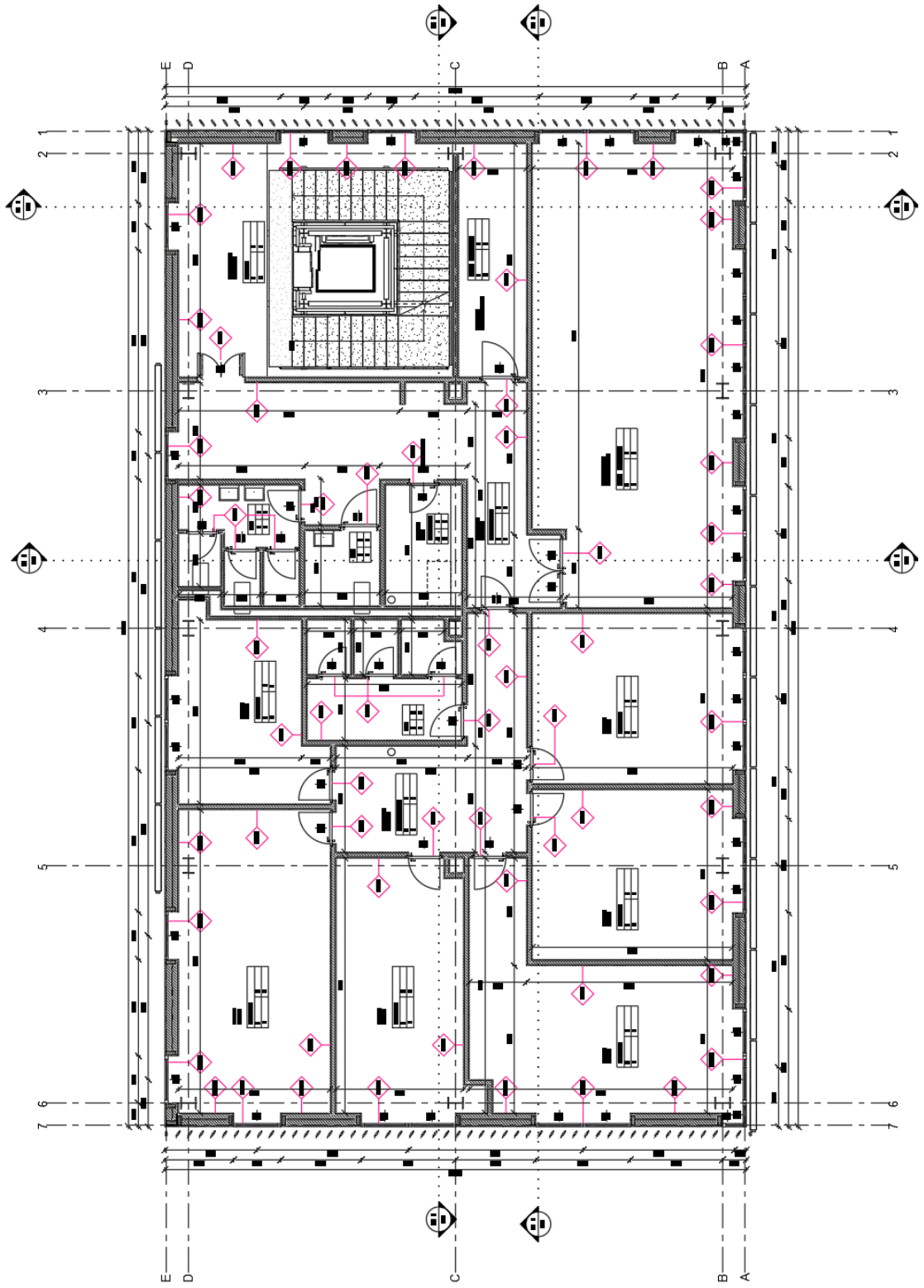

Figure 1.8: *Architectural design of the second floor*

The roof of the building is also devoted to a photovoltaic plant (Fig. 1.9). The structural system was also confirmed at this point: a steel frame with composite concrete slabs. The façade solution, however, was still under discussion.

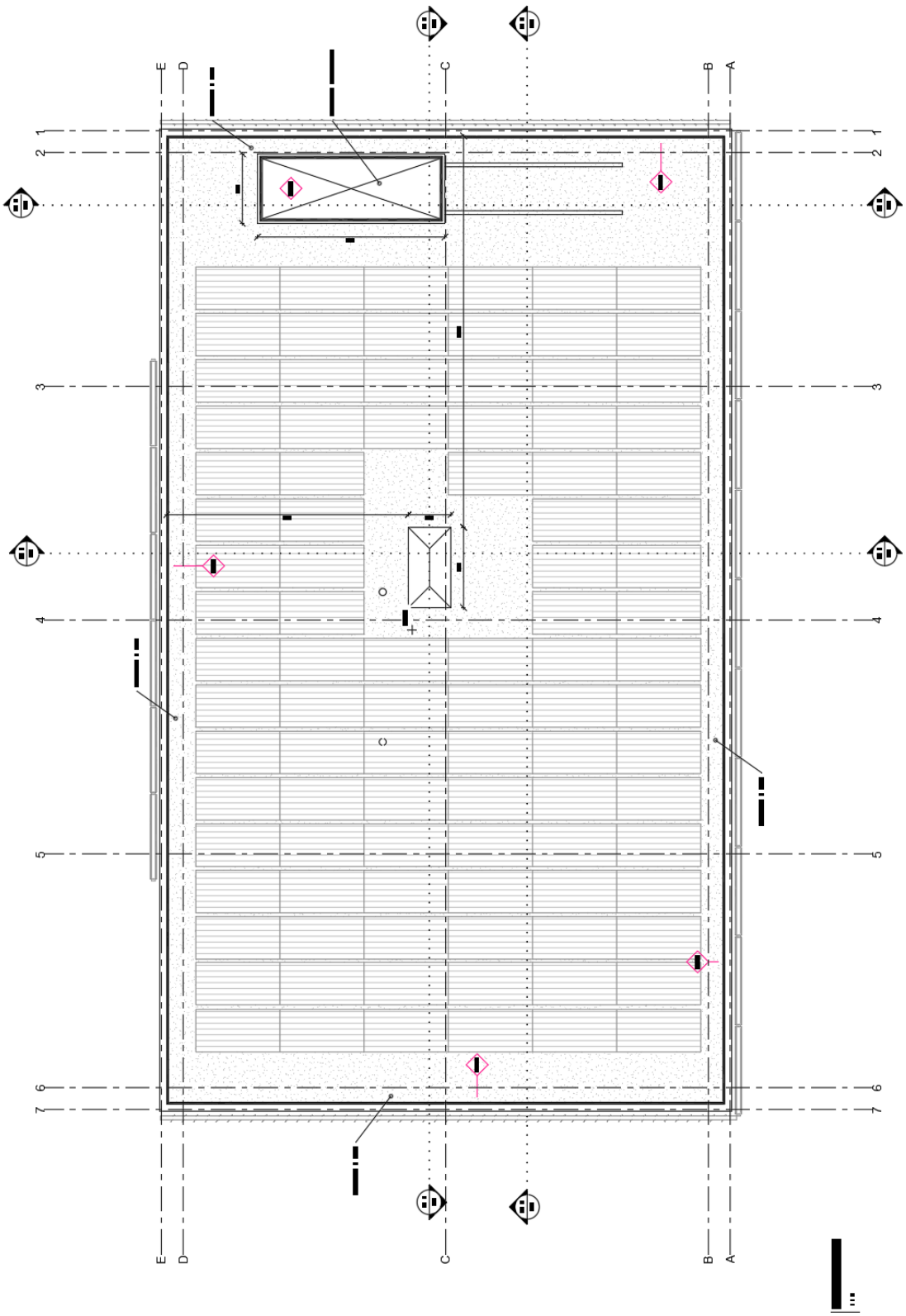

Figure 1.9: *Architectural design of the roof with the photovoltaic plant*

Figure 1.10 shows the transversal sections of the building

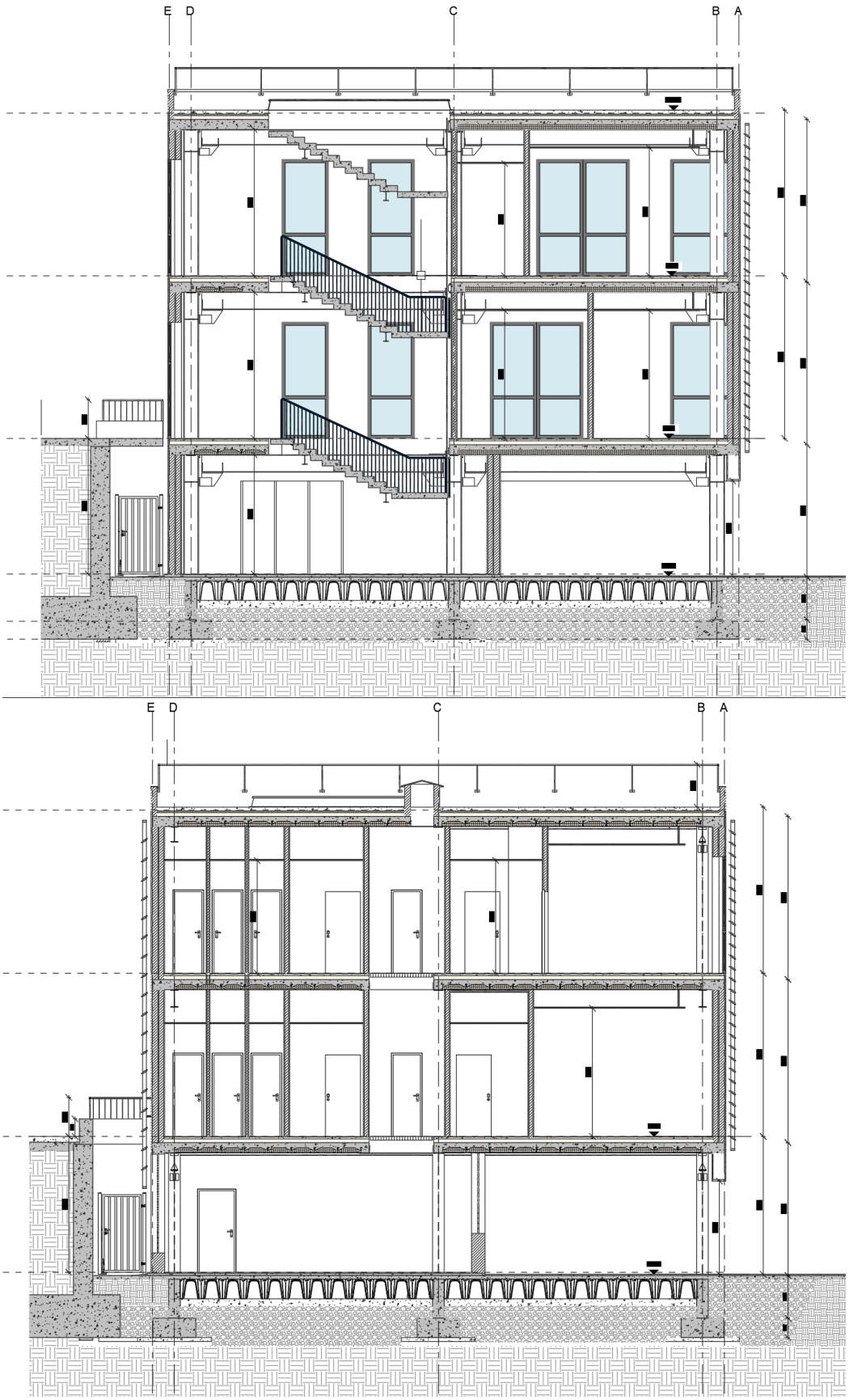

Figure 1.10: *Transversal sections of the building*

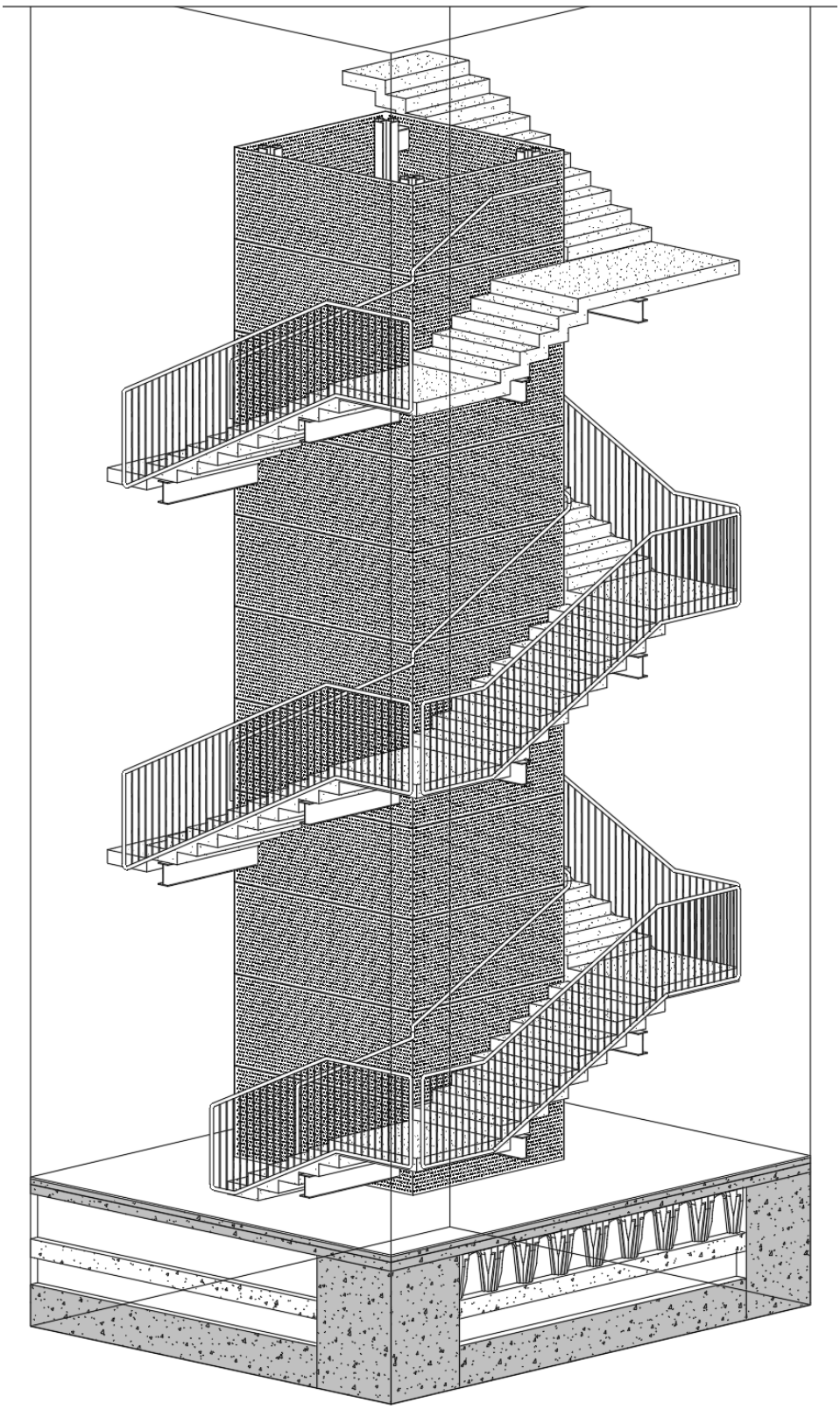

Figure 1.11: *Staircase-elevator body*

As the staircase-elevator body is located in an eccentric position in plan, it has been realized as a completely independent body (Fig. 1.11) detached from the main body of the building by means of seismic joints. The elevator shaft is enclosed by a perforated sheet metal with circular holes.

1.3 ARCHITECTURAL DESIGN OF THE FAÇADE

By spring 2022, the team focused on refining the façade (Fig. 1.12). Two main directions were considered.

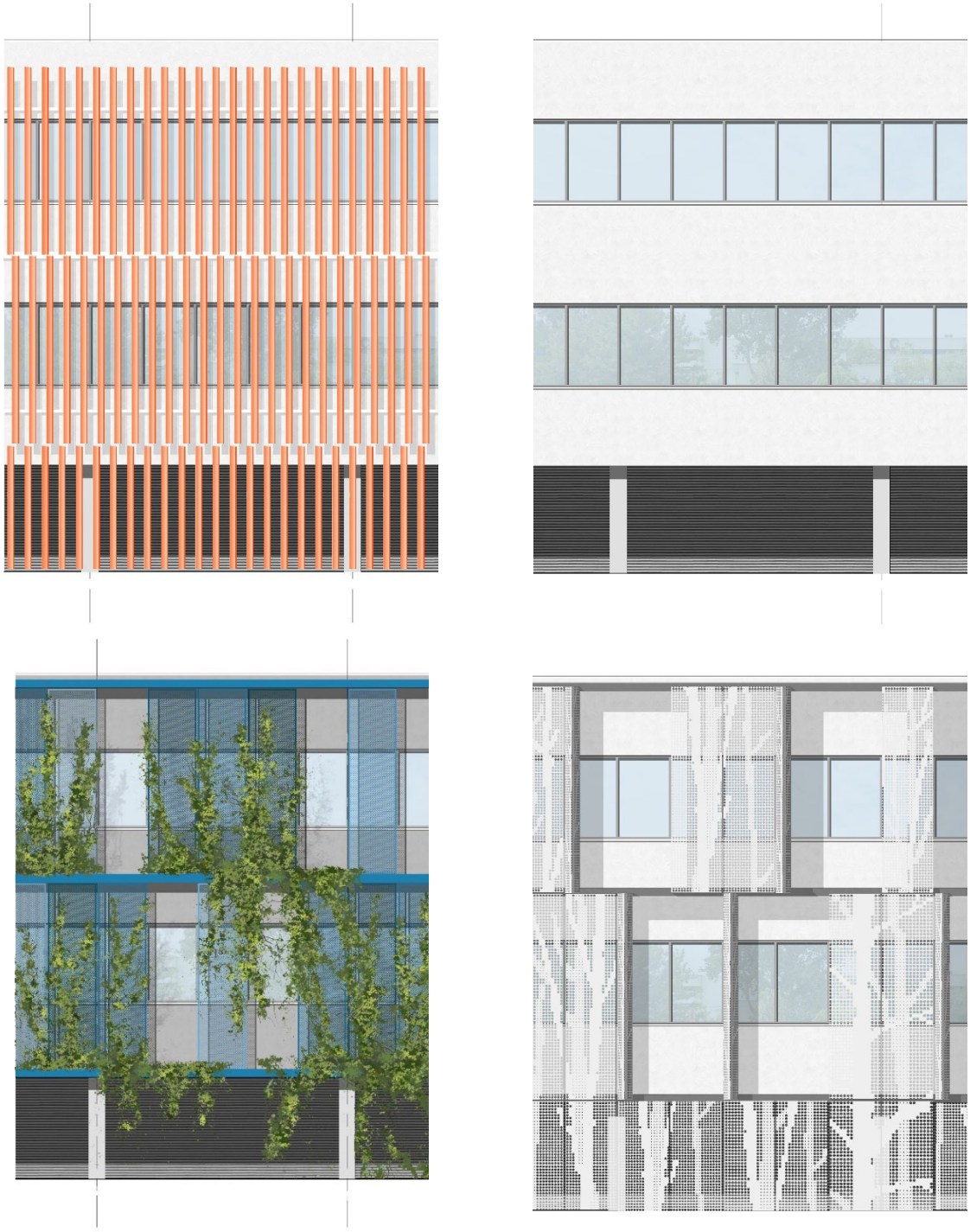

Figure 1.12: *Main directions in the study of façade options*

The first option featured dry-mounted horizontal and vertical fins, highlighting the rhythm of the openings and relying on internal shading (Fig. 1.13).

Figure 1.13: *First façade option*

In this case, the structure is detached from the external walls and fully visible, both from inside and outside. Coating is used to protect steel against corrosion and highlight the structural elements. The recessed detail of the suspended ceiling system does not conceive the FREEDAM joint, which is fully accessible for inspection and maintenance.

Figure 1.14: *Second façade option*

The external walls are made of highly insulated, double framed dry panels system, alternatively with full height glazing. Vertical and horizontal fins, individually designed for each facade, act as weather and shading device, in conjunction with internal rolling blinds. Those elements provide visual variation on each facade through a standardized system. The windows have been sized to balance the required light levels for office and lab activities, whilst ensuring that solar

heating loads are reduced. By placing the glazing on the inside of the boxing element it would be possible to use the full depth of the facade for shading.

The second proposed a more uniform system of aluminium louvers - horizontal on some sides, vertical on others - concealing the windows more effectively but providing better thermal performance (Fig. 1.14). In this case, the structure is detached from the external walls and partially visible from outside.

Figure 1.15: *Final choice for the façade system*

Coating is used to protect steel against corrosion and highlight the structural elements. Also in this solution, the recessed detail of the suspended ceiling system does not conceive the FREEDAM joint, which is fully accessible for inspection and maintenance.

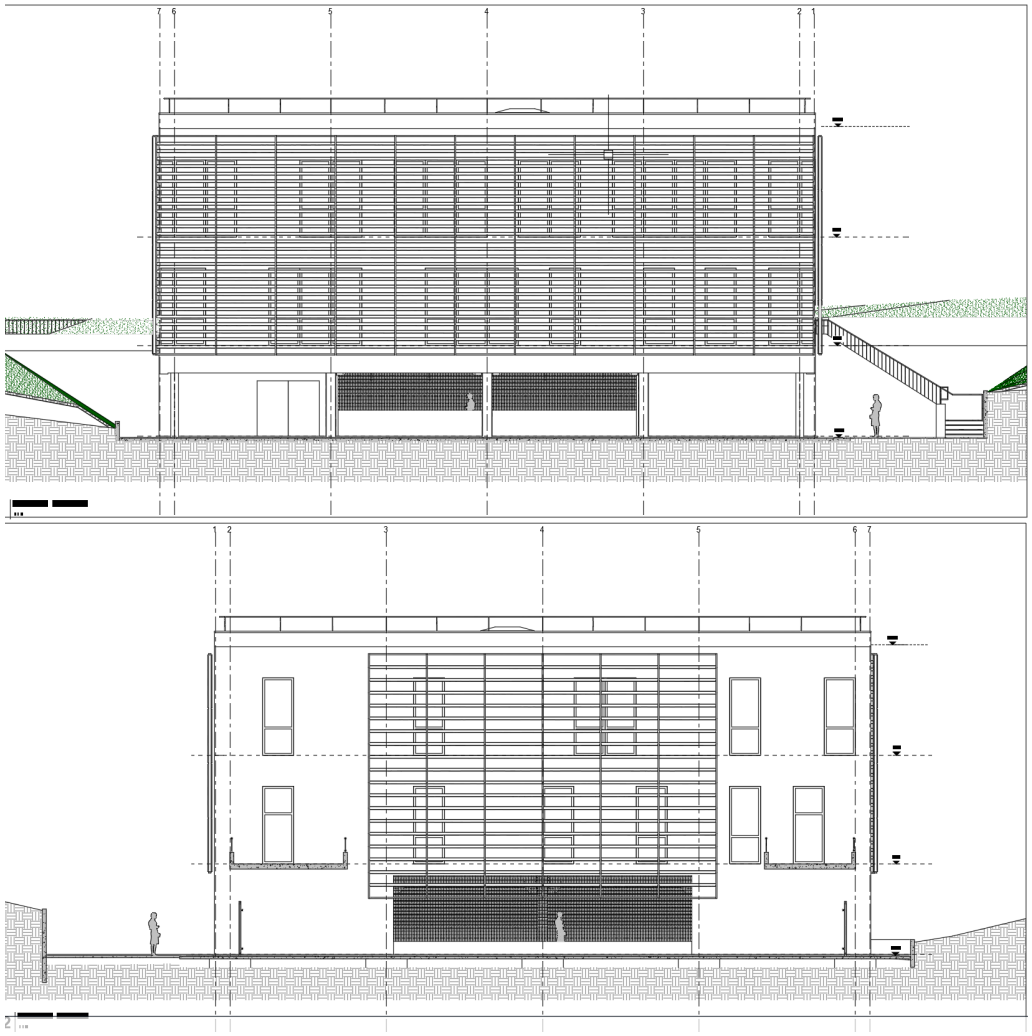

Figure 1.16: *Front elevation facing the street and the rear elevation*

The external walls are made of highly insulated, double framed dry panels system, alternatively with full height glazing. Horizontal and vertical louvers envelop the sides of the building, acting as shading device. This solution is clearly efficient in blocking direct solar irradiation, while flattening the exterior appearance and the perception of it from the inside and not providing any direct protection to the external walls. In March 2022, the university ultimately chose the louver-based façade (Fig. 1.15). This solution balanced aesthetics and function: fixed aluminium blades mounted on a supporting structure, carefully designed to accommodate seismic movement and ensure durability. The underlying wall system, built entirely with dry techniques, featured high insulation performance and allowed easy maintenance access. Figure 1.16 shows the two main elevations, the front one facing the street and the rear one. Figure 1.17 shows the two side elevations of the building.

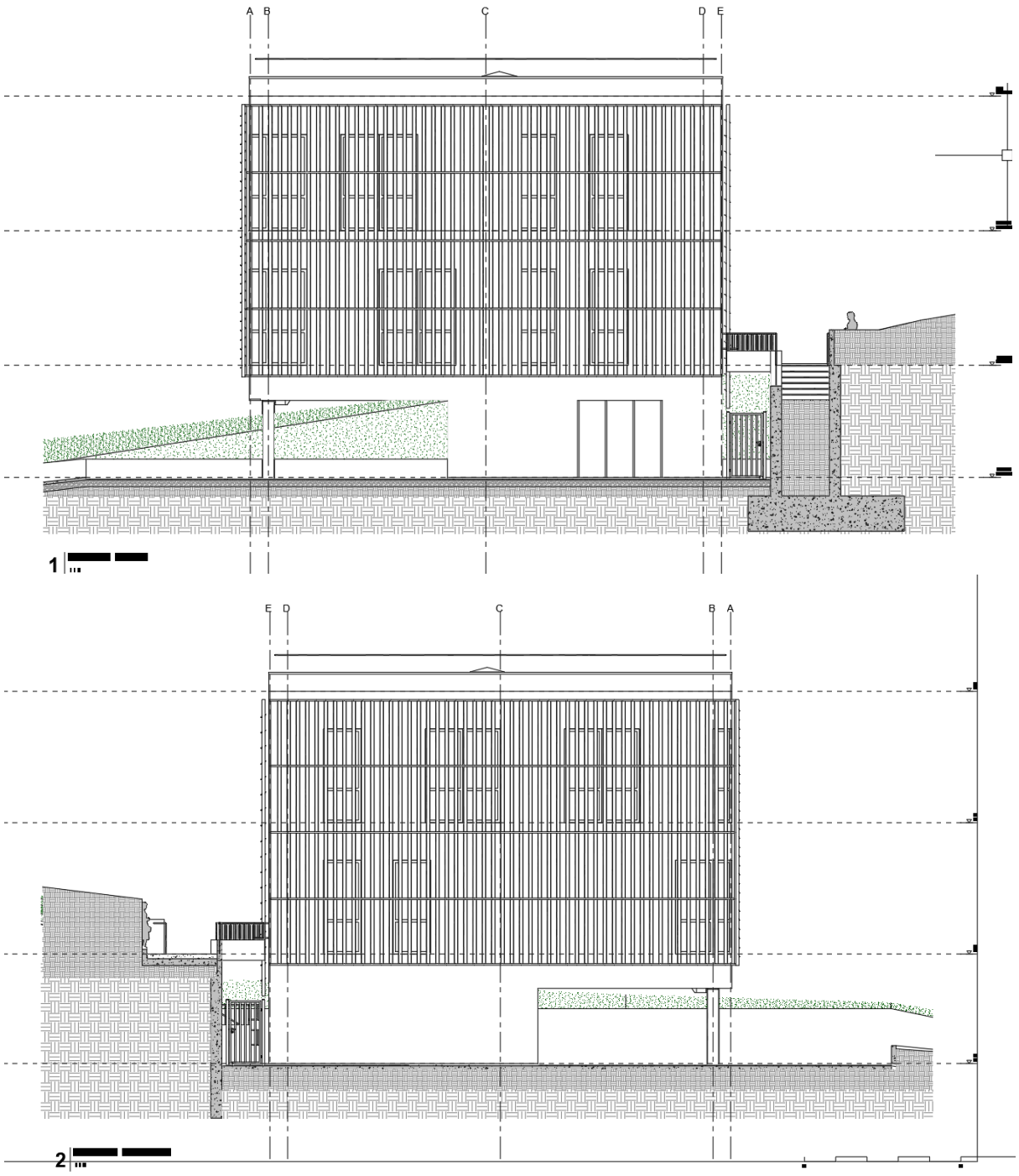

Figure 1.17: *Side elevations – south-east (top) and northwest (bottom)*

1.4 NON-STRUCTURAL ELEMENTS

Work continued with increasing precision. The collaboration between TiarStudio and the University of Naples has led to the development of the details concerning the internal and external walls were developed using dry systems provided by Knauf. Internal partitions were standard: metal studs with double plasterboard. The external walls were more complex, using

two separate stud frames, multiple insulation layers, Aquapanel on the outside, and vapor-barrier-protected plasterboard on the inside.

Steel box frames were also introduced around window openings to strengthen the façade and prevent thermal bridging - these hollow steel profiles were pre-insulated and fixed to the slabs at top and bottom.

To obtain a low-damage building, a requirement is that the façade elements and partition walls remain undamaged even in the case of destructive seismic events. For this reason, the design goal for the non-structural components is the compatibility with the inter-storey drift demands occurring in case of earthquakes. To this scope, certified low-damage systems for the façade, partition walls, and false ceilings have been provided by KNAUF which is a partner of the DREAMERS project. Therefore, the conception and design of the non-structural elements of the building has been carried out to accommodate the maximum displacements required by the structure under seismic loading conditions. Besides, false ceilings have been designed to allow the inspection of the FREEDAM connections during the lifecycle of the building. This is of primary importance to allow an easy inspection aimed at the monitoring of the friction dampers. The selection of LightWeight Steel (LWS) drywall products to guarantee a very good seismic response with respect to damage limit states has been made on the bases of the results of past research activities, funded by Knauf, on the seismic performance evaluation of LWS architectural non-structural systems (Pali et al 2017, Fiorino et al. 2018, Fiorino et al. 2019, Landolfo et al 2019). For this reason, the so called anti-seismic enhanced solutions have been selected for non-load bearing partitions (Fig. 1.18), suspended ceilings (Fig. 1.19) and façades (Fig. 1.20).

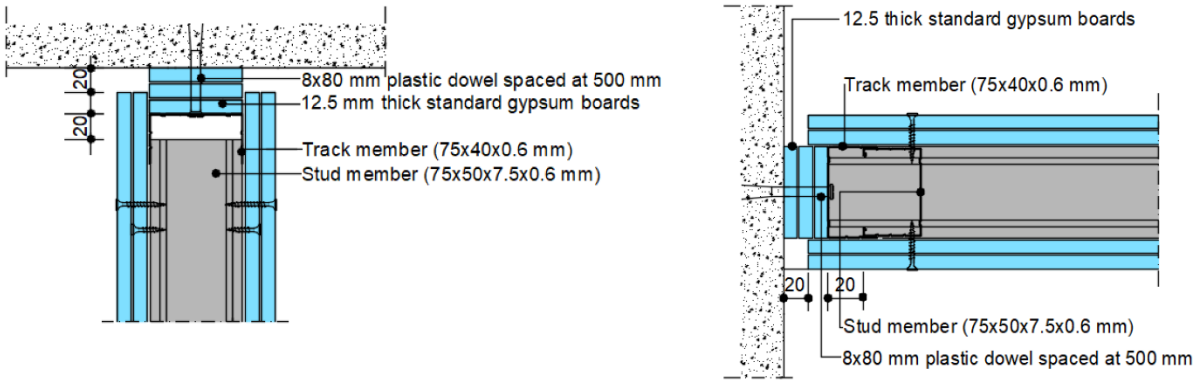

Figure 1.18: *Anti-seismic enhanced connection details for partitions*

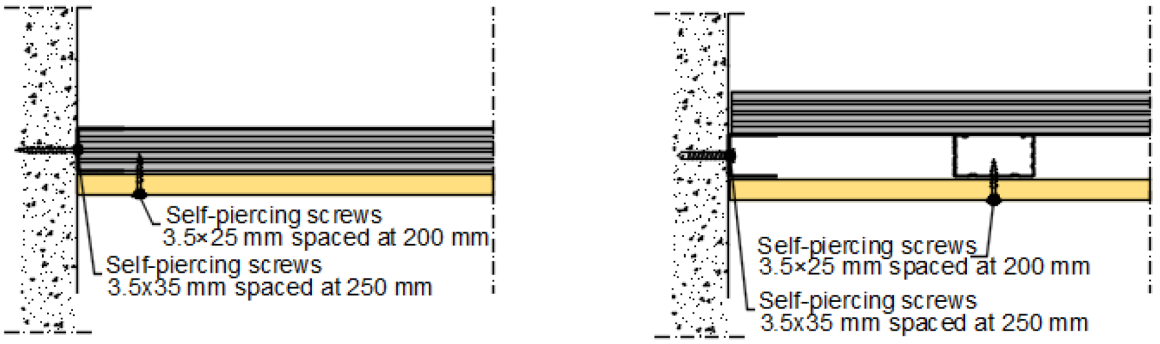

Connection between furring channels and wall Connection between carrying channels and wall

Figure 1.19: *Anti-seismic enhanced connection details adopted in ceilings*

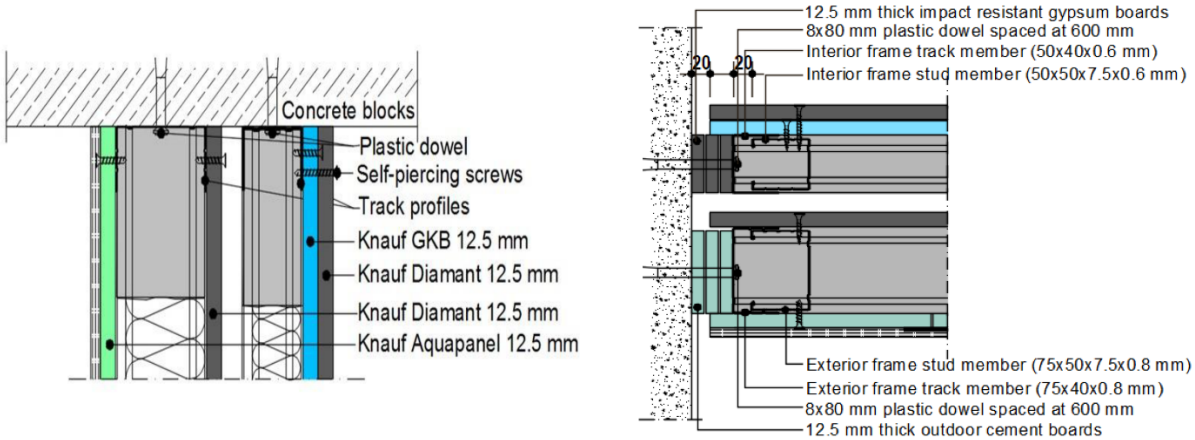

Horizontal basic (fixed) connections Vertical enhanced (sliding) connections

Figure 1.20: *Anti-seismic enhanced connection for façades*

The surrounding buildings are positioned at least 30 meters away, ensuring minimal solar obstruction. Consequently, solar mitigation was a key consideration guiding the design of the façades. The designed layout for the façade is reported in Fig. 1.21. The structure is designed to be detached from the external walls, allowing it to be partially visible from the outside. To facilitate maintenance and inspection, the joint are fully accessible.

The external walls of the building consist of a highly insulated, double-framed dry panel system provided by KNAUF (Fig. 1.20). Each side of the building is covered in a distinct manner, taking into account the level of solar radiation it receives. This feature, coupled with the ability to adjust the angle of the louvers, enables the regulation of solar heat gain and ensures a balance between natural daylight, electricity consumption for lighting, and thermal comfort. Moreover, the building accomplishes all the requirements to be NZEB.

Careful coordination with the structural team ensured that the FREEDAM joints remained accessible for inspection and maintenance, with technical hatches and buffer zones incorporated discreetly into the architecture.

Figure 1.21: *Final appearance of the façade of the building under construction (June 2025)*

1.5 CONCLUSION

The DREAMERS building represents a rare integration of architectural design and structural research. Over eighteen months of work were needed to develop a project that responds to functional, environmental, and experimental needs, within the specific scope of the building envelope and landscape design. The result is a structure that speaks both the language of architecture and of seismic engineering - a place for knowledge, and a subject of knowledge itself.

1.6 REFERENCES

[1] T. Pali, B. Bucciero, M.T. Terracciano, V. Macillo, L. Fiorino, R. Landolfo (2017), In-plane quasi-static cyclic tests on lightweight steel drywall non-structural partition walls, Ce/Papers. 1. 2857–2866. https://doi.org/10.1002/cepa.337.

[2] L. Fiorino, T. Pali, R. Landolfo (2018), Out-of-plane seismic design by testing of non-structural lightweight steel drywall partition walls, Thin-Walled Struct. 130. 213–230. https://doi.org/10.1016/j.tws.2018.03.032.

[3] L. Fiorino, B. Bucciero, R. Landolfo (2019) Evaluation of seismic dynamic behaviour of drywall partitions, façades and ceilings through shake table testing, Eng. Struct. 180. 103–123. https://doi.org/10.1016/j.engstruct.2018.11.028.

[4] Landolfo, R., Pali, T., Bucciero, B., Terracciano M.T., Shakeel, S., Macillo, V., Iuorio, O., Fiorino, L. (2019), Seismic response assessment of architectural non-structural LWS drywall components through experimental tests. Journal of Constructional Steel Research, Vol. 162, 105575. https://doi.org/10.1016/j.jcsr.2019.04.011.

CHAPTER 2

Structural Design of the Demonstration Building

2.1 INTRODUCTION

The traditional seismic design approach relies on performance levels, which imply the development of damage in structural members and/or connections which is difficult to repair. While structural damage is essential to dissipate the earthquake input energy, it is also the main source of direct and indirect losses. As demonstrated by the recent seismic events occurring in Europe and worldwide, even though such losses preserve human lives on the other hand they impair building functionality and are intolerable for advanced industrialized countries. The need to repair the structure after the seismic event is associated with high economic and social costs. To overcome the main drawback of the traditional design approach, some strategies have already been proposed and investigated. One of the most promising approaches, which has been largely tested in the past decades, is based on the use of supplementary energy dissipation devices or passive control, where the earthquake input energy is dissipated by viscous or hysteretic damping introducing energy absorbers. Nevertheless, also with this strategy, the damage is only reduced and not zeroed, and construction repair with the interruption of the building functionality is still a drawback. This is the main reason why, to take a step forward in the available technologies for the seismic protection of steel buildings, there is the need to shift the paradigm of modern seismic engineering from a damage-controlled to damage-prevented design philosophy.

To address this challenge, relevant research studies have been carried out within the FREEDAM research project [1], demonstrating the high potential of beam-to-column connections equipped with friction dampers to drastically reduce the structural damage to steel structures, hence maintaining the building fully operational even in the aftermath of severe seismic events. Implementing standardized types of friction dampers in beam-to-column connections of Moment-Resisting Frames (MRFs), whose stroke and resistance are properly calibrated by properly designing the length of slotted holes and controlling the tightening torque of pre-loadable bolts, it is possible to conceive beam-to-column connections able to accommodate the rotation demands deriving from high-intensity seismic events practically without any damage, leading to the concept of FREE from DAMage (FREEDAM) connections. Besides, after the

attainment of the stroke limit of the friction dampers, a new resisting mechanism is activated with the bolts acting in shear and the plate elements subjected to the bearing. Such an additional resisting mechanism constitutes a further reserve of strength, ductility, and energy dissipation capacity, which can be particularly useful in the case of exceptional loading conditions. As a result, also the structural robustness is significantly improved. FREEDAM project has addressed all the issues related to the behaviour of beam-to-column connections equipped with friction dampers providing design rules, a wide set of experimental results, FE modelling strategies, analytical tools and standardized kits of elements to be applied in connection realization, arriving at a Technology Readiness Level (TRL) equal to about 5. The objective of the DREAMERS project is to increase the TRL, arriving at about 8, providing the application of a demonstration building into an operational environment qualifying the connections.

The need to build resilient societies requires the adoption of resilient technologies able to avoid the impact of adverse events on people, such as those occurring in case of severe earthquakes. The free-from-damage technology fits exactly with this objective. The DREAMERS project, by implementing FREEDAM technology in the C3 building erected at the University Campus of Salerno provides a real-scale example within a relevant operational environment. Even though the C3 Building is a quite small building having only three storeys, it deserves attention because it is the first building worldwide to adopt FREEDAM technology. It is expected that the demonstration building and the dissemination activities developed around its construction will raise, in the professional engineers' community and industry, the awareness about the competitiveness of free-from-damage connections and the improvement of performance levels preserving people from the disruption deriving from the interruption of the functionality of buildings.

2.2 BEAM-TO-COLUMN CONNECTIONS EQUIPPED WITH FRICTION DAMPERS

Despite the traditional design approach, the required energy dissipation capacity needed to withstand destructive seismic events assuring the primary goal of the safeguarding of human lives, nevertheless, it leads to extensive damage, thus significantly compromising the building’s reparability after strong seismic events and leading to high socio-economic losses and downtime. To address these shortcomings, the use of beam-to-column connections equipped with friction dampers has been recently proposed. Recent research works have demonstrated the high potential of such innovative connection typology for the development of a new generation of resilient constructions conceived to avoid damage and repair costs.

The FREEDAM connections (Fig. 2.1) adopted for the C3 Building of Salerno University Campus are equipped with friction dampers whose pads are coated by a properly selected friction material and are located in between vertical sliding plates connected by high-strength bolts to the bottom flange of the beam [1-3]. The system is conceived as an industrialized kit. Two L-stubs accommodate the friction pads and connect them to a vertical sliding plate. Moreover, a T-stub is located at the top beam flange to fix the centre of rotation. Both the L-stubs and the T-stub are designed by exploiting hierarchy criteria at the component level to remain in the elastic range. The dissipative behaviour of the connection is assured by the slippage of the friction pads only. The rotation demands are transformed into displacement demands at the level of the friction damper whose stroke can be easily designed to accommodate such displacements without any damage. The connection is subjected only to minor yielding located in the stem of the T-stub close to the centre of rotation.

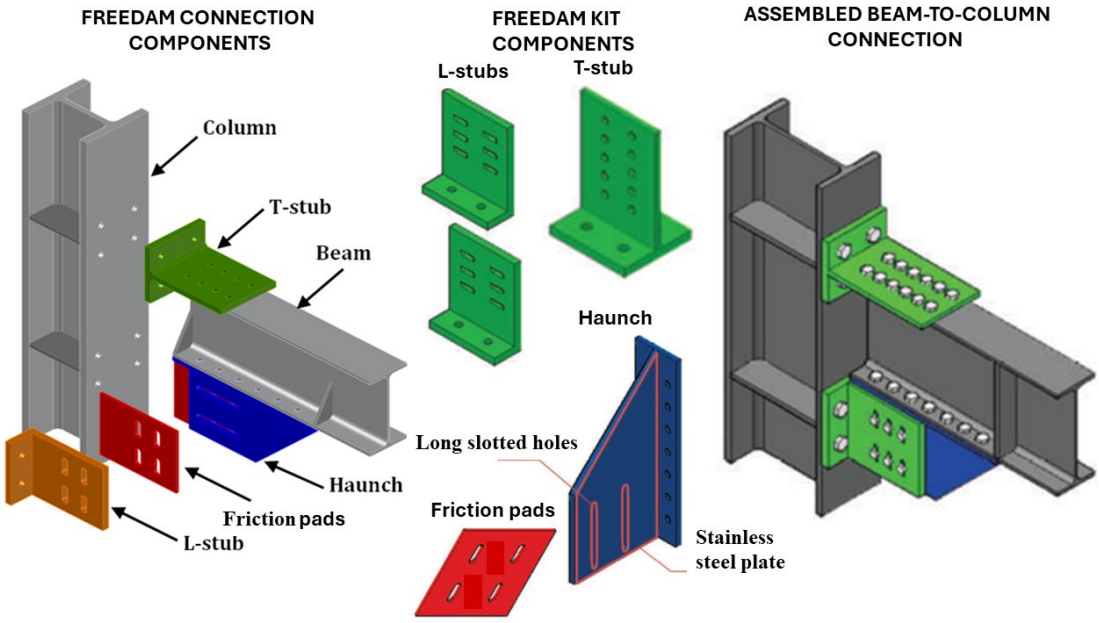

***Figure 2.1**: FREEDAM beam-to-column connection with its components*

2.3 STRUCTURAL CONCEPTION AND MAIN DESIGN ISSUES

2.3.1 Structural conception

The structural design of the building has been carried out complying with the Italian code NTC 2018 and structural Eurocodes 1, 3 (parts 1.1 and 1.8), 4 (part 1.1) and 8 (part 1.1). The building is conceived as two structurally independent bodies, the main body and the staircase-elevator body, which are split-up by means of seismic separation joints. This choice accounts for the

eccentric position of the staircase structure and, in addition, is aimed at avoiding any structural connection between the different storeys of the main structural body.
The seismic-resistant structural system is conceived to act as a bare steel perimeter moment-resisting frame. Conversely, the gravity load resisting system is constituted by composite beams connected by simple connections to the leaning columns.

Two perimeter frames in the longitudinal direction and two perimeter frames in the transversal direction constitute the seismic load-resisting system. The two frames in the longitudinal direction have four bays. The internal bays are equipped with FREEDAM connections and, therefore, are moment-resisting bays. Conversely, the external bays are characterized by traditional simple connections designed to transmit the shear forces only.
Therefore, the external bays belong to the gravity load-resisting system. The two frames in the transversal direction have all the bays equipped with FREEDAM connections so that, being moment-resisting, they constitute the seismic-resistant scheme for the transversal direction. All the inner frames are part of the gravity load-resisting system, so that all the beam-to-column connections are traditional simple connections designed to transmit the shear forces only. The building decks are based on a slim floor system.
In particular, the gravity load resisting system of the building is characterised by fifteen HE400B columns, made of S355JR steel grade, located at the intersections of the beams reported in the plan view of Figure 2.2. The seismic-resistant system is equipped with FREEDAM beam-to-column connections. The connected beams are IPE450 (first and second floor) or IPE400 (roof) made of S355JR steel grade. The beams of the gravity load resisting system are made by HE300B and HE240B beams, depending on the loading condition, whose top flange is partially cutted according to the Composite Slim Floor Beam (CoSFB) system and are equipped with simple connections.

2.3.2 Composite floor

The building decks are made up of Cofradal 260 prefabricated steel-concrete composite floors (Fig. 2.3), a solution patented by Arcelor Mittal. The choice of this composite system has been dictated by its easy and rapid realisation, the excellent performance from acoustic and thermal insulation point of view and the excellent fire resistance.

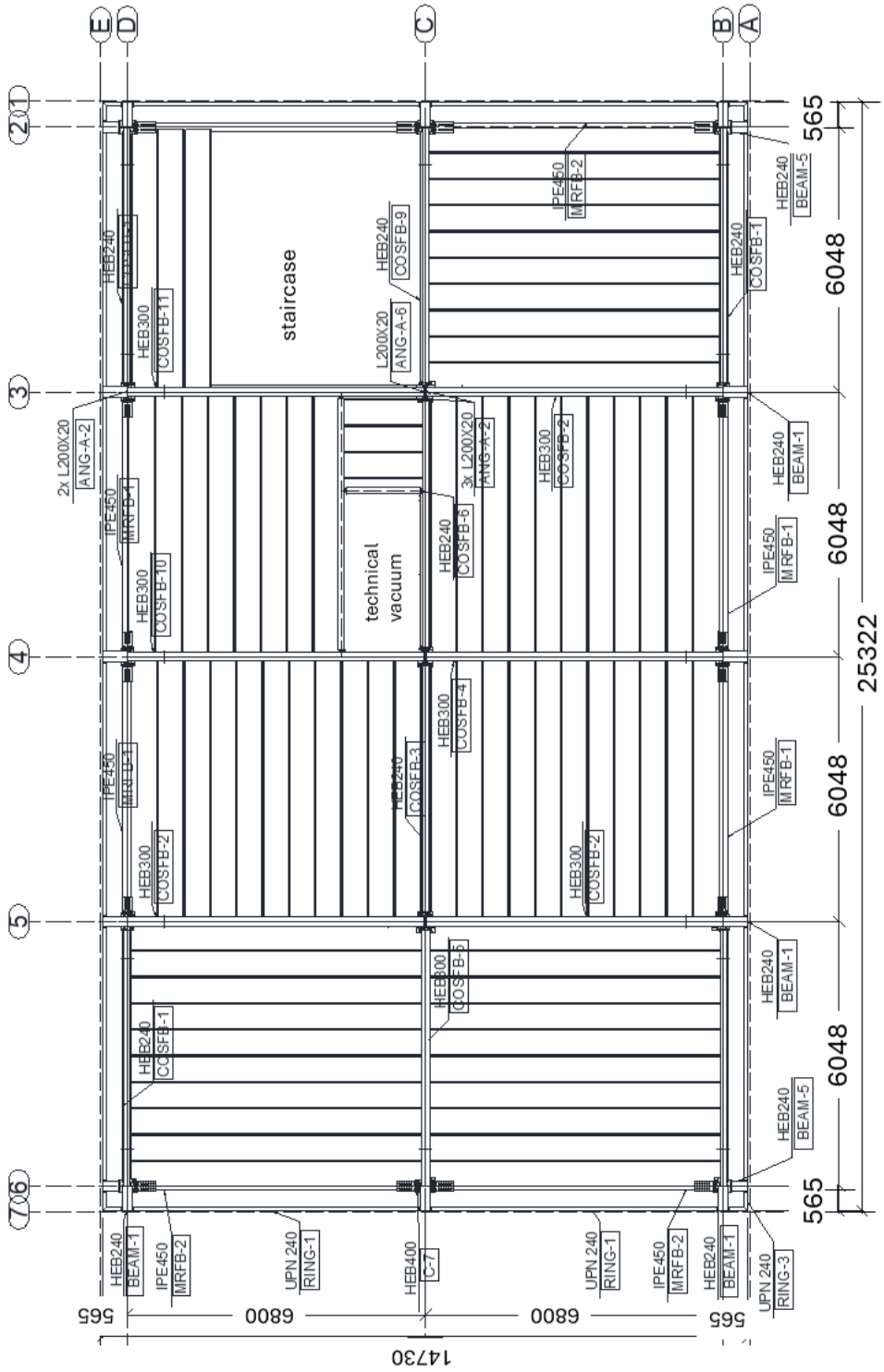

***Figure 2.2**: Structural layout of the building deck - 1st floor*

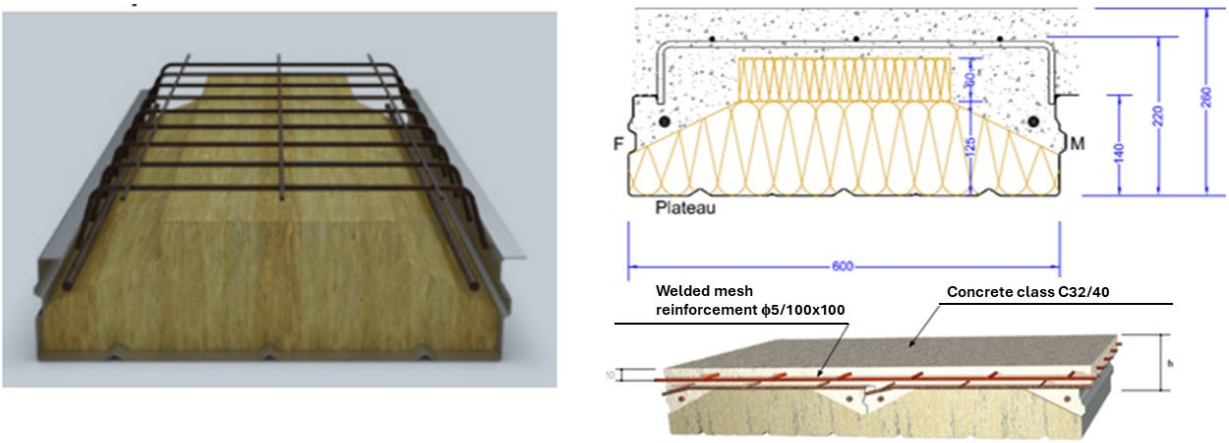

***Figure 2.3**: Cofradal 260 composite floor solution*

The role of the steel decking is twofold. Initially, during the construction phase, it allows casting concrete directly on site (with a limited number of supports) and works as a formwork. Subsequently, after that concrete is completely cured, concrete and steel realise a monolithic cross-section, in which the connection between the profiled steel sheeting and the concrete is assured mainly by adhesion or friction. In this second phase, the steel sheeting is a tension reinforcement for the sagging bending moment. The only additional steel needed in practice is typically provided to take care of shrinkage, limit cracking for temperature effects, and, considering the continuity of the slabs, it has to be provided to resist hogging bending moments. In both previous stages, for the analysis of a slab characterised by a length equal to 6.80 m, corresponding to the maximum bay span, the following checks have been fulfilled: i) Ultimate Limit State (ULS) check for bending (hogging or sagging); ii) ULS check for longitudinal shear; iii) ULS check for transverse shear; iv) ULS punching check; v) Serviceability Limit State (SLS) for deflection check; vi) SLS stress limitation check. Additional analyses have been devoted to the assessment of the vibration frequency of the floor. The Italian Code requires only that, considering the load combination $G_k+0.15Q_k$, the frequency of the deck has to greater than 3 Hz for non-cyclic loads and 5 Hz in the presence of cyclic loads. Reference has been made to documents of proven validity developed in the context of research projects. In particular, reference was made to the research project "Human induced Vibrations of Steel Structures" (HIVOSS), whose design and evaluation methods for floor vibrations are related to human-induced vibrations, mainly caused by walking in normal conditions. The analysis has highlighted that the frequency of the composite floor is about 6.90 Hz, the modal mass of two-bay model is about 11.5 tons, and the damping is 4%. As a result, the analysed floor falls into class D, which, concerning the intended use for offices, appears to be a performance requirement recommended by the research referred to.

2.3.3 The slim floor system

The Cofradal 260 slabs transfer the loads to secondary beams, designed according to a steel-concrete composite solution. These elements represent a solution proposed and patented by Arcelor Mittal and are marketed as CoSFB beams (Composite Slim Floor Beams).

The peculiarity of the CoSFB beams is that they consist of composite steel-concrete beams with the steel profile embedded in the thickness of the floor; moreover, the double T steel section has the particularity of having the upper flange with a smaller width than the lower flange (for this reason the term cut-off is used; this detail is shown in Fig. 2.4). These beams are obtained by cutting HE240B and HE300B profiles and designed to belong to the gravity load resisting system. For this reason, the adopted structural scheme is the beam simply supported at its ends. This behaviour is obtained by adopting simple beam-to-column connections designed to transmit the shear forces only.

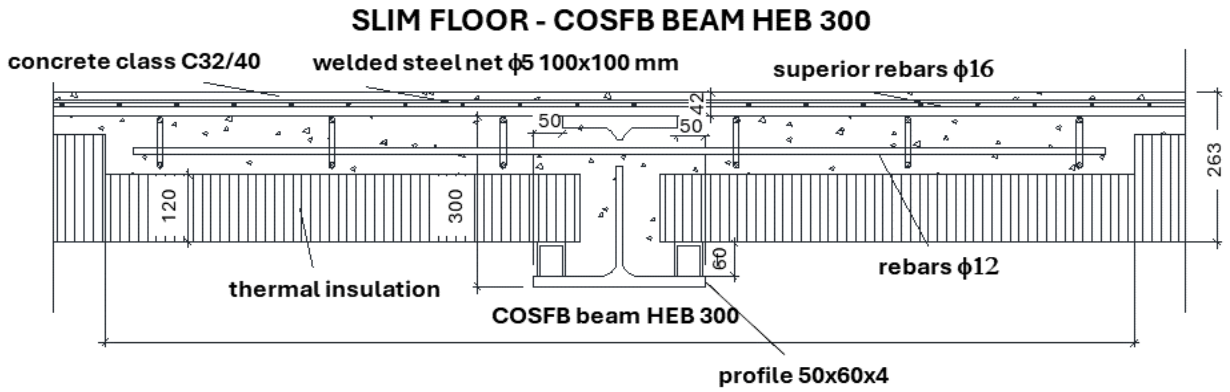

Figure 2.4: *Slim floor system with CoSFB beam*

The checks have been carried out controlling that the maximum bending moments and shear actions were lower than the capacity of the CoSFB beams and that the maximum deflections and the deflections induced by variable loads at SLS were lower than L/250 and L/300, respectively (where L is the span of the beams). Fig. 2.5 depicts the longitudinal frame belonging to the gravity load resisting system.

2.3.4 Seismic-resistant frames

The design of the MRFs, constituting the seismic-resistant structural system, has been carried out according to Italian Code NTC 2018, Eurocode 8 provisions and the Theory of Plastic Mechanism Control (TPMC) considering the seismic action defined referring to the construction site located in Fisciano, characterised by type-B soil and topography class T1.

In particular, TPMC is based on the kinematic theorem of plastic collapse and the concept of the equilibrium curve of the mechanism.

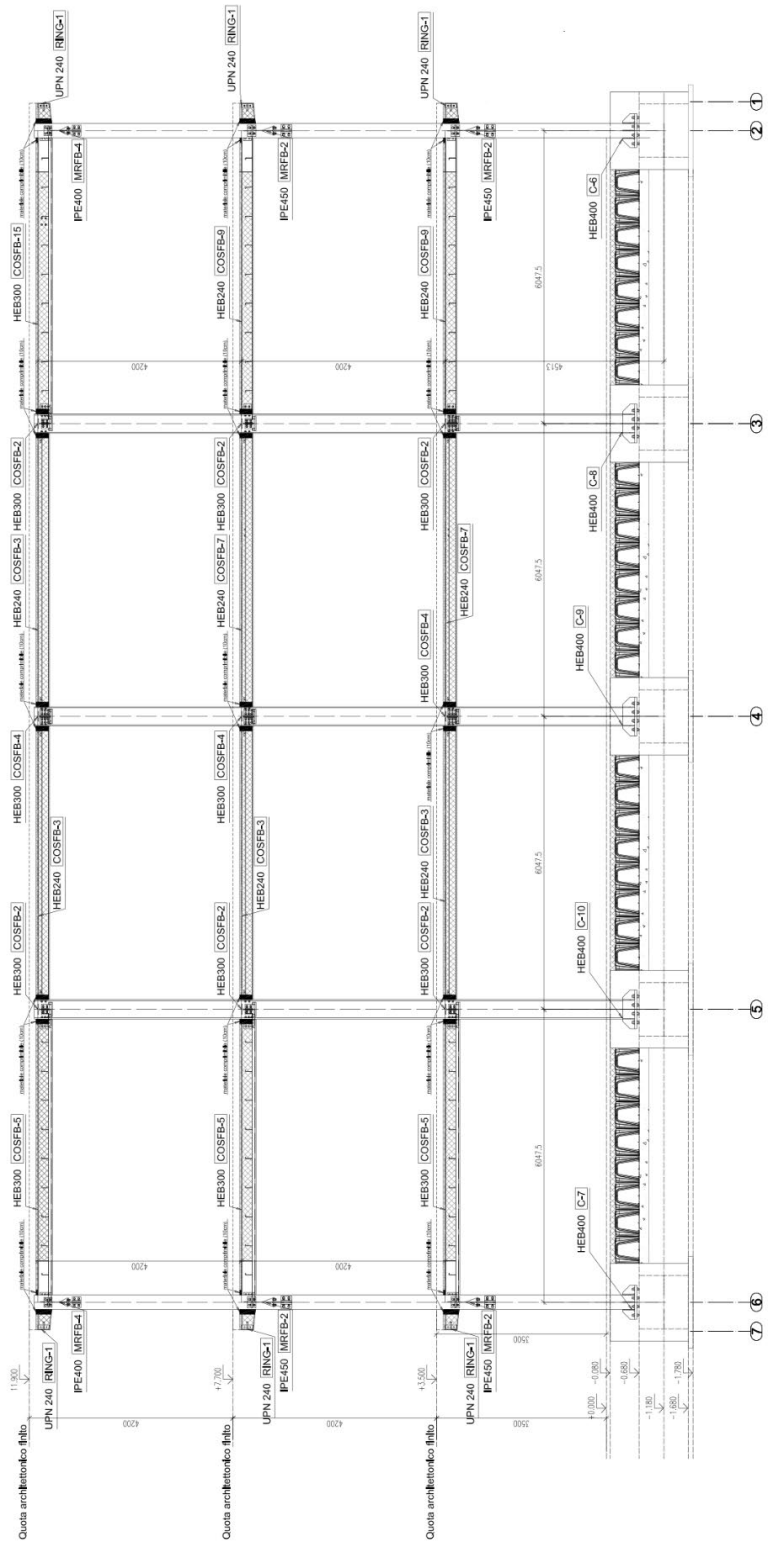

Figure 2.5: *Longitudinal frame of the gravity load resisting system*

The equilibrium curve of any possible collapse mechanism is obtained through a second-order rigid-plastic analysis in which the external work is calculated including the work due to second-order effects induced by the gravitational loads applied to the structure. The kinematic theorem of plastic collapse extended to the concept of mechanism equilibrium curve ensures that, in a

range of displacements compatible with the rotational capacity of the structural elements, the collapse mechanism developed is the one whose equilibrium curve is located below those of all the other possible mechanisms. Thus, the column sections at each level have been designed by imposing that the mechanism equilibrium curve corresponding to the desired global mechanism is below the equilibrium curves of all the undesired mechanisms. The second-order effects are explicitly and rigorously considered through the equilibrium curve of the collapse mechanism.

In the case of the seismic-resistant frames equipped with FREEDAM connections, the TPMC can be easily applied, provided that the internal work of the dissipative zones is suitably evaluated. For this purpose, in writing the internal work equation, the plastic moment of the beams has to be replaced by the sliding resistance moment of the FREEDAM connections. The behaviour of beam-column connections equipped with friction dampers has been considered in the design process as rigid-perfect plastic. Furthermore, according to the second principle of capacity design, the overstrength associated with the variability of the coefficient of friction has also been considered.

The final solution consisted of adopting HEB400 profiles for the columns, IPE450 beams for the first two levels, and IPE400 beams for the top floor (Fig. 2.6). Resistance and stability checks of the columns and beams have been satisfied.

The available rotational capacity has been demonstrated during the previous FREEDAM project by experimental tests according to EC8 provisions and AISC 358-16 prequalification protocols. Bare steel FREEDAM connections were tested during the research work [1] exhibiting excellent seismic performances. The bolted T-stub connecting to top flange of the beam to the column defines the location of the centre of rotation. The bending moment resistance, which corresponds to the slippage of the connection, is simply given by the product between the slippage resistance of the friction damper and the lever arm. This simple and controllable behaviour was confirmed by the experimental tests on bare steel connections. The same behaviour was also confirmed by the pseudo-dynamic tests carried out on a one-bay two-storey building [4], subjected to seismic simulation, where the building deck was constituted by a trapezoidal sheet with concrete topping located on the top flange of the beam.

Conversely, the decks of C3 building are based on the slim floor system and the Cofradal system. In particular, this last system has an important thickness (260 mm) so any possible collaboration with the beam could significantly affect the actual behaviour of the beam-to-column connections of the seismic-resistant system.

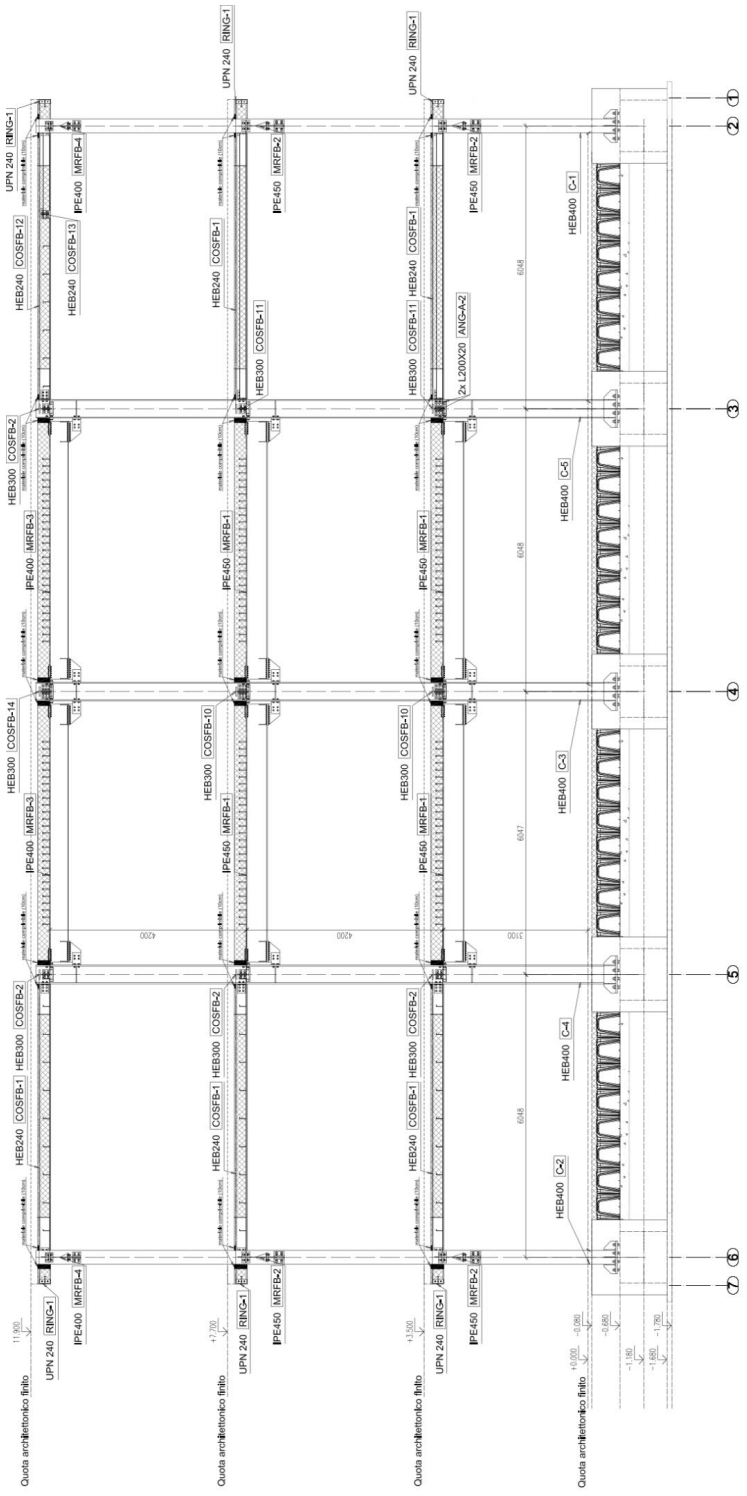

Figure 2.6: *Longitudinal frame of the seismic resisting system*

For the above reasons, an important design issue has concerned the structural details to be adopted to assure that the reinforced concrete slab due to the Cofradal composite floor does not participate in the rotational behaviour of beam-to-column joints and does not modify the intended location of the centre of rotation. To this scope, the seismic-resistant part of the building has been conceived to be completely independent of the gravity load-resisting system. The seismic-resistant part of the building is constituted only by the perimeter frames. Concerning the seis-

mic-resistant bays, this has allowed us to locate the Cofradal deck on the top flange of the beam. Conversely, in the case of non-seismic-resistant bays, the Cofradal deck has been located in the typical position of the slim floor system.

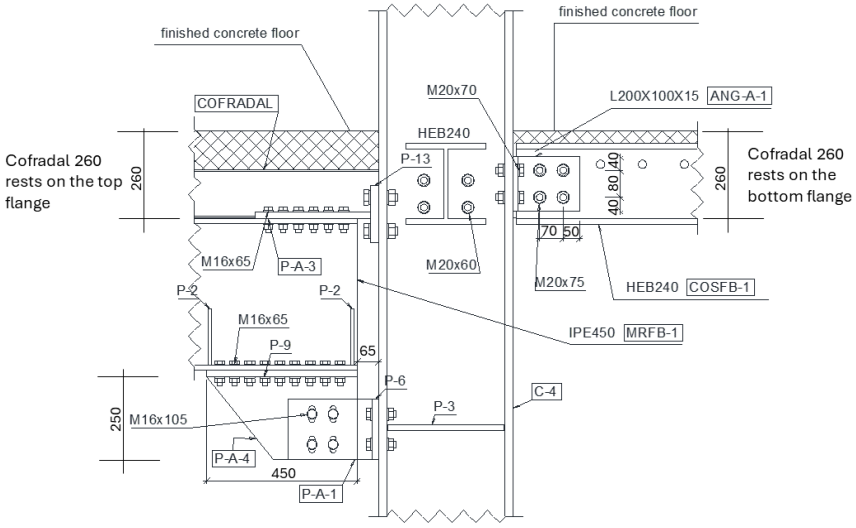

Figure 2.7: *Detail of the connection showing the different locations of the building deck*

This is the reason why the top flanges of the beams are not aligned at the same level (Fig. 2.7). In addition, following the suggestions of EN 1998-1, the shear studs on the beam have not been in the area close to the columns to ensure a bare steel behaviour for the connection. For the same reason, a gap between the slab and the column has been left and filled with very soft material. The disconnection between the slab and the beam-to-column connection is also assured by a carter to be adopted during the concrete casting separating the joint from the slab.

Fig. 2.8 shows the perimeter frame in the transversal direction constituting the seismic resisting system in the same direction. Fig. 2.9 shows one of the transversal frames (Frame 3-3) belonging to the gravity load resisting system.

It is also worthwhile mentioning that Figs. 2.5-2.6 and Figs. 2.8-2.9 show that the column-base connection is embedded in the reinforced concrete foundation. The reinforced concrete foundation is constituted by a grid of foundation beams in the two orthogonal directions, modelled as beams on elastic soil according to the Winkler model. The embedment of the column-base connection was selected with the aim of improving the rotational stiffness of the connection because the building structural model adopted for the design is a 3D-frame with all the columns fixed at their base.

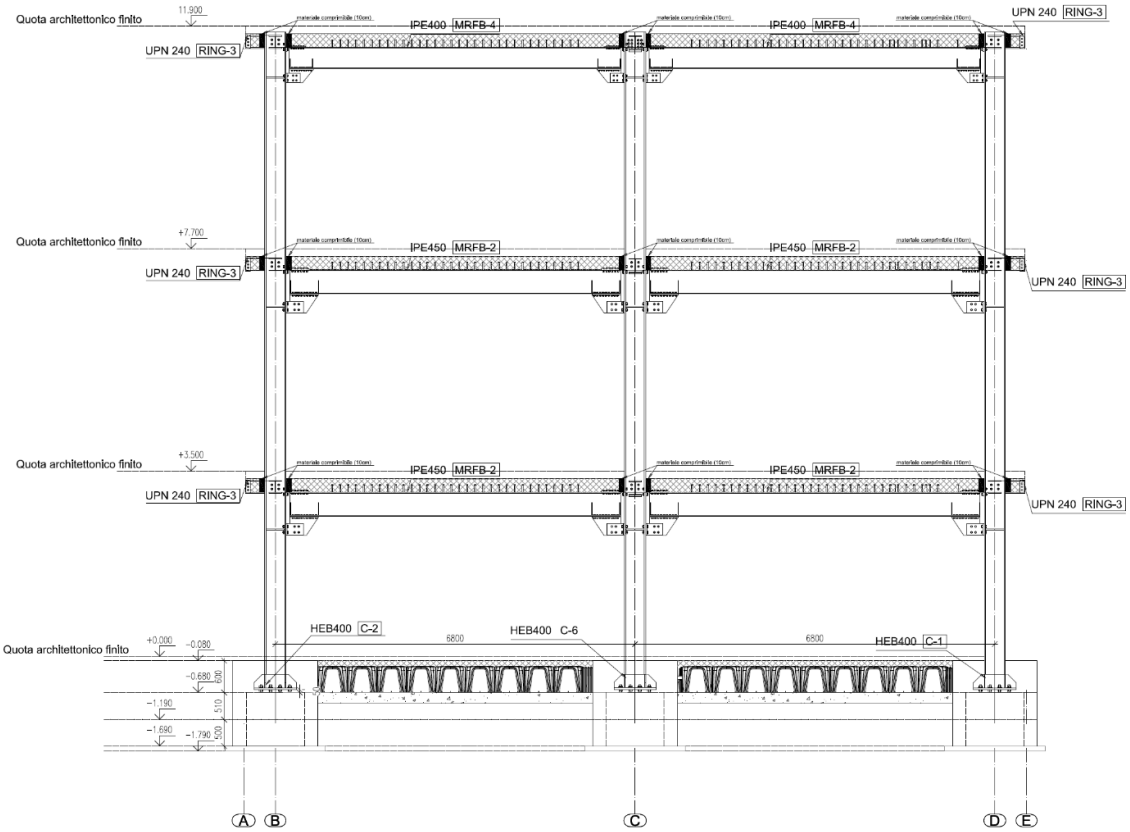

Figure 2.8: *Transversal frame of the seismic resisting system*

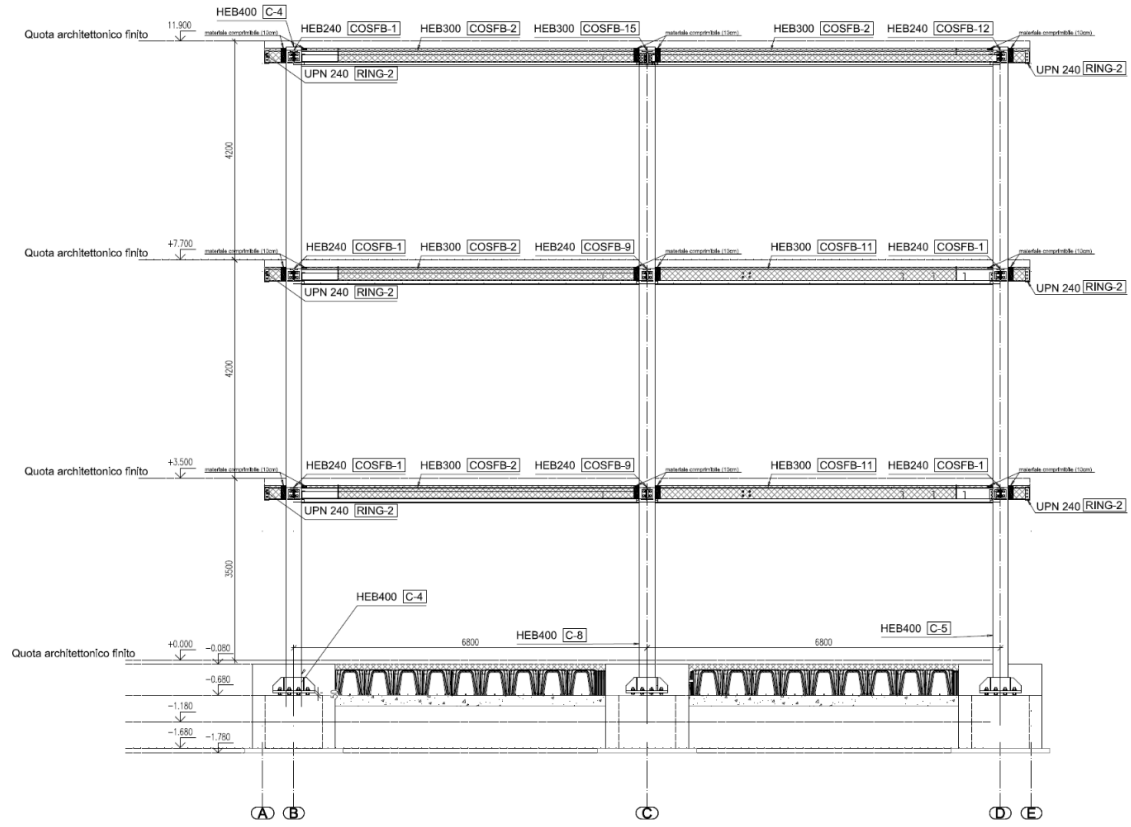

Figure 2.9: *Transversal frame of the gravity load resisting system (Frame 3-3)*

2.4 DESIGN CRITERIA OF THE MAIN STRUCTURAL BODY

As already stated, the two perimeter frames in the longitudinal direction and the two perimeter frames in the transversal directions constitute the seismic load-resisting system.

The two frames in the longitudinal direction have four bays. The internal bays are equipped with FREEDAM connections and, therefore, are moment-resisting bays. Conversely, the external bays are characterized by traditional simple connections designed to transmit the shear forces only. Therefore, the external bays belong to the gravity load-resisting system.

The two frames in the transversal directions have all the bays equipped with FREEDAM connections so that, being moment-resisting, they constitute the seismic-resistant scheme for the transversal direction.

All the inner frames are part of the gravity load-resisting system, so that all the beam-to-column connections are traditional simple connections designed to transmit the shear forces only.

With reference to the first and the second floor, the permanent structural load G_{k1} is equal to $3.25\ kN/m^2$ while the permanent non-structural load G_{k2} is equal to $1.85\ kN/m^2$; the variable (live) load Q_k is equal to $3.00\ kN/m^2$. With reference to the roof, the permanent structural load G_{k1} is equal to $3.25\ kN/m^2$ while the permanent non-structural load G_{k2} is equal to $2.20\ kN/m^2$; the variable (live) load Q_k is equal to $0.50\ kN/m^2$. The line load due to the cladding elements constituting the façade is equal to $4.50\ kN/m$ while the line load due to the parapet on the roof is equal to $1.12\ kN/m$. Accounting for the climatic zone of the construction site, the snow load on the roof is equal to $0.59\ kN/m^2$ while, concerning the wind action, the reference kinetic pressure is $0.59\ kN/m^2$.

According to the Italian Technical Code for Constructions (NTC 2018), the nominal life of the structure is $V_N = 50\ years$ and the building use coefficient is $C_U = 1.5$ leading to a building reference life $V_R = 75\ years$.

With reference to the construction site (Fisciano, SA), Fig. 2.10 show the elastic design spectra corresponding to the different limit states defined by NTC 2018 corresponding to immediate occupancy (IO), damage limitation (DL), life safety (LS) and collapse prevention (CP) limit states. The seismic action to be considered for each limit state is characterized by a probability of exceedance equal to 81%, 63%, 10% and 5%, respectively, in 75 years, i.e. in in the building reference life. They have been derived for soil category B and topographic class T1.

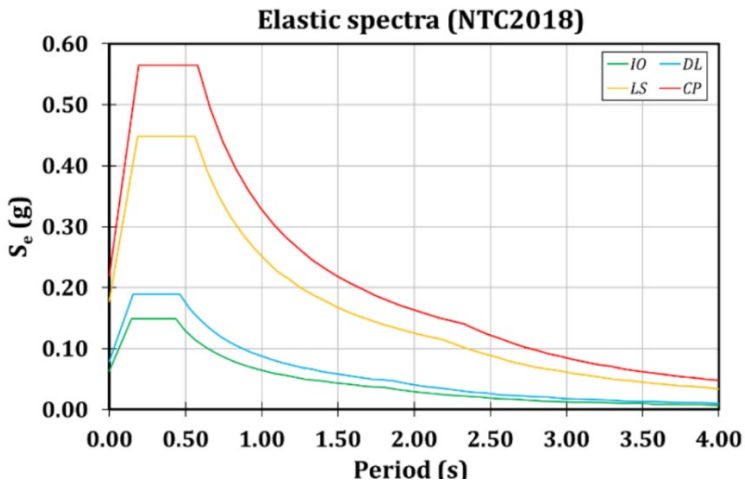

Figure 2.10: *Seismic action corresponding to the design limit states for the construction site*

From the point of view of the adopted design criteria, attention was focused on the slippage of FREEDAM connections. They are equipped with friction dampers whose slippage force governs the design bending moment of the connection. In particular, the following design criteria were adopted:

- The slippage of the friction dampers of the FREEDAM beam-to-column connections has to be prevented under the load combinations corresponding to the ultimate limit state under gravity load combinations, i.e. under the following load combinations:

  $$F_d = \gamma_{g1} G_{k1} + \gamma_{g2} G_{k2} + \gamma_q Q_k$$

  where G_{k1} is the characteristic value of the permanent (dead) structural load, G_{k2} is the characteristic value of the permanent (dead) non-structural load, Q_k is the characteristic value of the variable (live or snow) load depending on the building use and γ_{g1}, γ_{g2} and γ_q are the corresponding values of the partial safety factors.
- The slippage of the friction dampers of the FREEDAM beam-to-column connections has to be prevented under the load combination corresponding to the ultimate limit state under gravity loads and wind action.
- The slippage of the friction dampers of the FREEDAM beam-to-column connections has to be prevented under the load combination corresponding to the serviceability limit state under gravity loads and seismic action. In other words, the connection slippage has to be prevented under the seismic action corresponding to a return period comparable to the service or nominal life of the structure.
- The slippage of the friction dampers of the FREEDAM beam-to-column connections has to be prevented under the seismic load combination corresponding to the ultimate limit

state, i.e. earthquake action having 475 years return period, with the seismic forces scaled down according to the q-factor for moment-resisting frames.

- The connection slippage has to occur to dissipate the earthquake input energy as soon as the bending moment occurring in the connection exceeds the maximum value resulting from the above-mentioned design requirements.

The application of the above-mentioned design criteria has led to the choice of the standardized FREEDAM devices leading to beam-to-column connections equipped with friction dampers whose main properties are given in Figs. 2.11-2.13.

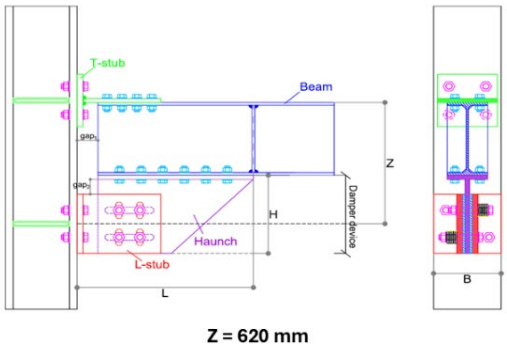

MARK	
FREEDAM - IPE 450 / 0.3	
DEVICE PROPERTIES	
Name	D1
$F_{slip,Rd}$	292.4 kN
$M_{j,Rd}$	181 kNm
Bolts	M16 HV 10.9
Number of bolts, n_b	4
Number of surfaces, n_s	2
Preload force, $F_{p,d}$	79.3 kN
GEOMETRY	
L	505 mm
H	260 mm
B	221 mm
MINIMUM COLUMN SIZE	
HE 240 B	

Figure 2.11: *Main properties of FREEDAM connections adopted for the internal bays of first and second storey of the longitudinal perimeter frames*

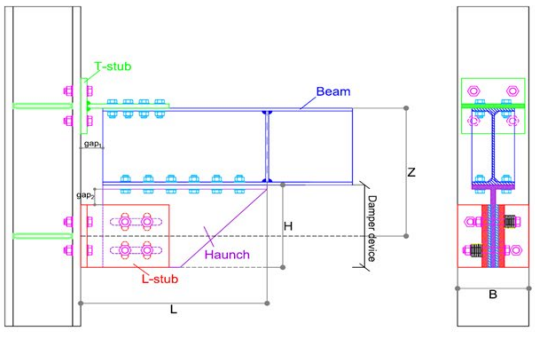

MARK	
FREEDAM - IPE 450 / 0.4	
DEVICE PROPERTIES	
Name	D-2A
$F_{slip,Rd}$	345.3 kN
$M_{j,Rd}$	242 kNm
Bolts	M20 HV 10.9
Number of bolts, n_b	4
Number of surfaces, n_s	2
Preload force, $F_{p,d}$	93.64 kN
GEOMETRY	
L	605 mm
H	360 mm
B	256 mm
MINIMUM COLUMN SIZE	
HE 280 B	

Figure 2.12: *Main properties of FREEDAM connections adopted for first and second storey of the transversal perimeter frames*

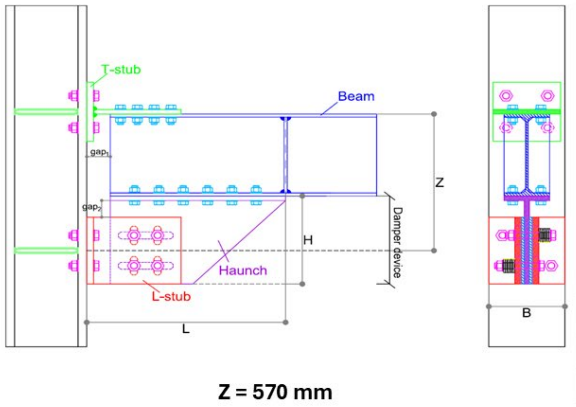

MARK	
FREEDAM - IPE 400 / 0.3	
DEVICE PROPERTIES	
Name	D1
$F_{slip,Rd}$	244.2 kN
$M_{j,Rd}$	139 kNm
Bolts	M16 HV 10.9
Number of bolts, n_b	4
Number of surfaces, n_s	2
Preload force, $F_{p,d}$	66.23 kN
GEOMETRY	
L	505 mm
H	260 mm
B	221 mm
MINIMUM COLUMN SIZE	
HE 240 B	

Figure 2.13: *Main properties of FREEDAM connections adopted for the top storey of the building*

In particular, Fig. 2.11 shows the main properties of FREEDAM connections adopted for the internal bays of first and second storey of the longitudinal perimeter frames. Fig. 2.12 concerns first and second storey of the transversal perimeter frames. Finally, Fig. 2.13 provides the main properties of FREEDAM connections adopted for the top storey of the building. All these figures provide the main geometrical properties of the damper with the number of bolts n_b, the bolt diameter and the bolt class, the number of contact surfaces n_s, the design value of the bolts' preload $F_{p.d}$, the resulting design resistance of the friction damper $F_{slip.Rd}$, the lever arm Z and the resulting value of the design bending moment $M_{slip.Rd}$ leading to the slippage of the beam-to-column connection.

In all the cases, the friction pads are coated by thermal spray technology with M4 material which has been selected among all the different coating materials tested within the FREEDAM project.

2.5 STAIRCASE-ELEVATOR BODY STRUCTURE

The structure of the stair-elevator body is designed in such a way as to be structurally independent of the structure of the main building (Fig. 2.14). In particular, it consists of a braced steel castle structure. The castle has four columns made up of a pair of IPE240 profiles arranged in a cross in welded composition. The castle has six levels, three of which coincide with the levels of the decks of the main building.

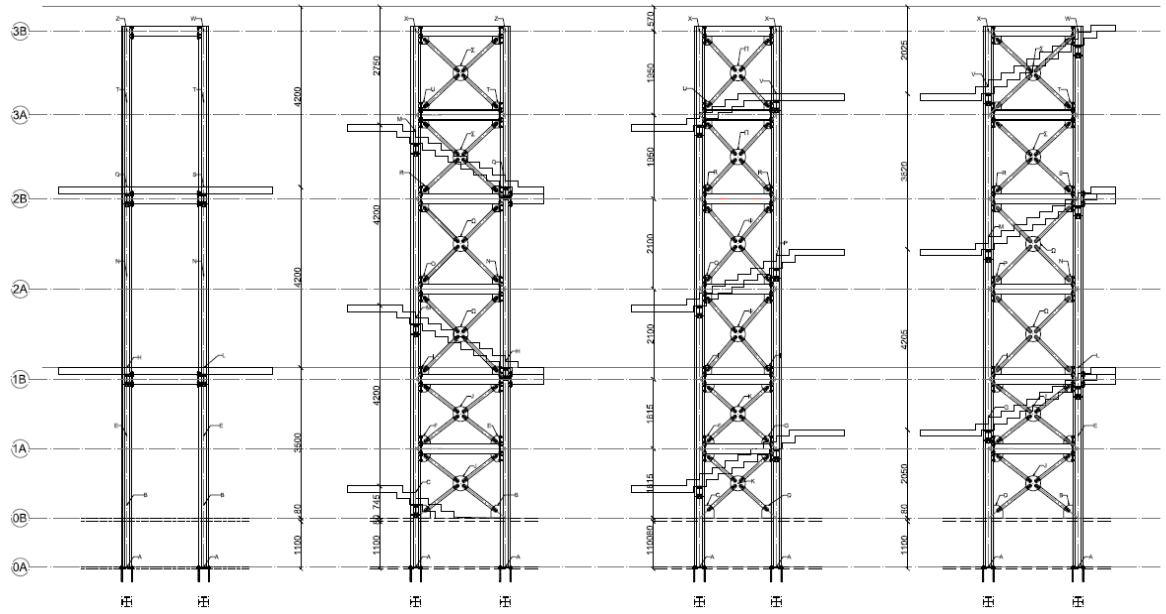

Figure 2.14: *Staircase-elevator body*

The beams are made of IPE240 profiles. The braces are made of CHS 76.1x3.2 round tubular profiles. All members are made of S355 steel. The flights of stairs and the landings are made using a reinforced concrete slab, folded according to the development of the steps, which rests on cantilever beams made of IPE240 profiles, connected to the castle. The beam-to-column connections are bolted according to the end-plate type. The connections of the bracing diagonals are made using a bolted system of the gusset and fork type. The foundation-column connections are made using a base plate with anchor bolts, embedded in the concrete casting for a length equal to the size of the webs of the foundation beams. Therefore, the column-foundation connection can be considered rigid.

Fig. 2.15 shows the plan layouts for the different levels of the staircase-elevator body structure pointing out the three flights and the two intermediate landings supported by the cantilever beams (IPE 240) bolted to the columns. It is possible to note that the column sections are composed by welding using a couple of IPE240 standard shapes.

Fig. 2.16 shows some examples of the connections between the bracing members and the primary structural elements, beams and columns, of the steel castle structure. Also in this figure, it is possible to note the column section composed by welding using a couple of IPE240 standard shapes.

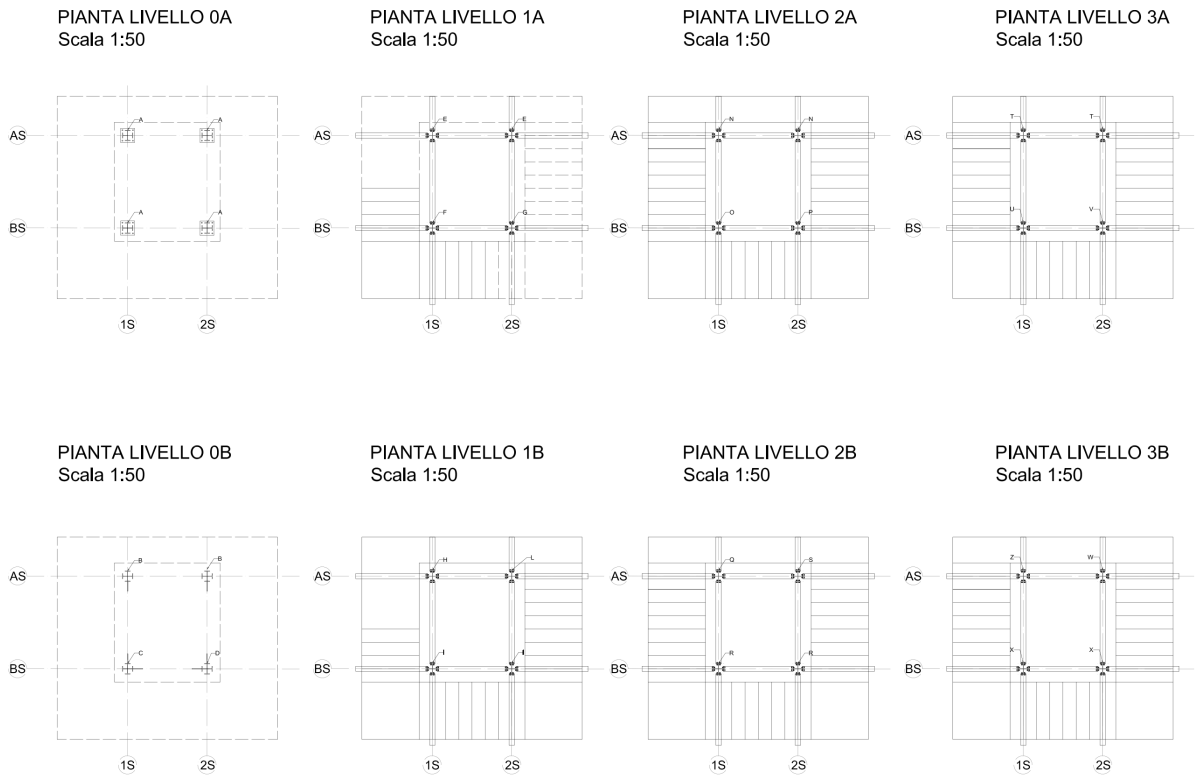

Figure 2.15: *Plan layouts for the different levels of the staircase-elevator body structure*

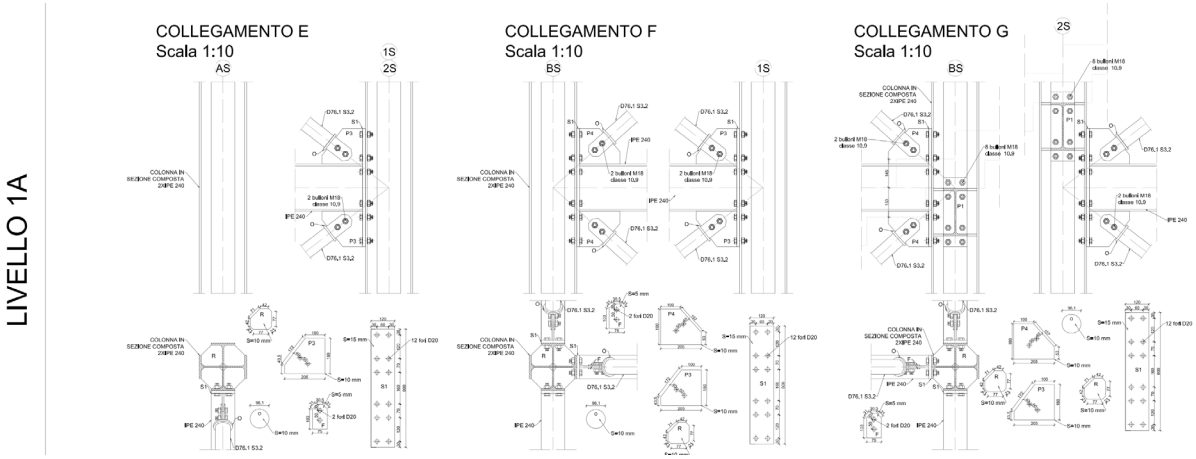

Figure 2.16: *Connection of bracing members to primary structural elements*

2.6 REFERENCES

[1] Piluso V (Coordinator), Rizzano G, Latour M, Montuori R, Nastri E, Francavilla AB, Di Benedetto S, Landolfo R, D'Aniello M, Simões da Silva L, Santiago A, Santos AF, Jaspart J-P, Demonceau J-F (2022) Seismic Design of Steel Structures with FREE from DAMage Steel Connections, 1st Edition, March 2022, Published by: ECCS – European Convention for Constructional Steelwork, ISBN: 978-92-9147-182-9.

[2] Di Lauro F, Montuori R, Nastri E, Piluso V (2019) Partial safety factors and overstrength coefficient evaluation for the design of connections equipped with friction dampers, Engineering Structures, 178, pp. 645-655.

[3] Francavilla AB, Latour M, Piluso V, Rizzano G (2020) Design criteria for beam-to-column connections equipped with friction devices, Journal of Constructional Steel Research, 172, art. no. 106240.

[4] Di Benedetto S, Francavilla AB, Latour M, Piluso V, Rizzano G (2022) Experimental response of a large-scale two-storey steel building equipped with low-yielding friction joints, Soil Dynamics and Earthquake Engineering, Volume 152, 107022, ISSN 0267-7261, https: //doi.org/10.1016/ j.soildyn.2021.107022, 2022.

CHAPTER 3

Seismic Performance: Testing and Analysis

3.1 DESCRIPTION OF THE EXPERIMENTAL CAMPAIGN

As part of the DREAMERS project, an extensive experimental campaign was carried out at the StrEngTH Laboratory of the University of Salerno (UNISA) to investigate the seismic performance of FREEDAM beam-to-column joints, specifically designed for implementation in the demonstration building. The objective was to determine the moment–rotation response of external joints under realistic seismic demands, using the "Design Assisted by Testing" (DAT) methodology in accordance with EN 1990 [1] and AISC 358-18 [2] provisions.

Four full-scale cyclic tests were performed: two quasi-static (low velocity) and two dynamic (high velocity), simulating various seismic intensity scenarios. The tested configuration, referred to as FREEDAM – D1 – IPE 450 / 0.3, was selected for its critical role in the global seismic response of the DREAMERS moment-resisting frame (MRF) system. This joint typology is adopted uniformly across all stories of the building, with a utilisation ratio of 0.3, thus representing a key element of the structural design (Fig. 3.1).

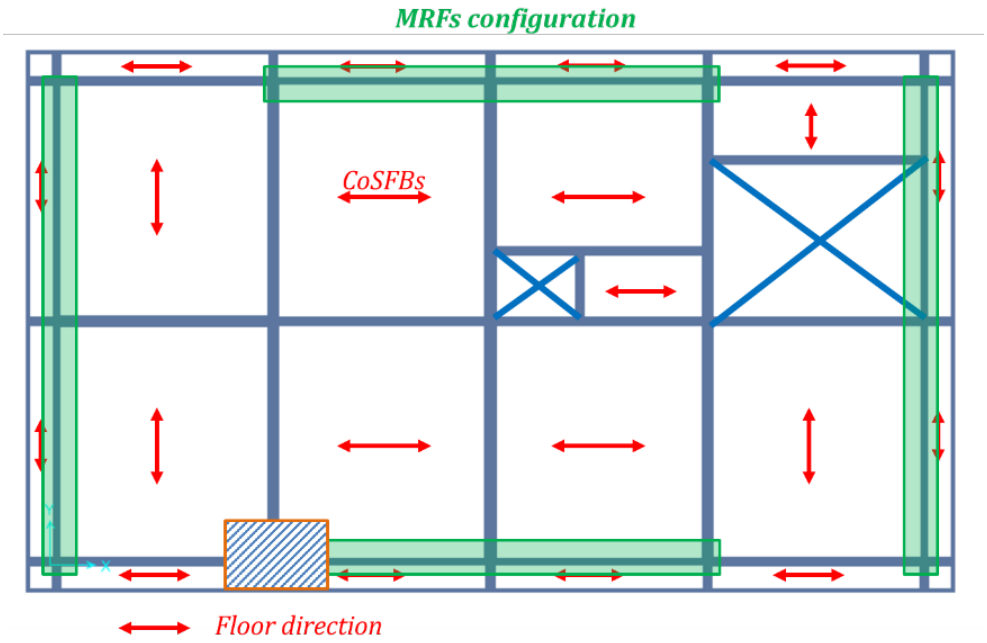

Figure 3.1: *Schematics of the DREAMERS floor plan and indication of the joint tested ( )*

All specimens reflected the actual structural configuration of the first-storey external joints of the X-direction MRF. Each subassembly included:

- A FREEDAM Device D1;
- An IPE 450 beam;
- An HEB 400 column;
- Secondary HE 300 B beams;
- A Cofradal® 260 composite steel–concrete floor system supplied by ArcelorMittal.

Joints were designed in compliance with Eurocodes and constructed using detailed production drawings developed via Advance Steel software to replicate all design constraints and interfaces with the floor system.

It is essential to emphasise that the joint tested, standardised during the FREEDAM research project, is engineered to remain elastic up to a bending moment capacity of approximately 340 kNm. Moreover, the design incorporates a specific safety factor to account for the long-term behaviour of the bolting assemblies. However, for the purposes of the short-duration tests presented in this report, this partial safety factor has been omitted as creep effects are not a concern. This approach ensures that the test accurately reflects the joint's immediate performance without the influence of long-term degradation factors.

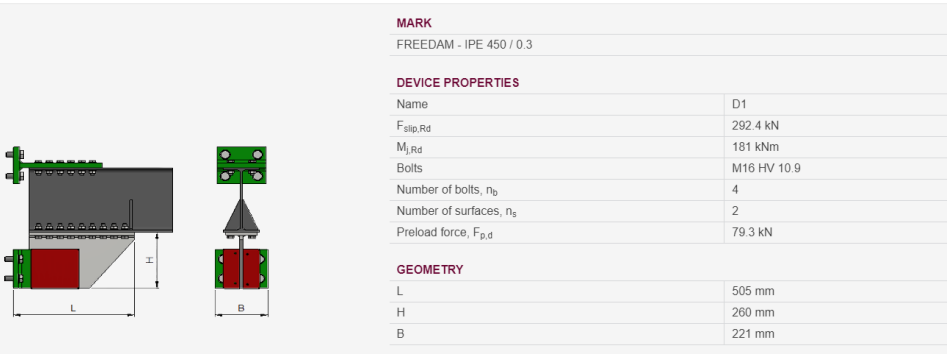

MARK	
FREEDAM - IPE 450 / 0.3	
DEVICE PROPERTIES	
Name	D1
$F_{slip,Rd}$	292.4 kN
$M_{j,Rd}$	181 kNm
Bolts	M16 HV 10.9
Number of bolts, n_b	4
Number of surfaces, n_s	2
Preload force, $F_{p,d}$	79.3 kN
GEOMETRY	
L	505 mm
H	260 mm
B	221 mm

Figure 3.2: *Characteristics of the joint tested*

The specimen was designed following the FREEDAM design guidelines [3], EN 1993-1-1 [4], and EN 1993-1-8 [5], ensuring that every detail of the joint's configuration was accurately represented. The production of the specimens was facilitated through the use of Advance Steel software, which allowed for precise modelling and visualisation of the joint's structural elements. The design process involved several critical steps to ensure that the specimen would meet the specific requirements of the UNISA Strength Laboratory. The design also incorporated the particularities of the laboratory setup, taking into account the dimensions, load capacities, and support conditions of the test rig used at the UNISA StrEngTH Laboratory. This careful integration ensured that the test environment could replicate real-world conditions as closely as possible, providing valid and reliable results.

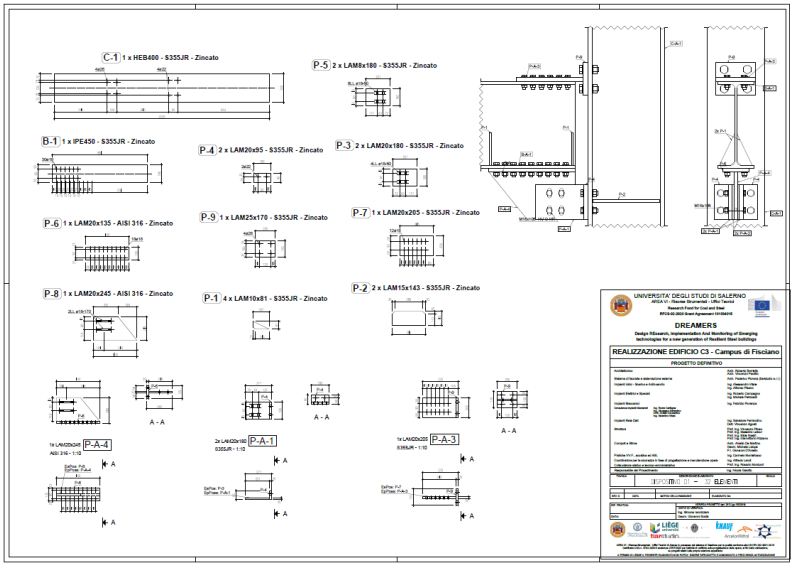

Figure 3.3: *Example of production drawing for the tested Device*

The test setup itself was designed to be comprehensive and aimed at simulating realistic structural loads and stresses. The joint specimen was securely positioned in a custom test rig, which was designed to apply forces and moments that reflect real-life scenarios. This rig was equipped to handle the complex loading conditions that the joint would experience during the test, ensuring that the applied loads could accurately mimic those that would be applied in an actual building structure. High-precision sensors were strategically placed throughout the setup to measure displacements and forces during the testing process. These sensors were calibrated to provide accurate and reliable data, capturing the joint's response to the applied loads. The experimental program consisted of four distinct tests performed at increasing values of the velocity from the quasi-static up to a displacement velocity imposed at the beam end equal to 150 mm/s. The test matrix is summarised in the next table for convenience.

Table 3.1: *Test matrix*

Test	Label	Load protocol	Test velocity
1	J1 LV	EQUALJOINTS	Quasi-static
2	J1 HV_50		50 mm/s
3	J2 HV_100		100 mm/s
4	J2 HV_150		150 mm/s

The tests include a first run (J1 LV and J2 HV_100) and a repetition (J1 HV_50 and J2 HV_150) after substitution of the friction pads and bolts. This approach allowed to demonstrate the repairability of the joints and repeatability of the joint properties.

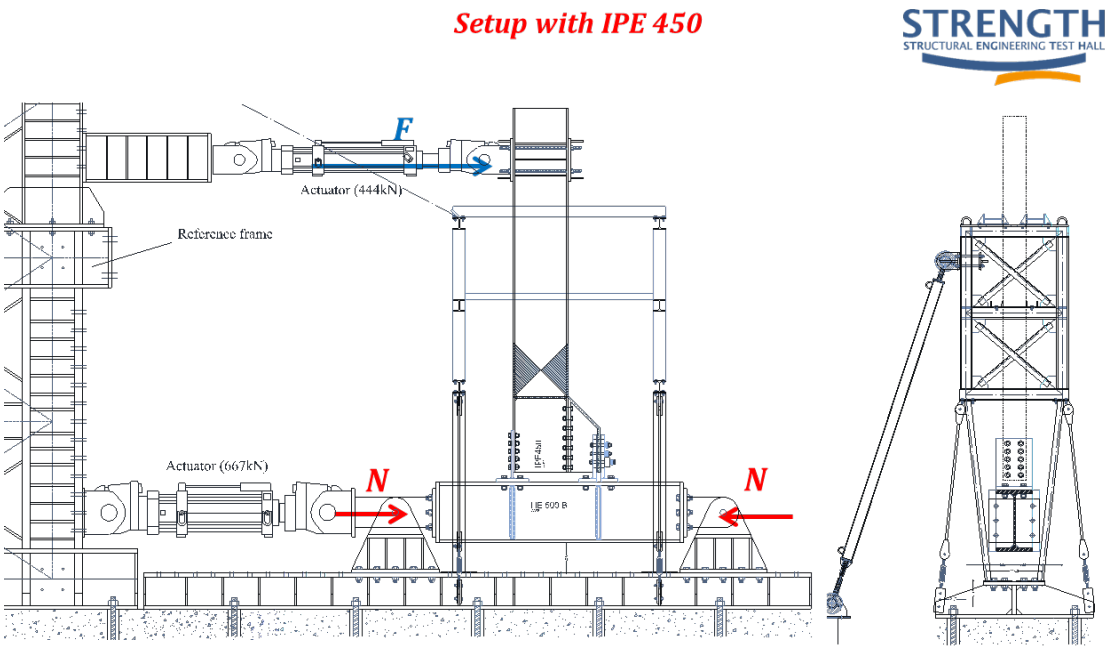

Figure 3.4: *Test rig*

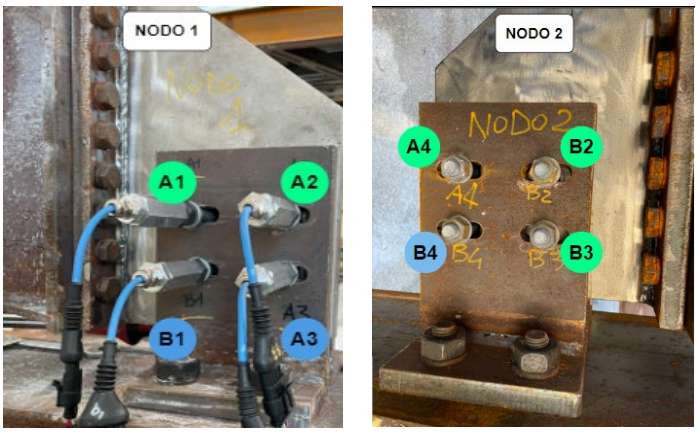

Figure 3.5: *Joints J1 and J2*

The loading protocol was carefully designed to reflect codified scenarios, as illustrated in the provided displacement-time graph. The joint was subjected to cyclic loading with progressively increasing amplitude. The displacement applied varied according to the EQUALJOINTS [6] protocol in order to impose chord rotations between 0.00375 rads and 0.04 rads.

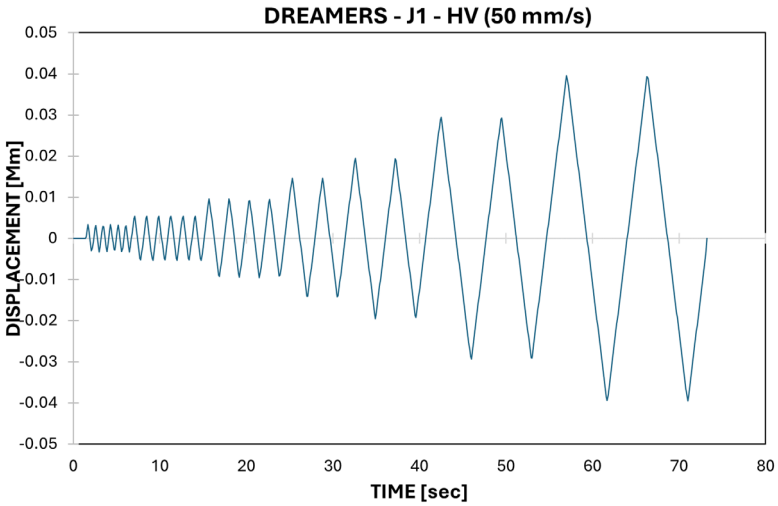

Figure 3.6: *EQUALJOINTS loading protocol*

The preparation of the specimen involved several critical steps, documented in a series of photographs. These images showcase the assembly of the joint components, the installation of sensors and other instrumentation, and the final setup ready for testing. Each stage of the preparation was carefully executed to ensure the accuracy and reliability of the test results.

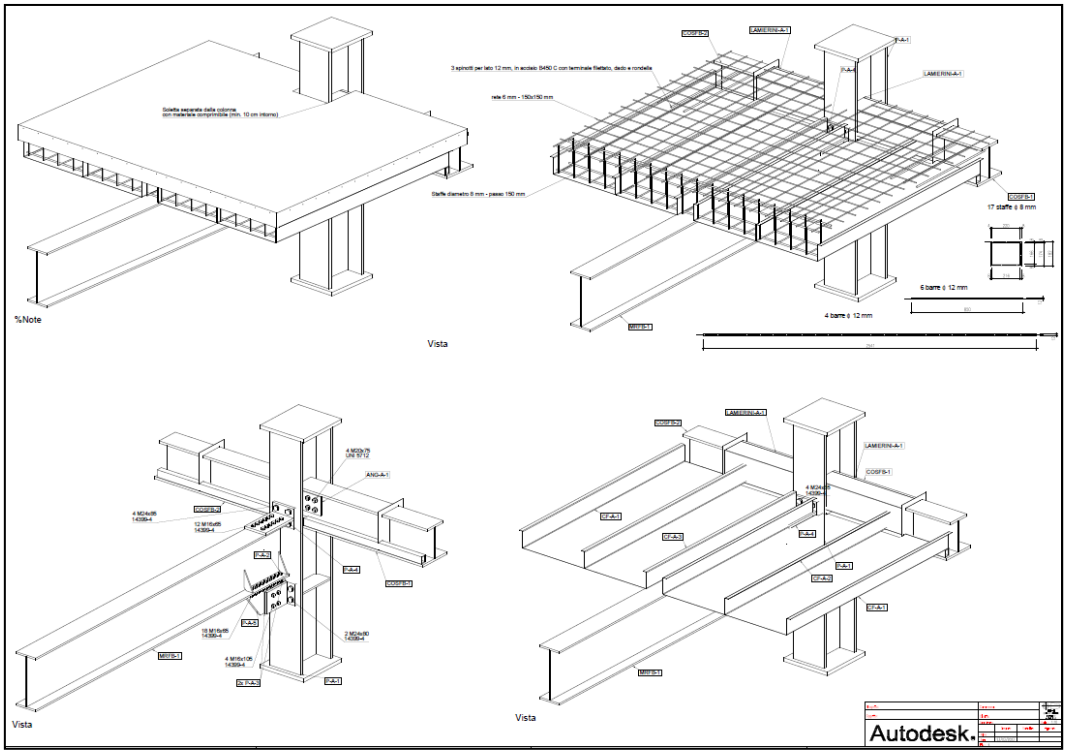

Figure 3.7: *3D construction view of the tested joints*

In the initial stages of the specimen preparation, the structural components were assembled and placed in a designated area of the laboratory. The provided image shows the primary steel framework consisting of beams and columns arranged according to the design specifications. Following the initial setup, the Cofradal system was placed onto the specimen. This composite

slab system typically consists of steel decking and concrete, designed to work together to support gravity loads. The images show the Cofradal in place, with the steel reinforcement visible through the grid of rebars. This setup is essential to simulate real-world conditions where the slab interacts with the steel framework. The placement of the Cofradal was executed meticulously to ensure its correct positioning.

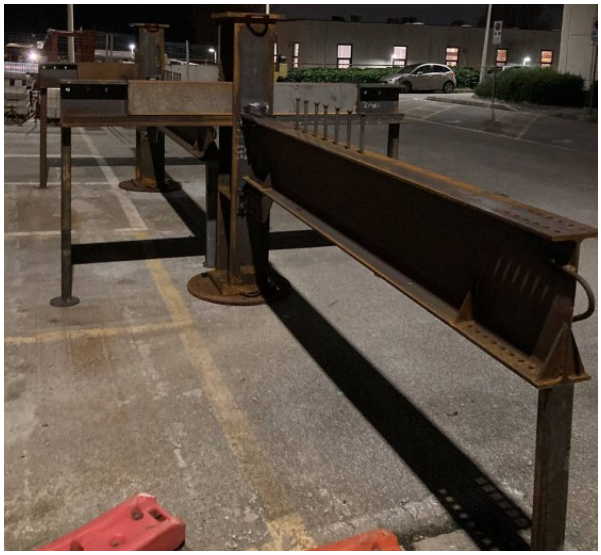

***Figure 3.8**: Specimen before placement of Cofradal*

A detailed close-up of the ring beam at the beam end is provided, highlighting critical aspects of the joint and connection detailing. Notably, there are no studs close to the joint area, and concrete has not yet been placed within the column sections. This image is crucial for understanding the joint behaviour under load, as it reveals the reinforcement detailing and the intended areas for concrete infill. This setup allows for precise monitoring of the joint's performance, especially under bending and shear forces during the testing phase.

***Figure 3.9:** Specimen after placement of Cofradal*

The final stage of specimen preparation is depicted in the image showing the specimens ready after a curing period of 28 days. By this point, the concrete within the Cofradal system has fully

set, ensuring it has reached the necessary strength for testing. The structural elements are now integrated, and the specimen stands prepared for load application.

Figure 3.10: *Specimen after the curing of concrete*

The next image provides a close-up view of the disconnection detail at the beam end within the specimen assembly. Notably, the area around the joint does not have studs, which are typically used to enhance the connection between steel and concrete in composite structures. This absence of studs near the joint is significant as it directly influences the load transfer mechanism and the interaction between the beam and the slab.

Figure 3.11: *Disconnection detail in the joint area*

Additionally, the column section adjacent to the beam joint is shown without concrete infill. The lack of concrete in the column at this stage indicates that the structural behaviour being studied

focuses on the steel framework's response without the additional composite action provided by the concrete. This setup is likely intended to isolate and analyse the steel joint's performance under specific loading conditions before integrating the concrete to study the composite behaviour.

3.2 TEST RESULTS

The objective of the tests is to determine the moment-rotation response of the external beam-to-column joints under conditions similar to those existing in the DREAMERS pilot building. This performance evaluation aims to ensure that the joints can sustain the expected loads and rotations without experiencing significant degradation or failure.

The design approach for the FREEDAM joints incorporates a detailed assessment of both the Ultimate Limit State (ULS) and the Serviceability Limit State (SLS) parameters. These parameters are essential for ensuring that the joints provide sufficient strength and stiffness under various loading scenarios, including seismic events. The expected performance criteria are based on the following considerations:

- Moment Capacity: The joints are designed to remain elastic up to a bending moment capacity of approximately 340 kNm. This capacity ensures that the joints can withstand significant moments without yielding, thereby maintaining the structural integrity of the building during severe seismic events.
- Slip Resistance: The device slip resistance is specified at 292 kN (corresponding to a moment resistance of 181 kNm).
- Load Transfer Efficiency: The absence of studs near the joint area and the non-filled concrete columns in the initial setup are intended to isolate the steel joint's performance. This configuration helps to understand the pure steel response and subsequently, the composite action when concrete is introduced.

The combination of these performance criteria provides a comprehensive understanding of the joints' behaviour under realistic conditions. The expected outcomes from these tests will inform future design modifications and ensure that the FREEDAM joints meet the necessary safety and performance standards as required by both AISC and EC0 guidelines. This thorough testing process will ultimately contribute to the resilience and robustness of the DREAMERS building, demonstrating its ability to withstand seismic forces and other dynamic loads effectively.

The experimental tests conducted on the beam-to-column joints yielded results that were entirely consistent with the anticipated behaviour, confirming the accuracy and efficiency of the proposed design. Throughout all tested specimens, minor yielding of T-stubs and L-stubs was observed,

which underlines the efficiency of the design in maintaining structural integrity allowing an easy repair even after a severe seismic event. The energy dissipation during the tests was provided solely by the FREEDAM friction dampers, leaving all other structural elements practically undamaged at the conclusion of the tests.

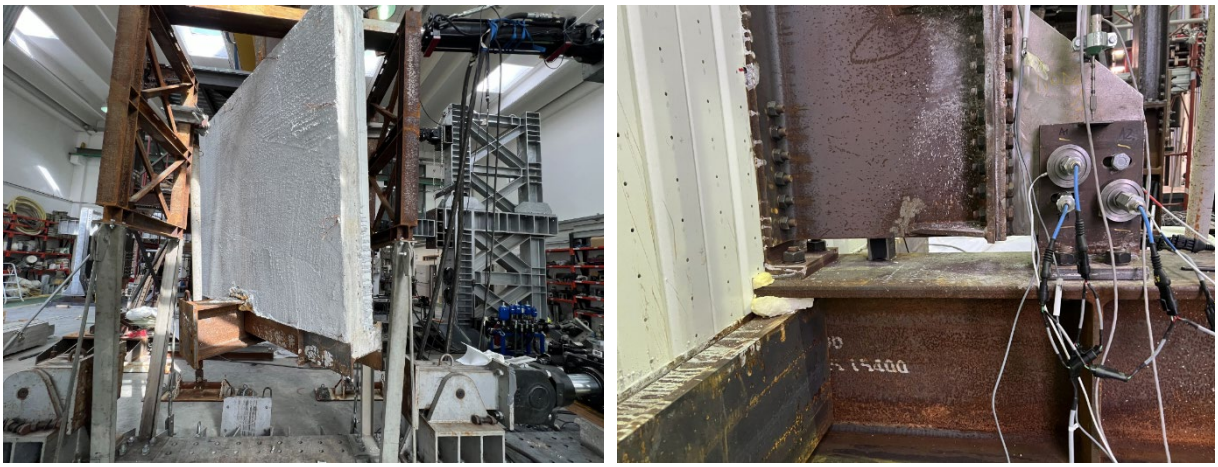

Figure 3.12: *Specimen during positioning and before the start of the test*

This report highlights the results of the four tests executed: J1 LV, J1 HV_50, J2 HV_100 and J2 HV_150. The ID tag is associated with a specific code for each unit, ensuring precise identification and differentiation. J1 or J2 individuates the specimen, LV or HV stands for Low Velocity or High Velocity and 50, 100 or 150 stands for the test velocity expressed in terms of mm/s of actuator speed.

All the tests demonstrated both global and local behaviours that are aligned with predictions. The non-dissipative components remained within the elastic range, with energy dissipation managed entirely by the friction damper. The joint behaviour was stable, showing no significant strength degradation. However, due to parasite bending of the T-stub web plates and variations in bolt forces under hogging/sagging moments, the behaviour was asymmetrical. The maximum bending moment due to hogging or sagging actions differed by approximately 25-30%.

Figure 3.13: *Sensors placed on the specimen before the test*

The next figures depict the bending moment vs rotation diagrams, calculated by multiplying the actuator-applied force by the distance between the load application point and the column axis (Lb=2910 mm). The displacement (δ) was measured at the load application point. The hysteretic loops, as shown in the figures, initially featured a higher force slippage, stabilising into consistent loops throughout the loading history. These observations are consistent with the outcomes of previous findings within the former FREEDAM research project [3].

The friction coefficients observed were in line with predictions, with initial peaks corresponding to the static friction coefficient and stabilized cycles aligning with the dynamic friction coefficient. Variations in slip force were noted due to the flexibility of the steel L-stubs, which caused oscillations in bolt forces under different bending moments.

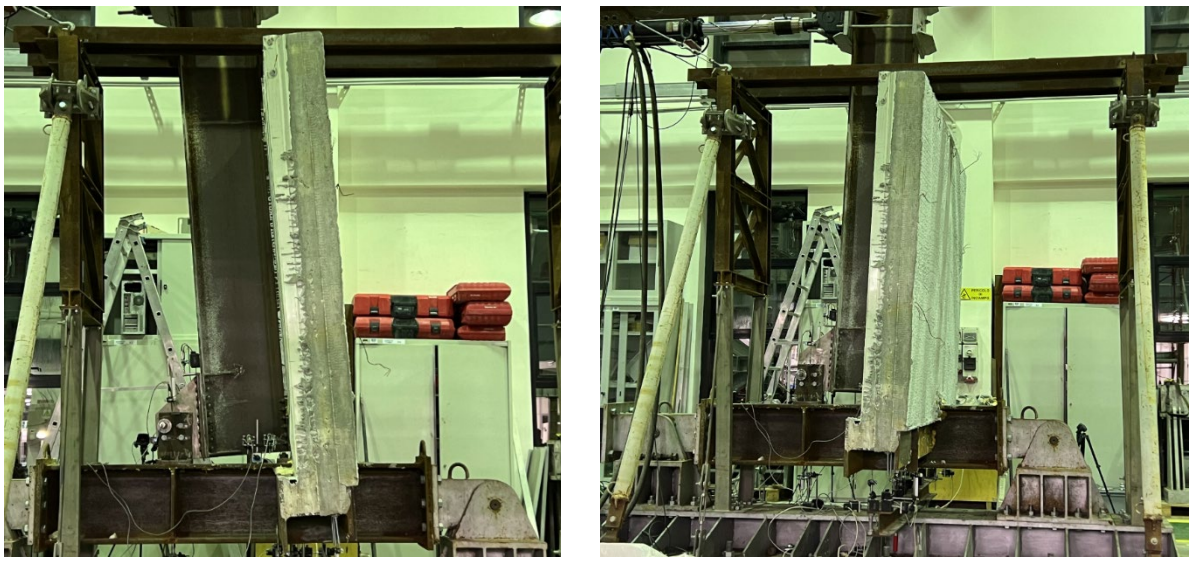

Figure 3.14: *Peak amplitude and specimen at the end of the test*

The hysteretic loops for all joints were similar, highlighting consistent performance across different specimens. The loops were wide and stable, indicating large energy dissipation with negligible degradation in stiffness and resistance. The bolt preloads and variations during tests were monitored using ultrasonic measurers manufactured by TOKBO srl, a company of the Agrati group. Initially, a loosening of bolts was observed, stabilising as displacement cycles increased. At peak displacement cycles, the bolt forces regained their initial values, confirming the robustness of the connection. As mentioned, for bolt preload monitoring, TOKBO sensors were employed, providing accurate and real-time data on clamping force. The TOKBO system is an advanced Intelligent Talking Bolt Network developed through a collaboration between Agrati SpA and the start-up accelerator e-Novia. This system integrates IoT technology into fastening elements, making it a benchmark in the fastener industry for combining mechanical components with digital electronics. Linear displacement transducers were also used for

measuring displacements, ensuring precise tracking of joint movements and responses throughout the tests.

Figure 3.15: *Damage patterns (negligible damage in the floor, only slight local buckling of the steel sheeting)*

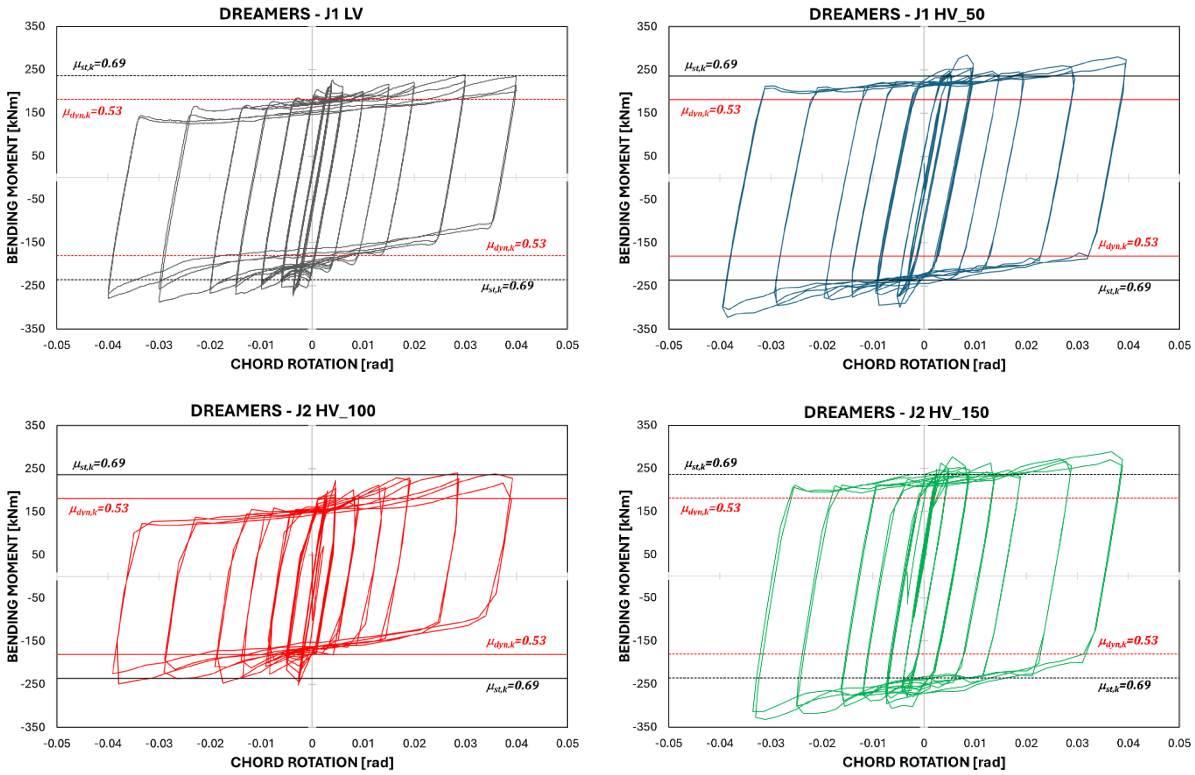

Figure 3.16: *Moment-rotation curves of the four specimens*

3.3 FE MODELLING

3.3.1 Generality

The numerical analyses were carried out by means of the general-purpose software Abaqus/CAE 6.14 [7]. In order to better understand the behaviour of the joint assembly, two different models were finalised (Fig. 3.17):

- A preliminary model, taking into account the steel members only.
- A definitive model, taking into account the steel members and the composite deck.

Boundary conditions (Fig. 3.18) are representative of the experimental setup. The lower end of the column is equipped with a pin restraint; the column top is equipped with a roller restraint allowing vertical displacement. Cyclic loading is imposed at the primary beam end. The primary beam is equipped with lateral–torsional restraints. Bolts were proof-loaded according to EN 1993-1-8 [5], while the bolts of the friction device were tightened up to the design preload.

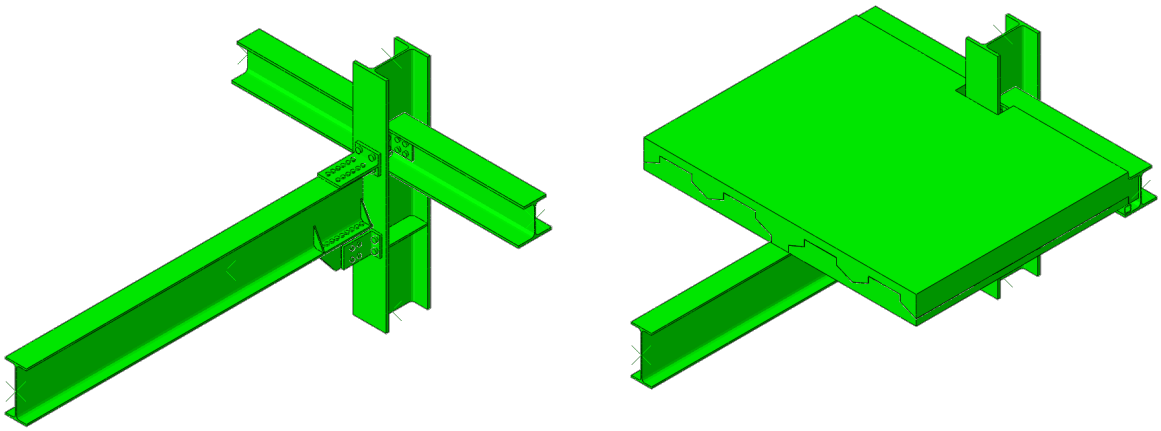

Figure 3.17: *3D view of the FE preliminary model (left) and definitive one (right)*

3.3.2 Description of the preliminary model

The preliminary model (Fig. 3.17 left) is made by the steel structural members only (so-called "bare-steel model"), and it is representative of the overall behaviour of the joint assembly, disregarding the composite deck.

Quasi-static Implicit analysis was carried out. Steel components were made of S355 grade steel, with an elastic modulus of 210'000 MPa and a Poisson's ratio of 0.3. Bolts were modelled as Grade 10.9, based on prior research [8]. Nonlinear steel behaviour was captured using true stress–strain curves derived from experimental tests, applying the Von Mises yield criterion with combined isotropic and kinematic hardening. Bolt clamping forces were simulated using the "bolt load" option in the Abaqus Load module.

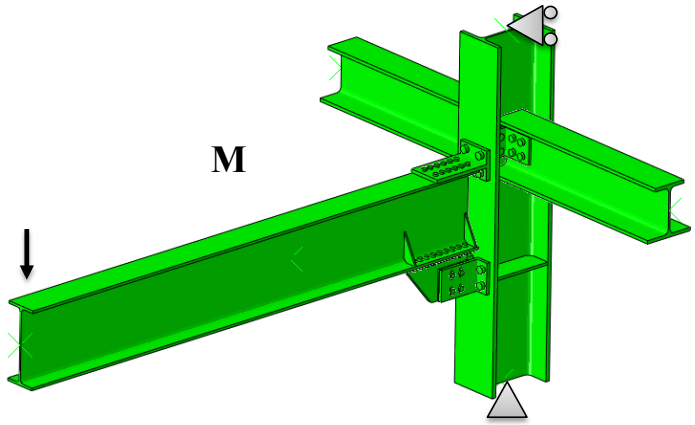

Figure 3.18: *Boundary Conditions*

Large displacement effects were included in all steps by activating the "Nlgeom" option. Contact interactions were defined using a penalty friction model for tangential behaviour and hard contact for normal behaviour. Two types of contact were modelled: a general steel-to-steel interface with a friction coefficient of 0.30, and steel-to-friction shim contact with a coefficient of 0.53, as specified by Latour et al. [9], Cavallaro et al. [10]. Full penetration welds were implemented using tie constraints, while rigid body constraints defined boundary conditions.

All components were meshed with C3D8R elements (8-node linear brick with reduced integration), chosen for their efficiency and reliable performance. The element formulation inherently prevents shear-locking, and hourglass control was included. Mesh sizes were selected based on sensitivity analyses from previous studies [11]. Specifically, plates and bolts were meshed with an average size of 5 mm, and the rest of the model used a 20 mm element size, in line with prior validation efforts [12-13].

3.3.3 Description of the definitive model

The final FE model (Fig. 3.17 right) accurately represents the experimental specimen. It is made of steel structural members and a composite deck.

Dynamic Explicit analysis was carried out. Steel components were made of S355 grade steel, with an elastic modulus of 210,000 MPa and a Poisson's ratio of 0.3. Bolts were modelled as Grade 10.9, based on prior research [8]. Rebars are made of B450C steel.

Nonlinear steel behaviour was captured using true stress–strain curves derived from experimental tests, applying the Von Mises yield criterion with combined isotropic hardening. Bolt clamping forces were simulated by means of a thermal load on the bolt shank. Concrete was modelled by using the Concrete Damage Plasticity model, and material properties were deduced from literature [14].

Large displacement effects were included in all steps by activating the “Nlgeom” option. Contact interactions were defined using a penalty friction model for tangential behaviour and hard contact for normal behaviour. Two types of contact were modelled: a general steel-to-steel interface with a friction coefficient of 0.30, and steel-to-friction shim contact with a coefficient of 0.53, as specified by Latour et al [9]. Full penetration welds were implemented using tie constraints, while rigid body constraints defined boundary conditions.

Solid components were meshed with C3D8R elements (8-node linear brick with reduced integration), chosen for their efficiency and reliable performance. The element formulation inherently prevents shear-locking, and hourglass control was included. Mesh sizes were selected based on sensitivity analyses from previous studies [11-13]. Rebars and shear studs were modelled as T3D2 truss element type and embedded in concrete (Figures 3.19 and 3.20). Plates and bolts were meshed with an average size of 5 mm, and the rest of the model used a 20 mm element size.

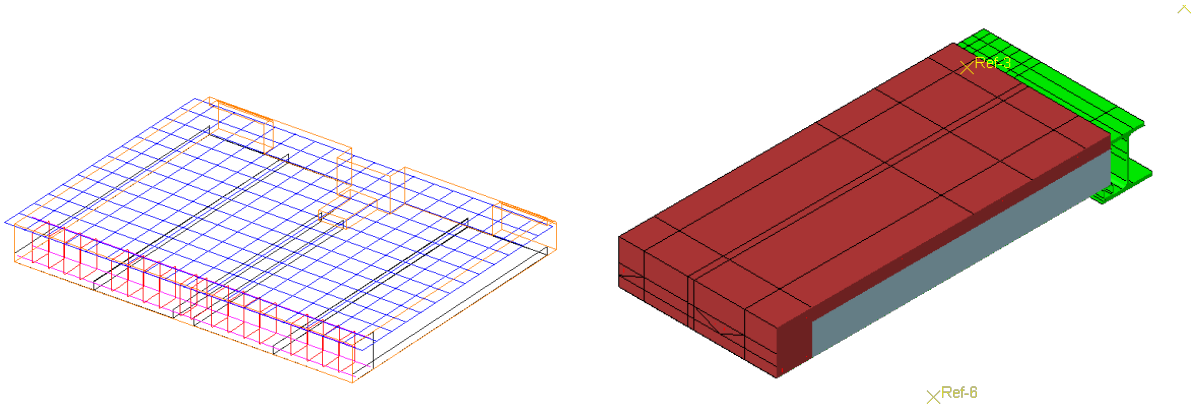

Figure 3.19: *Rebars of the composite deck (left), section cut of the composite deck (right)*

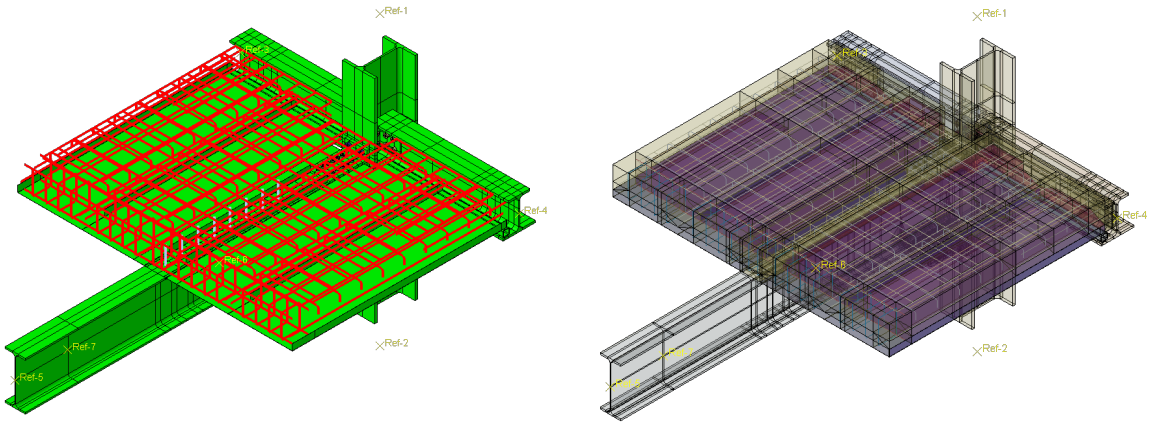

Figure 3.20: *Rebars of the composite deck as shown in the FE model*

3.3.4 Comparison between the experimental tests and the numerical analyses

Fig. 3.21 shows the hysteresis loop obtained by the experimental test named J1-LV, one of the quasi-static tests. Loops are rectangular and slightly inclined with respect to the principal diagonal of the first and third quadrants due to the contribution of the composite deck.

In Fig. 3.22 experimental curve derived by the J1-LV test and the numerical curve deduced by the definitive FE model are compared. The FE model is able to catch the strength and stiffness of the experimental test, and replicate the contribution to the overall behaviour of the joint given by the composite slab.

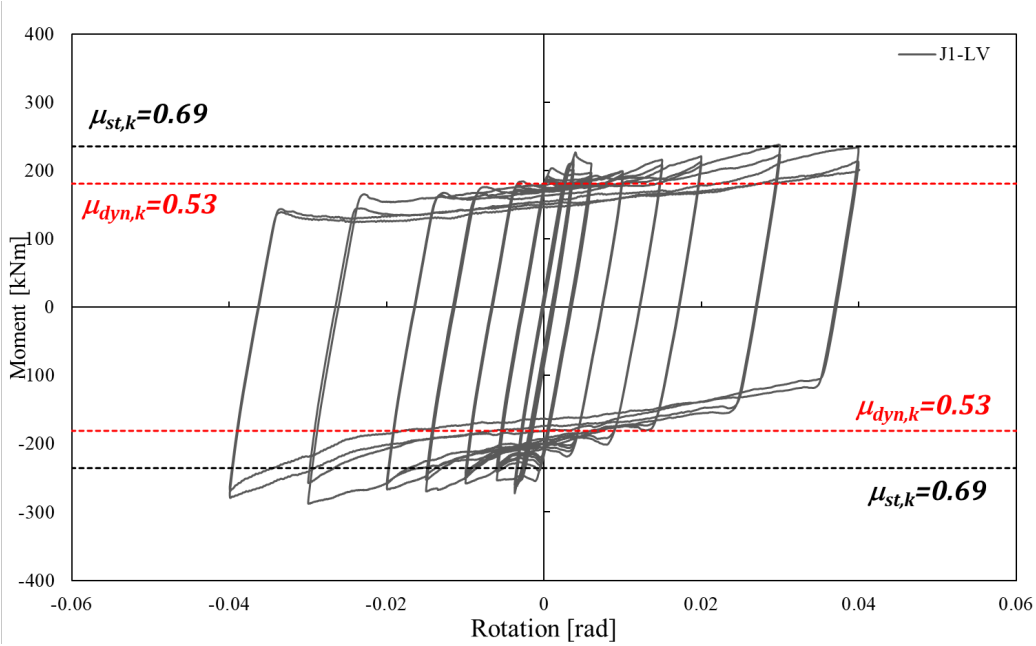

Figure 3.21: *Hysteresis loop for the J1-LV test*

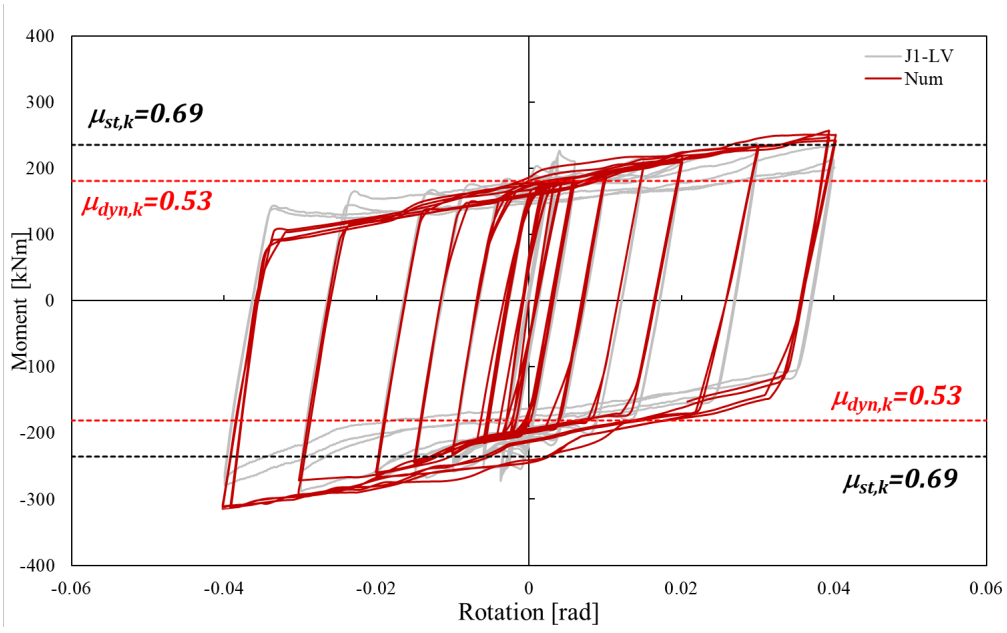

Figure 3.22: *Comparison between the experimental and numerical hysteresis loop*

In Fig. 3.23, the two FE models, namely the preliminary and the definitive model are compared in order to highlight the influence of the composite deck on the overall behaviour of the joint. The green curve, representative of the preliminary "bare-steel" model is characterised by a rectangular loop, with a plateau equal to the design resistance of the friction connection. The red curve, representative of the definitive model presents loops slightly tilted with respect to the principal diagonal passing through the first and the third quadrants. This is due to the presence of the composite deck, which although remaining in elastic range is able to give a significant increase of stiffness when the sliding of the friction device is activated.

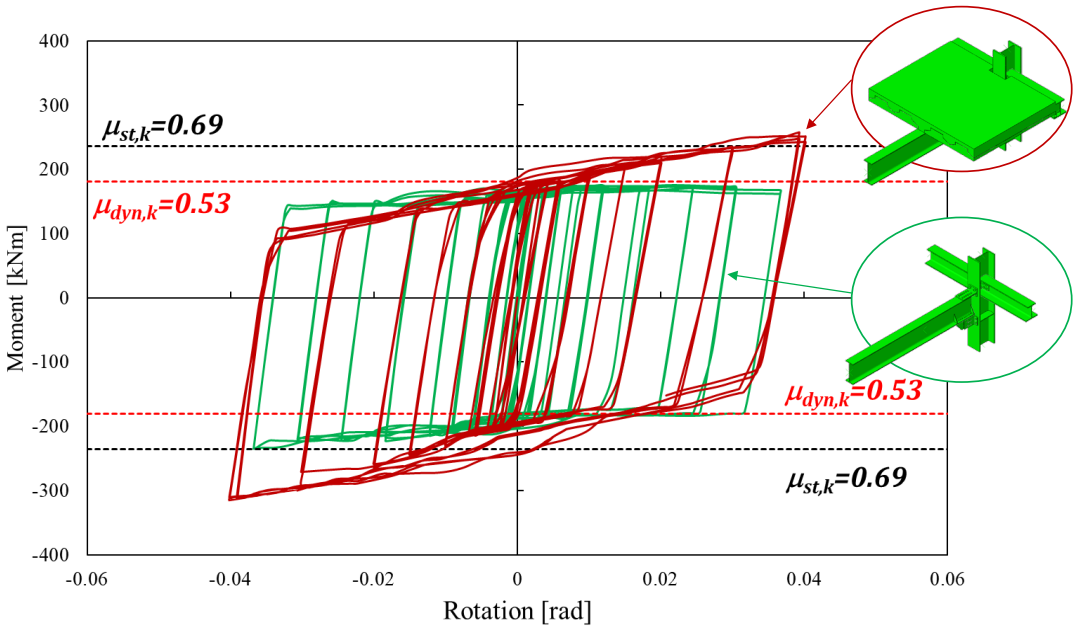

Figure 3.23: *Comparison between the two FE models*

Figs. 3.24-3.26 show the Von Mises stress distributions of the definitive FE model under sagging bending moment. Stresses along the beam length are due to the force transfer in between the beam and the concrete deck, by means of the shear studs at the top flange; these stresses are way below the yielding of the material. Fig. 3.27 shows the Von Mises stress distribution under bending in the other direction. Fig. 3.28 shows the tensile damage in the concrete deck for 0.04 rad of rotation under hogging bending moment and Fig. 3.29 shows the tensile stress in the rebars. As it can be notice, the rebars are not yielded.

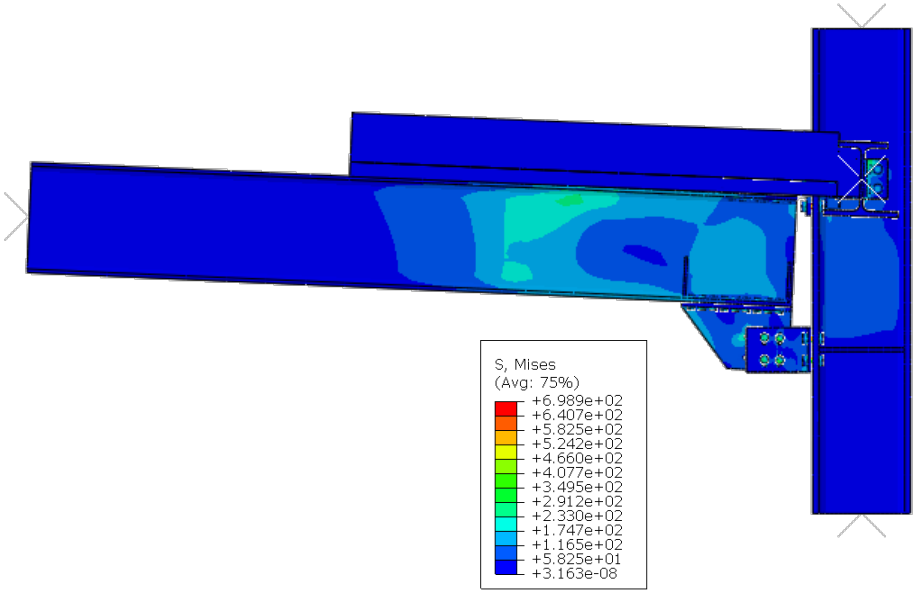

Figure 3.24: *Von Mises stress distribution at 0.04 rad of rotation (sagging bending moment)*

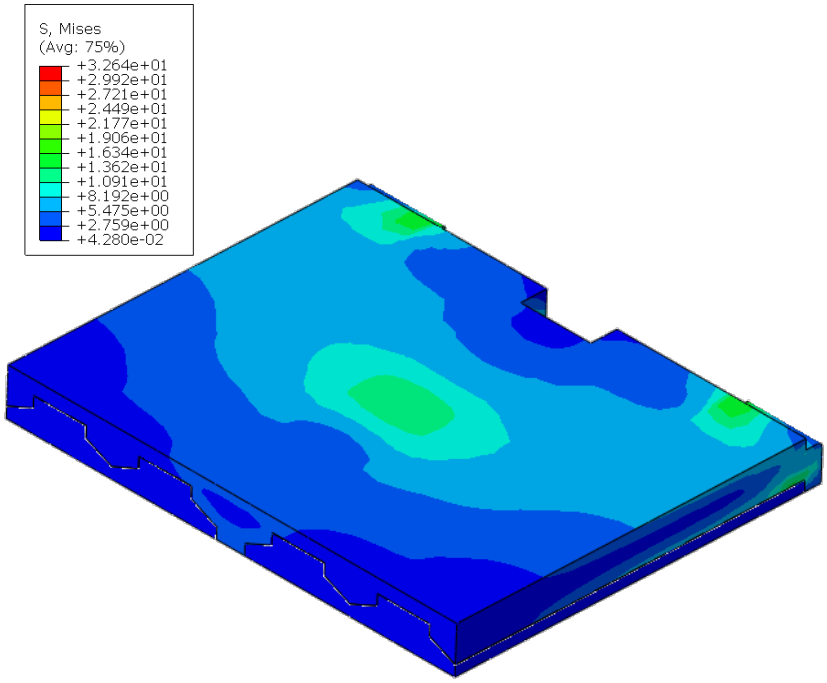

Figure 3.25: *Concrete deck, Von Mises stress distribution at 0.04 rad of rotation (sagging bending moment)*

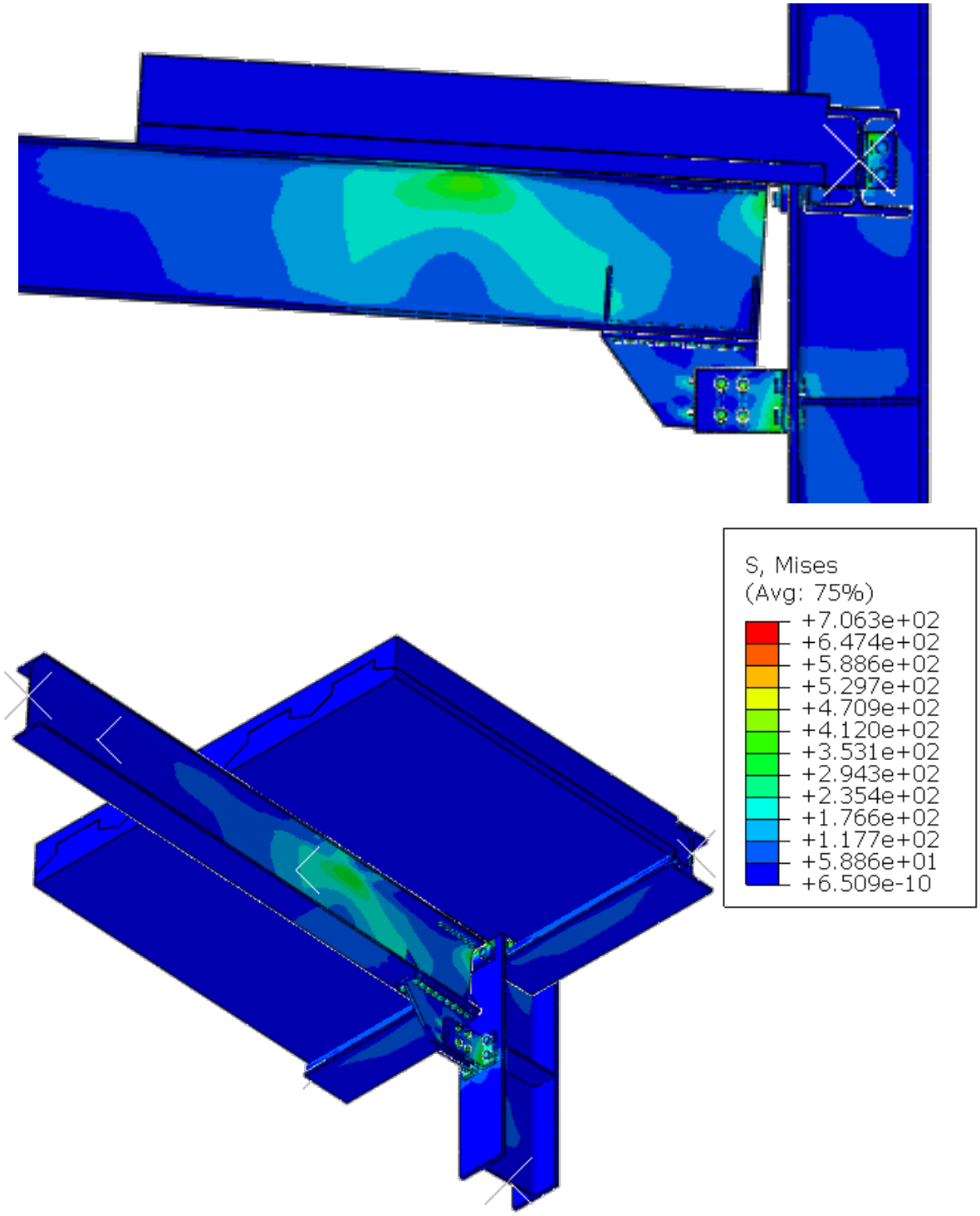

Figure 3.26: *Von Mises stress distribution at 0.04 rad of rotation (sagging bending moment), lateral view (top), 3D view (bottom)*

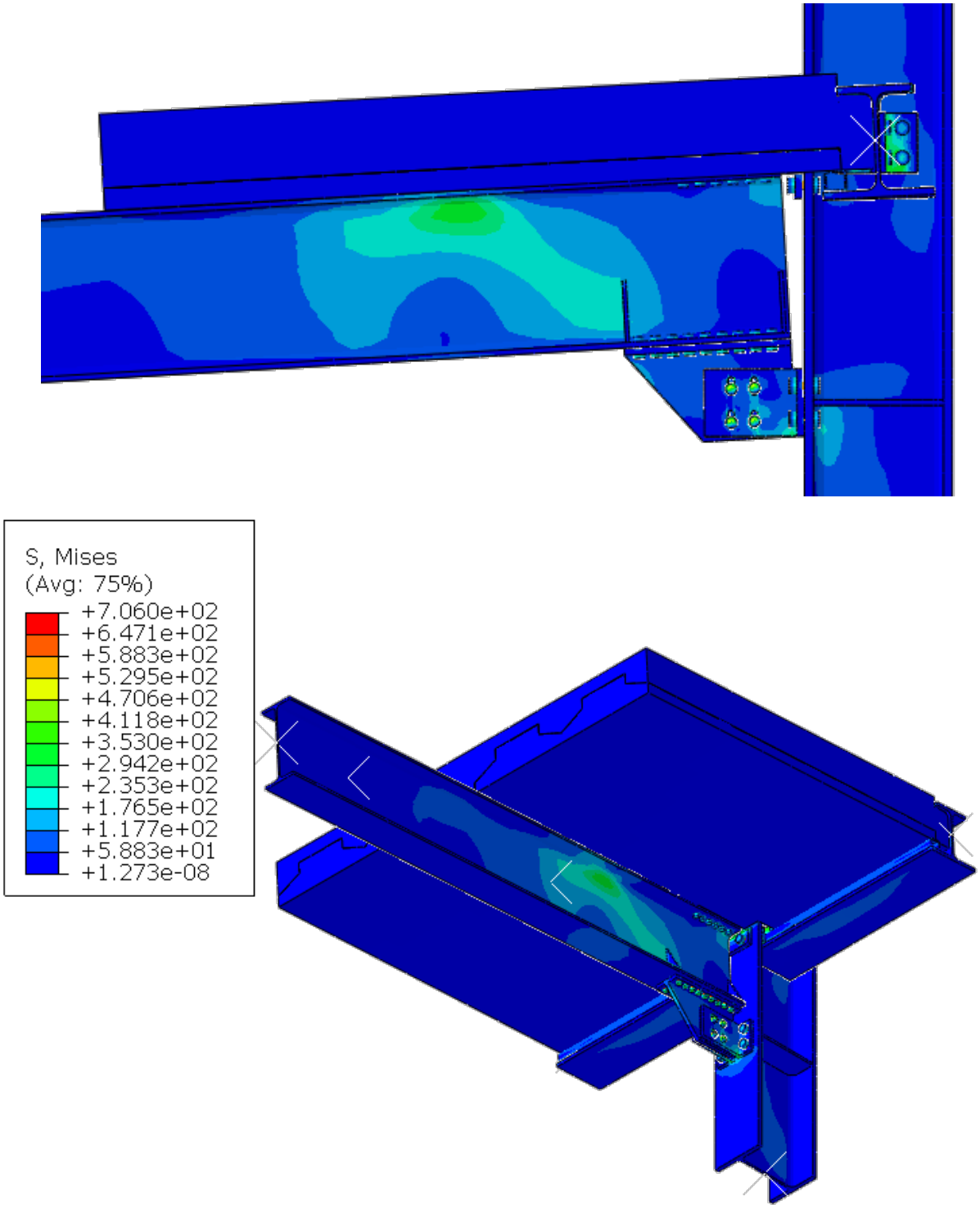

Figure 3.27: *Von Mises stress distribution at 0.04 rad of rotation (hogging bending moment), lateral view (top), 3D view (bottom)*

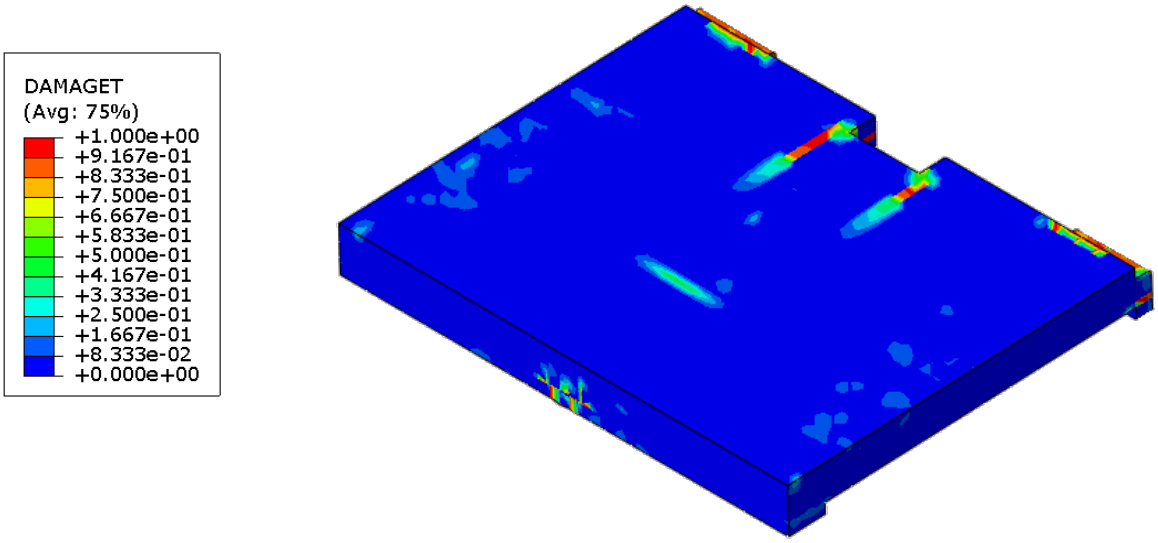

Figure 3.28: *tensile damage in the concrete deck, 0.04 rad of rotation (hogging bending moment)*

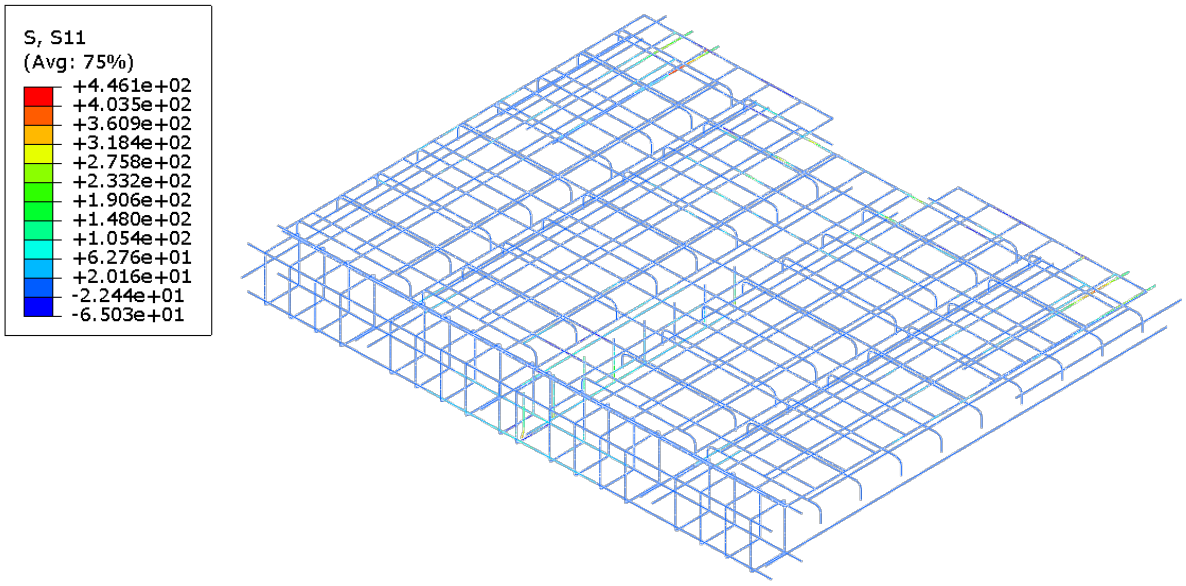

Figure 3.29: *tensile stresses in the steel rebars, 0.04 rad of rotation (hogging bending moment)*

3.4 REFERENCES

[1] European Committee for Standardization. (2002). *Eurocode 0: Basis of structural design (EN 1990:2002)*. Brussels, Belgium: CEN.

[2] American Institute of Steel Construction. (2018). Prequalified connections for special and intermediate steel moment frames for seismic applications (AISC 358-18). Chicago, IL: AISC.

[3] Piluso, V.; Rizzano, G.; Latour, M.; Francavilla, A.; Di Benedetto, S.; Landolfo, R.; D'Aniello, M.; Simoes da Silva, L.; Santiago, A.; Santos, A.; et al. Informative Documents of the Dissemination project FREEDAM-PLUS. GA 899321-2020. Available online: https://www.steelconstruct.com/eu-projects/freedam-2/documents/ (accessed on 1 April 2025).

[4] EN 1993-1-1; Eurocode 3—Design of Steel Structures—Part 1-1: General Rules and Rules for Buildings. European Committer for Standardization (CEN): Brussels, Belgium, 2005.

[5] EN 1993-1-8; Design of Steel Structures—Part 1-8: Design of Joints. European Committee for Standardization (CEN): Brussels, Belgium, 2005.

[6] Landolfo, R., D'Aniello, M., Costanzo, S., Tartaglia, R., Demonceau, J.-F., Jaspart, J.-P., Stratan, A., Jakab, D., Dubina, D., Elghazouli, A., & Bompa, D. (2018). Equaljoints PLUS: Volume with information brochures for 4 seismically qualified joints (1st ed.). ECCS – European Convention for Constructional Steelwork. ISBN 978-92-9147-143-0

[7] Dassault. Abaqus 6.14—Abaqus Analysis User's Manual; Dassault Systèmes Simulia Corp.: Johnston, RI, USA, 2014.

[8] D'Aniello, M.; Cassiano, D.; Landolfo, R. Simplified criteria for finite element modelling of European preloadable bolts. Steel Compos. Struct. 2017, 24, 643–658.

[9] Latour, M.; D'Aniello, M.; Zimbru, M.; Rizzano, G.; Piluso, V.; Landolfo, R. Removable friction dampers for low-damage steel beam-to-column joints. Soil Dyn. Earthq. Eng. 2018, 115, 66–81.

[10] Ferrante Cavallaro, G.; Francavilla, A.; Latour, M.; Piluso, V.; Rizzano, G. Cyclic response of friction materials for low yielding connections using different friction materials. Soil Dyn. Earthq. Eng. 2018, 114, 404–423.

[11] Tartaglia, R.; Carlevaris, R.; D'Aniello, M.; Landolfo, R. Steel Beam-to-Column Friction Joint under a Column Loss Scenario. Buildings 2024, 14, 784. https://doi.org/10.3390/buildings14030784

[12] Latour, M.; Piluso, V.; Rizzano, G. Free from damage beam-to-column joints: Testing and design of DST connections with friction pads. Eng. Struct. 2015, 85, 219–233.

[13] Tartaglia, R.; D'Aniello, M.; Campiche, A.; Latour, M. Symmetric friction dampers in beam-to-column joints for low-damage steel MRFs. J. Constr. Steel Res. 2021, 184, 106791.

[14] Lubliner J., Oliver J., Oller S., Oñate E., A plastic-damage model for concrete, International Journal of Solids and Structures, 25(3), 1989, 299-326.

CHAPTER 4

Structural Robustness: Testing and Analysis

4.1 INTRODUCTION

Modern structures are designed to resist various identified actions, the intensity of which is typically determined using semi-probabilistic methods or derived from experience. Despite this, structural collapses continue to occur - often triggered by unforeseen actions, abnormal action intensities, or adverse combinations of loads. Indeed, such unforeseen events may induce local damages that can propagate throughout the structure, potentially leading to progressive or disproportionate collapses.

To address this risk, modern codes and standards are nowadays requesting for an adequate structural robustness, defined in EN 1991-1-7 [1] as *"the ability of a structure to withstand events like fire, explosions, impact or the consequences of human error, without being damaged to an extent disproportionate to the original cause*".

However, although widely recognized as fundamental and extremely important, robustness is only described in a general way in the current version EN 1991-1-7 with limited information on how to ensure it effectively in the design process. The standard outlines several design strategies intended to meet minimum robustness requirements. However, the acceptable extent of damage and the specific accidental scenarios to be considered remain critical concerns for all stakeholders involved in the design and use of a building (e.g., designers, owners, and relevant authorities).

This lack of normative consistency often leads practitioners to overlook structural robustness considerations during design process. For this reason, different research projects have been undertaken over the past decades to derive scientifically grounded design recommendations for ensuring adequate robustness in structures. Notably, the FAILNOMORE valorisation project [2], funded by the Research Fund for Coal and Steel (RFCS), resulted in a practice-oriented design manual targeting the design for robustness of steel and steel-concrete composite structures.

Moment resisting frames (MRFs) equipped with FREEDAM joints are typically considered as highly resilient structures due to their ability to localise post-earthquake damage in easily

replaceable components, enabling the restoration of the pre-event performance through targeted and limited interventions. Nevertheless, their robustness is of particular interest in case of severe accidental events, which can impose abnormal resistance and displacement demands. In the standard-prescribed scenario involving the loss of a load-bearing element (e.g., columns, beam supporting columns, or walls), robustness becomes the structure's last line of defense, ensuring survival through the activation of alternative load paths.

Recent studies [3], [4], [5], [6] have identified the connections as critical components in this context, as they play a key role in enabling the development of catenary actions—mechanisms that allow the structure to achieve a new equilibrium in the large displacement and deformation domain.

The robustness of the FREEDAM joints has been studied in previous RFCS research projects [7] relying on analytical and numerical tools partially validated against few experimental tests performed on scaled down specimens of these joints.

A first study on the robustness of MRFs subjected to impact revealed that the FREEDAM joints may considerably improve the structural performance compared to similar frames with conventional joints [8]. The authors concluded that, for most of the considered vehicle collision scenarios, no additional structural measures were necessary; however, replacing the friction pads would be required to restore pre-event structural performance.

This finding underscores the importance of evaluating whether structures incorporating such prequalified joints meet the robustness requirements outlined in EN 1991-1-7. Particular attention is given to the standard-defined scenario involving the accidental loss of a column.

Given that an accurate characterisation of the joints is essential for evaluating the structural robustness, this chapter provides valuable insights into the full-range behaviour of FREEDAM joints based on experimental testing. Full-scale double-sided joints were tested to failure under monotonic bending (Test 1) and a quasi-static test simulating a column loss scenario (Test 2). The experimental findings enabled the validation of a previously developed mechanical model used to simulate these joints in global frame analyses [9], [10] and revealed key aspects of FREEDAM joint behaviour under robustness-related conditions.

4.2 EXPERIMENTAL TESTING UNDER ROBUSTNESS SCENARIOS

4.2.1 General description of the performed tests

Two experimental tests were conducted on real-scale double-sided beam-to-column FREEDAM joints assumed to be extracted from the moment-resisting frame (MRF) located on the perimeter

of the pilot building constructed in the framework of the DREAMERS RFCS project. More precisely, the tested joint corresponds to an internal joint connecting the IPE450 beams to the HE400B columns of the 1st and 2nd floors of the perimeter frames as shown in Fig. 4.1. Thus, the specimens consist of two IPE450 beams connected to a HE400B column through a FREEDAM connection (Device D1). S355 steel grade was used for structural members (i.e., beams and columns) and plate components of the dissipative joints with the only exception for the rib that was made of AISI304 stainless steel. The fasteners used to connect the different joint components are 10.9 grade bolts with varying diameters between M16 and M24.

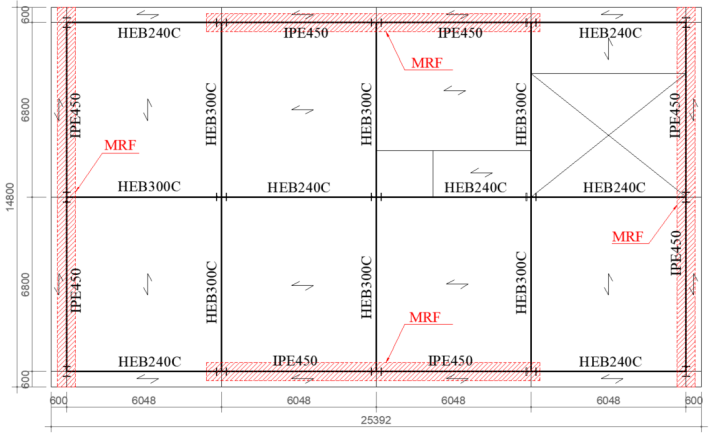

***Figure 4.1**: Plan view of the DREAMERS pilot structure*

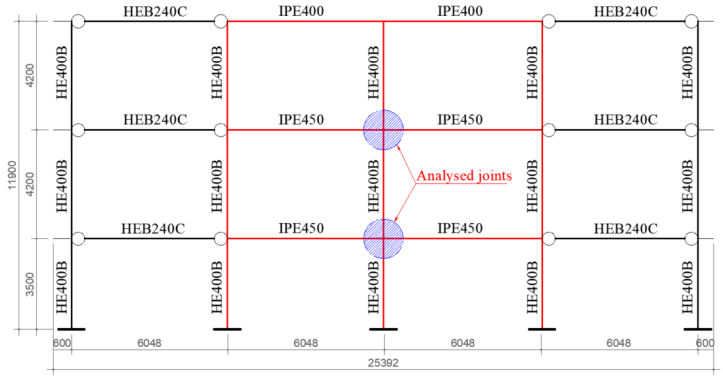

***Figure 4.2**: Location of the investigated FREEDAM joint within the perimeter frames*

The performed tests aimed at characterising the full-range behaviour of FREEDAM joints under i) monotonic bending (Test 1) and ii) simultaneously applied bending moment and axial forces – loading conditions that mimic a hypothetic column loss scenario (Test 2). A quasi-static loading protocol was applied in both tests, thus allowing the execution of the experimental tests in a well-controlled manner with accurate and reliable "noise-free" recordings that provided valuable insights into the global response and local phenomena occurring within the FREEDAM joints. This approach is endorsed as well by the fact that, in previous research projects [11], it

has been shown that the dynamic response of a frame subjected to a column loss can be predicted based on its quasi-static response.

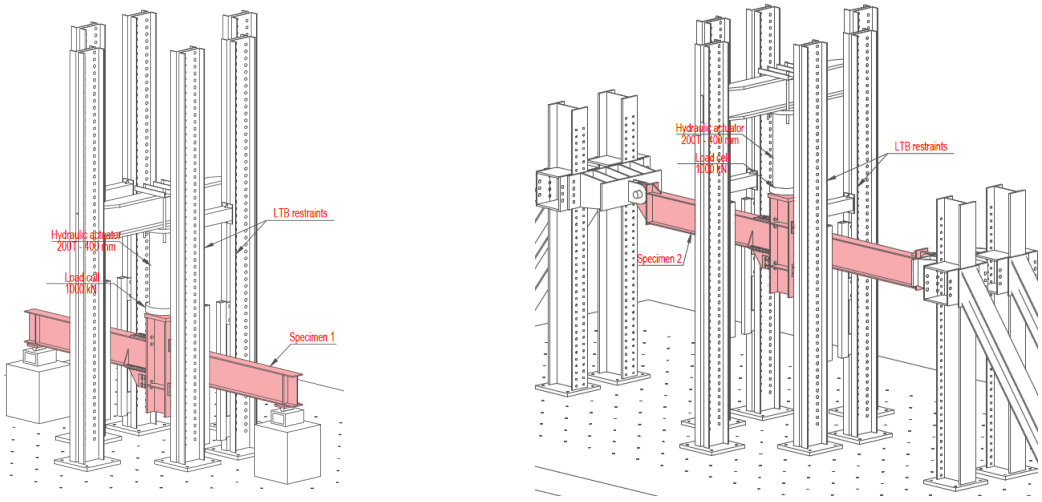

a) Joint under monotonic bending (Test 1)

b) Joint under combined bending and axial force (Test 2)

***Figure 4.3**: 3D views of the test setups*

The test specimens were manufactured with the objective of reproducing the actual performance of the joints used in the DREAMERS building designed to fulfil the ULS and SLS requirements. The sliding resistance of the joint was set in the design phase to match a corresponding bending moment $M_{j,Rd}$ = 181 kNm by adjusting the design preload of bolts that fasten the dissipative device ($F_{p,d}$ = 79.3 kN). For this purpose, the moment (sliding) resistance of the joint was calculated as:

$$M_{j,Rd} = \mu_{dyn,s} n_s n_b \frac{F_{p,d}}{\gamma_{creep}} z \tag{4.1}$$

where $\mu_{dyn,k}$ is the characteristic dynamic friction coefficient taken as 0.53, n_s is the number of friction surfaces, n_b is the number of preloaded bolts clamping the damper, $F_{p,d}$ is the design bolt preload, and z is the joint lever arm (considered 620 mm). The γ_{creep} safety factor accounts for the loss of the initial bolt preload due to relaxation (creep) phenomena and is taken equal to 1.15 [12].

To apply the targeted preload to the damper M16 bolts of the test specimens, the torque method was employed according to [13]. A series of 5 tests were conducted on M16 gr. 10.9 bolts from the same production batch as the ones used in the tested specimens in order to determine the *k*-class of bolts used for computing the required torque to be applied to reach the targeted preload. The results of the tests allowed determining the mean value for the *k*-class coefficient as:

$$k_m = \frac{\sum k_i}{n} = 0.1443 \tag{4.2}$$

with a standard deviation of:

$$s_k = \sqrt{\frac{\sum (k_i - k_m)^2}{n-1}} = 1.528 \cdot 10^{-3} \tag{4.3}$$

and a coefficient of variation of:

$$V_k = \frac{s_k}{k_m} = 0.0105 \tag{4.4}$$

The value of the target preload applied to the damper bolts of the test specimens was determined as:

$$F_p = \frac{F_{p,d}}{\gamma_{creep}} = \frac{79.3}{1.15} = 69 \text{ kN} \tag{4.5}$$

and the corresponding torque to be applied through the torque method was set according to the prescriptions of [13] as follows:

$$M_r = k_m d F_p = 0.1443 \cdot 16 \cdot 69 = 159.3 \text{ kN} \tag{4.6}$$

This torque was applied in two steps in which at first all the bolts were tightened to approximately $0.75M_r$, and subsequently with a torque of $1.1M_r$ as prescribed by [13]. Therefore, the final value of the target preload applied to the damper bolts reached the value of $1.1F_p$ = 75.8 kN. During the 2nd experimental test, the evolution of bolt preload was monitored with strain gauges installed in two damper bolts. The measurements of the initial bolt preload applied through the torque method confirmed the accuracy of the adopted tightening method.

4.2.2 Test layouts and instrumentation

The test under monotonic bending (Test 1) was performed using a simple setup comprising an assembly of restraining frames and a system of supports equipped with horizontal rollers to allow for horizontal movement at the extremities of the specimen. Lateral restraints were provided at 1.0 m from the column's axis to prevent instabilities related to the lateral torsional buckling (LTB) of the beams observed in previous research [14] in tests performed under similar conditions. A hydraulic actuator of 2000 kN capacity and 400 mm stroke length was used to apply a vertical load at the stiffened top end of the column, as shown in Fig. 4.3a.

As shown in Fig. 4.3b, the setup for Test 2 consisted of an assembly of restraining frames and a horizontal in-plane restraining system comprising some transfer beams and columns anchored to the reinforced concrete floor of the lab. The latter allows transferring the beam membrane forces developed during testing to the reaction floor. Pinned connections that allow for frictionless in-

plane rotations through a radial bearing and a pin were provided at the extremities of the specimen. The reaction frame supporting the hydraulic actuator as well as the frames providing the lateral restraints (in- and out-of-plane) were anchored to the reinforced concrete reaction floor using pretensioned high-strength anchor rods.

During both tests, the vertically applied quasi-static load was continuously monitored using a load cell positioned between the actuator and the column head (loading plate). The load transfer to the column head was ensured by means of a load button with a convex contact surface, maintaining the alignment between the applied load and the column's axis.

As indicated in Fig. 4.4, test specimen 1 was equipped with ten Linear Variable Displacement Transducers (LVDTs 01 to 10) used to measure the global displacements (vertical with LVDTs 01&02 and horizontal with LVDTs 09&10) and relative displacements (LVDTs 03-08) between the different parts of the connections. Additionally, to monitor the rotations of the beam-to-column connections as well as the potential in-plane tilt of the column, three inclinometers (IMs 01-03) were installed at the beams' ends in the proximity of the joint and the column web.

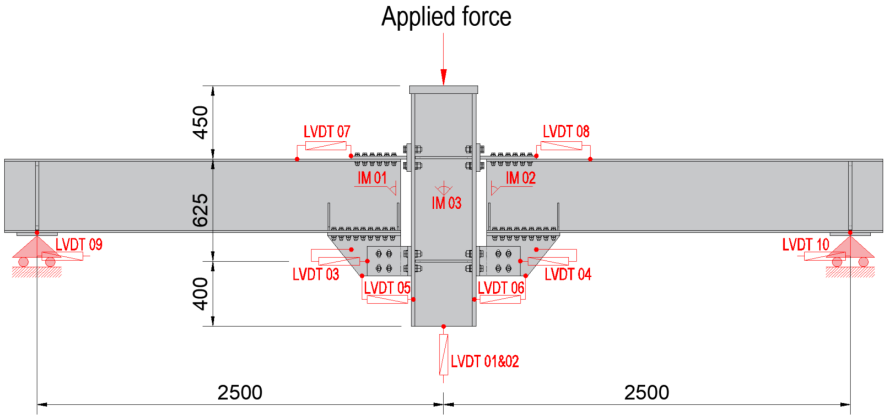

***Figure 4.4**: Instrumentation used on test specimen 1*

Fig. 4.5 shows the instrumentation used for capturing the response of the FREEDAM joint subjected to a virtual column loss during Test 2. In addition to the measurement instrumentation used for Test 1, two more LVDTs (11-12) were provided at the mid-span of the beams to measure the vertical displacements. Two more inclinometers (IMs 04-05) were installed at the beam ends close to the lateral supports serving for estimating the potential horizontal displacements of the restraining system. Eighteen strain gauges (SG 01-18) were installed on the beams' flanges and webs serving for quantifying the membrane forces developing in the axially restrained beams. Additional strain gauges were installed in two M16 damper bolts (one for each connection) used for monitoring the evolution of the preload in the damper bolts along the test.

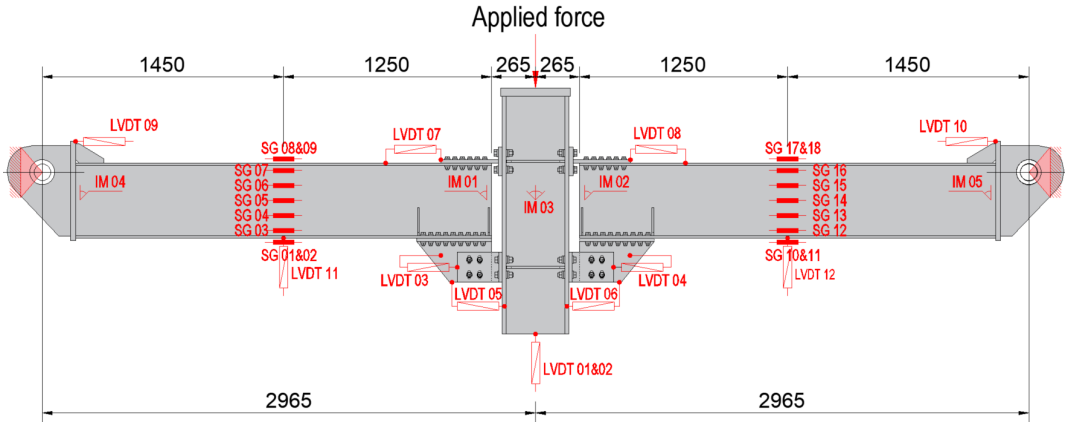

***Figure 4.5**: Instrumentation used on test specimen 2*

4.2.3 Material properties

The properties of steel material used in the constitutive parts of the test specimens were determined through tensile tests performed on coupons extracted from profiles/plates coming from the same production batch as the elements of the test specimens. No coupons were available for the AISI304 stainless steel haunch and the 10.9 grade bolts. Table 4.1 summarizes the mechanical characteristics of the tested materials according to [15].

***Table 4.1**: Mechanical properties from steel coupon tensile tests*

Tested plate	ID	a_0	b_0	L_0	R_{eH}	$R_{p0.2}$	F_{max}	R_m	A
		mm	mm	mm	MPa	MPa	N	MPa	%
HEB400 web	W1-1	13.24	28.11	100.02		520.1	225008.1	604.6	21.6
	W2-1	13.28	28.07	100.01		429.5	218946.8	587.4	26.8
HEB400 flanges	F1-1	23.47	28.06	100.01	428.0	415.3	372957.4	566.3	30.7
	F2-1	23.45	28.03	100.01	431.3	415.5	378812.2	576.3	31.2
IPE450 web	W1-2	8.83	28.09	100.01	515.2	469.7	147472.0	594.6	24.6
	W2-2	8.86	28.09	100.02	522.5	478.5	148613.0	597.1	24.7
IPE450 flanges	F1-2	14.2	28.14	100.02	494.6	459.2	236412.0	591.6	27.5
	F2-2	14.55	28.14	100.02	493.7	453.5	239074.1	583.9	27.4
Plate 25 mm	P25-1	24.84	28.05	100.01	413.1	391.9	389452.4	558.9	33.9
	P25-2	24.77	28.13	100.02	422.8	387.3	389023.2	558.3	33.4
Plate 20 mm	P20-1	19.61	28.18	100.02	450.4	423.4	284693.2	515.2	34.5
	P20-2	19.61	28.17	100.01	450.7	430.2	283883.6	513.9	34.3

The nomenclature used in Table 4.1 is consistent with the terms and definitions given in [15] where a_0 is the original thickness of the flat test piece, b_0 is the original width of the parallel length of the flat test piece, L_0 is the original gauge length, R_{eH} is the upper yield strength, $R_{p0.2}$ is the proof strength at 0.2% plastic extension, F_{max} is the maximum force, R_m is the tensile strength, A is the percentage elongation after fracture.

4.2.4 Experimental results

Response under monotonic bending moment

Fig. 4.6 shows the experimental results in terms of applied force-vertical displacement measured during Test 1. The experimental curve along with real-time observations of the specimen response indicate that the sliding resistance of the two connections (left and right) was not reached simultaneously.

In fact, the results reveal a 7% difference between the sliding resistances of the two connections. The slippage in the right connection was initiated under an applied vertical force of approximately F=182 kN, whereas the left connection reached its sliding resistance at approximately F=195 kN. This discrepancy may come from the slight variation of the preload applied to the damper bolts as well as from differences in terms of initial states of the coated surfaces of the friction pads and their contact with the other plate components of the damper (haunch and L-stubs). The sliding resistances of both connections fall in between the design estimates corresponding to the characteristic dynamic and static friction coefficients $\mu_{dyn,k}$=0.53 and $\mu_{st,k}$=0.69 respectively.

Unfortunately, it was not possible to restrain the in-plane rotation of the column, as monitoring the horizontal in-plane reactions that would develop at the restraint points proved unfeasible. This limitation, combined with the difference in sliding resistance between the two connections, led to a strongly asymmetric response characterized by five distinct phases, as illustrated in Fig. 4.6 and 4.7.

The 5 phases illustrated in Fig. 4.6 correspond to the following particular response stages:

(1) The attainment of sliding resistance of right connection at approximately 182 kN and a vertical displacement of 8.3 mm. After this point, the vertical displacement increased to 74.6 mm with a significant decrease in the applied force (from 182 kN to 114 kN). Since no sliding occurred in the left connection, the left beam-to-column joint remained in its elastic range and the relative rotation between the left connection and the column's axis was virtually zero (IM 01-IM 03≈0). Thus, the rotational response of the left joint at this load step is characterised by the initial stiffness $S_{j,ini}$. This led to the in-plane rotation of the column as shown in Fig. 4.8 (stages (2) & (3)).

(2) The stroke-end limit was reached in the damper of the right connection. The two peripheral M16 bolts closer to the end of the slotted holes were gradually engaged in bearing with the haunch plate. The activation of this additional bearing mechanism in the right connection

led to the increase of the applied load until the sliding resistance of the left connection was reached.

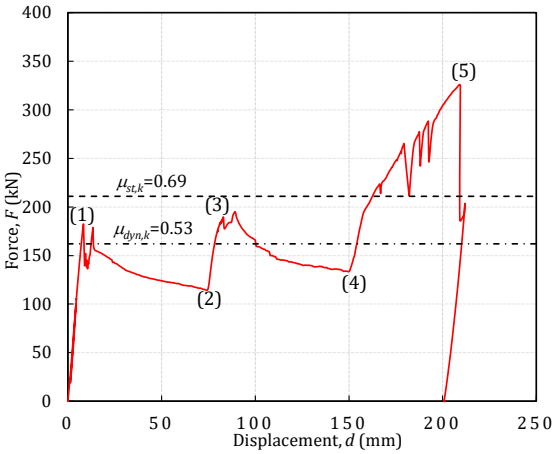

***Figure 4.6**: Global force vs. vertical displacement curve*

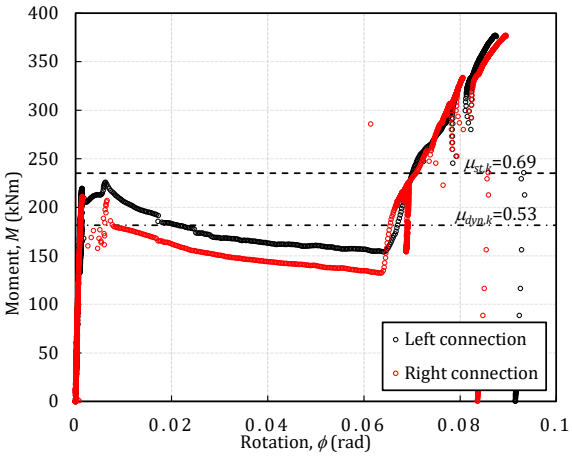

***Figure 4.7**: Moment vs. rotation curve at the connection level*

(3) The peak sliding resistance of the left connection was reached under an applied force of 195 kN and a corresponding vertical displacement of 89 mm. From this instant on, the vertical displacement started once again increasing under a gradually decreasing applied load. The column rotation decreased as well until the column's verticality was restored.

(4) When the stroke-end limit was reached in the left connection at a corresponding vertical displacement of 150 mm, the in-plane rotation of the column decreased to negligible values. Similar to the right connection at stroke capacity, the additional resisting mechanism provided by the bolts engaged in bearing with the haunch induced a further increase of the applied force and both joints (left and right) entered the post-slippage range of response.

The applied force increased continuously until the first failure occurred at the level of the damper bolts in the left connection (bolt fracture in shear). The test was stopped due to safety considerations, yet the brittle failure of the bottom bolt in shear and the excessive plastic deformations at the level of the other bolts active in bearing in the dampers indicate that the ultimate capacity of the joint was reached at 326 kN and a displacement of 209 mm.

Response under combined bending moment and axial force

The force-vertical displacement curve reported in Fig. 4.10 shows that, during the test, the specimen has shown a similar behaviour to that observed for specimen 1 subjected to bending moment (Test 1). However, due to the presence of tensile forces in the beams, the slippage occurred at lower values of the applied vertical load compared to the joint subjected to bending moment (and shear force) only. Both shape of the curve and real-time observations suggest that a slight difference in slippage resistance between the two connections induced an asymmetric response characterised by 5 distinct stages similar to Test 1.

(1) The slippage was first observed in the left connection for an applied load of approximately 130 kN and a corresponding vertical displacement of 8.7 mm (1). After reaching the damper slippage length in the left connection (2), the applied force increased up to approximately 141 kN, load at which the slippage was initiated in the right connection (3). After the attainment of the stroke capacity of the right connection (4), the applied load increased until 294 kN and a corresponding vertical displacement of 220 mm (5) when the test was stopped once again due to safety reasons. Although the bolt fracture didn't expressly occur in Test 2, the comparison between the deformations observed at the level of the damper bolts (see Fig. 4.8) in both tests indicate that the ultimate capacity of the specimen was reached as well in the second test.

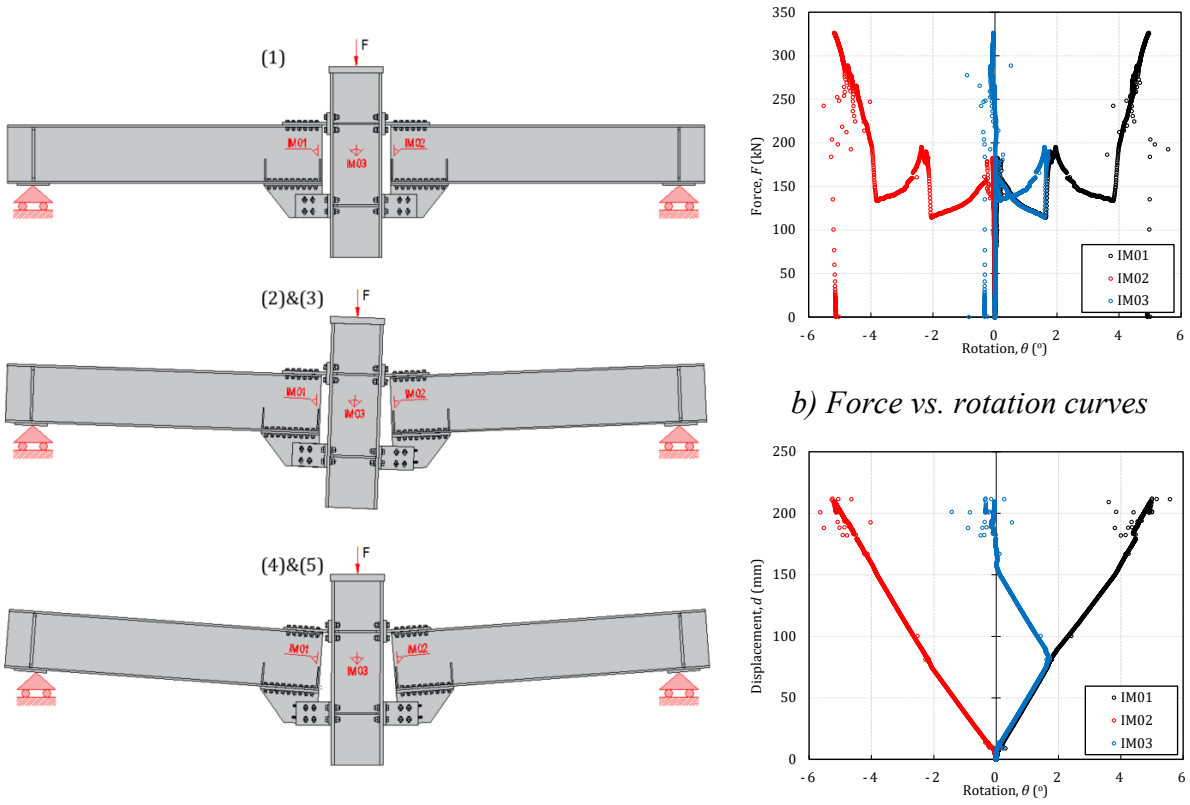

a) Response stages during testing

b) Force vs. rotation curves

c) Vertical displacement vs. rotation curves

***Figure 4.8**: Response stages and observed failure of the specimen (Test 1)*

Additionally, to explain the decay in the friction resistance of the connections along the slippage plateau, the evolution of the preload in the 2 instrumented damper bolts (one for each damper) with respect to the (corrected) connection rotation is shown in Fig. 4.11. The experimental evidence indicates a decrease of preload of approximately 28% (from 78.6 KN to 56.8 kN for the left damper) and 30% (from 84.8 kN to 58.8 kN for the right damper) between the slippage onset and the stroke limit condition. Based on this variation, it can be concluded that the decay in the friction resistance along the slippage phase observed in both tests is strongly related to the bolt preload loss.

a) General view

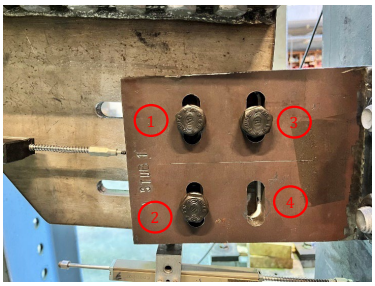

b) Damper after test

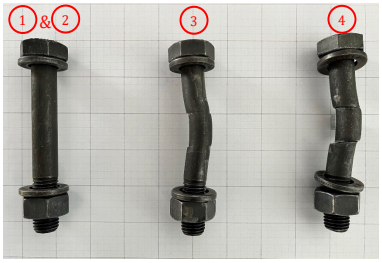

c) Damper bolts after test

***Figure 4.9**: Specimen 1 after test*

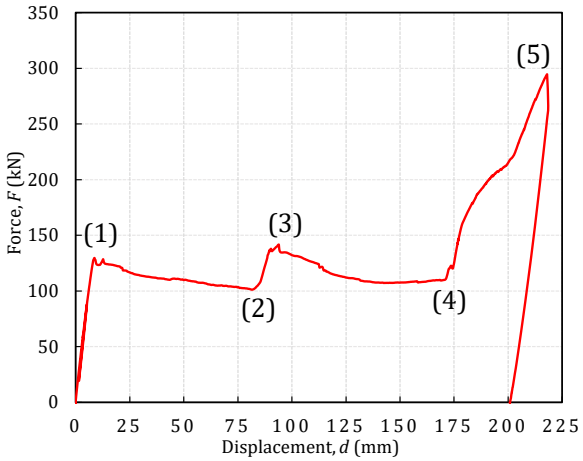

***Figure 4.10**: Global force vs. vertical displacement curve*

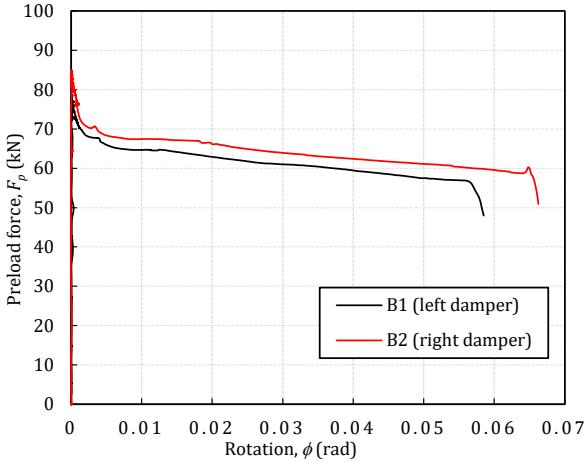

***Figure 4.11**: Damper bolts preload vs. connection rotation*

The axial force acting in the beams (see Fig. 4.12) was estimated based on the recordings of the strain-gauges located on the beam axis: SG05 and SG14 for the left and right beam respectively.

The moment-rotation curves for both connections were determined with account for the corrected connection rotations by subtracting (for right connection) or adding (for left connection) the in-plane rotation (tilt) of the column. To estimate the bending moment at the connection level, the lever arm L was taken as the distance between the supports and the mid-thickness of the column's flange. The bending moment acting on the connection was calculated at the beam axis and so, the eccentricity of 170 mm of the horizontal reaction at the end supports was also considered. Therefore, the bending moment was finally estimated as:

$$M = \frac{F}{2}L - N(170 - d) \tag{4.7}$$

where F is the applied vertical force, N is the axial force in the beam, and d is the corresponding vertical displacement recorded during test.

Fig. 4.13 shows the variation of the bending moment with respect to the rotation of connections (with account for the column tilt). It is evident that the connections were not subjected to the same bending moment along their slippage phase. This difference may be explained relying on the evolution of the axial force in the beams reported in Fig. 4.12.

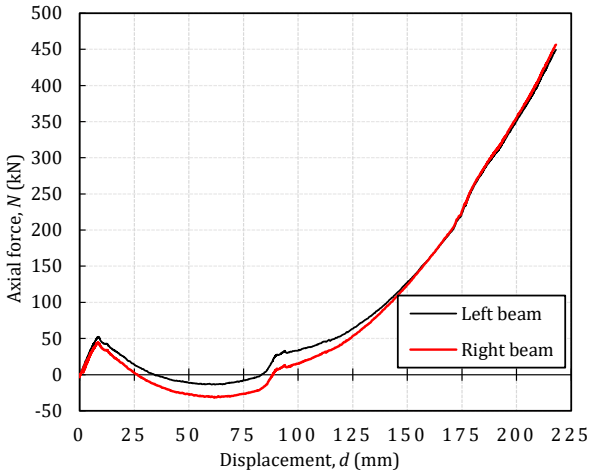

***Figure 4.12**: Beam axial force vs. vertical displacement*

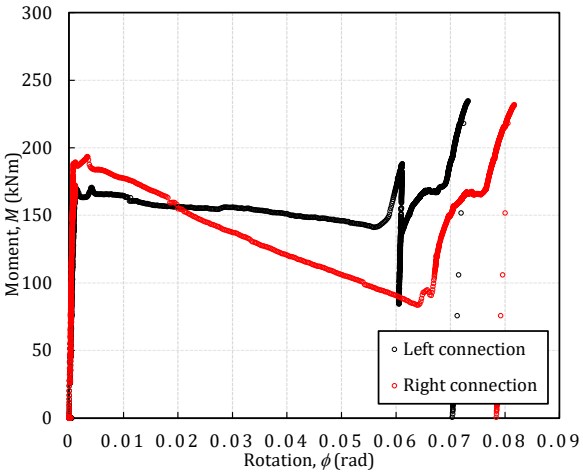

***Figure 4.13**: Moment vs. rotation curve at the connection level*

Since a significant tensile action develops in the beams of the specimen only after the left damper has reached its stroke capacity, the left connection is subjected to negligible second order effects during its slippage phase. Therefore, the bending moment acting on this connection during slippage is mainly induced by the vertical support reaction (*F/2*).

This loading state changes however with the increase of beam axial forces once the vertical displacement reaches approximately 90 mm. The response of the specimen enters the catenary action stage which is characterised by significant second order effects (large displacements) and a steady increase of membrane forces in the beams. This combination of changing parameters leads to the decrease of the bending moment acting on the right connection during its slippage phase. However, after the stroke limit is reached in both dampers, the response of both connections is similar.

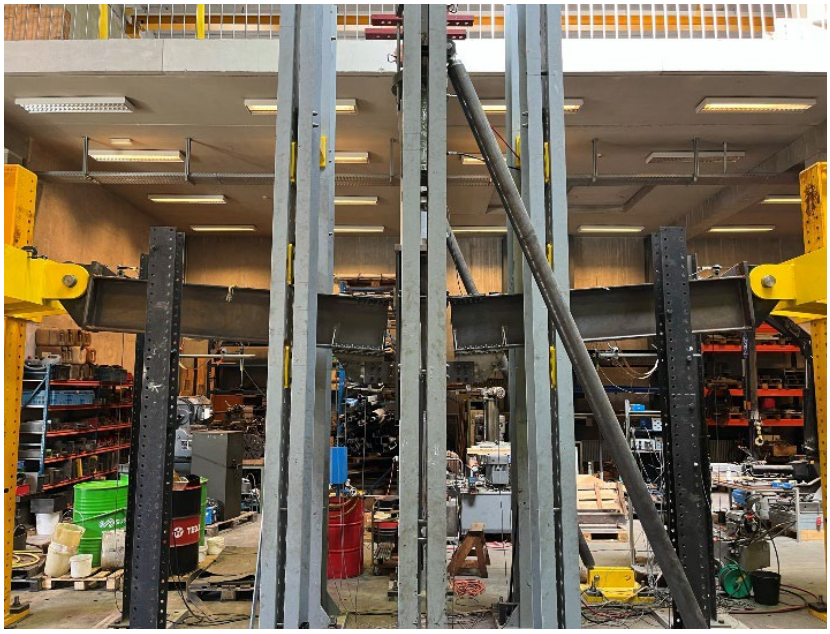

a) *General view*

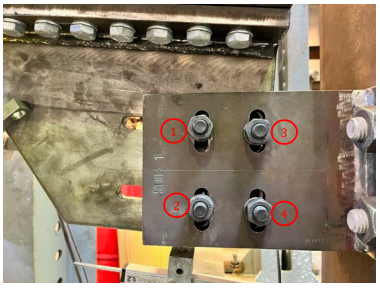

b) Damper after test

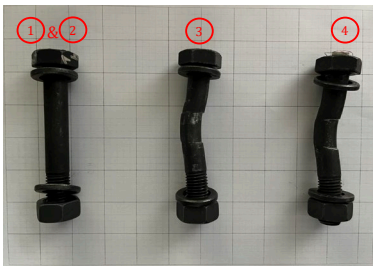

c) Damper bolts after test

***Figure 4.14**: Specimen 2 after test*

4.3 MODELLING OF JOINTS FOR ROBUSTNESS-RELATED SCENARIOS

4.3.1 Simplified spring model for FREEDAM joints

The structural robustness of a building strongly depends on the local behaviour of structural members and their end connections. Depending on their characteristics (e.g., stiffness, strength, and ductility), the joints may significantly influence the distribution of internal forces and displacements in frame structures as well as the ultimate structural capacity and residual strength.

Typically, the behaviour of joints is integrated in structural analyses through rotational springs simulating the response of joints under bending action. However, this modelling approach does not allow for a proper consideration of the moment-axial force (*M*-*N*) interaction in the joints, which makes it unsuitable for simulations of column loss scenarios for which the joints may be subject to such combinations of internal forces once catenary actions develop in the part of the structure that bridges over the lost column.

Based on the well-known Component Method introduced in EN 1993-1-8 [16], a simplified two-spring model (2SM) for FREEDAM joints was developed and partially validated against experimental evidence by D'Antimo[14] and Santos et al. [17]. The model consists of two extensional springs (top and bottom) interconnected by rigid elements as represented in Fig 4.16. An additional rigid shear spring ensures the transfer of shear forces at the beam ends.

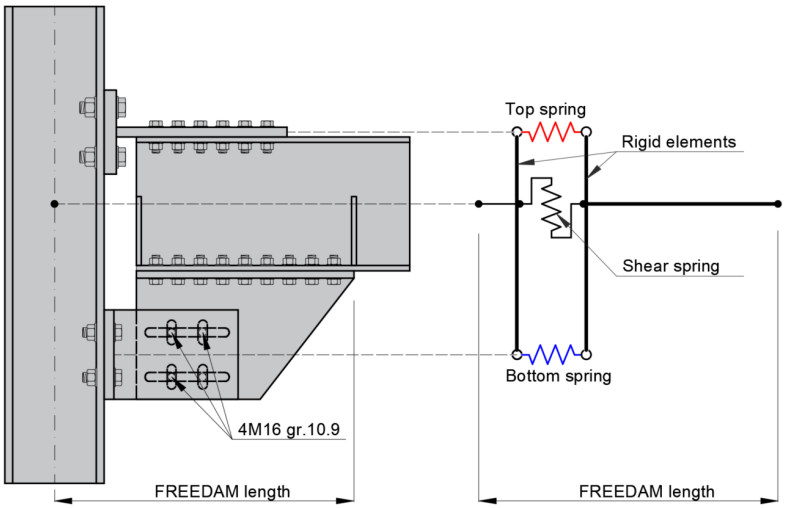

***Figure 4.16**: Simplified two-spring model for FREEDAM joints*

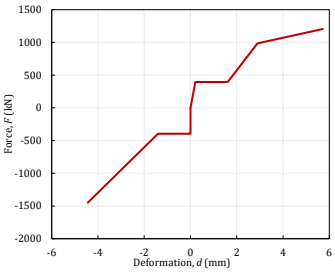

***Figure 4.15**: Top spring law*

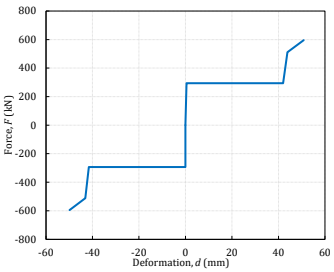

***Figure 4.17**: Bottom spring law*

The so-built model accommodates the *M-N* interaction and accounts for the behaviour of basic joint components characterised by extensional springs with nonlinear behaviour laws (Fig. 4.15 and 4.17) derived with the Component Method of EN 1993-1-8 [16]. As demonstrated by Santos et al. [17], the component method can be effectively extended to characterise both pre- and post-sliding behaviour of the FREEDAM joints. The plastic range of behaviour for basic joint components is characterised by a strain-hardening stiffness and an ultimate strength analytically estimated as proposed by Jaspart et al. [18].

4.3.2 Model validation

Response under monotonic bending moment

The performance of the proposed 2SM is hereinafter assessed through comparisons between numerical predictions and the experimental results acquired from the test performed on the FREEDAM joint subjected to monotonic bending moment (Test 1). The test was numerically simulated using the 2SM with the spring behaviour laws given in Fig. 4.15 combined with classical beam elements in the FINELG finite element (FE) software. The numerical model overlapped with the configuration of the test specimen is represented in Fig. 4.17.

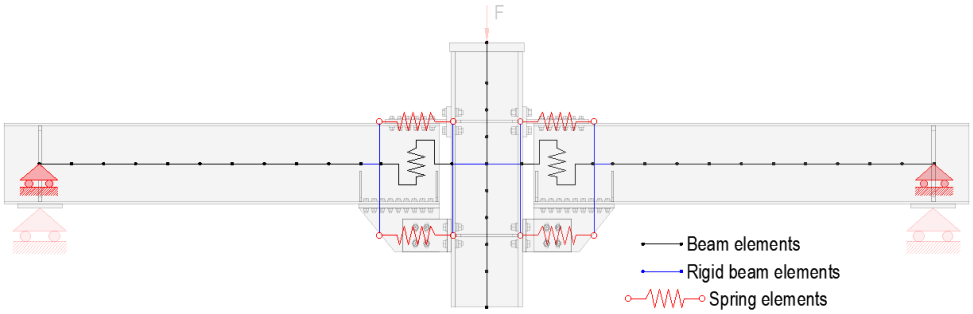

***Figure 4.18**: Schematic view of the numerical model – Test 1*

The prediction in terms of applied force vs. vertical displacement recorded during testing at the level of the column is given in Fig. 4.19. The results reveal some inconsistencies between the experimental force-displacement curve and the prediction of the 2SM in terms of overall curve shape and the ultimate capacity of the specimen. These inconsistencies arise from the approach used to characterise the behaviour of the friction damper integrated in the 2SM. Indeed, the initial modelling approach doesn't account for any preload loss that occurs in the preloaded high-strength (HS) M16 damper bolts along the slippage phase (2SM-w/oPL). This leads to a 6.4% overestimation of the ultimate capacity of the specimen as well as to an overall plateau-shaped *F-d* curve along the slippage phase of the dampers.

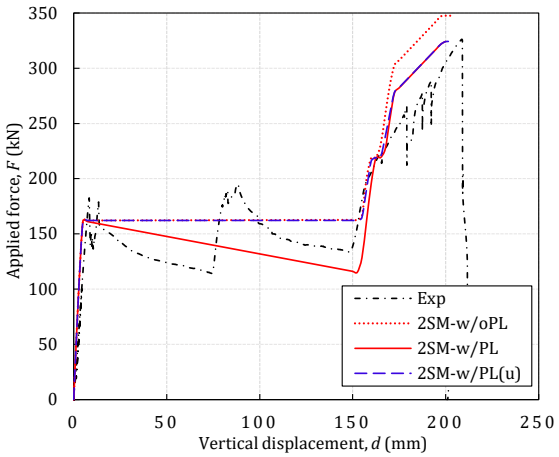

***Figure 4.19**: Global force vs. vertical displacement curve: Test 1*

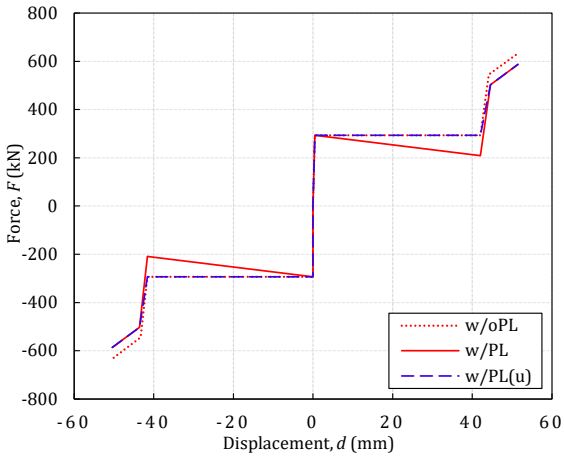

***Figure 4.20**: Bottom spring (damper) behaviour law*

Nonetheless, experimental observations and measurements taken during the previously presented Test 2 allowed concluding that an averaged 29% preload loss was registered during the slippage phase of the damper.

To account for the expected preload loss, the behaviour law assigned to the lower spring of the 2SM was modified by integrating the preload loss (PL) as a linear decrease of the damper friction resistance along the slippage phase (w/PL behaviour law in Fig. 4.20). However, since the resistance decay due to the preload loss is not an indicative of the joint's robustness but rather a

phenomenon that influences mainly the hysteretic energy dissipated under seismic excitation, an additional way of characterising the behaviour of the components acting at the level of the damper was considered for robustness-related investigations. This behaviour law disregards the resistance decay along the slippage phase of the damper, yet it accounts for the effects of preload loss on the ultimate resistance of the damper assembly (behaviour law w/PL(u) in Fig. 4.20). This modelling approach safely idealises the joint behaviour in the slippage phase through a plateau, which in turn allows performing stable numerical simulations in robustness-related scenarios accounting for the actual post-slippage behaviour of the joints.

Therefore, three numerical models were built by implementing the preload loss in the HS M16 bolts of the friction dampers in three different ways as follows:

- 2SM-w/oPL: the 2SM without any preload loss considered
- 2SM-w/PL: the 2SM with the preload loss considered linear along the slippage phase of the dampers and integrated in the ultimate capacity of the joint
- 2SM-w/PL(u): the 2SM with the preload loss integrated only for the ultimate capacity of the joint with a plateau-shaped slippage phase of the dampers.

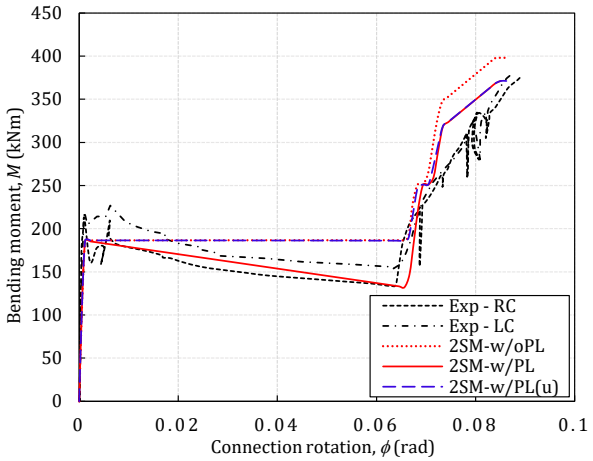

Figure 4.21: *Predicted moment vs. rotation curves – Test 1*

Fig. 4.21 reflects the comparison between the predicted and the experimental moment-rotation curves for the right and left connections (RC and LC) of the tested joint. Generally, the 2SM predicts with an acceptable accuracy the full-range behaviour of the FREEDAM joints, although the results reveal the model sensitivity to the characterisation of basic joint components. Indeed, the behaviour law considered for the characterisation of the friction damper plays a crucial role in achieving accurate predictions in terms of both deformation and strength capacities.

It is evident that, in order to accurately predict the ultimate capacity of the connections, the preload loss in the HS M16 bolts and its inherent effects on the friction resistance of the dampers should be considered. For both cases where the expected preload loss was considered (2SM-

w/PL and 2SM-w/PL(u)), the 2SM provides predictions with acceptable accuracy for the full-range behaviour of the tested joint with a notable perfect match between the recorded and predicted ultimate moment resistance and deformation capacities, both parameters being of key importance for assessing the robustness of the joints.

Response under combined bending moment and axial force

The numerical model used to replicate the behaviour of the FREEDAM joint tested under combined bending moment and axial force (Test 2) comprised the 2SM combined with classical beam elements as schematically represented in Fig. 4.22.

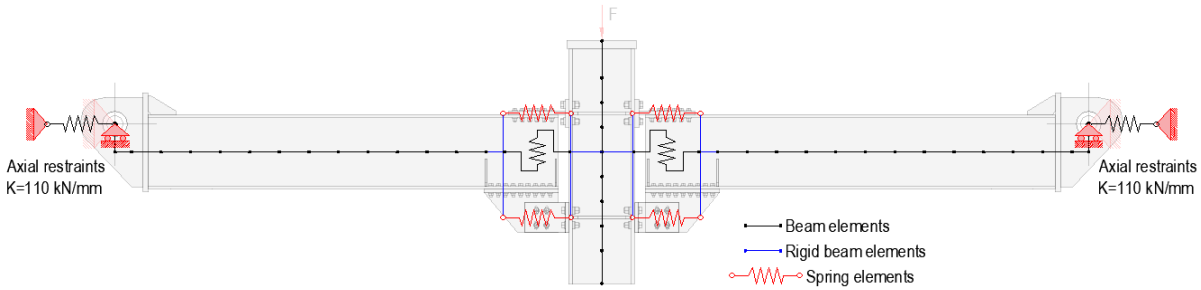

***Figure 4.22**: Schematic view of the numerical model – Test 2*

The axial restraints provided in the numerical model through extensional springs simulate the deformability of the experimental in-plane restraining system. The axial stiffness of these restraints was estimated based on experimental recordings of the axial forces in the beams of the specimen and the corresponding horizontal displacement recorded at the extremities of the test specimen. As reflected in Fig. 4.24, the axial stiffness of the in-plane restraining system was estimated at 110 kN/mm, and it was assigned to the extensional springs at the extremities of the numerical model to account for the actual boundary conditions provided by the test rig.

The comparison between the predicted and experimental force-displacement curves shown in Fig. 4.22 highlight the sensitivity of the 2SM to the method used for characterising the behaviour of basic joint components. In particular, the implementation of the effects of preload losses in the response of the friction damper seems to govern the accuracy of predictions provided by the 2SM. It is worth noting that the best agreement between the prediction and experimentally observed response is provided by the numerical model in which the preload loss was considered as occurring along the slippage phase of the dampers with inherent effects over the friction and ultimate resistance of the FREEDAM joints (2SM-w/PL).

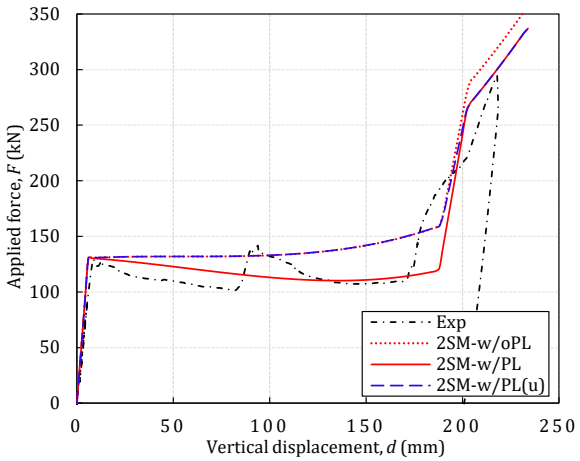

***Figure 4.23**: Applied force vs. vertical displacement curves*

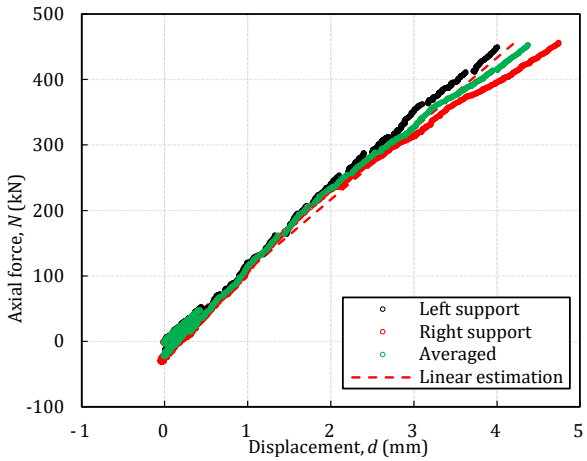

***Figure 4.24**: Beam axial force vs. lateral support horizontal displacement*

However, an acceptable prediction is also provided by the numerical model in which the preload loss was considered as affecting exclusively the ultimate strength of the joint (2SM-w/PL(u)) and the slippage phase characterised by a plateau. Although the decay in the applied force along the slippage phase of the connections is not captured, the model provides an identical post-slippage response in terms of stiffness and ultimate capacity as the 2SM-w/PL model.

An overestimation of the specimen's ultimate capacity of approximately 9% is observed for both numerical models in which the preload loss was implemented. This discrepancy may be attributed to the fact that the experimental test was stopped due to safety reasons before reaching the actual ultimate capacity of the specimen which would correspond to the brittle rupture of the damper bolts subjected to shear. Indeed, since the actual failure was not reached, some residual strength should be envisaged. This was highlighted by the perfect agreement between the predicted and actual capacity of the specimen used in Test 1 where the ultimate failure was reached during the test.

Fig. 4.25 shows the development of beam catenary action during testing and the predictions provided by the three numerical models. It is worth noting that the evolution of beam axial forces seems to be insensitive to the approach chosen to characterise the response of the friction damper with respect to the bolt preload loss.

As previously mentioned, in contrast to the beam axial force, the evolution of the bending moment at the level of connections is highly relying on the considered response of the friction damper. This observation is endorsed by the results reported in Fig. 4.26 where the comparison between the experimental response of the right connection (RC) and the numerical prediction highlights the accuracy of the 2SM in replicating the behaviour of the FREEDAM joint under combined *M-N* when the preload loss is accounted for.

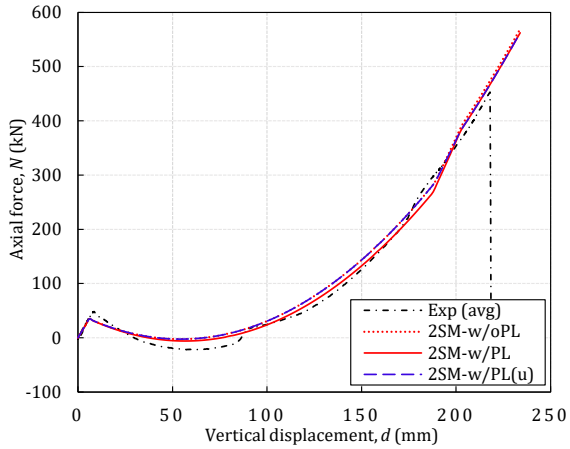

***Figure 4.25**: Beam axial force vs. vertical displacement curves*

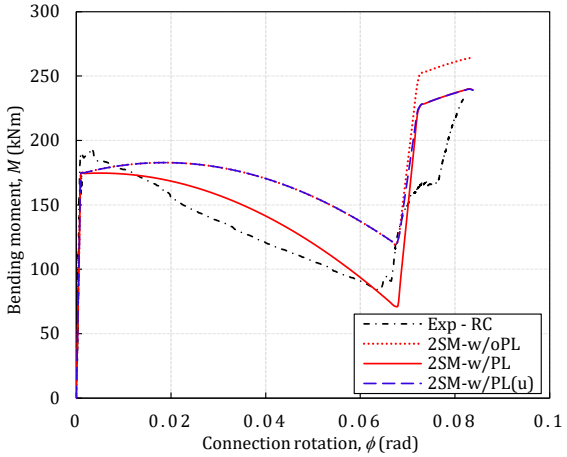

***Figure 4.26**: Connection moment vs. rotation curves*

4.3.3 Concluding remarks on the simplified modelling of FREEDAM joints

The results discussed in the previous sections prove the suitability of the 2SM for numerical studies in which the full-range behaviour of FREEDAM joints is of interest. Moreover, for robustness-related investigations such as simulations of column loss scenarios in which the proper integration of the post-slippage response of the FREEDAM joints is critical, the validation of the 2SM allowed identifying an acceptable compromise in terms of model complexity.

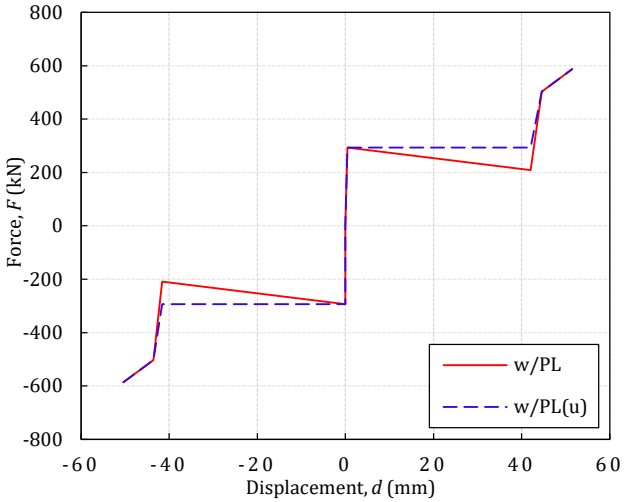

***Figure 4.27**: Behaviour laws for the assembly of components active at the damper level*

The identified modelling solution accounts for an expectable preload loss of 29% at the damper stroke limit which affects the ultimate capacity of the overall FREEDAM joint (w/PL). However, in order to ensure the convergence of large numerical simulations performed on global structural models, the preload loss can be considered as affecting exclusively the ultimate capacity of the joints (w/PL(u)). Therefore, the slippage phase of the damper's response can be defined as a plateau, and the effects of the preload loss can be integrated into the estimation of the damper's ultimate resistance as reflected in Fig. 4.27. This modelling approach eliminates the need for

introducing response regions with negative stiffness, which in turn facilitates the convergence for numerical solvers with a marginal influence on the overall accuracy of the results when the post-slippage response of FREEDAM joints is of concern. In the following section, this approach is used for numerical simulations for column loss scenarios used for evaluating the robustness of the DREAMERS pilot building.

4.4 ROBUSTNESS ANALYSIS OF THE DREAMERS PILOT BUILDING

Although the tying method is normatively prescribed for the design for robustness of all structures in consequences class 2, the so-achieved level of structural robustness remains uncertain. The application of this design method can be seen as a minimum but not necessarily sufficient requirement. Moreover, the analytical formulae for determining the tying resistance demand are not endorsed by a solid scientific background, which raises doubts about the method's applicability and reliability.

Therefore, the use of more advanced procedures such as the standard-prescribed "notional removal of supporting elements" approach, also known as the alternative load path approach, requiring the consideration of geometrical and material non-linearities, is justified for any structure with significant consequences of failure. The requirement to be met is to prove that, upon the removal of any supporting column (or beam supporting a column), the stability of the structure is not affected, and the extent of local damages remains under specific limits. Since the loss of a supporting member can be caused by a multitude of accidental events, this approach allows assessing the robustness of a structure regardless of the accidental action that triggers the member loss, thus covering a wide range of unidentifiable accidental actions. As recommended in EN 1991-1-7, when the loss of a member leads to a progressive collapse or the local damage associated to the member loss exceeds the predefined limits, the design should turn towards methods of local enhancement of resistance and ductility of the member under consideration. The application of the alternative load path method to the DREAMERS building is presented hereafter with a specific attention paid to local response of the FREEDAM joints and the influence of non-structural elements on the structure's collapse resistance.

4.4.1 Assumed column loss scenarios

Given the variety of accidental actions that can lead to a column loss (e.g., fire, explosions, impacts), the latter can be treated as a dynamic or quasi-static event. However, EN 1991-1-7 which deals with the design for accidental actions is not stating if this notional column removal has to be assumed as instantaneous, i.e. as "dynamic", or as "quasi-static". Only for buildings

falling into the Consequence Class 3 (CC3) the design standard recommends using advanced analysis tools with account for dynamic effects.

Considering that the DREAMERS building is included in CC2, lower risk group, the structural behaviour upon the loss of supporting columns was analysed under quasi-static conditions. The consideration of a "quasi-static" removal allows (i) the use of more simple tools as no dynamic effects need to be accounted for and (ii) to have a good indication on the structure's ability to activate alternative load paths.

Three distinct scenarios were chosen for investigating the structural robustness further to a column loss. As depicted in Fig. 4.28, an internal column loss is assumed, which allows evaluating the level of tensile forces reached in the hinged beams in the inner bays of the structure further to the column loss. The other two scenarios concern perimeter and corner column losses and highlight the influence of the local behaviour of the FREEDAM joints on the global response and robustness of the DREAMERS building.

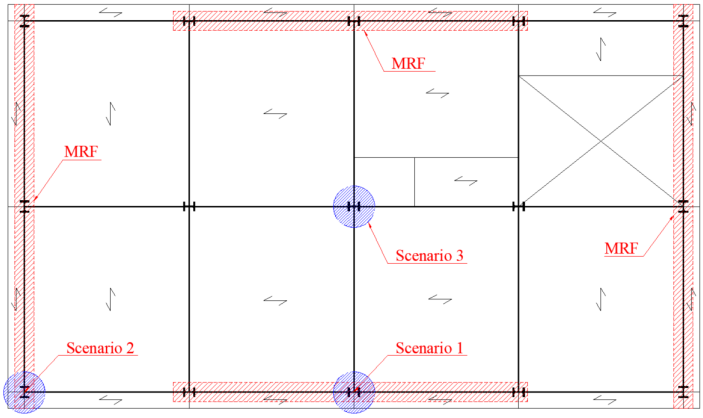

***Figure 4.28**: Assumed base floor column loss scenarios within the DREAMERS pilot building*

4.4.2 Modelling assumptions

The column loss was numerically simulated through nonlinear static analyses in the homemade finite element software FINELG [19]. The software allows performing different types of analyses (e.g., elastic, nonlinear, static/dynamic) with account for geometric and material nonlinearities.

The structural model was built using classical 3D beam elements (7 degrees of freedom) with material behaviour laws incorporating the yielding plateau and the strain hardening of steel material. The provisions of the new draft of prEN 1993-1-14 [20] were used to define the nonlinear behaviour law for the S355 steel.

The composite slab consisting of a Cofradal 260 floor solution was not explicitly modelled. However, given the importance of the slab contribution to the structural response under lateral

loads due to the diaphragm effect, the latter was considered through a horizontal bracing system at the level of each floor as illustrated in Fig. 4.29 and as recommended in the FAILNOMORE design manual. Rigid beam elements with circular cross-section were used to model the bracing elements such that the relative horizontal displacements between the columns at the level of each slab are prevented. This modelling approach generally leads to conservative results when column loss scenarios are considered since the slab contribution to the floor plastic mechanism and the possible activation of membrane action within the slab are neglected.

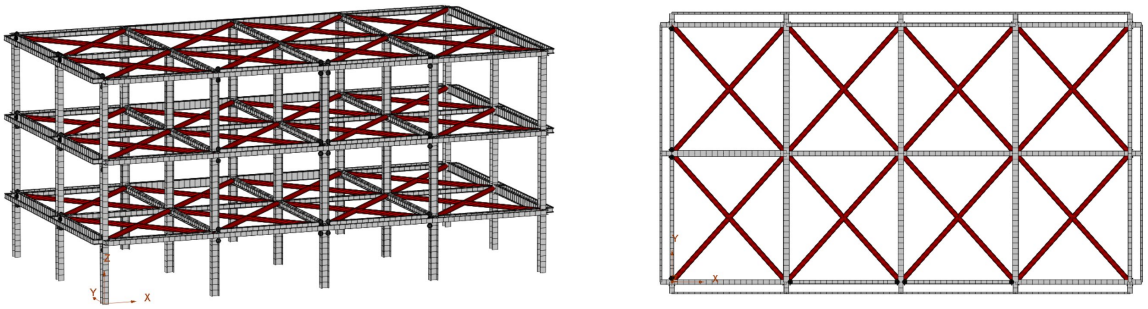

a)3D view ***b) Plan view***

Figure 4.29*: Modelling of slab diaphragm effects*

The loads perpendicularly applied on the one-way slabs were assigned to the supporting beams as uniform line loads estimated based on the direction of slab load transfer and tributary areas. The accidental load combination was considered in the analyses according to the prescriptions of EN 1990 [21].

$$\sum_{j\geq 1} G_{k,j} + A_d + \psi_{1,1} Q_{k,1} + \psi_{2,i} Q_{k,i} \qquad (4.8)$$

The permanent and variable actions ($G_{k,j}$ and $Q_{k,1}$) were taken identical to the ones used in the regular design of the building for the Serviceability Limit State (SLS) and Ultimate Limit State (ULS) as reported in Table 4.2. No specific values for the accidental action A_d were considered in the structural model as this action represents the loss of a supporting column (i.e. A_d is in this case the removal of a support). A combination factor $\psi_{1,1}$=0.5 as recommended in the Eurocodes was used for the variable loads $Q_{k,1}$, even though the Italian normative [22] allows using a less demanding combination factor $\psi_{1,1}$=0.3 for office buildings in accidental situations.

Table 4.2*: Design loads*

Load	Type	1st floor	2nd floor	3rd floor
Dead load (kN/m^2)	$G_{k,1}$	5.35	5.35	4.15
Live load (kN/m^2)	$Q_{k,1}$	3.0	3.0	-
Cladding (kN/m)	$q_{k,1}$	4.4	4.4	-
Snow load (kN/m^2)	$Q_{k,2}$	-	-	0.6

The loss of supporting columns in the pilot building was simulated through a two-sequence analysis. For the first sequence, the lost column was replaced by a reaction force equal to the column design axial force N_d in the accidental load combination. The second sequence initiates a nonlinear analysis in which an incremental downward force $F=\lambda N_d$ was applied at the same location as Nd as depicted in Fig. 4.29.

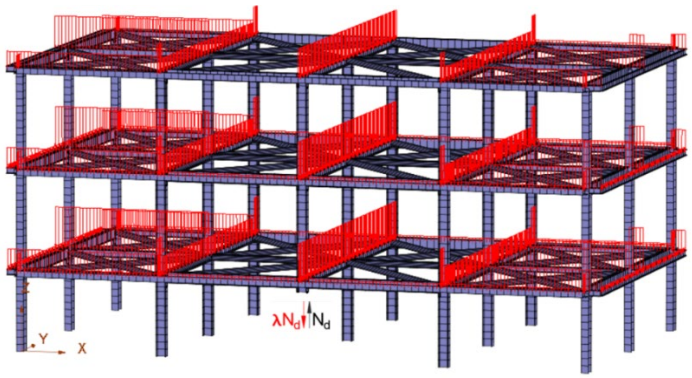

***Figure 4.30**: Column loss loading sequence*

The evolution of the axial force N in the lost column is then plotted with respect to the vertical displacement d of the force application point. The full nonlinear structural response is thus characterised by a force-displacement N-d curve (pushdown curve) which is used further to evaluate the robustness of the structure under the considered column removal scenario.

4.4.3 Structural robustness under column removals

Robustness under a perimeter column removal scenario

To evaluate the response further to the assumed column removal, the pilot building was initially considered as a bare steel structure (BSS). This allows drawing conclusions on the robustness of the main structural system as well as observing the local contribution of the FREEDAM joints for collapse resistance. Fig. 4.30 depicts the structural behaviour of the pilot building under the perimeter column loss (Scenario 1).

It is noticeable that the large rotational capacity of the dissipative joints provided in the two bays adjacent to the lost column allows for the development of significant membrane forces in the beams (920 kN) of the directly affected part (DAP). This enables the structure to sustain the column loss with significant residual strength yielding a Demand/Capacity (D/C) ratio D/C=0.52. The collapse is triggered by the successive failure of the FREEDAM joints located at the 1st and 2nd storeys (highlighted in red in Fig. 4.31a) which are subjected to a combination of hogging moment and axial tensile force that leads to the failure of the T-stub in bending component (upper spring in the 2SM).

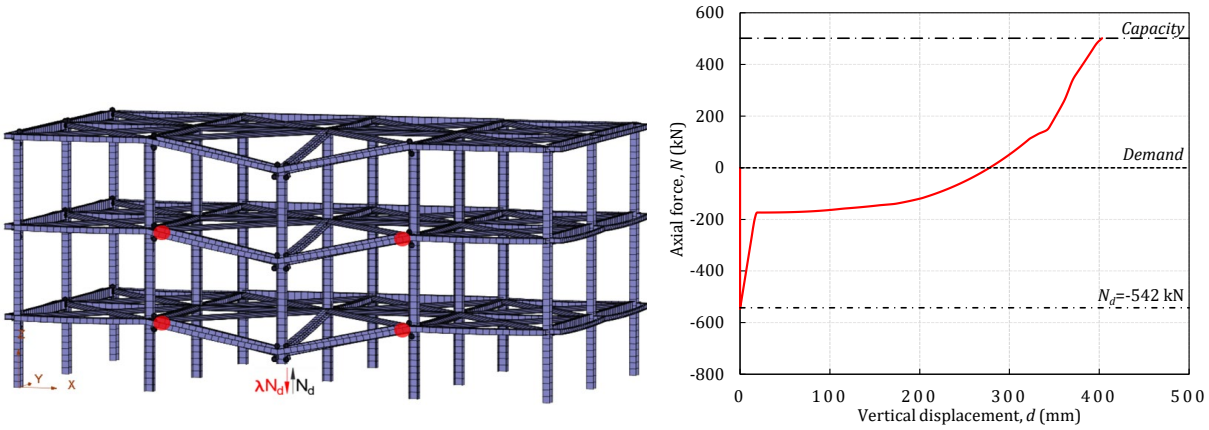

a) Deformed shape ***b) Column axial force vs. vertical displacement***

***Figure 4.31**: Response of the bare steel structure under the perimeter column loss (Scenario 1)*

Fig. 4.32 shows the variation of internal forces with respect to the chord rotation in the failing joints. The evolution of internal forces within the structure reveals some important peculiarities related to the behaviour of the FREEDAM joints and the fact that the structural response of buildings equipped with such joints is quite different when compared to structures with conventional joints subjected to column losses. Notably, the bending moment acting on the joints located at the extremities of the bays adjacent to the removed column increases even after membrane forces start emerging in the beams. This contrasts with the typical behaviour observed in structures with conventional semi-rigid joints, as demonstrated by [4], [23], and [24] among others.

Complementary resisting mechanisms ensured by the interaction between structural elements and non-structural infill façade walls can be envisaged in addition to the collapse resistance of the bare steel structure (BSS).

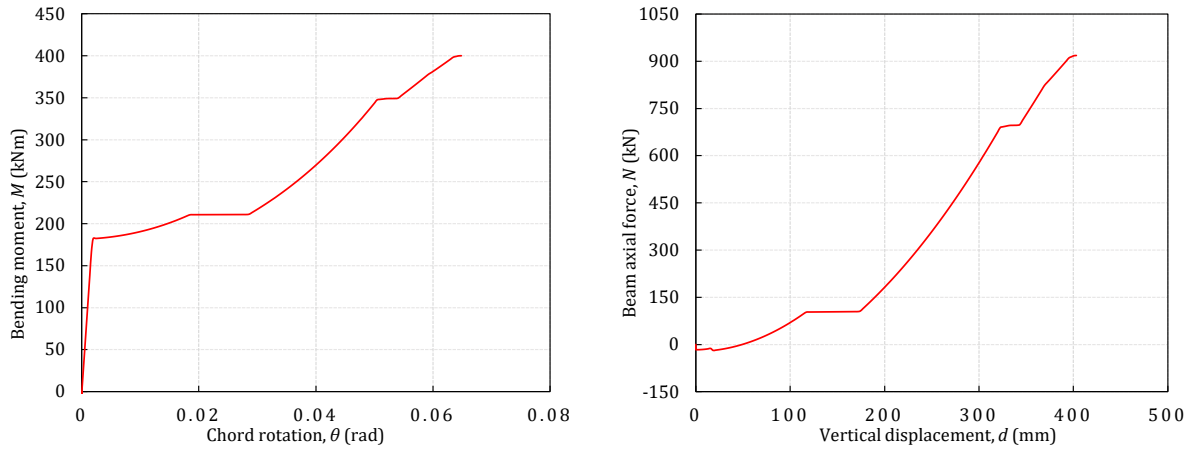

a) Moment vs. chord rotation ***b) Axial force vs. chord rotation***

***Figure 4.32**: Evolution of internal forces at the level of the failing FREDAM joint*

An experimental campaign performed by [25] on exterior façade walls subjected to seismic action revealed that, depending on their connectivity to the surrounding structural members, these non-structural elements exhibit a non-negligible stiffness and strength when subjected to in-plane loads. The main outcomes of the experimental programme were reported in terms of fragility curves for façade (and partition) walls that correlate the extent of damage observed on non-structural walls to the Inter-storey Drift Ratios (IDRs) as illustrated in Fig. 4.33a.

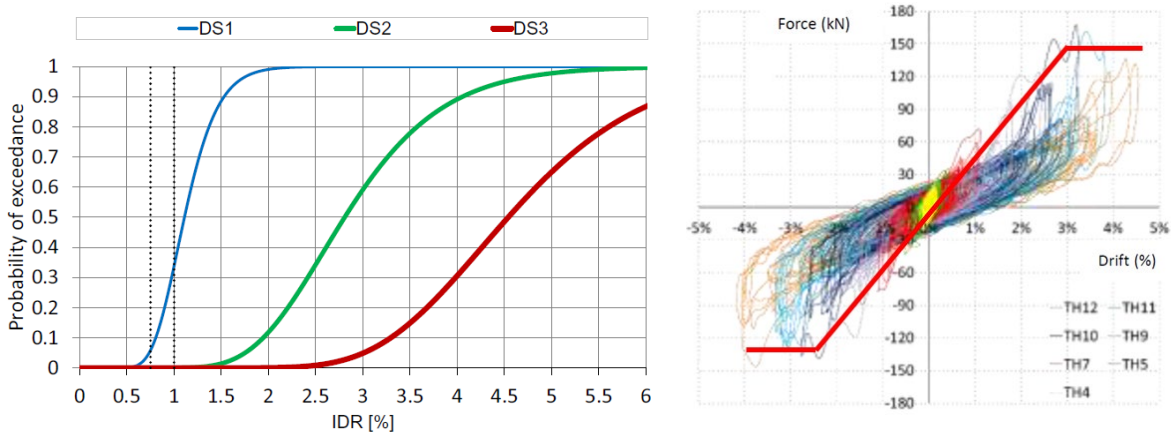

a) Fragility curves ***b) Backbone resistance curve for cyclic loads***

Figure 4.33*: Experimental results for façade walls with enhanced connections subjected to dynamic loads [25]*

For façade walls with enhanced anti-earthquake connections similar to the ones used on the perimeter of the DREAMERS building, the results of seven experimental tests performed under cyclic loads (ground motion) with different intensities allowed deriving a simplified backbone curve that characterises the individual response of façade walls subjected to in-plane loads. In Fig. 4.33b, the red thick curve represents the so-determined backbone curve based on the peak resistance of each specimen reached throughout testing. This can be viewed as a behaviour law of façade panels subjected to in-plane horizontal loads.

Due to the lack of experimental evidence on the response of façade panels subjected to vertical (i.e., along-panel) in-plane loads, the behaviour of the non-structural façade panels was incorporated in the numerical simulations using the following simplifying assumptions:

- The panel response was assumed to be identical under both horizontal and vertical in-plane loads;
- In column loss scenarios, the concept of IDR was estimated as the equivalent relative drift between the ends of the bay adjacent to the lost column;
- Façade panels was assumed to occur at an IDR of 4.5%.

Based on these assumptions, the façade panels were integrated into the numerical model by introducing several shear springs as depicted in Fig. 4.33a. The behaviour of these springs was

defined using a generic backbone curve (see Fig. 4.33b), scaled according to the dimensions of the façade panels employed in the DREAMERS building.

Initially, the panels were considered to cover the entire surface of the façade in the spans adjacent to the lost column (BSS+NSE (plain Fig. 4.34a) in). However, due to the extensive glazing on the façade, the actual dimensions of the solid panels may significantly reduce their structural contribution. To address this, an additional model was developed to reflect the actual façade configuration, in which window and glazed areas were treated as non-contributory to the resisting system (BSS+NSE (actual) in Fig. 4.34b).

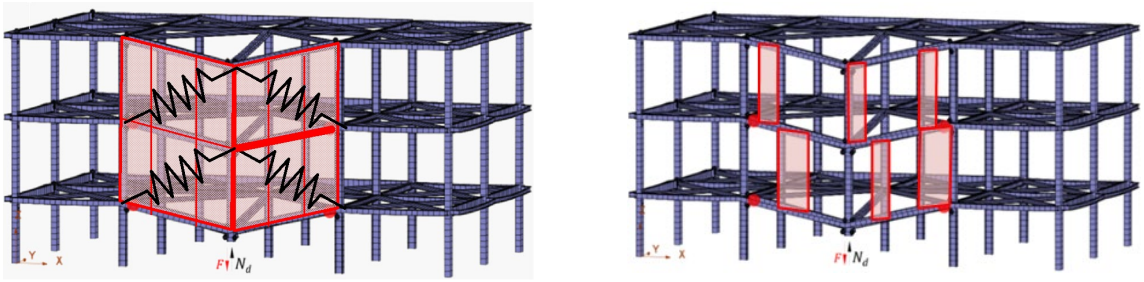

a) BSS+NSE (plain) ***b) BSS+NSE (actual)***

Figure 4.34*: Façade panels integration in the numerical model*

Non-linear finite element (FE) analyses were carried out on the developed models to evaluate the impact of non-structural façade panels on the overall structural robustness of the pilot building in the event of a perimeter column loss. The results presented in Fig. 4.35 indicate that the contribution of these elements is far from negligible. In particular, when the façade panels are assumed to cover the entire façade surface (BSS+NSE (plain)), the structure demonstrates an enhanced response, characterised by increased stiffness during the slippage phase of the FREEDAM connections and a significantly higher ultimate capacity. This is reflected in a demand-to-capacity (D/C) ratio of 0.48, indicating improved performance even compared to the BSS configuration (D/C = 0.52), albeit with a slightly reduced deformation capacity (ductility). The integration of actual panel dimensions into the numerical model (BSS+NSE (actual)) indicates that, in the actual configuration, the façade panels contribute to structural robustness, although to a lesser extent than in the idealised case with continuous panels. The ductility supply is limited by the assumed failure of the façade panels at an interstorey drift ratio (IDR) of 4.5%, corresponding to a 50% probability of exceeding Damage Limit State 3 (DS3), as defined by the fragility curves in Fig. 4.33a. Based on this failure criterion, the resulting D/C ratio is approximately 0.67. This suggests that the pilot building would withstand the perimeter column removal scenario with a 33% reserve in resistance.

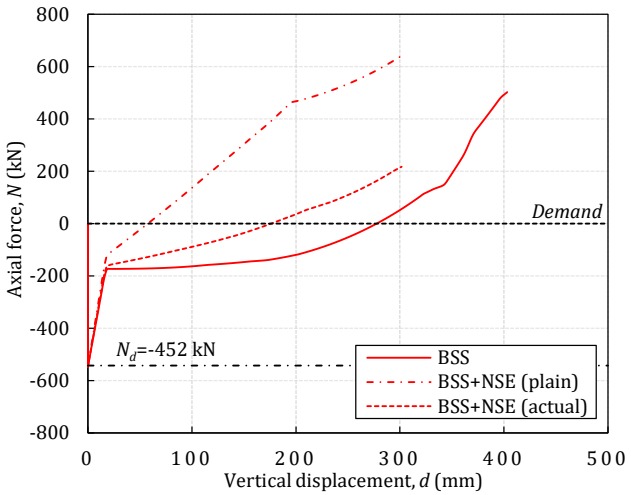

***Figure 4.35**: Column axial force vs. displacement further to the perimeter column loss*

It is important to note that this D/C ratio is associated to the failure of the non-structural façade panels. In practice, once these panels fail, the structural response is expected to align with the BSS case—where façade panels are not considered—ultimately resulting in the same D/C ratio observed for the BSS model (i.e., D/C = 0.52)

Robustness under a corner column removal scenario

Generally, the loss of a corner column is among the most demanding scenarios in terms of structural robustness. The absence of axial restraints at one end of the orthogonal beams converging at the corner column prevents the development of catenary action. As a result, the primary resistance scheme relies on the plastic mechanism of the beams, which—within the pilot building—is governed by the ultimate bending resistance of the FREEDAM joints.

It is important to highlight that along the Y-direction perimeter moment-resisting frames (MRFs), the joints on the first two floors are equipped with D2 FREEDAM devices, which provide a higher ultimate bending capacity of $M_{u(D2)}$ = 520 kNm. In contrast, the joints along the X-direction, fitted with D1 devices, have a lower ultimate capacity of $M_{u(D1)}$ = 365 kNm.

Since catenary action cannot be amobilised in this scenario, the joints are primarily subjected to bending. However, given the significantly higher bending resistance of the D2 FREEDAM joints along the Y-direction, the structure is able to withstand the corner column removal with a D/C ratio of 0.87 when considering the bare steel structure (BSS, Figure 24b). Collapse is ultimately triggered by premature shear failure of the bolts within the friction devices.

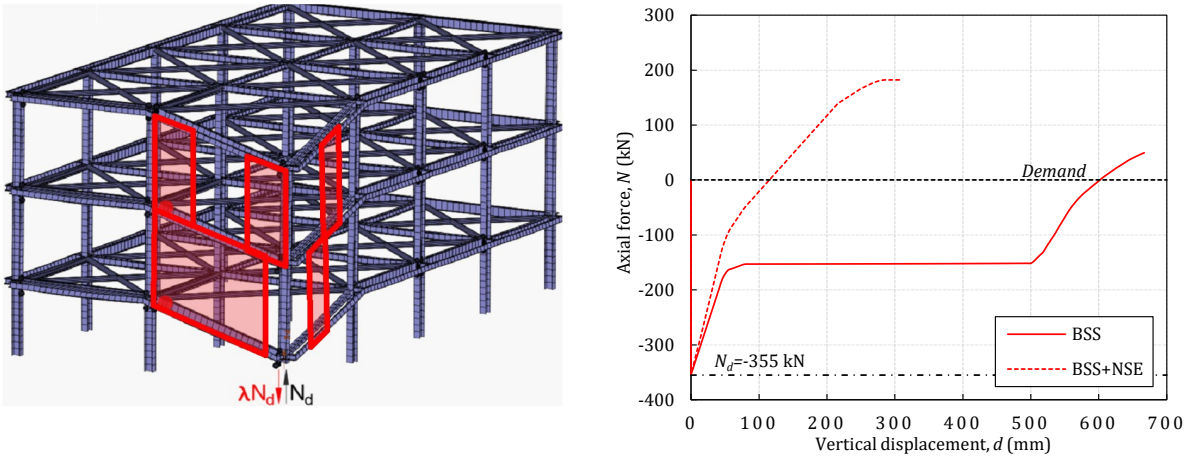

a) Deformed shape ***b) Column axial force vs. vertical displacement***

Figure 4.36*: Structural response under the corner column loss (Scenario 2)*

The response of the bare steel structure (BSS) is significantly enhanced by the contribution of the façade panels present in the directly affected part (DAP) of the structure, as shown Fig. 4.36. Non-linear FE analysis of the model incorporating these non-structural façade elements (BSS+NSE) demonstrates a substantial improvement in structural robustness. This is primarily due to the increased stiffness provided by the façade panels during the slippage phase of the dissipative joints. As a result, the D/C ratio decreases to 0.66, indicating that the pilot building is capable of withstanding the loss of the corner column with considerably reduced ductility demand for the joints.

Robustness under an internal column removal scenario

The pushdown curve reported in Fig. 4.37b (where $F=\lambda N_d$) reveals that, to survive an internal column loss, the beams and their simple end-connections should provide sufficient rotation capacity and resistance to accommodate a vertical displacement of 232 mm.

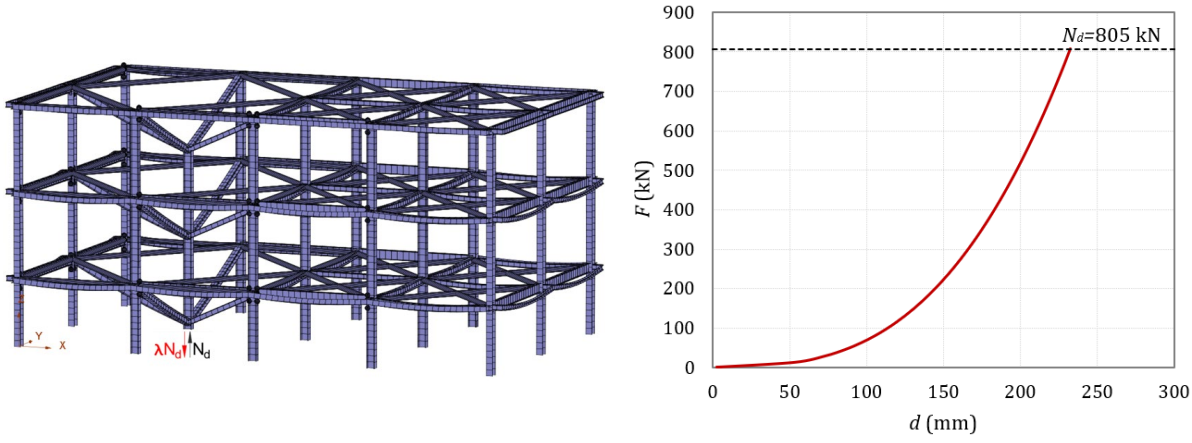

a) Deformed shape ***b) Downard force vs. vertical displacement***

Figure 4.37*: Structural response under the internal column loss (Scenario3)*

Provided that the ductility and strength requirements are met, the tensile forces in the directly affected part (DAP) of the structure bridging over the lost column reach values of 1810 kN and 1940 kN in the beams along the X and Y direction, respectively (see Fig. 4.38). In comparison, the simple end-connections of the internal beams exhibit an ultimate tensile resistance of only 429.1 kN, which is significantly lower than the demand imposed by the column loss scenario.

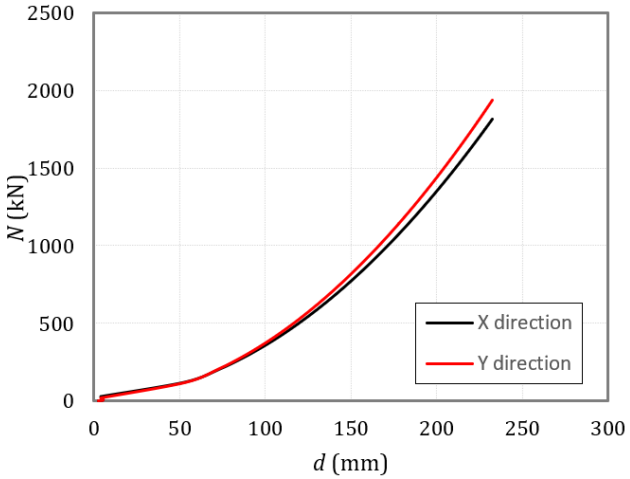

***Figure 4.38**: Evolution of tensile forces in the beams of the DAP*

Normally, solutions to enhance the resistance of the simple connections could be envisaged; however, such measures would lead to unrealistic/unpractical solutions for the simple (hinged) joints as highlighted in the FAILNOMORE Design Manual [2]. Therefore, to resist these high tensile forces, semi-rigid joints should be used instead of simple connections; yet this change is to be avoided for the pilot building due to its influence on the structural seismic performance thus implying a redesign of the structure.

The alternative is to prevent the column loss that triggers the collapse by designing the column as a *key element*. Practically, as prescribed by EN 1991-1-7 [1], the normative method is to design the column so that it is capable of sustaining an accidental design action of 34 kN/m^2 applied in horizontal and vertical directions (one at a time) to the column and any components attached to it.

Nonetheless, given the absence of non-structural components connected to the internal column at the base floor of the pilot building (serving as parking), this design method leads to rather low demands in terms of strength and stability, when applied to the column under consideration. Furthermore, when compared to the Ultimate Limit State requirements for which this column was initially designed, the demand in terms of bending moment and shear forces resulting from the application of the accidental design action of 34 kN/m^2 as prescribed by EN 1991-1-7, are trivial, and the checks for the key element requirements can be deemed fulfilled.

4.5 REFERENCES

[1] EN 1991-1-7, *Eurocode 1 - Actions on structures - Part 1-7: General actions - Accidental actions*. Brussels: European Committee for Standardisation, 2006.

[2] J.-F. Demonceau *et al.*, *FAILNOMORE - D3-1: Design recommendations against progressive collapse in steel and steel-concrete buildings*, 1st ed. ECCS – European Convention for Constructional Steelwork, 2021.

[3] B. A. Francavilla, M. Latour, G. Rizzano, J.-P. Jaspart, and J.-F. Demonceau, "On the robustness of earthquake-resistant moment-resistant frames: influence of innovative beam-to-column joints," *Open Construction and Building Technology Journal*, vol. 12, 2018, doi: 10.2174/1874836801812010101.

[4] J.-F. Demonceau, "Steel and composite building frames: sway response under conventional loading and development of membrane effects in beams further to an exceptional action," PhD Thesis, Université de Liège, 2008.

[5] U. Kuhlmann, "Redundant and Robust Frame Structures by Joint Ductility," presented at the COST Action TU0601, 1st Workshop, Zurich, Switzerland, 2008, p. 14.

[6] J.-F. Demonceau and J.-P. Jaspart, "Experimental test simulating a column loss in a composite frame," *Advanced Steel Construction*, vol. 6, no. 3, pp. 891–913, 2010.

[7] FREEDAM (2015-2018): "FREE from DAMage Steel Connections". Fund for Coal and Steel Grant Agreement No. RFSR-CT-2015-00022

[8] A. F. Santos, A. Santiago, M. Latour, and G. Rizzano, "Robustness analysis of steel frames subjected to vehicle collisions," *Structures*, vol. 25, pp. 930–942, Iunie 2020, doi: 10.1016/j.istruc.2020.03.043.

[9] T. Golea, A. F. Santos, J.-P. Jaspart, M. Latour, A. Santiago, and J.-F. Demonceau, "Robustness of Steel Frame Structures Equipped with FREEDAM Dissipative Joints," *ce/papers*, vol. 5, no. 4, pp. 210–217, 2022, doi: 10.1002/cepa.1747.

[10] T. Golea, A. F. Santos, J.-P. Jaspart, M. Latour, A. Santiago, and J. Demonceau, "Design for robustness of steel structures with dissipative FREEDAM joints," *International Journal of Earthquake Engineering*, vol. 2, 2022.

[11] U. Kuhlmann *et al.*, *Robust impact design of stel and composite building structures (ROBUSTIMPACT)*. European Commission, 2017.

[12] G. F. Cavallaro, M. Latour, A. B. Francavilla, V. Piluso, and G. Rizzano, "Standardised friction damper bolt assemblies time-related relaxation and installed tension variability,"

Journal of Constructional Steel Research, no. 141, pp. 145–155, 2018, doi: 10.1016/j.jcsr.2017.10.029.

[13] EN 1090-2, "EN 1090-2-2018, Execution of steel structures and aluminium structures. Part 2:Technical requirements for steel structures." 2018.

[14] M. D'Antimo, "Impact characterization of innovative seismically designed connections for robustness application," Université de Liège, Liège, Belgique, 2020. Accessed: Nov. 06, 2020. [Online]. Available: https://orbi.uliege.be/handle/2268/246289

[15] ISO 6892-1:2009(E), *INTERNATIONAL STANDARD ISO 6892-1 — Metallic materials — Tensile testing — Part 1: Method of test at room temperature*. Switzerland: International Organization for Standardization, 2009.

[16] EN 1993-1-8, *Eurocode 3 - Design of steel structures - Part 1-8: Design of joints*. Brussels: European Committee for Standardisation, 2005.

[17] A. F. Santos, A. Santiago, M. Latour, G. Rizzano, and L. Simões da Silva, "Response of friction joints under different velocity rates," *Journal of Constructional Steel Research*, vol. 168, 2020, doi: https://doi.org/10.1016/j.jcsr.2020.106004.

[18] J.-P. Jaspart, A. Corman, and J.-F. Demonceau, "Ductility assessment of structural steel and composite joints," Sep. 2019. https://orbi.uliege.be/handle/2268/239363.

[19] FineLg user's manual, "Nonlinear finite element analysis program." Edition 2019.

[20] prEN 1993-1-14, "Design of steel structures - Part 1-14: Design assisted by finite element analysis." European Committee for Standardisation, Brussels, 2021.

[21] EN 1990, *Eurocode 0 - Basis of structural design*. Brussels: European Committee for Standardisation, 2002.

[22] NTC, "Norme techniche per le construzioni." Ministero delle Infrastrutture e dei Trasporti, 2018.

[23] I. Marginean, "Robustness of moment steel frames under column loss scenarios," Politehnica University of Timisoara, 2017.

[24] A. Kozlowski and D. Kukla, "Experimental Tests of Steel Unstiffened Double Side Joints with Flush and Extended End Plate," *Arch. Civ. Eng.*, vol. 65, no. 4, pp. 127–154, Dec. 2019, doi: 10.2478/ace-2019-0051.

[25] R. Landolfo *et al.*, "Seismic response assessment of architectural non-structural LWS drywall components through experimental tests," *Journal of Constructional Steel Research*, vol. 162, p. 105575, Nov. 2019, doi: 10.1016/j.jcsr.2019.04.011.

CHAPTER 5

Fire Vulnerability: Testing and Analysis

5.1 INTRODUCTION

In this chapter, the features related to fire safety and the design of the DREAMERS building are reported and detailed. In particular, it starts by evaluating the minimum fire resistance requirements of the compartments according to the Italian fire code [1] and EN1991-1-2 [2]. Afterwards, the building's resistance is analysed through finite element analysis. The analyses considered the external frames of the DREAMERS building. For this analysis, several fire scenarios are considered, and the fire action is considered through the standard time-temperature ISO 834 curve and parametric curves, which consider the specifications of the different utilisation typologies of the rooms in the building. Numerically, the performance of the DREAMERS building under fire action is checked considering the level of deformation of the structural elements, as well as the level of damage to the FREEDAM beam-to-column connections affected by the fire action.

5.2 FIRE MINIMUM REQUIREMENTS

A first step through the evaluation of the performance level of the building under fire is to assess the required fire resistance of the different compartments. This can be evaluated by using the Italian national code [1] and Eurocodes [2], where one is meant to support the other and vice versa. From the Italian code, quantitative criteria to find the Fire resistance can be assessed, whereas, from the European code, fire actions and parameters leading to the fire definition can be found.

5.2.1 Activities subjected to project revision by the Italian fire authorities

The national Italian regulation DPR 151/2011 [3] establish whether the design of a building is subject or not to a revision by the Italian fire authorities. This is done by considering which is the use of the building by identifying the main activities for which the building has been designed. In the DREAMERS' building, three main activities can be identified: 1) Open car park;

2) Medical laboratory; 3) Office. In Table 5.1**Table 5.1** are listed the minimum requirements associated with each activity to be subjected to a revision by the authorities.

***Table 5.1**: Minimum requirements to be subjected to revision by the Italian fire authorities*

Activity	Minimum requirement (DPR 151)
Open car park	Surface > 300 m^2
Medical Laboratory	Surface > 500 m^2
Office	More than 300 people

The DREAMERS building is not subject to any revision by the Italian fire authorities. Nevertheless, the building design should follow the general rules of fire safety provided at national and European levels [1], [2].

5.2.2 Fire Resistance of the building

Methodology

According to the Italian fire code, DM 3 Agosto 2015 [1], the fire resistance is defined as a function of the design fire load density, where the fire load density is linked to the properties of the combustible material. The minimum fire resistance obtained from Table 5.2 is associated with a compartment of the building (S.2.4.3) [1]. Therefore, in case of more than one single compartment in the building, the minimum fire resistance must be evaluated for each compartment.

***Table 5.2**: Minimum fire resistance as a function of the design fire load: "DM 3 Agosto 2015" [1]*

Design Fire load density $q_{f,d}$ [MJ/m^2]	Minimum fire resistance
$q_{f,d} \leq 200$	-
$q_{f,d} \leq 300$	15
$q_{f,d} \leq 450$	30
$q_{f,d} \leq 600$	45
$q_{f,d} \leq 900$	60
$q_{f,d} \leq 1200$	90
$q_{f,d} \leq 1800$	120
$q_{f,d} \leq 2400$	180
$q_{f,d} > 2400$	240

The design fire load density can be evaluated from the average or characteristic fuel load density "q_f" [MJ/m^2], which can be evaluated using statistical studies already performed and documented in literature or through Eq.(5.1).

$$q_f = \sum_{i=1}^{n} g_i \, H_i \, m_i \, \varphi_i / A \tag{5.1}$$

where:

g_i is the mass [kg] of the i-combustible material

H_i is the calorific value of the i-combustible material

m_i and φ_i factors of combustion and combustion participation for the i-combustible material

A is the total surface of the compartment

The design fuel load density "$q_{f,d}$" is obtained by multiplying the characteristic fire load density "$q_{f,80\%}$" at 80% fractile by several coefficients that account for active safety measures within the building, Eq.(5.2):

$$q_{f,d} = \gamma_{q1} \cdot \gamma_{q2} \cdot \gamma_{ni} \cdot q_{f,80\%} \quad (5.2)$$

where:

$q_{f,d}$ is the design fire load density [MJ/m2]

γ_{q1} , γ_{q2} are parameters related to the size of the compartment and ignition probability. γq1 γq2 are assumed equal to one according to DM 03 Agosto 2015 [1] (Table S.2-6 and Table S.2-7).

γ_{ni} are coefficients accounting for the fire risk related to the size of the compartment and eventual active fire protection measures, Table S.2-7 of DM 03 Agosto 2015 [1].

Compartment 1: Office

The characteristic fire load density for an office compartment can be assumed according to EN1991-1-2 Annex E equal to 511 [MJ/m2] [2], as shown in Table 5.3.

The design fuel load density "$q_{f,d}$" is evaluated according to Eq.(5.2):

$$q_{f,d} = \gamma_{q1} \cdot \gamma_{q2} \cdot \gamma_{ni} \cdot q_{f,80\%} = 1 \cdot 0.9 \cdot 0.85 \cdot 511 = 390.15\ [MJ/m^2]$$

According to Table 5.2, the minimum fire resistance associated with this design fuel load density is R30. This value is also confirmed by Table V.4-1 in DM 3 Agosto 2015 [1], which classifies an office building with a maximum height < 12 meters as R30.

Table 5.3. *Characteristic fuel load density as a function of the occupancy. (table E.4, EN1991-1-2)*

Occupancy	Average Fire Load Density [MJ/m^2]	80% Fractile fire load Density [MJ/m^2]
Dwelling	780	948
Hospital (room)	230	280
Hotel (room)	310	377
Library	1500	1824
Office	420	511
Classroom	285	347
Shopping Centre	600	730
Theatre (Cinema)	300	365
Transport	100	122

Fire Resistance: medical laboratory

For the medical laboratory compartment, at the time when the fire requirement was assessed, there was an uncertainty about the furniture and equipment that this compartment would have. For this reason, several fuel loads coming from statistical studies were considered as close as possible to what one would expect in a medical laboratory, according to [4], Table 5.4.

***Table 5.4**. Fire load densities as close as possible to a medical lab [4]*

Occupancy	80% Fractile fire load Density [MJ/m^2]
Hospital (room)	336
Bacteriological Lab	400
Chemical Lab	600

In Table 5.5, characteristic fuel load density values have been evaluated by multiplying their average value by a coefficient accounting for the variability of the occupancy, as suggested by the Italian national fire code and the International Fire Engineering Guidelines. The design fuel load density "$q_{f,d}$", according to Eq.(5.2), for each occupancy is reported in Table 5.5.

***Table 5.5.** Design fuel load density for the medical lab*

Occupancy	80% Fractile fire load Density [MJ/m^2]	γ_{q1}	γ_{q2}	γ_{ini}	$q_{f,d}$ [MJ/m^2]
Hospital (room)	336	1	0.9	0.85	257
Bacteriological Lab	400	1	0.9	0.85	306
Chemical Lab	600	1.2	0.9	0.85	551

The Hospital room does not seem to be the best choice, mainly because the fuel load is too low, whereas the chemical lab seems to be too conservative. In a chemical lab, one would expect storage of highly flammable materials and so in general, a fuel load higher than a medical lab.
The bacteriological lab seems to be an educated guess among the design fire load densities found. According to Table 5.2, the minimum fire resistance associated with the Bacteriological Lab is R30 and with the Medical Lab R45.

Compartment 2: Car park

Car parks smaller than 300 m2 are defined according to the Italian code as "under threshold" and regulated by a "circolare protocollo 18/12/2020". This document, to be taken as a guide for practitioners, suggests a fire resistance equal to R30.

A further check to ensure that R30 is an appropriate choice can be done by evaluating the fuel load density through Eq.(5.1), considering the fuel load of each car. The maximum number of cars foreseen in the parking lot is equal to eight, and the fuel load associated with a car ranges between 6000 - 12 000 MJ per car [5]. The fuel load density can be evaluated according to Eq.(5.3).

$$q_f = nb_{vehicles} \cdot q_{f,vehicle} \,/\, Area \tag{5.3}$$

Assuming an average value for the car fuel load, a fuel load density equal to 333 MJ/m2 is obtained. The fractile fuel load is evaluated according to suggestions in [4], multiplying fuel load density by 1.2 (qf,80% = 400 MJ/m^2). Finally, the design fuel load density $q_{f,d}$ is evaluated (conservatively) considering no active fire safety protections, meaning $\gamma_n = 1$:

$$q_{f,d} = \gamma_{q1} \cdot \gamma_{q2} \cdot \gamma_{ni} \cdot q_{f,80\%} = 1 \cdot 1 \cdot 1 \cdot 400 = 400\ [MJ/m^2]$$

According to Table 5.2, the minimum fire resistance associated with this design fuel load density is R30.

Fire Resistance: Plant room

The plant rooms foreseen in the building are aimed at containing the heating, air treatment and wastewater discharge systems. The characteristic fuel load for such a compartment has been evaluated from statistical studies published in the international fire engineering guidelines [4].

***Table 5.6**. Fire load density for the plant room [4]*

Occupancy	Fire load Density [MJ/m^2]	80% Fractile Fire load Density [MJ/m^2]
Heating equipment room	300	375

In Table 5.6, the average fuel load density and the 80% fractile, where the latter has been evaluated by multiplying the former by a factor of 1.25 according to the international fire engineering guidelines and the DM 3 Agosto 2015 [1]. The design fuel load density $q_{f,d}$ is evaluated using Eq. (5.2), with γ_{q1} equal to 1.0, γ_{q2} equal to 0.9 and γ_{ini} equal 0.85, obtaining a value of 375MJ/m2 for this load.

According to Table 5.2 the minimum fire resistance associated with this design fuel load density is R15.

It is important to mention that usually plant rooms are subjected to the norm UNI 1192:2019 since there are pump systems aimed to supply water to the active fire protection (sprinklers, internal hydraulic water system) or heating systems with diesel or electrical engines. In this case, the norm UNI 1192:2019 establish a minimum fire resistance of R60.

5.2.3 Fire minimum requirements

In conclusion, the fire resistance requirements can be summarised in Table 5.7. Critical assumptions on this evaluation are on the active fire protection measures (Section 1.3) that can change with the evolution of the building design. Moreover, sources of uncertainties on the evaluated fire load are given by the fact that, at this stage, it is still not possible to know exactly which kind of materials and in what quantities are present in a compartment such as a medical laboratory.

***Table 5.7**. Minimum fire resistance criteria*

Occupancy	Fire resistance in Minutes
Open Car Park	30
Plant Room/Plant room*	15/60*
Medical Lab	30/45**
Office	30

*Case in which the plant room is subjected to UNI 1192:2019
** Depending on the materials in the medical lab.

5.3 FIRE VULNERABILITY ANALYSIS

After assessing the minimum fire requirements for the building, analyses are conducted to check if these requirements are met. These analyses included: (i) a simplified analysis by considering the critical temperatures of the structural members, and ii) an advanced analysis by considering the level of deformation of the structural elements and the level of damage to the FREEDAM beam-to-column joints affected by the fire action.

Several fire scenarios are studied, and the fire action is considered through the standard time-temperature ISO 834 curve and parametric curves that consider the specifications of the different compartments of the building.

5.3.1 Case study

The frames considered for the case study represent three of the external frames of the DREAMERS building, as shown in Fig. 5.2 and Fig. 5.3.

The frames have a total height of 11.92 m. The frames in the XX direction (frames in green in Fig. 5.1) have 4 spans with a column spacing equal to 6.05 m, as shown in Fig. 5.2. The beam-to-column connections in the external spans are pinned (fin plate connections), and in the internal spans, FREEDAM connections are used as beam-to-column connections (D1 device in IPE 400 and IPE 450 beams). The frame in YY direction (frame in blue in Fig. 5.1) has 2 spans with a

column spacing equal to 6.80 m, as shown in Fig. 5.3. In all spans, FREEDAM connections are used as beam-to-column connections (D1 device in IPE 400 beams and D2-A device in IPE 450 beams).

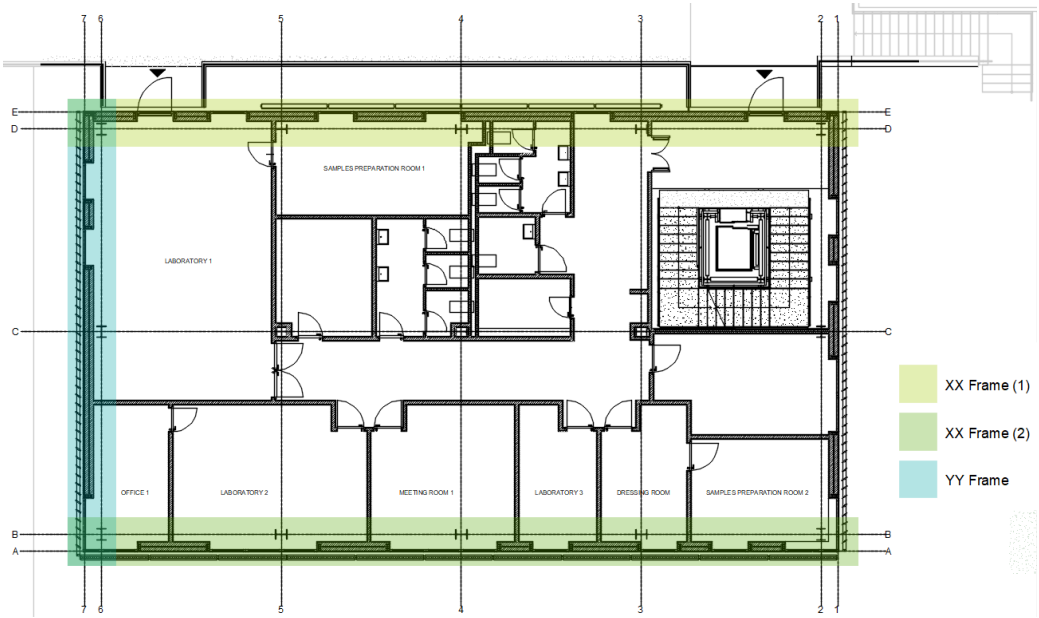

Figure 5.1: *Selected Frames shown in the first-floor plan*

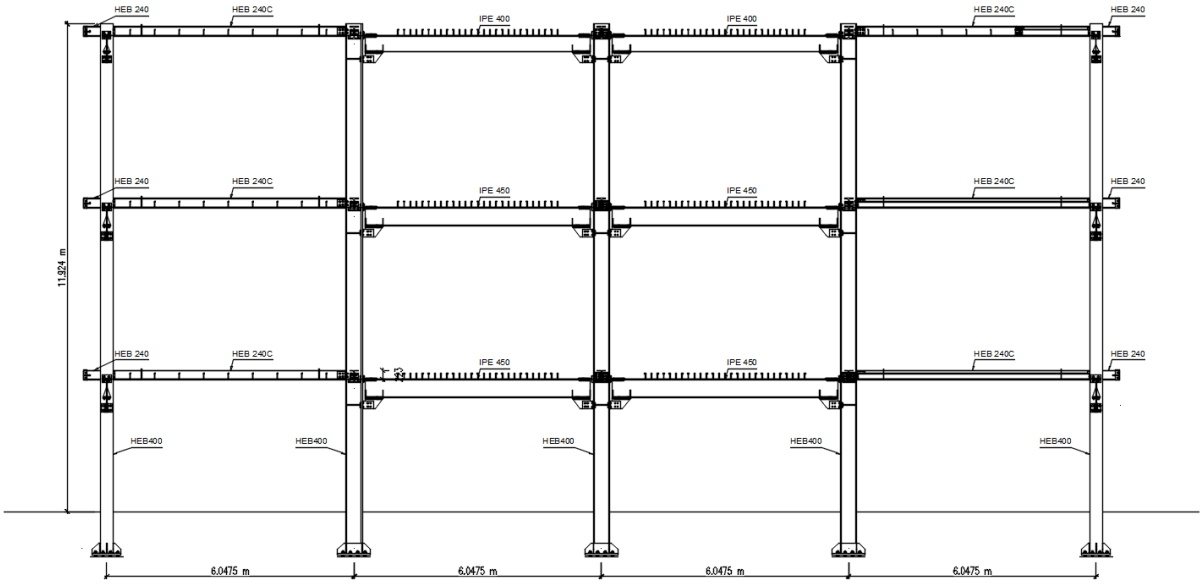

Figure 5.2: *Elevation of XX Frame*

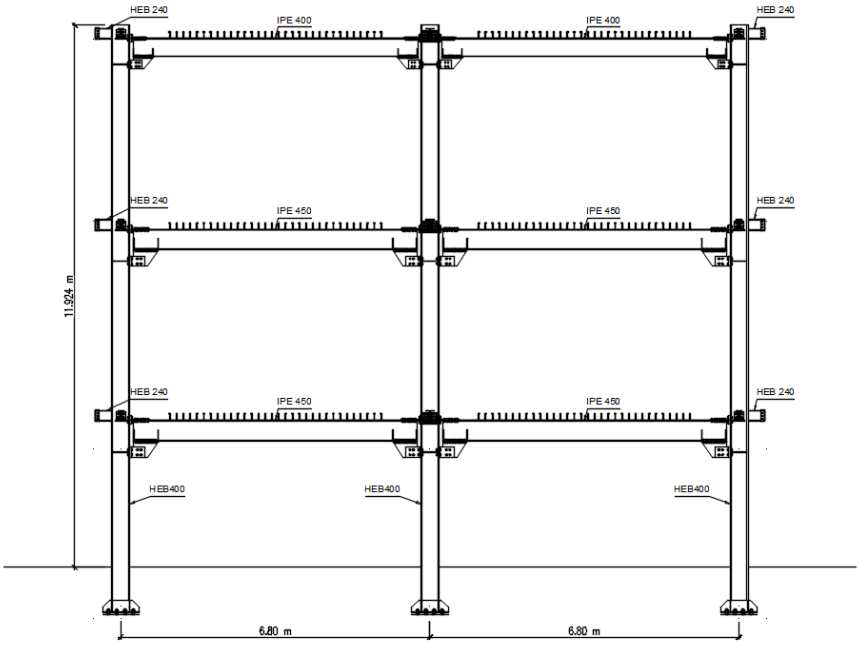

Figure 5.3: *Elevation of YY Frame*

5.3.2 Fire Scenarios

The most critical fire scenarios were selected along the external frames of the building, each corresponding to a different compartment. A total of 3 fire scenarios were selected for the external frames along the XX axis (Fig. 5.4) and 6 along the external frame along the YY axis (Fig. 5.5 and 5.6). The compartments in which the fire scenarios occur are reported in Table 5.8.

Table 5.8*: Fire scenarios for the selected frames*

Frame	XX Frame (1)	YY Frame
Compartment	FS1: Plant room	FS1: Plant room
	FS3: Sample preparation room 1	FS2: Laboratory 1
	FS13: Meeting room 2	FS3: Office 1
		FS4: Office 2
		FS5: Office 3
		FS6: Office 4

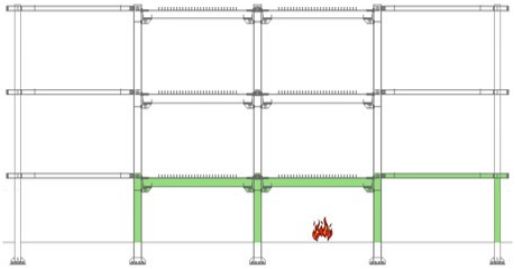

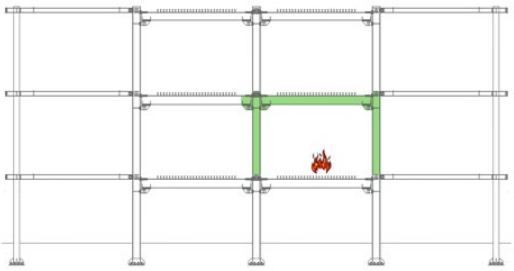

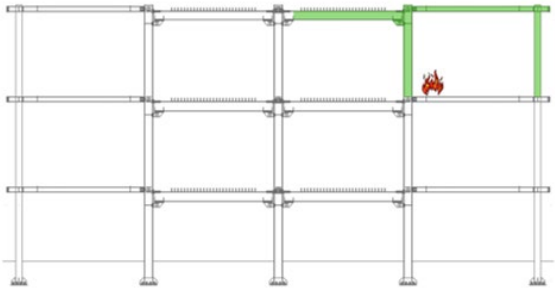

***Figure 5.4**: Fire scenarios along the XX Frame (1): FS1, FS2 and FS13*

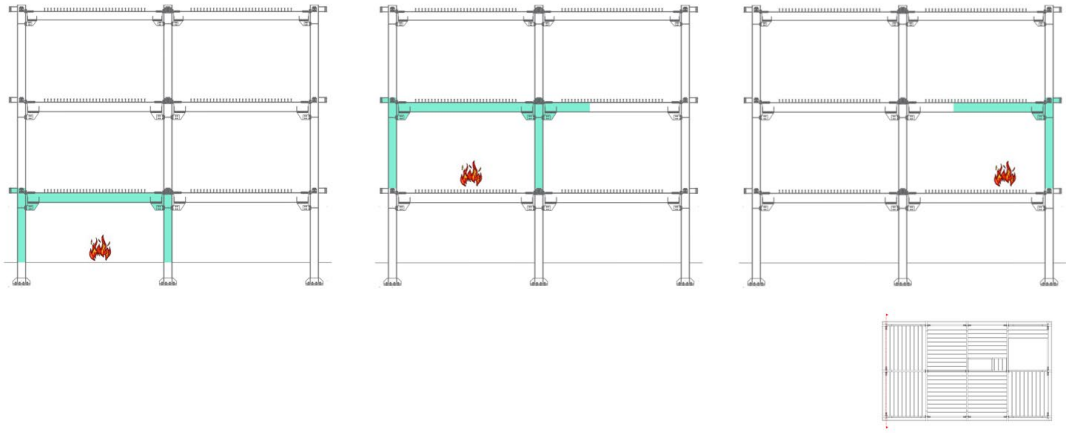

***Figure 5.5**: Fire scenarios along the YY Frame: FS1, FS2 and FS3*

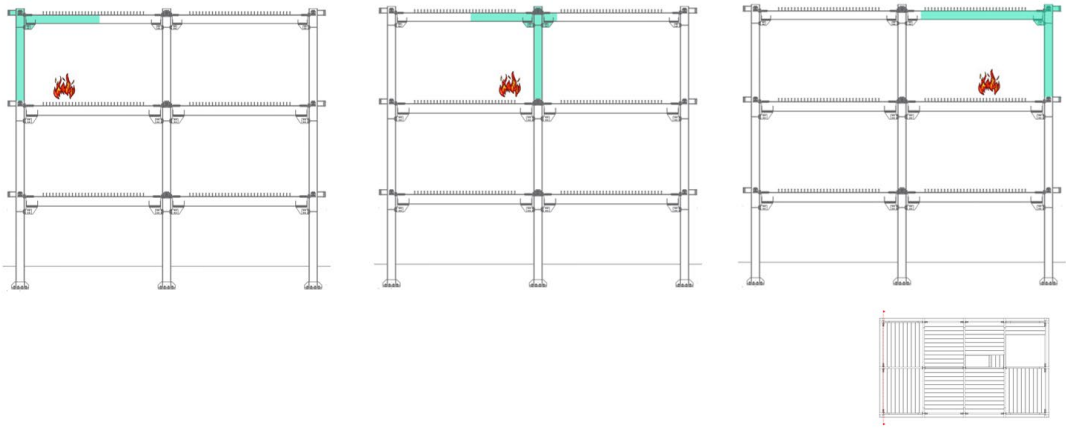

***Figure 5.6**: Fire scenarios along the YY Frame: FS4, FS5 and FS6*

5.3.3 Fire curves

Thermal action is considered in the form of temperature-time relationships. EN 1991-1-2 [2] differentiates between nominal temperature-time curves, which include the standard temperature-time curve, the hydrocarbon curve, and the external fire curve, and natural fire models. The standard temperature curve, also referred to as the ISO 834 [6] and parametric curves are used in modelling the fire scenarios, and the results are compared.

The Standard temperature-time curve (ISO 834)

The standard temperature-time curve is used for closed compartments and represents fully developed fire within them. Unlike the parametric temperature-time curves, there is no cooling phase. The standard temperature-time curve, according to ISO 834-1[6], is given by:

$$\theta_g = 20 + 345 \log_{10}(8\,t + 1) \tag{5.4}$$

where θ_g is the gas temperature in the compartment during fire, in °C, and t is the time, in minutes. The ISO 834 curve is shown in Fig.5.7.

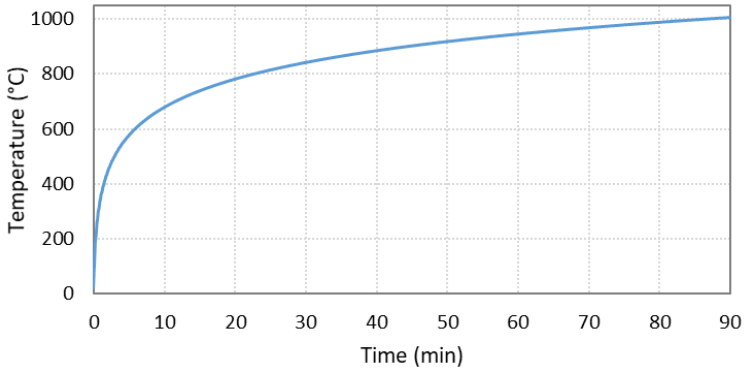

***Figure 5.7**: Standard temperature-time curve*

Parametric Curves

Parametric temperature-time curves describe the progression of gas temperature within a fire compartment over time. Annex A of EN1991-1-2 [2] provides the formulation for such curves, which apply to fire compartments with floor areas up to 500 m², a maximum height of 4 meters, and no roof openings. The heating phase is followed by a cooling phase, which can be controlled by the fire load density or by ventilation.

Parametric curves are based on parameters that consider various physical phenomena that affect fire development, such as the lining materials' thermal properties, the compartment's ventilation and the design fire load density. Because every compartment in the building has different characteristics, a parametric curve is defined for each.

The detailed calculation of each parameter required to assess the parametric fire curves is reported in the project deliverable. In Fig. 5.8, the parametric fire curves for the fire scenarios of Table 5.7.

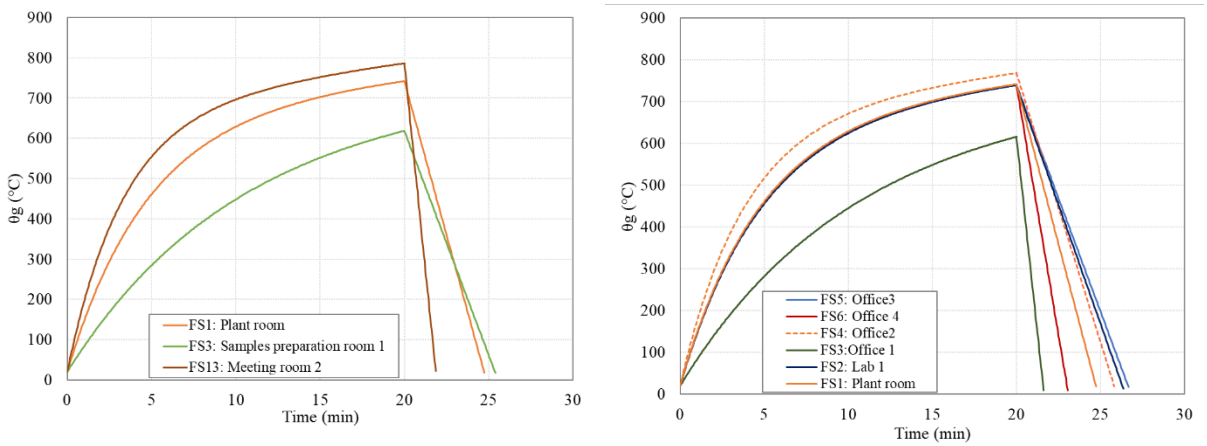

Frame XX Frame YY

***Figure 5.8**: Standard temperature-time curve*

5.3.4 Simplified analysis

The fire resistance is verified in the temperature domain using parametric curves and the ISO 834 curve. A structural member within a compartment is assumed to be able to resist the fire action if, for the required fire resistance time, $t_{fi.requ}$, of that compartment, the temperature in the member is lower than its critical temperature, $\theta_{a,cr}$ (Eq.(5.4)), when using the ISO 834 fire curve and if the temperature of the member is always lower than its critical temperature during the entire duration of the fire.

$$\theta_{a,cr} = 39.19 \ \ln\left(\frac{1}{0.9674\ \mu_0^{3.833}} - 1\right) + 482 \qquad (5.4)$$

The temperatures at the steel sections for a certain fire curve were assessed following EN 1933-1-2 [2] rule for unprotected members:

$$\Delta\theta_{a,t} = k_{sh}\frac{A_m/V}{c_a\ \rho_a}\dot{h}_{net}\ \Delta t \qquad (5.5)$$

where

k_{sh} is the correction factor for the shadow effect;

A_m/V is the section factor for unprotected steel members, in m^{-1};

$h_{net,d}$ is the design value of the net heat flux per unit area, in W/m^2;

Δt is the time interval, 5, in s;

c_a is the specific heat of steel, in J/kgK;

ρ_a is the unit mass of steel, 7850, in kg/m^3.

Safety of Beams

The beams are considered to be laterally restrained due to the action of the concrete slab; therefore, lateral-torsional buckling is not a potential failure mode.

The degree of utilization μ0 to assess the critical temperature in Eq.(5.4) is given by:

$$\mu_0 = M_{fi,Ed}/M_{fi,Rd,0} \geq 0.013 \quad (5.6)$$

where $M_{fi,Ed}$ is the bending moment for the fire design situation and $M_{fi,Rd,0}$ is the bending moment resistance for the fire design situation; both for time t = 0, calculated through EN 1993-1-1[7]

The critical temperatures of all beams in bending are shown in Table 5.9 and 5.10. Low utilisation ratios and consequently high critical temperatures (between 830-1200ºC) are obtained, which is due to the fact that the analysed beams are designed as non-dissipative members according to seismic design principles.

If the parametric curves are used, steel temperatures are lower than the critical temperatures of the beams in all fire scenarios, verifying the fire resistance of all beams.

Using the ISO 834 curve, it depends on the compartment. For the medical labs, if the required fire resistance is considered to be R30, the critical temperatures of IPE 450 beams are higher than the steel temperature at 30 minutes, verifying the fire resistance. However, if the required fire resistance is considered to be R45, the critical temperatures of IPE 450 beams are lower than the steel temperature at 45 minutes, not verifying the safety.

Fire resistance is verified in the offices and meeting rooms (required fire resistance time of 30 minutes), but not in the plant room (required fire resistance time of 60 minutes), as reported in Fig. 5.9.

Table 5.9*: Critical temperatures of beams - XX Frames*

Beam	M_{Rd} (kNm)	$M^+_{fi,Rd}$ (kNm)	$M^+_{fi,Ed}$ (kNm)	$M^+_{fi,Rd}$ (kNm)	$M^+_{fi,Ed}$ (kNm)	μ_0	$\theta_{a,cr}$ (°C)
IPE 450 (basement and ground floor)	604.21	863.16	43.87	1015.48	87.33	0.086	851.8
IPE 400 (1st floor)	463.99	662.84	35.62	779.81	70.71	0.091	843.8
HEB 240 (basement and ground floor)	373.82	534.02	0.0	628.26	14.19	0.023	1052.6
HEB 240 (1st floor)	373.82	534.02	0.0	628.26	5.88	0.009*	1185.0
HEB 240C (basement and ground floor)	311.05	444.35	3.75	522.77	9.09	0.017	1092.0
HEB 240C (1st floor)	311.05	444.35	2.52	522.77	10.07	0.019	1076.6

** The degree of utilization must be higher than 0.013 for Equation 4.4 to be applied.*

Table 5.10*: Critical temperatures of beams - YY Frame*

Beam	M_{Rd} **(kNm)**	$M^+_{fi,Rd}$ **(kNm)**	$M^+_{fi,Ed}$ **(kNm)**	$M^+_{fi,Rd}$ **(kNm)**	$M^+_{fi,Ed}$ **(kNm)**	μ_0	$\theta_{a,cr}$ **(°C)**
IPE 450 (basement and ground floor)	604.21	863.16	49.66	1015.48	97.78	0.096	834.8
IPE 400 (1st floor)	463.99	662.84	40.78	779.81	79.11	0.101	827.0
HEB 240 (basement and ground floor)	373.82	534.02	0.0	628.26	12.85	0.020	1067.5
HEB 240 (1st floor)	373.82	534.02	0.0	628.26	5.31	0.008*	1200.3

** The degree of utilization must be higher than 0.013 for Equation 4.4 to be applied.*

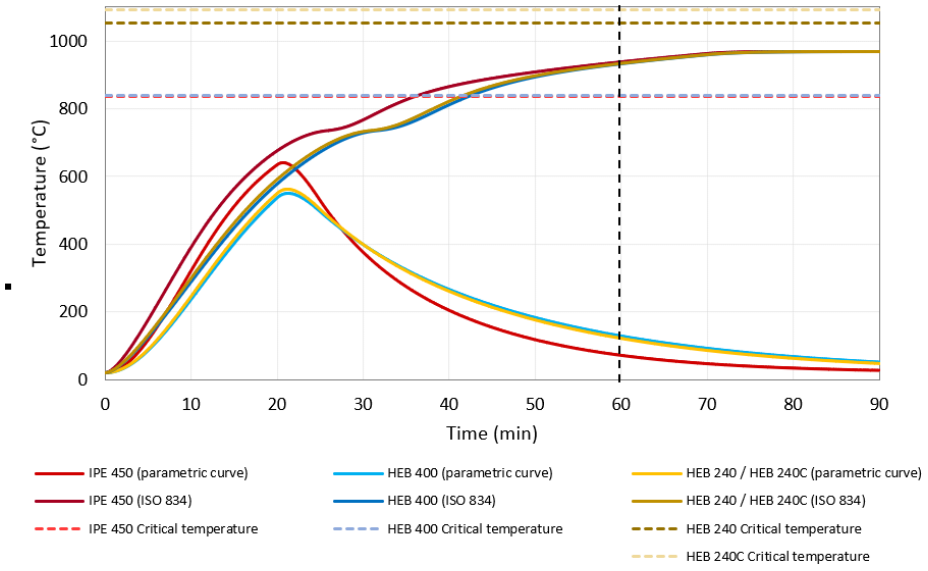

***Figure 5.9**: Temperature in steel sections and critical temperature – FS1: Plant room*

Safety of Columns

For columns, the degree of utilization to use in Eq.(5.4) is given by the ratio between the compression force for the fire design situation, $N_{\mathrm{b,fi,Ed}}$, and the buckling resistance of a compression member at time t = 0, $N_{\mathrm{b,fi,Rd,0}}$, Eq. (5.7). The definition of buckling resistance is an interactive process as it requires the simultaneous computation of both the reduction factor of resistance and the reduction factor of buckling for a fire situation.

$$N_{\mathrm{b,fi,Rd,0}} = A\, f_{\mathrm{y}}\, \chi_{\mathrm{fi}} \frac{1}{\gamma_{\mathrm{M,fi}}} \qquad (5.7)$$

Similar to the beams, low utilisation ratios (between 10-13%) and high critical temperatures (between 788-830ºC) are obtained for the columns, which comes from the fact that the analysed columns are also designed as non-dissipative members according to seismic design principles (Table 5.11).

***Table 5.11:** Critical temperatures of columns*

Section	N_{Ed} (kNm)	$N_{b,fi,Rd,0}$ [kN]	μ_0	$\theta_{a,cr}$ (ºC)
HEB 400 (1st floor)	597	5951.0	0.10	828.7
HEB 400 (2nd floor)	735	5577.3	0.13	787.7
HEB 400 (3rd floor)	340	5577.3	0.13	787.7

Using the parametric curves, fire resistance is verified, i.e. steel temperatures are lower than the critical temperatures of the columns in all fire scenarios. Using the ISO 834 curve, fire resistance is verified in all fire scenarios, except for fire scenario 1 (Plant room), where, at the required fire resistance time of 60 minutes, steel temperatures of all four columns are higher than the respective critical temperatures. These critical temperatures are reached in approximately 42 minutes, Fig. 5.9.

5.3.5 Finite element models for advanced fire analyses

The frames were modelled in ABAQUS software 2021 [8], using a Dynamic Implicit quasi-static analysis. The structural elements, i.e. beams and columns, were modelled as beam elements, adopting mesh elements type B31 with sizes of approximately 0.10 m. Concerning the material properties of these elements, both elastic and plastic nonlinear material properties were considered. Moreover, the degradation of the mechanical properties due to elevated temperatures was implemented into the model, considering the reduction factors provided in EN1993-1-2.

The fin plate connections were modelled as hinges and the FREEDAM joints were modelled as springs - two axial springs located at the level of the T-stub and two axial springs at the level of the L-stubs -, connected by rigid beam elements, as shown in Fig. 5.4. In both models, the column bases were considered fixed.

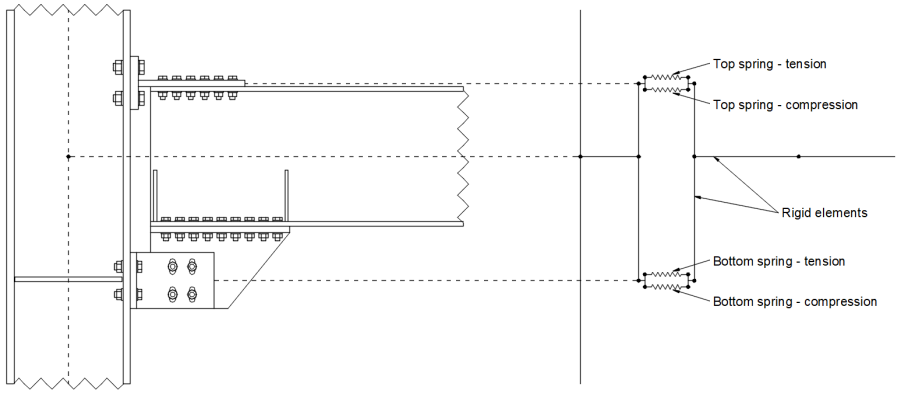

***Figure 5.10**: Springs chosen to model the FREEDAM joint*

All the analyses considered two steps: Step 1 is the application of the mechanical loads and Step 2 is the application of the fire action. Regarding Step 1, mechanical loads were determined according to the combination of actions for accidental design situations, as defined in EN 1990 sim, which can be written as follows. The loads considered are self-weight of the steel elements ($G_{k,1,sw}$), other permanent structural and non-structural loads ($G_{k,1}$ and $G_{k,2}$), weight of the cladding panels ($G_{k,2,pan}$), variable action ($Q_{k,1}$) and fire action Ad. The load values are taken from the DREAMERS Structural Calculation Report [9].

Composite beams were modelled in Abaqus as steel beams, ignoring the contribution of the concrete to their strength. After the application of the mechanical load, the fire action was applied directly to the affected elements and connections, following the considered fire curve. The temperature is uniform through the steel cross-sections.

Behaviour of springs

The axial springs represent the active components in compression and tension in the upper and lower regions of the joint. Their force-deformation curves (plastic and ultimate resistance and

the initial stiffness coefficient) were characterised using the component method of EN 1993-1-8 [10] for temperatures ranging from 20 °C to 1000 °C. The post-elastic phase of the components (i.e ultimate resistance) was assessed by replacing, as suggested by Jaspart et al. [11], in the component formula, the yield strength f_y for ultimate strength, fu, and by replacing the 0.9 by 1.0 for the bolts in tension.

The components considered to model the behaviour of the upper and lower springs are detailed in Table 5.12.

Table 5.12*: Components considered to model the behaviour of each spring*

Spring	Upper springs	Lower springs
Compression	T-stub slippage	Damper slippage
	Column web in compression	Column web in compression
	T-stub web in bearing	L-stubs webs in bearing
	Upper beam flange in bending	Haunch in bearing
	Bolts in shear	Bolts in shear
Tension	T-stub slippage	Damper slippage
	Column web in tension	Column web in tension
	Column flange in bending	Bolts in tension
	Bolts in tension	L-stubs flanges in bending
	T-stub flange in bending	L-stubs webs in tension
	T-stub web in tension	L-stubs webs in bearing
	T-stub web in bearing	Haunch in bearing
	Upper beam flange in bending	Bolts in shear
	Bolts in shear	

To characterise properly the behaviour of the joints under elevated temperatures, the evolution of the temperature at the joint was based on the experimental fire tests on the FREEDAM joint carried out at the University of Coimbra, see Deliverable D4.3 [12].

From these tests, it was possible to observe that the evolution of temperatures is not uniform in the whole joint, as reported in Figure 5.11, where it can be seen that the web zone of the beam is the component reaching higher temperatures, followed by the upper zone of the joint.

Following these results, in the spring models, 4 regions of similar temperature were identified, as shown in Fig. 5.12, and the evolution of steel temperature in each region was registered relative to the temperature in Region 1 (beam) for temperatures up to 760 °C. In this way, when the fire action is applied to the beam (Region 1), the temperature in each region can be obtained.

The material properties of the joint components were updated according to the evolution of temperature in their respective regions.

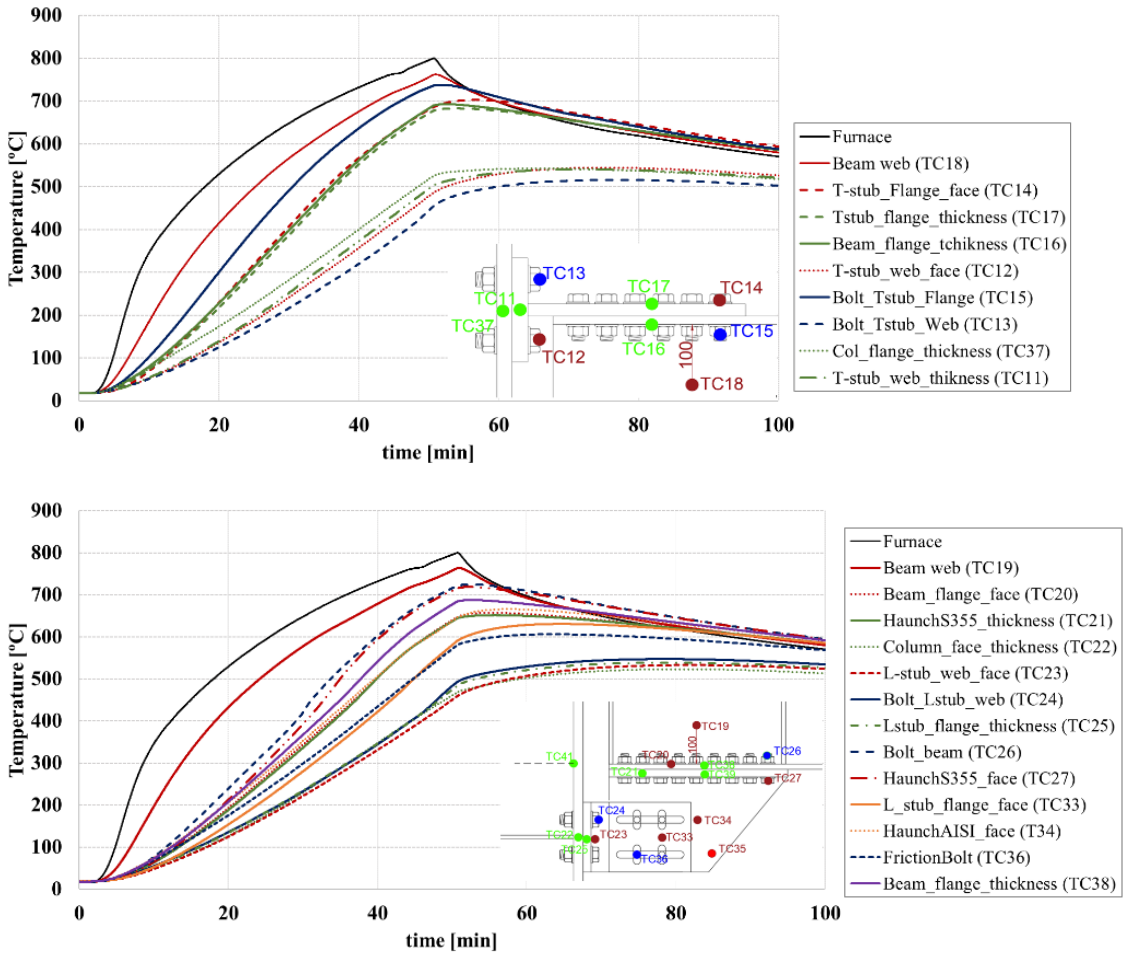

***Figure 5.11**: FREEDAM joint – experimental tests*

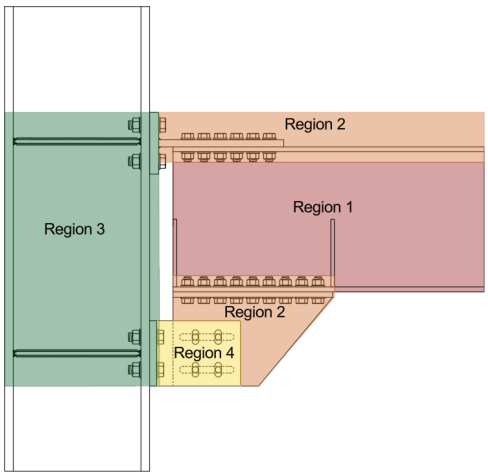

***Figure 5.12**: FREEDAM joint temperature regions*

Another important feature that can be affected by temperature is the preload at the bolts. In the experimental tests, the loss of preload during the fire was not measured. However, from calibrated FE models this relation could be obtained (Fig. 5.13), where the loss of preload force

at high temperatures observed in the FEM models is given as the ratio between the preload force found at a certain temperature and the initial preload force.

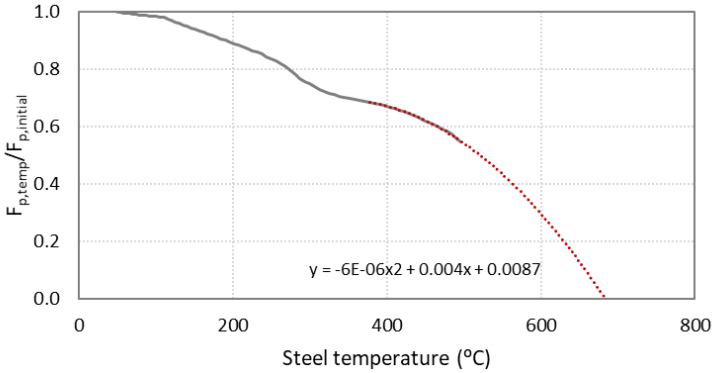

***Figure 5.13**: Bolts preload force as a function of temperature*

As an example, the force-displacement relationships of the upper and lower springs, respectively, for temperatures up to 1000 °C are shown in Fig. 14a and b, respectively, for the D1 device, IPE 450 beam, located at the internal spans of the XX Frames (Basement and ground floor). For temperatures in Region 1 equal to or higher than 800 °C, the slip in the upper springs happens before any increase in force or displacement, due to the complete loss of preload. For the lower springs, slip happens before any force or displacement increase for Region 1 temperatures equal to or higher than 900°C.

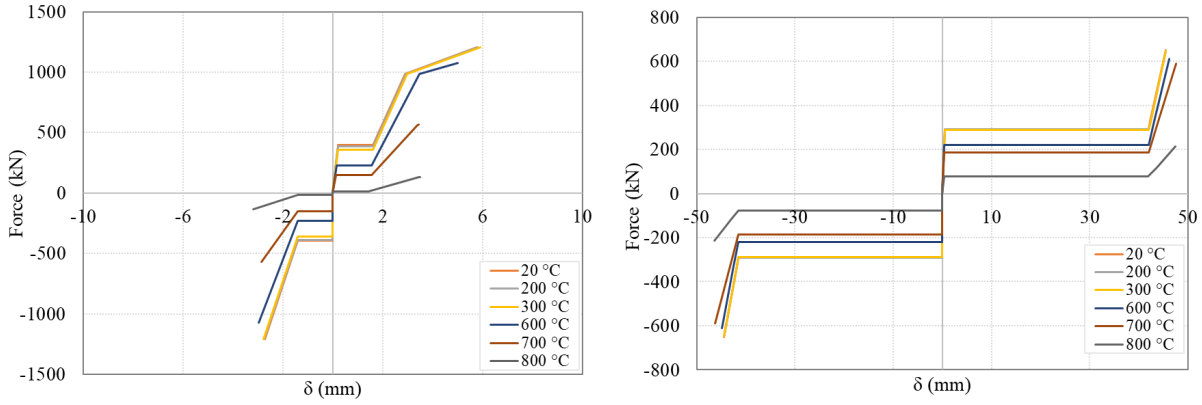

a) Top Spring b) Lower Spring

***Figure 5.14**: Force-displacement relationships for D1 device, IPE 450 beam*

5.3.6 Results from the advanced finite element analysis

Using the advanced analysis, the performance of the DREAMERS building under fire action is evaluated by examining the deflection and contraction of the structural elements, as well as the damage sustained by the FREEDAM beam-to-column connections due to the fire action (damage to the FREEDAM connections is considered to happen when either upper springs or lower springs are no longer able to bear load). The results for Fire Scenario 1 are presented in detail, while for the remaining scenarios, the results are summarised within the same sections.

Regarding the deformation of structural elements, the Standard ISO 834 offers criteria to evaluate their load-bearing capacity.

According to this standard, failure of a structural element subjected to bending (e.g. beams) under fire is considered to occur when both of the following conditions are met:

- The deflection exceeds the limit deflection, given by:

$$D_{lim} = \frac{L^2}{400\ d}$$

- The rate of deflection exceeds the limit rate of deflection, given by (this condition is only applied after deflection is greater than L/30 [mm]):

$$\frac{dD}{dt}_{lim} = \frac{L^2}{9000\ d}$$

where L is the span of the beam, in mm, and d is the distance from the extreme fibre of the design compression zone to the extreme fibre of the design tensile zone of the structural section, in mm.

The same standard indicates that the failure to support load in axially loaded elements (e.g. column) can be considered to occur when:

- The axial contraction exceeds the limit axial contraction, given by:

$$C_{lim} = \frac{h}{100}$$

- The rate of axial contraction exceeds the limit rate of axial contraction, given by:

$$\frac{dC}{dt}_{lim} = \frac{3\ h}{1000}$$

where h is the initial height, in mm.

Failure criteria according to ISO 834-1

Fig. 5.15depicts the deformation of the frame in the XX direction after fire for the Fire Scenario 1, highlighting the most damaged members.

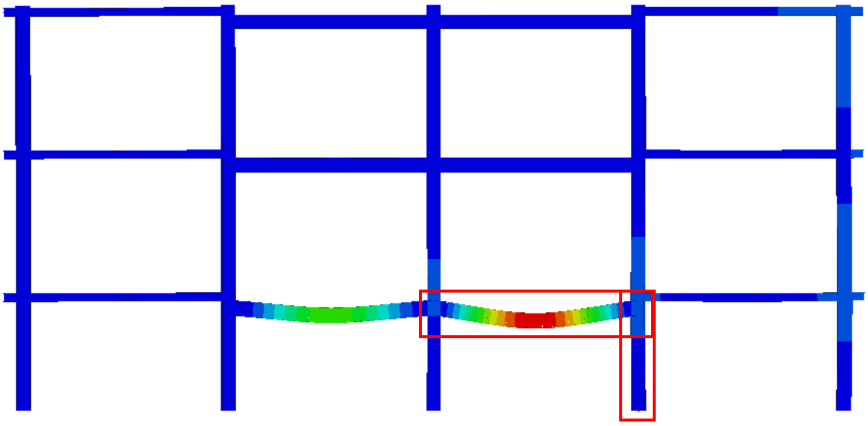

Figure 5.15*: XX Frame (1) (Fire scenario 1, rigid joints), and analysed beam and column*

Concerning the columns, there is no failure according to the failure criteria of ISO 834-1 [10] criteria for axial contraction (Fig. 5.16 (a)) and rate of axial contraction (Fig. 5.16 (b)), for both considered fire curves (ISO 834 and parametric curve), as depicted in Fig. 5.16.

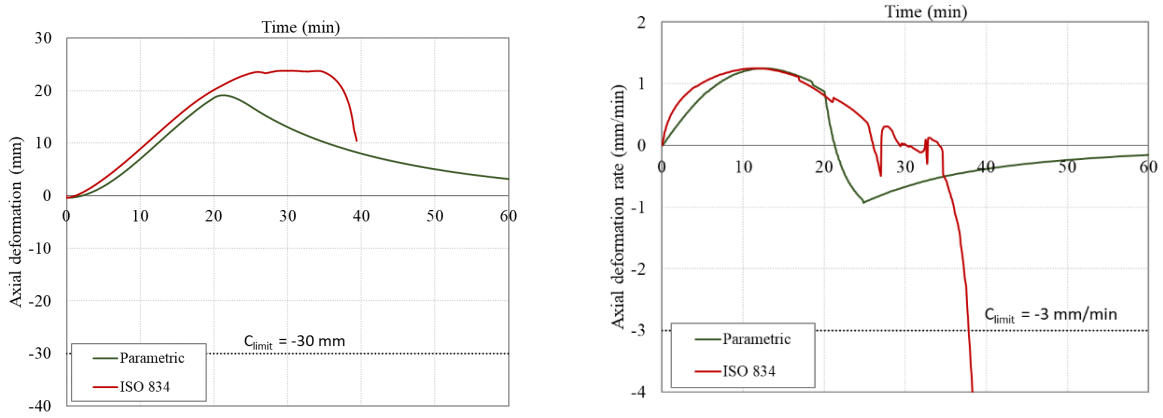

a) Column axial deformation

b) Column axial deformation rate

***Figure 5.16**: Column axial deformation and contraction rate for XX Frame, FS1*

On the other hand, failure of the beam is observed with respect to the deflection (Fig. 5.16 (a)) and rate of deflection (Fig. 5.16(b)) criteria defined in ISO 834, when exposed to the ISO 834 fire curve, occurred at 36 minutes with a steel temperature of approximately 836 °C. Because the required fire resistance time for fire scenario 1 (Plant room) is 60 minutes, fire resistance requirements is achieved only when the parametric temperature-time curve is considered.

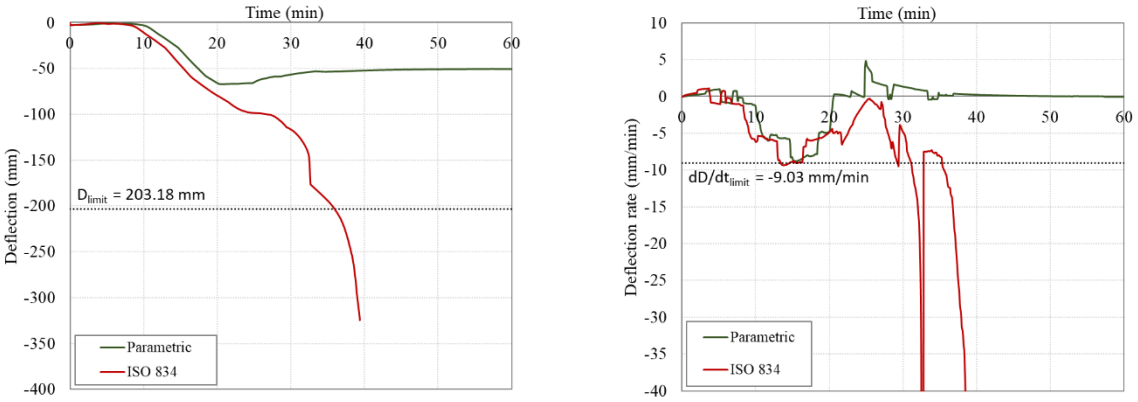

a) Beam deflection

b) Beam deflection rate

***Figure 5.17**: Beam deflection and deflection rate for XX Frame, FS1*

Table 5.13 summarises the results for all the considered fire scenarios for the frame in the XX direction, namely FS 1, 3 and 13. Beam failure only occurs when the ISO 834 fire curve is applied, and there is no column failure.

The required fire resistance for fire scenario 13 (Meeting Room 2) is R30, which confirms the fire resistance of the structure. The minimum required fire resistance for fire scenario 3 (Samples Preparation Room 1) depends on the materials present in the compartment, as outlined in section

3.4. If the required fire resistance is considered to be R45, fire resistance is only ensured when the parametric curve is considered (same for R30).

Table 5.13: Fire scenarios 1, 3 and 13 results (XX Frames)

Fire scenarios	Fire curve	Beam failure		REI	Safety	Column failure	
		Time (min)	θ_a (°C)			Time (min)	θ_a (°C)
FS 1	ISO 834	36.0	835.6	60 min	KO	No	
	Parametric	No			OK	No	
FS 3	ISO 834	36.3	838.6	30/45 min	OK/KO	No	
	Parametric	No			OK	No	
FS 13	ISO 834	34.6	827.9	30 min	OK	No	
	Parametric	No			OK	No	

Concerning the frame in YY direction (Table 5.14), the results are as follows:

- There is no column failure, independently of the fire curve and scenario.
- In fire scenario 1, beam failure occurs at 35 minutes (with steel temperature of 829 °C), when the frames are subjected to the ISO 834 fire curve. As previously stated, the minimum required fire resistance for fire scenario 1 (Plant room) is R60 minutes; thus, fire resistance is only verified when the parametric temperature-time curve is applied.
- In fire scenario 2, beam failure occurs at 35.3 minutes. Since the analysed compartment in this scenario is a medical laboratory, if the required fire resistance considered is R30 (see section 3.4), fire resistance is verified. However, if R45 is adopted, fire resistance is only ensured when using the parametric curve;
- In fire scenario 3, the beam deflection limit of ISO 834-1 is not reached. The required fire resistance time R30 is verified.
- In fire scenario 6, beam failure happens at 32.5 minutes. The required fire resistance time R30 is not verified.
- In fire scenarios 3, 4 and 5, the beam deflection limit of ISO 834-1 is not reached.

Insights into joint behaviour

The behaviour of the frames was further evaluated based on the resistance and deformation of the joints.

Similar to what was observed for the members, failure is only observed when the ISO fire curve is considered. Furthermore, for these cases, joint failure happens just before the beam reaches its deformation limit.

Table 5.14: Fire scenarios 1-6 results (YY Frame)

Fire scenario	Fire curve	Joint type	Beam failure		Column failure	
			Time (min)	θ_a (°C)	Time (min)	θ_a (°C)
FS 1	ISO 834	Rigid joints	30.2	769.4	No	
		FREEDAM joints	35.3	829.0	No	
	Parametric	Rigid joints	No		No	
		FREEDAM joints	No		No	
FS 2	ISO 834	Rigid joints	30.3	771.0	No	
		FREEDAM joints	35.7	832.9	No	
	Parametric	Rigid joints	No		No	
		FREEDAM joints	No		No	
FS 3	ISO 834	Rigid joints	69.7	961.9	No	
		FREEDAM joints	No		No	
	Parametric	Rigid joints	No		No	
		FREEDAM joints	No		No	
FS 4	ISO 834	Rigid joints	No		No	
		FREEDAM joints	No		No	
	Parametric	Rigid joints	No		No	
		FREEDAM joints	No		No	
FS 5	ISO 834	Rigid joints	No		No	
		FREEDAM joints	No		No	
	Parametric	Rigid joints	No		No	
		FREEDAM joints	No		No	
FS 6	ISO 834	Rigid joints	33.4	809.6	No	
		FREEDAM joints	32.5	805.6	No	
	Parametric	Rigid joints	No		No	
		FREEDAM joints	No		No	

For instance, in fire scenario 1, when the ISO 834 curve is applied, joint failure occurred at approximately 33 minutes in the joint highlighted in Fig. 5.18, when the upper spring loses its load-bearing capacity under tension. This moment corresponds to an increase in beam deflection (Fig. 5.19). However, according to the ISO 834-1 criteria, the failure would happen at 36 min by beam failure, highlighting the importance is knowing the exact joint behaviour under fire actions to assess more rigorously the frame behaviour.

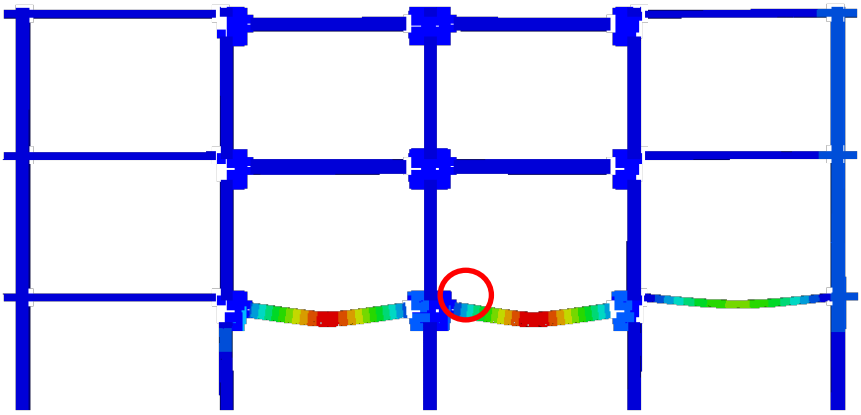

***Figure 5.18**: Frame XX - Fire scenario 1*

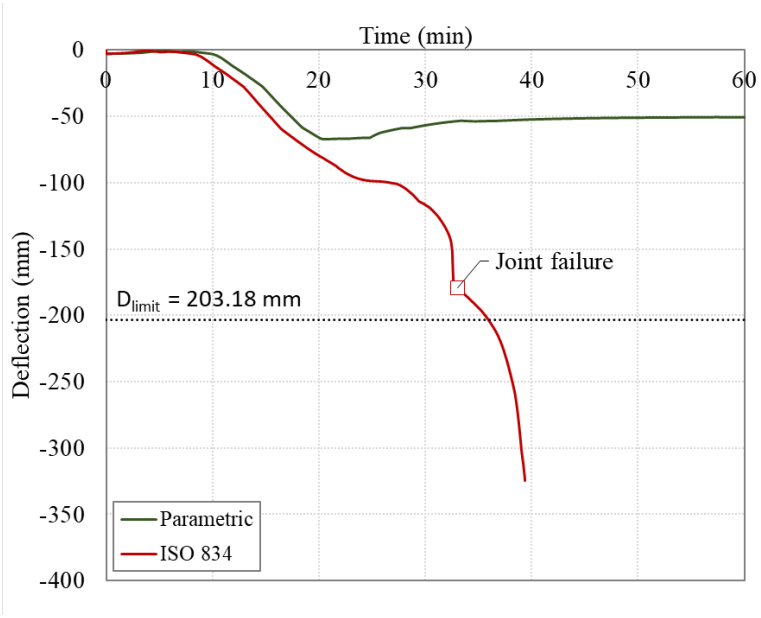

***Figure 5.19**: Frame XX - Fire scenario: beam deflection and joint failure*

5.4 CONCLUSIONS

This chapter summarises the study conducted to evaluate the behaviour of the DREAMERS building under elevated temperatures. The study focuses on the external frames of the building.

The fire action is modelled using both the Standard temperature-time curve and parametric curves. The fire performance of the DREAMERS building under fire action is assessed through two approaches:

- A simplified analysis based on the critical temperatures of structural members;
- An advanced analysis evaluating structural deformations and damage to FREEDAM beam-to-column joints. Here, additional simulations were performed on the same frames but using rigid beam-to-column joints to assess the joints' influence on overall frame behaviour.

When using the ISO 834 fire curve, the fire resistance is verified if, at the required fire resistance time for each compartment, the steel temperature has not yet reached the critical temperature and

no structural member has failed. On the other hand, when using the parametric fire curve, the temperature at the member should be lower than the critical temperature during the entire duration of the fire.

Regarding the simplified analysis, if the parametric curves are used, the fire resistance of all beams and columns is verified. Using the ISO 834 curve, fire resistance is verified in all structural members, with two exceptions: the IPE 450 beams in the Medical Laboratories, if the required fire resistance for this occupancy is considered to be R45, and the IPE 450 beams and HEB 400 columns in the Plant Room (R60).

With regard to the advanced analysis, and in accordance with the ISO 834-1 criteria for load-bearing capacity, no column failure is observed in any analysed fire scenario, while beam failure occurs only under the ISO 834 fire curve.

Regarding the XX Frames, fire resistance with the ISO 834 curve is not verified in fire scenario 1 (Plant Room), but is ensured in fire scenario 13 (Meeting Room 2). Safety in fire scenario 3 (Samples preparation room 1) depends on the required fire resistance: R45 or R30. In the first case, fire resistance is only verified using the parametric curve; in the second, it is also verified under the ISO 834 curve when using FREEDAM joints.

Regarding the YY Frame, fire resistance with the ISO 834 curve is verified in fire scenarios 3 to 6, but is not ensured in fire scenario 1 (Plant Room). In fire scenario 2, since the analysed compartment in this scenario is a medical laboratory, if the required fire resistance considered is R30, fire resistance is verified. However, if R45 is adopted, fire resistance is only ensured when using the parametric curve.

Joint damage was observed when using the ISO 834 fire curve, just before the beam's deflection limit was achieved, proving that just considering the ISO 834 failure criteria to assess damage can be unsafe. The slip of the connections started between 4 to 7 minutes after the fire start. There was no spring damage using parametric curves, and the slip happened a few minutes later than with the ISO 834 curve.

5.5 REFERENCES

[1] Ministero dell'Interno, "Testo coordinato dell'allegato I del DM 3 agosto 2015," 2015.

[2] CEN, "EN 1991-1-2 - Eurocode 1: Actions on structures - Part 1-2: General actions - Actions on structures exposed to fire," Brussels, 2002.

[3] Ministero dell'Interno, DPR 1 agosto 2011, n.151 -Regolamento recante semplificazione della disciplina dei procedimenti relativi alla prevenzione dgli incendi. 2011.

[4] A. Building Codes Board, “International Fire Engineering Guidelines Edition 2005,” 2005.

[5] A. réunies de B. E. et D. C. T. I. de la C. M. T. K. J. et al. European Commission: Directorate-General for Research and Innovation, “Demonstration of real fire tests in car parks and high buildings – Final report,” 2002.

[6] ISO 834, “Fire-resistance tests-Elements of building construction - Part 1: General requirements,” 1999.

[7] CEN, “EN 1993-1-1: Eurocode 3: Design of steel structures - Part 1-1: General rules and rules for buildings,” Brussels, 2005.

[8] Simulia, “"Abaqus user Manual [online],” Dassault Syst`emes R2021x User Assistance, 2021. [Online]. Available: https://help.3ds.com/HelpProductsDS.aspx.”

[9] V. Piluso, L. Massimo, E. Nastri, and et al., “DREAMERS – Realizzazione Edificio C3 – Campus di Fisciano – Progetto Esecutivo,” Salerno: , 2023.

[10] CEN, EN 1993-1-8: Eurocode 3: Design of steel structures - Part 1-8: Design of joints. European Committee for Standardization, 2005.

[11] J.-P. Jaspart, A. Corman, and J.-F. Demonceau, “Ductility assessment of structural steel and composite joints,” in Stability and Ductility of Steel Structures 2019, 2019.

[12] A. F. Santos, A. Santiago, and L. Simões da Silva, “ DREAMERS – D4.3 – Task 4.3 – Testing of FREEDAM joints used in the demonstration building under fire conditions.,” 2024.

CHAPTER 6

Building Construction

6.1 INTRODUCTION

This chapter provides a comprehensive overview of the construction site with the preliminary works needed for the construction of the DREAMERS demonstration building realized at the University of Salerno. In particular, every stage of the building's realization from the initial excavation works, through the whole structural assembly and enclosure, to the final fit-out and commissioning culminating in a fully operational facility ready for research activities have been documented.

6.2 ERECTION OF THE BUILDING AND MAIN CONSTRUCTION PHASES

6.2.1 Location of C3 Building in the Campus Area

Fig. 6.1 presents an aerial and close up photograph that situates the future building within the broader campus environment. This aerial photograph presents the whole Fisciano Campus of the University of Salerno, with the FRCS-funded building site highlighted in red. From this vantage point you can see how the new facility will integrate into the broader academic environment. The marker shows the exact footprint of the upcoming construction, providing a clear sense of scale against the surrounding university infrastructure.

***Figure 6.1**: Location of the building in the general area*

In close-up image of Fig. 6.2, the future building site sits at the heart of three key campus amenities: directly to the east is the main student canteen, ensuring easy access for both staff and visitors; to the north are the student residence halls, facilitating quick transit between living quarters and research spaces; and to the south, the covered parking lot equipped with photovoltaic panels, underscoring the project's commitment to sustainable energy. This perspective illustrates not only the site's immediate neighbors but also the strategic placement that maximizes convenience, social interaction, and environmental performance.

Figure 6.2: *Location of the building in the local area*

6.2.2 Excavation Phase

The initial phase of construction involved excavating soil for the the realization of the retaining wall and for the building's foundations (Fig. 6.3). As can be seen from Fig. 6.4 part of the ground coming from the excavation has been stored near the site.

The possibility of storing the ground near the site provides several advantages. In fact, the on-site storage strategy not only significantly reduces earth-moving distances—thereby cutting fuel consumption, equipment wear, and labor hours—but also drives down overall backfill costs behind the retaining wall and within the foundation trenches. By minimizing haulage, we achieve both economic savings and a smaller carbon footprint, supporting the project's broader commitment to resource efficiency and environmental sustainability.

***Figure 6.3**: Excavation Phase*

***Figure 6.4**: Ground stored near the construction site*

6.2.3 Realization of the retaining wall

6.2.1.1 The Foundation

Upon completion of the excavation phase, the construction started with the realization of the foundation of the retaining wall. Fig. 6.5 and illustrates the placement of the reinforcement and the subsequent pouring of the foundation.

***Figure 6.5**: Positioning of the rebars for the foundation*

***Figure 6.6**: Concrete casting of restraining wall*

6.2.1.2 The Wall

Once the foundation was complete, the reinforcement for the retaining wall was installed (Fig. 6.7). Self-climbing formwork was used for the concrete pour. The use of this system speeded up the operations and entirely eliminated the need for disposable formwork (Fig. 6.8).

Due to the use of the climbing formwork, it was impossible to realize the staircase and the cantilever slabs at the same time of the retaining wall. Their casting was so postponed, in Fig. 6.9 the starter bars of the slabs and the reinforcements of the staircase are clearly visible when the retaining wall was completely casted.

***Figure 6.7**: Positioning of rebars of the retaining wall*

***Figure 6.8:** Self-climbing formwork*

Figure 6.9: *Staircase and cantilever slabs realized on the retaining wall*

6.2.4 The Foundation of the Building

Once the lean-concrete blinding layer was poured, it became necessary to precisely position the structural columns. To that end, temporary bracing was installed to maintain the correct mutual spacing of the columns (Fig. 6.10).

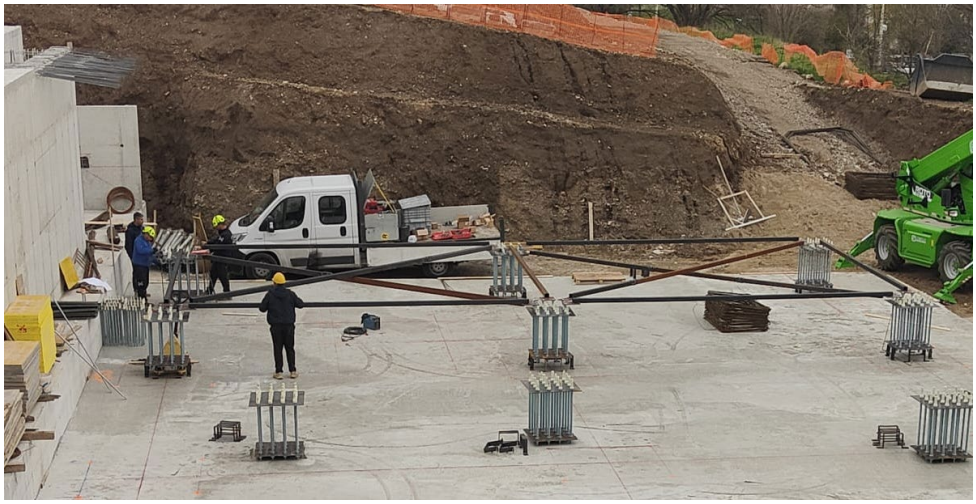

Figure 6.10*: Positioning of the base plates and anchor bolts of the steel columns*

The threaded rods - onto which the steel columns would later be connected - were then held in place by dedicated base plates, suitably anchored into the blinding concrete (Fig. 6.11).

***Figure 6.11**: Staircase and cantilever slabs realized on the retaining wall*

Once the base plates and threaded rods intended to receive the steel columns were anchored into the blinding concrete, the temporary bracing was removed, and all of the foundation reinforcement was installed (Fig. 6.12 and 6.13).

***Figure 6.12:** Foundation reinforcement*

***Figure 6.13**: Foundation reinforcement*

The foundations were cast in three successive pours: first the larger base of the inverted foundation beams were formed (Fig. 6.14); next, the beams were poured up to the level of the plates designed to receive the steel columns (Fig. 6.15); and only in a final stage - as shown later - was the remainder of the foundation beams cast, fully enveloping the bases of the steel columns.

***Figure 6.14:** Concrete casting of the larger base of the inverted foundation beams*

Figure 6.15: *Concrete casting of the upper part of the inverted foundation beams*

At this stage, it was necessary to fill the space between the foundation beams. For this operation, the soil previously stockpiled during the excavation phase was used (Fig. 6.16 and 6.17).

At this point, it was possible to realize the slab forming the base for the positioning of the iglù fromwork (Fig. 6.18).

Figure 6.16*: Filling of the spaces between the foundation beams with the soil coming from the excavation phase*

***Figure 6.17**: Filling of the spaces between the foundation beams with the soil coming from the excavation phase*

***Figure 6.18**: Realization of the concrete slab constituting the base for the iglù formwork*

6.2.5 Erection of Steel Columns and Steel Beams

At this stage of the construction, only the bars for the steel columns and the bars for completing the upper part of the foundation beam protrude from the foundation. So that the steel column can be easily positioned (Fig. 6.19). Once all the vertical steel parts have been placed, the steel beams could be positioned as reported in Fig. 6.20 and Fig. 6.21. Finally, in Fig. 6.22 there is the wiew of all steel columns and steel beams of the structure.

***Figure 6.19**: Erection of steel columns*

***Figure 6.20**: Erection of steel beams*

***Figure 6.21**: Erection of first steel beam equipped with Freedam connections*

***Figure 6.22**: Erection of steel beam equipped with Freedam connections*

6.2.6 Realization of the Upper Part of the Foundation and Positioning of Iglu' Formwork

At this stage there is the need of completing the foundation. First of all, the additional reinforcements have been placed as reported in Fig. 6.23, and then the Iglù formwork have been positioned for the realization of the crawl space (Fig. 6.24 and Fig. 6.25). In this way the upper part of the of the foundation and the crawl space can be realized together, with the same concrete cast (Fig. 6.26).

***Figure 6.23**: Additional reinforcement for the completion of the foundation*

***Figure 6.24**: Positioning of the Iglù formwork*

***Figure 6.25**: Positioning of the Iglù formwork*

***Figure 6.26:** Concrete casting of upper part of the foundation and of the crawl space*

6.2.7 Realization of the First Floor

6.2.7.1 *Assembly of Cofradal for the first floor*

The assembly of the Cofradal panels was very straightforward because, as shown in Fig. 6.27, it can be moved without mechanical equipment. Such equipment was only used to lift the Cofradal panels from the ground floor to the first floor (Fig. 6.28).

Figure 6.27: *Assembly of Cofradal panels for first floor*

Figure 6.28: *Handling of Cofradal Panel from ground floor to first floor*

6.2.7.2 *The slab decoupling at the FREEDAM connection location*

At the FREEDAM connection, particular care was taken to decouple the slab from the steel beam. In particular, attention was paid to executing the construction detail exactly as it had been carried out during the laboratory tests. This can assure that in case of seismic events the damages of the slab are negligible and that the behaviour of the FREEDAM connection is not influenced by the presence of the slab.

SPECIMEN TESTED IN LAB

CONNECTION REALIZED IN SITU

Figure 6.29: *Comparison between the specimen tested in lab and the connection realized in situ*

6.2.7.3 *Concrete casting of the first floor*

When al Cofradal panels and all the additional reinforcements have been positioned, the concrete casting of the first floor has been realized in one day without any interruption (Fig. 6.30).

After some days from the concrete cast, according to the design provision, the screed has been realized (Fig. 6.31).

Figure 6.30: *Concrete casting of the first floor*

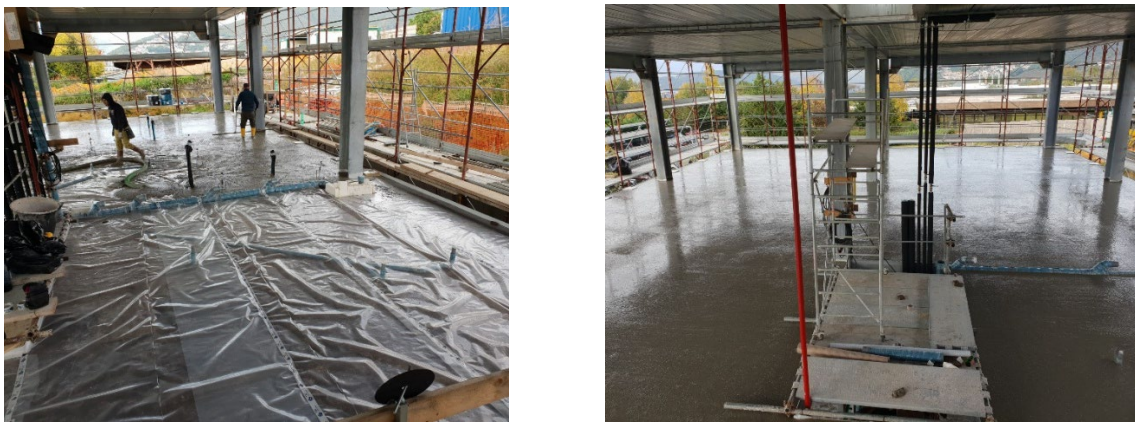

Figure 6.31: *Realization of the screed*

6.2.8 Realization of the Second Floor

The second floor is the same as the first floor. In Fig. 6.32 and 6.33 some photos related to this step have been reported.

Figure 6.32*: Realization of second floor*

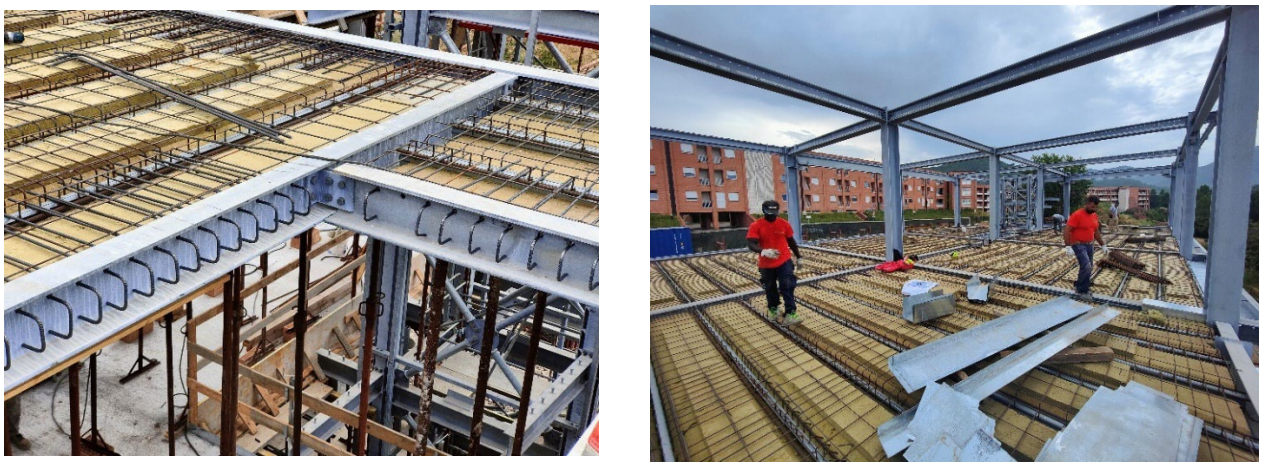

Figure 6.33*: Realization of second floor*

6.2.9 Realization of the Third Floor

The third floor is the same of first two floor except for the additional presence of the parapet wall. In Fig. 6.34 and Fig. 6.35 some photos related to this step have been reported. Furthermore, the specified thermal insulation and waterproofing were installed on the roof as shown in Fig 6.36.

***Figure 6.34**: Realization of third floor*

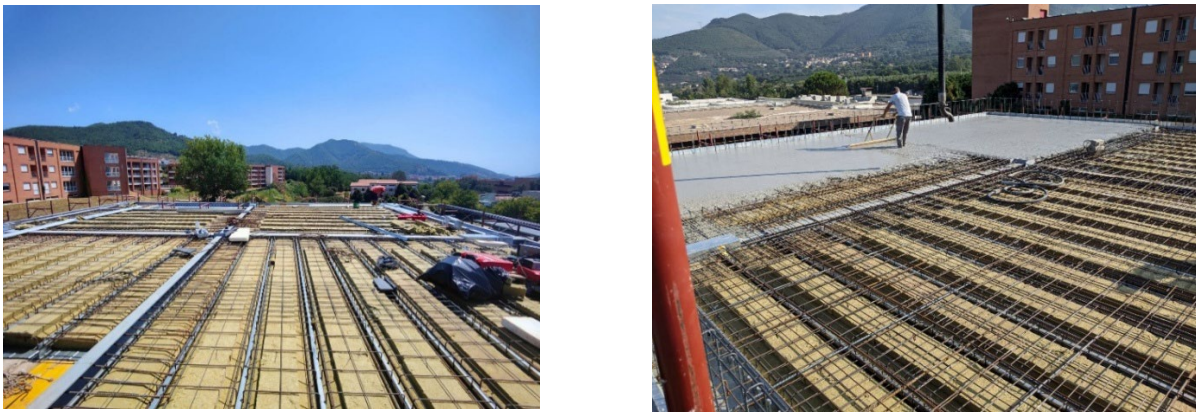

***Figure 6.35**: Realization of third floor*

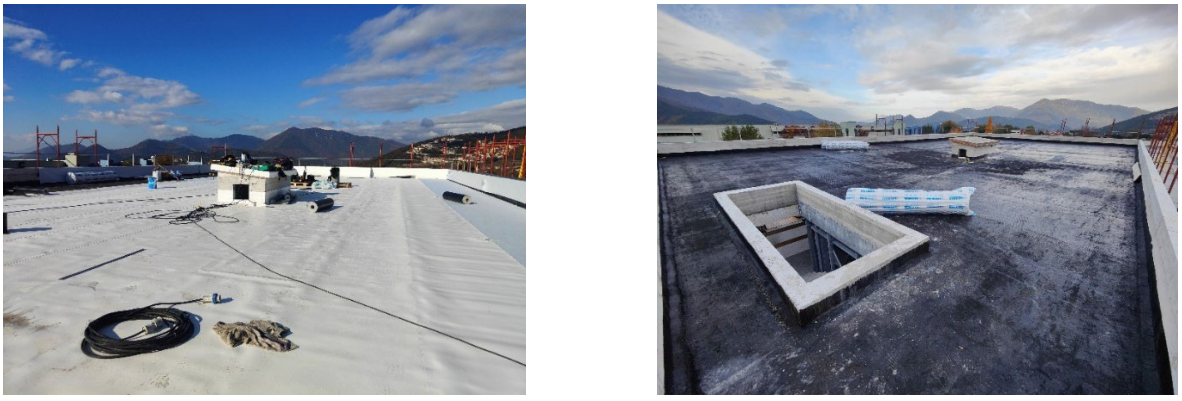

***Figure 6.36**: Thermal insulation and waterproofing of third floor*

6.2.10 Realization of Staircase

As provided in the final design, the staircase was constructed in reinforced concrete and is arranged around the steel elevator core. Reinforcements and concrete cast are reported in Fig. 6.37 and 6.38, respectively.

***Figure 6.37**: Staircase reinforcements*

***Figure 6.38**: Concrete casting of staircase*

6.2.11 Realization Building Services, External and Internal Finishes

Once the structural elements have been completed, electrical installations for power and lighting, plumbing systems for water supply and drainage, installations for heating, ventilation and Air-Conditioning have been togheter with internal and external partition walls have been realized. Some photos related to these steps are reported in Fig. 6.39 – 6.43.

Figure 6.39: *Installation of building services*

Figure 6.40*: Installation external and internal partition walls*

***Figure 6.41**: Windows installation*

***Figure 6.42**: Installation of the suspended ceiling and painting of the interior and exterior walls*

***Figure 6.43**: Installation of the external sunshades*

CHAPTER 7

Building on Site Testing and Monitoring

7.1 DYNAMIC IDENTIFICATION PROGRAM: IMPORTANCE AND OBJECTIVES

Dynamic identification is a non-destructive testing method, aimed at determining the modal properties of a structure — such as natural frequencies, mode shapes, and damping ratios — based on its vibrational response. Unlike traditional static testing, this technique captures the dynamic behaviour of the entire system being excited by either a natural or an artificial vibration source. It is widely used to assess the global stiffness distribution, detect changes in boundary conditions, and validate numerical models under realistic operating conditions.

In the context of the DREAMERS project, the dynamic identification of the C3 building was essential to evaluate the actual performance of the FREEDAM joints under real-scale conditions. In particular, the analysis of the building response to ambient vibrations reveals its dynamic reaction to the complex interactions between its structural and non-structural components, allowing engineers to monitor the evolution of its dynamic characteristics throughout the construction process. This approach is particularly crucial in this case, where an innovative seismic-resistant systems was used. Consequently, it is necessary to assess and verify experimentally the effects of the interactions between energy-dissipating joints and the main structural frame against design expectations.

The need of testing the innovative application of FREEDAM joints under real-scale conditions for a pilot building, required to opt for the use of high-sensitivity broadband vibration mechanical seismometers to ensure a higher detection capacity of the experimental measure system. In fact, unlike traditional methods involving the use of accelerometers and an artificial vibration source (i.e., a vibrodyne), this setup captures all the ambient vibrations with extreme precision and high sensitivity across a broad frequency spectrum. This not only reduces the invasiveness of the test procedure — allowing measurements to be taken without interfering with the construction process — but also ensures greater sensitivity to lower-frequency modes, which are typically dominant in multi-storey steel structures. Furthermore, this choice aligns with the innovative nature of the C3 demonstrator itself, emphasizing experimental solutions consistent with its research-oriented objectives.

Two ambient vibration test campaigns were performed: the first on October 12, 2024, during an intermediate construction phase, when the steel frame was in place, but non-structural elements were absent; the second on June 7, 2025, when the structure was almost complete, including partition walls, façade elements, solar panels, and mechanical systems. This dual approach allowed for a comparative analysis of the building's dynamic response in two distinct configurations, providing a rare opportunity to monitor how architectural and service components affect the structural system's vibration characteristics.

The Operational Modal Analysis (OMA) revealed natural frequencies ranging from approximately 1.0 Hz to 20 Hz in both campaigns. However, several significant differences were observed. The number of clearly identifiable vibration modes decreased from ten to seven, and a systematic reduction in natural frequencies was detected in the second campaign, consistent with the added mass and increased stiffness from non-structural components. Most notably, the first-mode damping ratio increased, indicating the enhanced energy dissipation provided by partition walls, façades, and technical systems. These results were validated through SSI-COV analysis, stabilization diagrams, and Modal Assurance Criterion (MAC).

7.2 HIGH-SENSITIVITY BROADBAND VIBRATION CHARACTERIZATION

To perform a detailed dynamic analysis of the C3 demonstration building, a high-sensitivity broadband monolithic seismometer was chosen as the core of the experimental measure system. Unlike conventional accelerometers coupled with an external vibration source (e.g., vibrodyne), this solution enables to perform an output-only analysis, due to its high sensitivity and broadband, without the need of integration with an external vibration source. The core sensing element is a horizontal monolithic seismometer (Fig. 7.1), produced and commercialized by ADV3STM. Based on a Watt's linkage architecture, the system behaves as a second-order mechanical oscillator with tuneable resonance frequency, linear response above the resonance frequency and known signal transfer function, easily allowing the removal of instrumental noise. To convert the mechanical signal into an electric signal, the oscillator is coupled with a highly sensitive LVDT (Linear Variable Differential Transformer) for displacement readout. The sensor offers a spectral sensitivity higher than 10^{-8} m/√Hz in the 3.5–100 Hz range and operates in an open-loop configuration, which drastically reduces the electronic noise, making it particularly suitable also for the detection of lower-frequencies structural responses. Moreover, due to its high signal-to-noise ratio, the chosen monitoring solution allowed for non-invasive identification of the building's dynamic properties at different stages of construction.

Each sensor was integrated into a portable and modular standalone monitoring unit, equipped with a 24-bit National Instruments™ FieldDAQ acquisition system and managed through a portable PC, with an installed Windows operating system, used to synchronize the vibration monitoring system, to manage the sensors, as well as to collect and store the sensors data. The acquisition system can collect and store the data with a sampling frequency up to 50,000 Hz. However, for the purpose of these experimental campaigns, the sampling rate was reduced to 5,000 Hz. Then, considering the typical range of structural vibrations, to increase the computation speed, all the recorded time series were downsampled to 500 Hz, guaranteeing a validity of data up to the Nyquist frequency (250 Hz).

This setup, originally developed for vibroacoustic characterization of cultural heritage structures, was adapted for structural health monitoring (SHM) in innovative buildings. The system's modular architecture supports integration of multiple sensors types and ensures reliable data acquisition even under variable environmental conditions.

***Figure 7.1**. The monolithic mechanical seismometer, produced by ADV3S™ and used for the dynamic identification*

7.3 SITE TEST SETUP

Two ambient vibration test campaigns were carried out at different construction stages to monitor the evolution of the dynamic properties of the C3 demonstration building. The first campaign was conducted on October 12, 2024, when the construction reached an intermediate stage. In detail, the steel frame was complete, but the building was devoid of any non-structural elements, such as internal partitions, façade cladding, and equipment. The second campaign took place on June 7, 2025, when the building was nearly completed, with architectural finishes, partition walls, "brise soleil" elements, photovoltaic panels, and technical systems fully installed. This two-phase testing strategy was designed to capture and compare the dynamic characteristics of

the structure in its bare and operational configurations, providing valuable insights into the effects of added mass and structural damping introduced by non-structural components.

In both campaigns, a total of six sensors were deployed at the first-floor level, where the vibration response is representative of the building's global dynamic behaviour. This was possible thanks to the very high displacement sensitivity and low-noise performance of the broadband seismometers, allowing to avoid the installation of further sensors in the upper floors and the roof. Moreover, thanks to the adopted experimental solution, the environmental vibrations, triggered by both natural and anthropogenic sources, were used as excitation source for the building, being sufficiently strong to be detected by the sensors. Consequently, the experimental test campaigns were performed in a fully non-invasive and passive manner, without requiring any artificial excitation system. This ensured that the structure remained unaffected by the testing procedure, aligning with the principles of operational modal analysis and enabling a realistic assessment of the as-built performance of the FREEDAM-based structure.

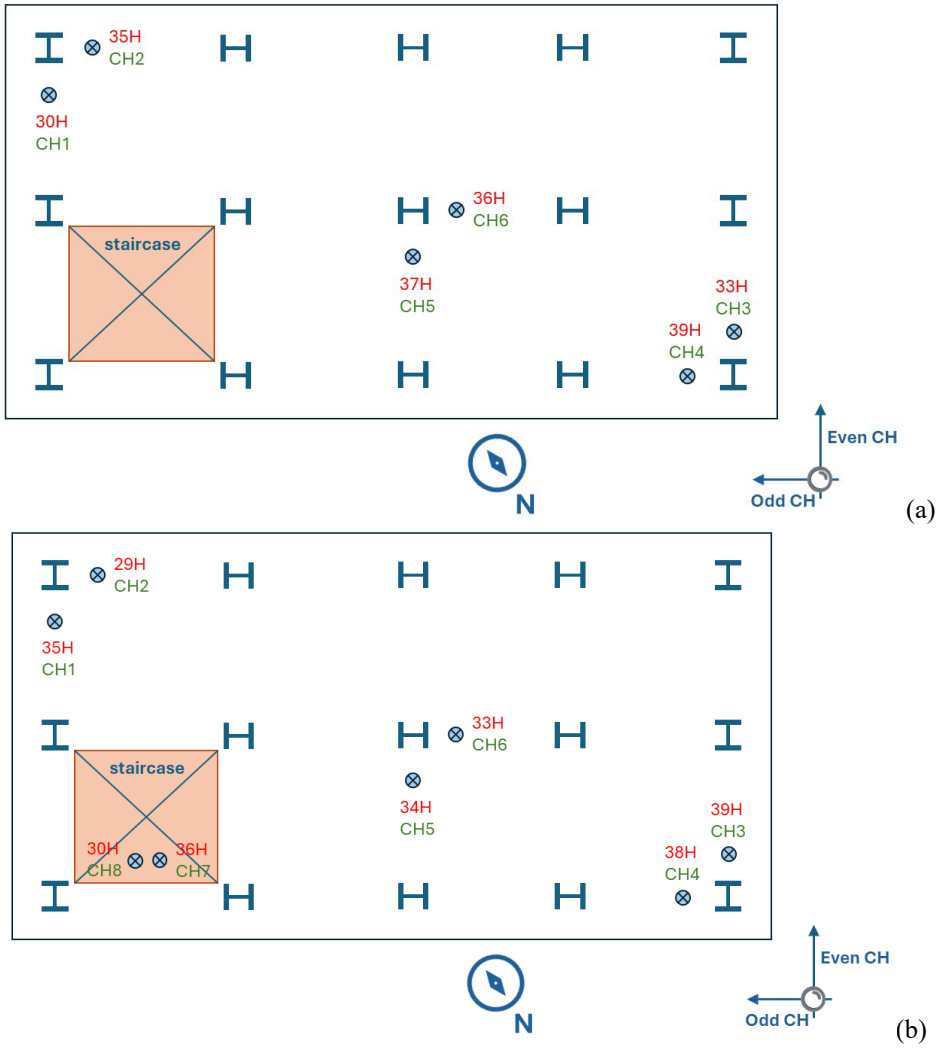

Figure 7.2: *Positioning of the sensors at the first floor in the first campaign (a) and in the second campaign (b)*

The sensors were strategically aligned in three orthogonal pairs, positioned along the two principal directions of the floor plan as reported in Fig. 7.2. Each pair consisted of one sensor oriented along the longitudinal axis and one along the transverse axis, enabling independent monitoring of the horizontal motion components, based on the high directivity of the sensors. All sensors were carefully aligned with a consistent orientation in the global reference frame to preserve directional coherence and phase integrity across channels. To ensure optimal coupling and minimize external noise, the instruments were placed on rigid, mechanically isolated stone slabs in the first campaign, and on the floor in the second campaign, creating a stable and repeatable foundation for measurements (Fig. 7.3 and 7.4).

Figure 7.3: *A couple of sensors placed near the corner column during the first campaign*

Figure 7.4: *A couple of sensors placed near one of the middle columns during the second campaign*

7.4 DYNAMIC IDENTIFICATION OF THE STRUCTURE

The data, collected during the experimental tests, were processed through a multi-step procedure aimed at extracting the modal parameters of the C3 building. All the data were processed through MATLAB software. The seismometers output signals, consisting in data time series, sampled with a frequency of 5,000 Hz, were, first, pre-processed to remove the instrumental noise and obtain the real signals from the sensors through a deconvolution procedure used for any seismometer or accelerometer. Then, the time-domain signals were converted into the frequency domain to have both the time- and frequency-domain plots of the data. Fast Fourier Transform (FFT) techniques were also used to identify the distinct frequency peaks corresponding to the local natural frequencies detected buy each sensor. This procedure enabled also a preliminary visualization of dominant resonant frequency peaks observed by multiple seismometers, thereby increasing the reliability of the mode identification.

The dynamic identification was performed through an Operational Modal Analysis (OMA). In particular, the Stochastic Subspace Identification with Covariance-driven approach (SSI-COV) technique was adopted. This technique, well-suited for the purpose of the project, allowed for the extraction of modal frequencies, mode shapes, and damping ratios directly from the output-only measurements. Stabilization diagrams were constructed to assess the consistency of identified modes across multiple model orders. Only stable poles — confirmed across at least three consecutive model orders and with high modal observability — were retained for further analysis. Only the modes with Modal Assurance Criterion (MAC) above 0.9 were selected. Conversely, data with lower MAC values were excluded.

The identified natural frequencies ranged from approximately 1.0 Hz to 20 Hz (Table 7.1), with 35 vibration modes successfully identified in both test campaigns. This dense modal spectrum was made accessible thanks to the high-resolution capabilities of the mechanical seismometers and the effectiveness of the ambient vibration strategy employed. The first campaign, conducted in the absence of non-structural elements, already revealed a rich set of modal responses, confirming the sensitivity of the acquisition and processing method. In the second campaign, a similarly large number of modes were captured despite the increased damping introduced by finishing elements and installations, demonstrating the robustness of the setup even in low-amplitude excitation scenarios.

The lowest-frequency modes correspond to global translational behaviour of the building in the longitudinal and transverse directions, with the two three modes located between 1.7 Hz and 2.0 Hz in the first campaign, and shifting upwards to between 1.2 Hz and 1.7 Hz in the second

campaign. This variation reflects the increased global mass of the structure following the completion of architectural elements. In contrast, the higher-frequency modes (above 10 Hz) are mainly associated with local flexural vibrations, floor modes, and possible torsional responses, particularly involving non-structural mass and stiff subsystems like the stair-elevator core.

Table 7.1: *Identified modes in both the campaigns (frequencies, periods and damping)*

Mode No.	1st campaign			2nd campaign		
	Freq [Hz]	Period [s]	Damping [%]	Freq [Hz]	Period [s]	Damping [%]
1	1.783	0.561	0.09	1.199	0.834	4.3
2	1.959	0.510	1.43	1.695	0.590	1.47
3	2.442	0.410	0.07	2.119	0.472	0.44
4	2.496	0.401	0.22	2.318	0.431	3.72
5	2.782	0.359	0.77	2.443	0.409	0.6
6	3.322	0.301	0.82	2.558	0.391	0.03
7	3.835	0.261	0.34	2.671	0.374	0.54
8	3.985	0.251	0.09	2.829	0.353	0.31
9	4.108	0.243	0.86	2.898	0.345	0.09
10	5.253	0.190	0.49	3.525	0.284	0.12
11	5.424	0.184	0.01	3.664	0.273	0.42
12	5.522	0.181	0.05	3.942	0.254	1.22
13	5.725	0.175	0.05	4.131	0.242	0.25
14	5.871	0.170	0.4	4.268	0.234	0.7
15	7.137	0.140	1	6.242	0.160	0.51
16	7.788	0.128	0.12	7.588	0.132	0.13
17	7.913	0.126	0.04	7.883	0.127	0.47
18	8.175	0.122	0.12	8.085	0.124	0.34
19	8.559	0.117	0.04	8.701	0.115	0.23
20	9.358	0.107	0.05	9.233	0.108	0.25
21	9.728	0.103	0.26	9.608	0.104	0.83
22	9.938	0.101	0.14	10.268	0.097	0.13
23	10.147	0.099	0.24	10.497	0.095	0.15
24	10.303	0.097	0.06	10.656	0.094	0.2
25	10.663	0.094	0.25	11.025	0.091	0.22
26	11.037	0.091	0.08	12.163	0.082	0.21
27	11.528	0.087	0.24	12.947	0.077	0.47
28	12.481	0.080	0.12	13.255	0.075	0.36
29	12.913	0.077	0.11	13.665	0.073	0.42
30	13.144	0.076	0.17	13.912	0.072	0.27
31	13.362	0.075	0.09	14.227	0.070	0.55
32	13.686	0.073	0.31	16.081	0.062	0.56
33	14.312	0.070	0.22	16.764	0.060	0.2
34	14.985	0.067	0.3	17.174	0.058	0.25
35	15.460	0.065	0.21	17.408	0.057	0.74

The damping ratios were derived from the logarithmic decrement of the identified modal responses. As expected for a bolted steel-frame structure, damping values were low in the first campaign (October 2024), where the structure was composed solely of the bare frame. In contrast, the second campaign (June 2025) revealed an increase in damping, attributable to the energy dissipation provided by partition walls, cladding systems, and technical installations. In particular, the first-mode damping ratio increased, indicating the growing contribution of non-structural components to the overall dissipative behaviour.

Overall, the comparative analysis of both campaigns demonstrates the critical impact of architectural finishes on the dynamic behaviour of the structure, both in terms of modal frequencies and damping properties. These observations validate the need to perform modal identification at multiple stages of construction and provide essential input for the calibration and validation of numerical models developed within the project framework.

7.5 THE LONG-TERM MONITORING PROGRAM: OBJECTIVES AND CONTEXT

In recent decades, seismic engineering has made significant advances in ensuring the life safety of buildings during earthquakes. However, most traditional structures are still designed according to principles that accept damage as inevitable in the event of a strong seismic event. These buildings, while successfully preventing collapse, often suffer localized damage that can severely compromise their usability and require lengthy and expensive repairs.

It is in response to this challenge that the FREEDAM (FREE from DAMage) philosophy was conceived: to develop structural systems that can withstand destructive seismic events without sustaining damage. The DREAMERS project builds directly on this concept, aiming to demonstrate that a new generation of resilient steel buildings is not only possible but practical, economically viable, and sustainable. The objective is not just to save lives, but also to preserve the functionality of critical infrastructure immediately after an earthquake—an increasingly urgent goal in modern urban and industrial contexts.

A central pillar of the DREAMERS project is the monitoring of the demonstration building constructed on the campus of the University of Salerno. Monitoring is not treated here as a secondary or post-construction activity, but as a fundamental part of the design and validation process. In fact, one of the distinctive traits of DREAMERS lies in the integration of advanced monitoring technologies from the earliest phases of the project, with the goal of transforming the building itself into a living laboratory. The DREAMERS project (Design, REsearch, implementation And Monitoring of Emerging technologies for a new generation of Resilient

Steel buildings), funded by the European Commission under the RFCS program, represents an ambitious step forward in the application of damage-free design strategies to seismic-resistant steel buildings. The core technological innovation of the project lies in the use of FREEDAM connections, which allow energy dissipation through friction-based devices without inducing damage to the main structural members.

Among the various tasks of the project, Task 5.3 plays a crucial role by focusing on the implementation and validation of a comprehensive Structural Health Monitoring (SHM) system. This activity is not limited to data acquisition but is instead intended as a fundamental demonstration tool that supports the entire philosophy of the DREAMERS project: namely, that it is possible to design and build steel structures that remain operational even after severe seismic events, with negligible repair needs.

The SHM activities are carried out on the full-scale, three-storey steel building located on the campus of the University of Salerno. The demonstration building was designed to accommodate both typical architectural and functional requirements as well as experimental and monitoring instrumentation. It serves as a real-world testbed for the DREAMERS approach, allowing for long-term tracking of performance, data collection during seismic events, and continuous evaluation of the FREEDAM technology under operational conditions.

The long-term monitoring system implemented in the DREAMERS building serves as a fundamental component in validating the performance and resilience of FREEDAM structural connections in a real-world environment. Unlike conventional post-construction evaluations, this continuous monitoring initiative is integrated into the building's lifecycle from the outset, reflecting a proactive and data-driven approach to structural safety, reliability, and sustainability. The primary objective of the monitoring system is to assess the in-service performance of the FREEDAM beam-to-column joints over time, particularly in the aftermath of seismic or extreme loading events. By capturing and analyzing real-time data on clamping force, vibration, inclination, and temperature, the system enables a precise understanding of how the structural connections behave under operational and exceptional conditions.

A key goal of this activity is to validate the "free-from-damage" design philosophy. FREEDAM joints are engineered to dissipate seismic energy without damage to the primary structural elements. The monitoring system plays a crucial role in confirming that the clamping forces remain within the predefined thresholds and that no residual deformation or mechanical degradation occurs, even after significant dynamic loads.

Another core objective is to build a digital history of the building's structural behavior. The collected data allow for the creation of a baseline "health fingerprint" for each connection,

against which future changes can be detected and interpreted. This fingerprint becomes invaluable for post-earthquake assessments, supporting rapid decision-making about building usability and maintenance needs.

From a technological standpoint, the system supports the advancement of digital twin methodologies in structural engineering. Through continuous data acquisition and integration with Building Information Modeling (BIM), the monitored building becomes an evolving digital representation of itself, enabling simulations, predictive diagnostics, and remote management capabilities.

In addition, the system contributes to the broader objective of increasing the lifespan and operational continuity of the structure. The ability to detect early signs of bolt relaxation, friction loss, or unexpected vibrational behaviour allows for targeted maintenance interventions, reducing lifecycle costs and avoiding unplanned service interruptions. Finally, from a research and innovation perspective, the long-term monitoring efforts provide critical empirical evidence to inform future guidelines, Eurocode developments, and standardization efforts for damage-free construction. The data and insights generated will also serve as a reference model for future steel buildings aiming to adopt high-resilience technologies.

7.6 THE MONITORING SYSTEM: ARCHITECTURE AND TECHNOLOGY

The monitoring system deployed in the DREAMERS building has been developed by Tokbo, a spin-off from the Agrati Group specialized in the application of IoT and AI technologies to structural monitoring. Tokbo's solution is particularly well-suited for the FREEDAM joints due to its ability to accurately measure clamping forces in preloaded bolts, which are key to the proper functioning of the friction dampers.

The Tokbo Monitoring System consists of a network of IoT sensors applied to bolted joints to measure several key parameters, including:

- Clamping force
- Temperature
- Inclination
- Acceleration
- Vibration frequencies

This set of metrics provides a comprehensive picture of the threaded joint's health, turning each bolt into a sentinel capable of detecting damage or wear of components, joints, or connected parts.

The hardware component includes field sensors communicating via CAN-open protocol to a centralized Gateway, which transmits the data via LTE (with 3G/2G fallback) to the Tokbo cloud server. The force measurement is based on ultrasonic Time of Flight (TOF) technology, which is non-invasive and preserves the certified mechanical properties of the bolts.

Figure 7.5: *Hardware system produced by TOKBO srl*

Each sensor uses ultrasonic technology to measure clamping force. Specifically, the control electronics have been developed to measure the variation of the so-called Time of Flight (TOF), which can be correlated to changes in the bolt's length and, consequently, to the force exerted by the joint as a result of tightening (5). This type of measurement is extremely accurate and, most importantly, non-invasive, preserving the certified mechanical strength, tribological properties, and corrosion resistance of the instrumented bolts.

Each sensor includes an integrated MEMS inertial unit, which acquires vibration frequencies, accelerations, and the tilt of the bolt axis relative to the vertical, allowing for comprehensive static and dynamic monitoring.

Figure 7.6: *TOKBO sensor*

The data is transmitted, aggregated, analyzed, and visualized within the Tokbo cloud platform. Each user can view both the real-time data of each individual sensor and historical time series, enabling them to monitor the current state of the structure as well as analyze events over specific periods.

The monitoring platform includes an automated notification section: if two threshold levels—warning and alert—are exceeded, an anomaly detection event is triggered, which results in automatic email and SMS notifications to stakeholders, alerting them to the need for inspection and further assessment aimed at maintenance. The software platform aggregates, analyzes, and visualizes real-time and historical data, enabling stakeholders to assess the current state and behavior of each connection.

The service component consists of continuous data analysis and interpretation of the phenomena affecting the bolts, carried out by Tokbo's engineering department.

Thanks to monitoring and the detection of damage mechanisms, improved tightening and bolted joint design solutions can be proposed, with the aim of extending the asset's service life and preventing potentially critical events.

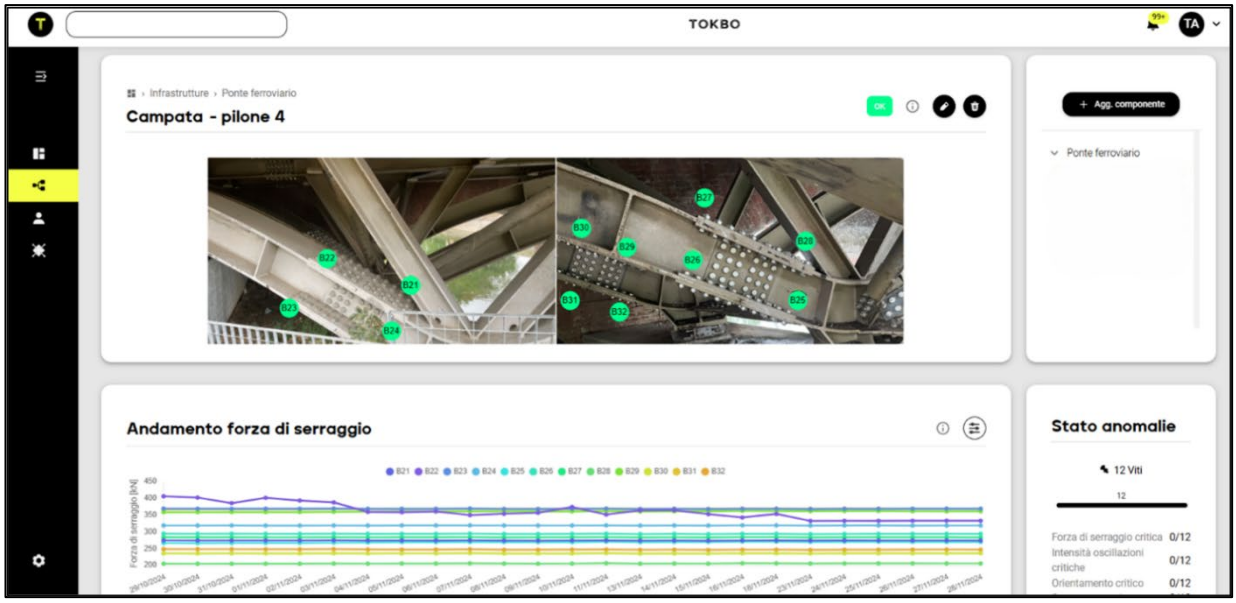

Figure 7.7: *Software*

Tokbo implements algorithmic models based on iterative analysis methods of the collected telemetry (Machine Learning – ML), tailored to each application. These models identify abnormal trends and specific events.

The ML algorithms are designed for continuous learning, which is essential for improving their accuracy over time. When a notification is triggered, Tokbo specialists inspect and classify the behavior; this feedback serves as training for the models and contributes to increased accuracy

in future anomaly detection. Additionally, predictive models are employed to infer future behavior from historical time series data. After detecting an anomaly, these models provide an indication of the probable future behavior of the bolted joint, enabling the predictive maintenance paradigm through targeted and timely interventions.

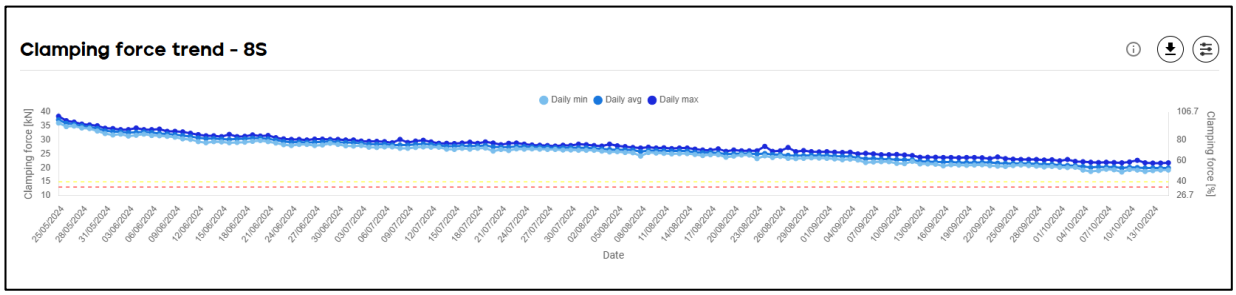

Figure 7.8: *Clamping force trend*

7.7 LABORATORY VERIFICATION OF THE MONITORING SYSTEM

Prior to full deployment, the Tokbo monitoring system was rigorously validated in laboratory conditions during cyclic dynamic testing on sub-assemblies of FREEDAM beam-to-column joints designed for the DREAMERS building. This testing aimed to simulate seismic effects and observe the joint behavior in real-time using instrumented bolts. The tests are those on beam-to-column joints previously described. Their objective was to evaluate the moment-rotation response of external beam-to-column joints identical to those used in the DREAMERS pilot building. Since FREEDAM joints are not yet codified under Italian design standards, the testing followed the "Design Assisted by Testing" approach from Eurocode 0 and incorporated provisions from AISC 358-18. The tests aimed to determine key structural parameters at both the Ultimate and Serviceability Limit States. Specimens matched the real structural configuration, using materials such as Cofradal 260 and C30/37 concrete. Displacements and forces were recorded using potentiometric transducers and load sensors. The tests, carried out by the University of Salerno in collaboration with UNINA and ArcelorMittal, also explored how the floor system influences joint behavior—an aspect not addressed in previous FREEDAM studies.

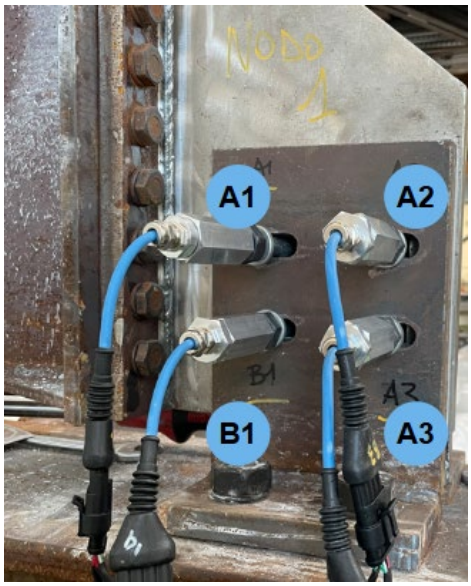

Figure 7.9: *FREEDAM joint monitored with TOKBO sensors*

A subassembly was extracted to represent the most frequently used joint configuration within the demonstrator building. Specifically, the selected joint is applied consistently across all stories, emphasizing its importance. In the first two stories, it is used in the form of Device D1 with an IPE450 beam, with an utilization ratio of 0.3. In the top story, it is utilized as Device D1 with an IPE400 beam, with an utilization ratio again of 0.3. This selection underlined the joint's relevance and widespread application throughout the structure, making it a vital component to study for understanding the building's overall resilience and performance. In particular, the tested joint, marked as FREEDAM - IPE 450 / 0.3, has the following specifications:

- Joint moment resistance (slip resistance): 181 kNm;
- Device slip resistance: 292 kN;
- Lever arm: 620 mm;
- Bolts: n.4 M16 HV 10.9;
- Bolt preloading force imposed in the tests: 75.8 kN;
- Connected beam: IPE 450;
- Connected column: HEB 400.

The tested joint was equipped within the experimental campaign with Tokbo sensors. These were monitored before, during, and after the test, with data collected across different loading phases. The load history was analyzed in terms of moment-rotation behavior, clamp force evolution, and response trends using Tokbo's machine learning tools. Below is a series of graphs illustrating the applied load history in terms of the joint's moment-rotation behavior, the force values measured by Tokbo during the various phases of the test, and the output of the machine learning algorithms used for data analysis and event detection.

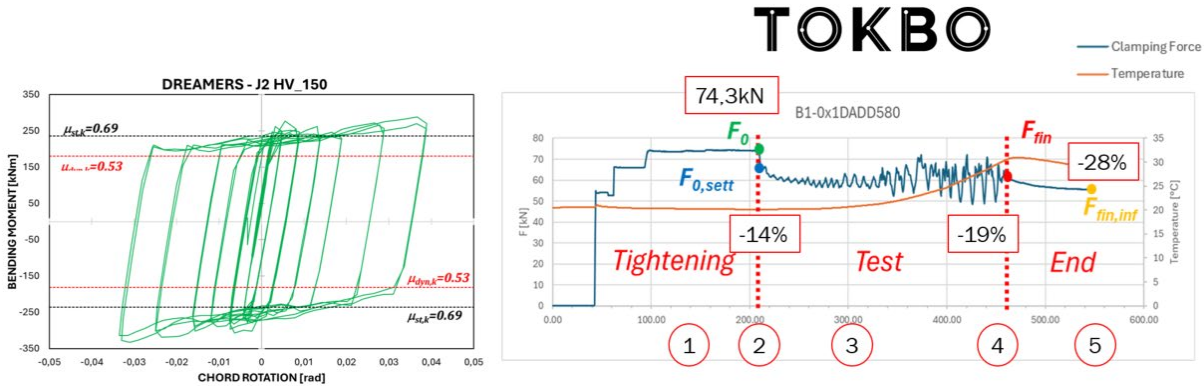

Figure 7.10: *Test response and bolts telemetry*

The outcome of the automated anomaly detection, performed through a machine learning algorithm, is illustrated in the form of a two-dimensional PCA (Principal Component Analysis) plot. This visualization effectively segments the various phases of the dynamic test based on the time series data previously described.

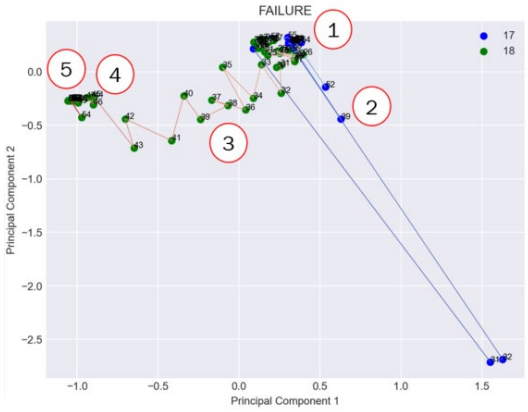

Figure 7.11: *Damage state monitored with unsupervised ML tools*

The figure highlights five distinct clusters, each corresponding to a specific phase of the test procedure:

1. **Initial tightening** under force control to the nominal target value, which forms the initial centroid in the PCA space.
2. **Start of the dynamic loading**, marking a clear departure from the initial state.
3. **During the dynamic test**, where the system experiences evolving conditions and increasing stresses—this phase shows a trajectory away from the initial centroid, capturing the transition in joint behavior.
4. **End of the dynamic test**, where the system begins to stabilize.
5. **Post-test phase (settling)**, where a new centroid is established, representing the joint's stabilized condition in its new operational state.

This data-driven clustering confirms the system's ability to autonomously detect and classify structural behavioral changes, reinforcing the importance of machine learning tools in advanced structural health monitoring frameworks.

Additionally, the obtained results indicated several critical findings:

- Even when torque-controlled tightening strategies aimed to exceed nominal clamping force by 15%, actual measurements revealed deviations due to bolt interaction effects and dynamic friction. Tokbo's sensors accurately quantified and allower to correct this discrepancy reducing the initial clamping error to about 0%.
- The system allowed real-time analysis of bolt behavior during the test, detecting anomalies associated with shear-induced stress during extreme rotations, ultimately leading to bolt plasticization.
- Telemetry clearly identified the distinct test phases: initial tightening, pre-test force relaxation, joint loading evolution, and post-test stabilization.
- Unsupervised ML algorithms provided effective data segmentation, accurately classifying joint states from initial operation through transitional stress phases to the new equilibrium state.

These insights validated Tokbo’s monitoring approach and informed the decision to apply continuous monitoring to 25% of the DREAMERS pilot building joints and to use Tokbo sensors for torque verification across all 192 bolts.

7.8 THE LONG TERM MONITORING SYSTEM

The monitoring system was installed during calendar week 05/2025 by Tokbo's technical team, in coordination with structural engineers from the University of Salerno. The installation procedure followed a meticulous protocol designed to ensure measurement accuracy and long-term reliability.

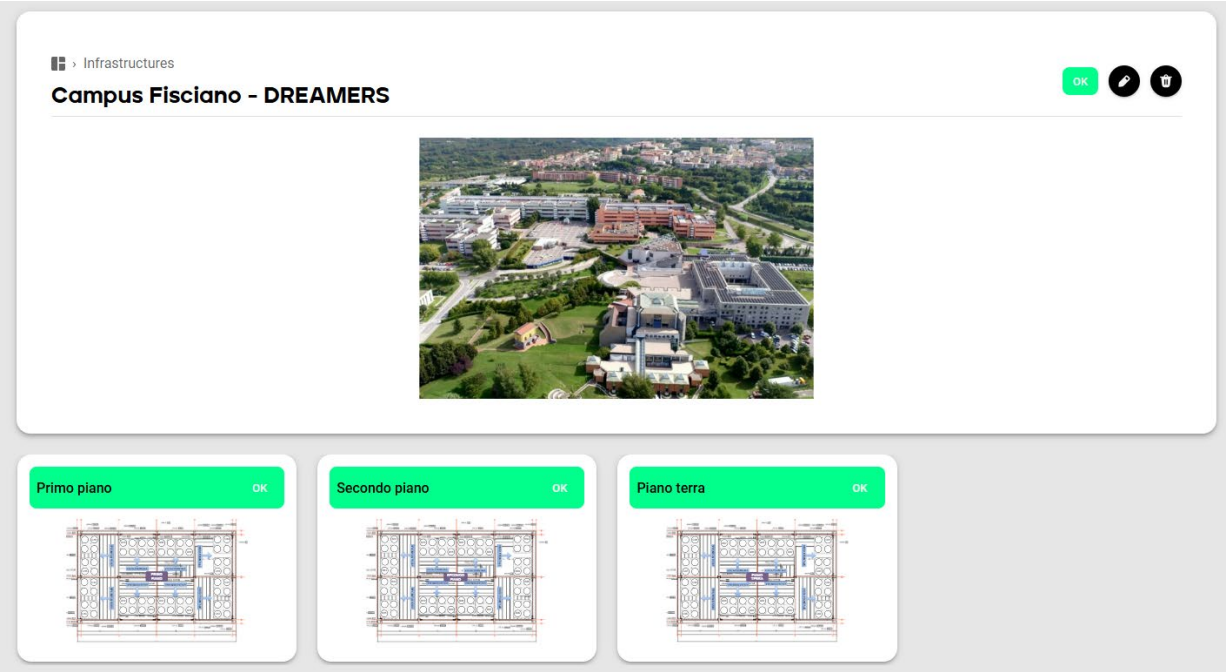

Figure 7.12: *Cloud infrastructure page*

The process included the removal of one bolt at a time from the FREEDAM joints, replacement with a sensorized bolt, mounting of the sensor electronics, and progressive tightening in force-controlled steps. Final calibration ensured that all bolts met the design clamping force values, typically around 83.3 kN for M16 bolts and 98.3 kN for M20 bolts, depending on the location within the building. A re-check phase accounted for force relaxation phenomena, guaranteeing that long-term monitoring would start from a validated preload state.

The distribution matrix of sensorized bolts over storeys, with related target of clamping force, is reported on the following table

Storey	Bolt size + nr Belleville	F target [kN]
1S – ground floor	M16 HV + 6x belleville	83,3
	M20 HV + 4x belleville	98,3
2S – first floor	M16 HV + 6x belleville	83,3
	M20 HV + 4x belleville	98,3
3S – second floor	M16 HV + 4x belleville	69,5

M16 and M20 bolt/nut assembly installed in a single friction joints are composed by:

- EN14399-4 HV M16 10.9/10 assembly, with thread locking feature applied on threaded shank according to DIN267-28
- M16- EH-4.0-177 Solon belleville washer in 17-7PH (nr 4 or nr 6 pieces)

- EN14399-4 HV M20 10.9/10 assembly, with addition of thread locking feature applied on threaded shank according to DIN267-28
- M20- EH-4.9-177 Solon belleville washer in 17-7PH (nr 4 pieces)

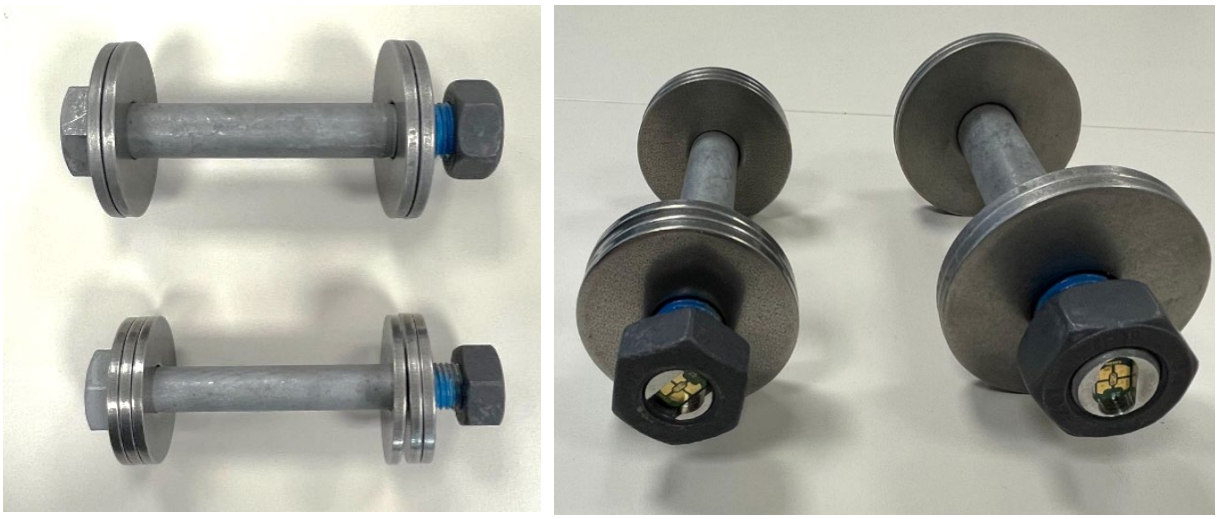

Figure 7.13: *M16 and M20 assemblies (bolt with thread locking feature / nut / belleville washers)*

For a single bolted joint equipped with FREEDAM dampers, nr. 4 sensorized bolts has been installed by tightening in force control. To target the target clamp force, the following procedure has been applied by the TOKBO technicians:

1. Disassembly of a single existing bolt
2. Screwing of the sensorized bolt
3. Mounting of Tokbo electronics
4. Start of clamping force monitoring
5. Pre-tightening of sensorized bolt with tightening tool
6. Final tightening in force control by manual torque wrench
7. Repeat from step 1 to step 6 for the single bolt, from bolt 1 to bolt 4
8. Control of final clamping force of all the 4 sensorized bolt, in consideration of the mutual influence and relaxation phenomena
9. Recovery of the clamped force relaxation by manual torque wrench re-tightening for a single bolt, where necessary
10. Release of the joint

As per requirements, for a single friction joint one Tokbo sensor has been permanently maintained on the joint for long term monitoring, while three sensorized bolts have been maintained without the control electronics, but available for future inspections activities.

Consequently, a differentiation in terminology has been applied in the reference documentation based on two different utility modes:

- Tokbo permanent sensors: placed to monitor permanently the beam to column joint
- Tokbo temporary sensors, named “only piezo”: located temporarily to tightening the bolt in force control

Figure 7.14: *Sensorized bolts of the friction joints – 1x permanent sensor; 3x temporary sensors*

For a single permanent sensor, the following telemetries are made available by the Tokbo cloud platform:

- Clamping force
- Temperature
- Orientation
- Acceleration
- Main frequencies of vibration over time domain (spectrogram)

The network architecture and identification of the sensorized nodes, are reported in the following figures and in the relevant reference documents.

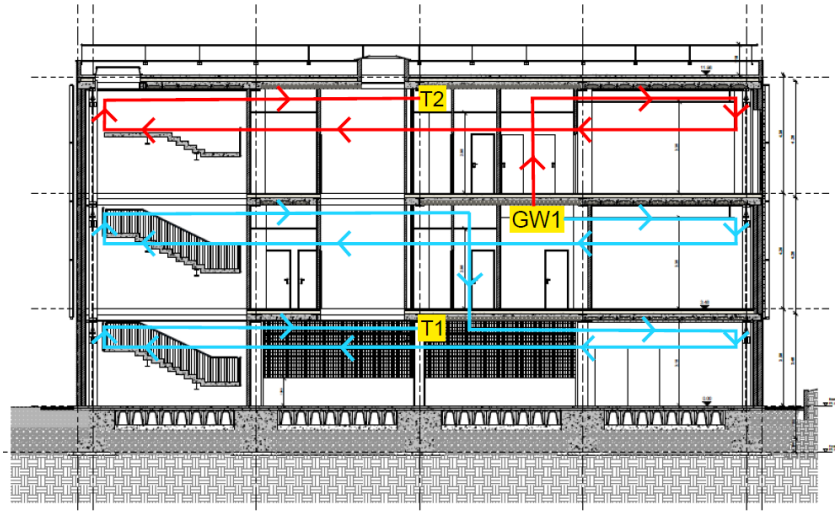

Figure 7.15: *Can bus distribution from gateway to sensors, place on the thrtee storey: two can buses with corresponding termination T1 and T2*

In the following tables are reported the clamping force values of the single bolted connection, as a result of the tightening operation performed during the installation work, in comparison with the nominal target values.

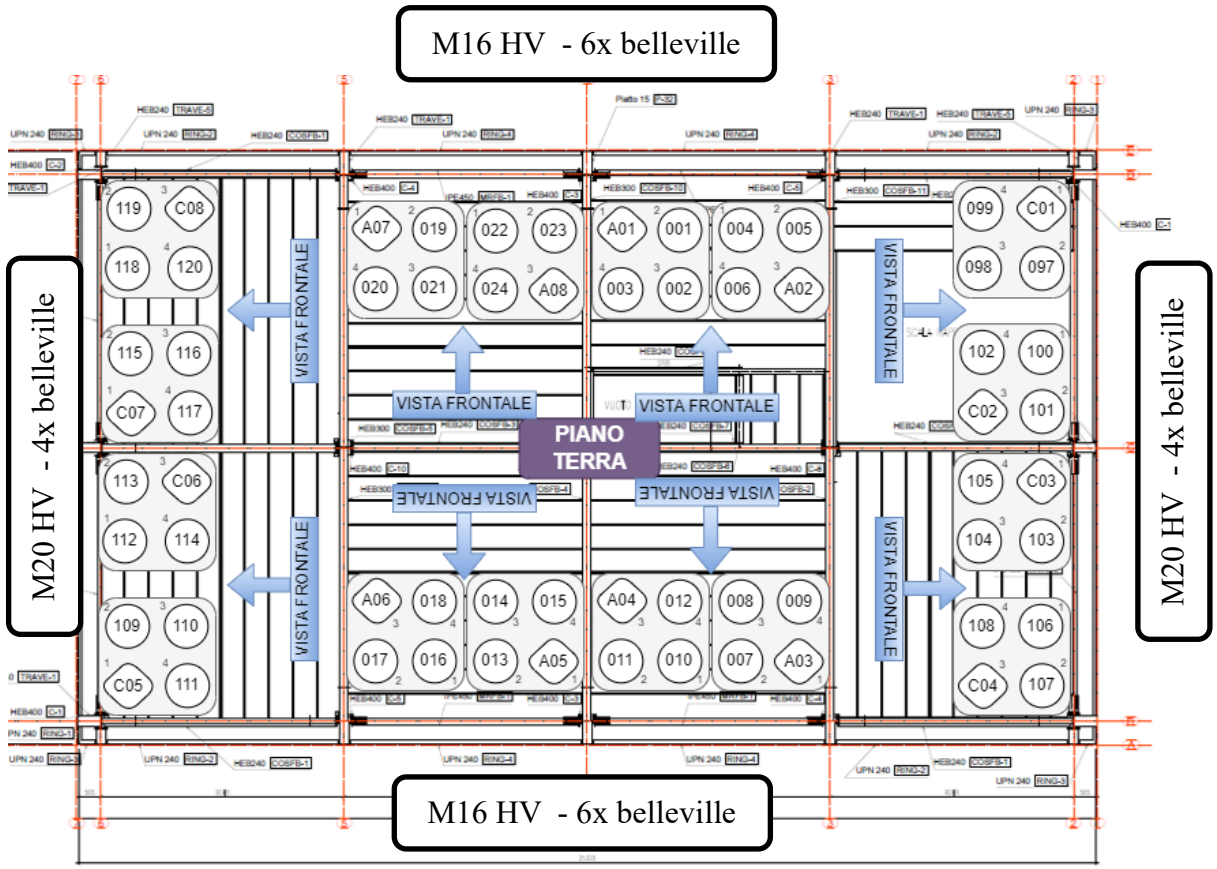

Figure 7.16: *Ground Floor - sensor ID*

Position	Node	Infrastructure	MAC DEF	Bolt Size	Nr belleville washers	F target	F0 [kN]	F0/ F target [%]
Node 1S-D4-3								
A01	1S-D4-3-B1	CAMPUS FISCIANO PT	0xFE372B6C	M16X130	6	83,3	82,9	100%
1PT	1S-D4-3-B2	CAMPUS FISCIANO PT ONLYPIEZO	0x20A5D540	M16X125	6	83,3	85,5	103%
2PT	1S-D4-3-B3	CAMPUS FISCIANO PT ONLYPIEZO	0xA040D540	M16X125	6	83,3	85,3	102%
3PT	1S-D4-3-B4	CAMPUS FISCIANO PT ONLYPIEZO	0xA03ED540	M16X125	6	83,3	86,2	103%
Node 1S-D4-4								
A02	1S-D3-4-B3	CAMPUS FISCIANO PT	0xE68E4688	M16X130	6	83,3	81,9	98%
4PT	1S-D3-4-B1	CAMPUS FISCIANO PT ONLYPIEZO	0xA07DD540	M16X125	6	83,3	84,8	102%
5PT	1S-D3-4-B2	CAMPUS FISCIANO PT ONLYPIEZO	0xA09BD540	M16X125	6	83,3	85,1	102%
6PT	1S-D3-4-B4	CAMPUS FISCIANO PT ONLYPIEZO	0x1DA4D580	M16X125	6	83,3	82,8	99%
Node 1S-B3-4								
A03	1S-B3-4-B1	CAMPUS FISCIANO PT	0xB0E9F2B0	M16X130	6	83,3	84,2	101%
7PT	1S-B3-4-B2	CAMPUS FISCIANO PT ONLYPIEZO	0xA0AED580	M16X125	6	83,3	84	101%
8PT	1S-B3-4-B3	CAMPUS FISCIANO PT ONLYPIEZO	0x1DA6D580	M16X125	6	83,3	84,5	101%
9PT	1S-B3-4-B4	CAMPUS FISCIANO PT ONLYPIEZO	0x1DAFD580	M16X125	6	83,3	84,3	101%
Node 1S-B4-3								
A04	1S-B4-3-B3	CAMPUS FISCIANO PT	0xD670C582	M16X130	6	83,3	86	103%
10PT	1S-B4-3-B1	CAMPUS FISCIANO PT ONLYPIEZO	0x1D9FD580	M16X125	6	83,3	84,5	101%
11PT	1S-B4-3-B2	CAMPUS FISCIANO PT ONLYPIEZO	0xA085D540	M16X125	6	83,3	85,6	103%
12PT	1S-B4-3-B4	CAMPUS FISCIANO PT ONLYPIEZO	0x20ACD540	M16X125	6	83,3	83,7	100%
Node 1S-B4-5								
A05	1S-B4-5-B1	CAMPUS FISCIANO PT	0x3DC37CB5	M16X130	6	83,3	83,1	100%
13PT	1S-B4-5-B2	CAMPUS FISCIANO PT ONLYPIEZO	0xA089D580	M16X125	6	83,3	84,5	101%
14PT	1S-B4-5-B3	CAMPUS FISCIANO PT ONLYPIEZO	0xA08CD540	M16X125	6	83,3	84,5	101%
15PT	1S-B4-5-B4	CAMPUS FISCIANO PT ONLYPIEZO	0x2089D540	M16X125	6	83,3	86,9	104%
Node 1S-B5-4								
A06	1S-B5-4-B3	CAMPUS FISCIANO PT	0xADBD8BD3	M16X130	6	83,3	85,2	102%
16PT	1S-B5-4-B1	CAMPUS FISCIANO PT ONLYPIEZO	0xA084D580	M16X125	6	83,3	85,1	102%
17PT	1S-B5-4-B2	CAMPUS FISCIANO PT ONLYPIEZO	0xA0A4D540	M16X125	6	83,3	84,7	102%
18PT	1S-B5-4-B4	CAMPUS FISCIANO PT ONLYPIEZO	0x207CD580	M16X125	6	83,3	84,1	101%
Node 1S-D5-4								
A07	1S-D5-4-B1	CAMPUS FISCIANO PT	0xB4CF7772	M16X130	6	83,3	80,5	97%
19PT	1S-D5-4-B2	CAMPUS FISCIANO PT ONLYPIEZO	0x2093D540	M16X125	6	83,3	82,2	99%
20PT	1S-D5-4-B3	CAMPUS FISCIANO PT ONLYPIEZO	0xA09FD540	M16X125	6	83,3	84,3	101%
21PT	1S-D5-4-B4	CAMPUS FISCIANO PT ONLYPIEZO	0xA095D540	M16X125	6	83,3	84,4	101%
Node 1S-D4-5								
A08	1S-D4-5-B3	CAMPUS FISCIANO PT	0x99C1DFF8	M16X130	6	83,3	85,7	103%
22PT	1S-D4-5-B1	CAMPUS FISCIANO PT ONLYPIEZO	0xA0A1D540	M16X125	6	83,3	83,7	100%
23PT	1S-D4-5-B2	CAMPUS FISCIANO PT ONLYPIEZO	0x20A2D540	M16X125	6	83,3	82,4	99%
24PT	1S-D4-5-B4	CAMPUS FISCIANO PT ONLYPIEZO	0x20A2D580	M16X125	6	83,3	84,5	101%
Node 1S-2D-C								

C01	1S-2D-C-B1	CAMPUS FISCIANO PT	0xB781F594	M20X140	4	98,3	96,6	98%
97P2	1S-2D-C-B2	CAMPUS FISCIANO PT ONLYPIEZO	0x454BF784	M20X140	4	98,3	96,2	98%
98P2	1S-2D-C-B3	CAMPUS FISCIANO PT ONLYPIEZO	0x484BF704	M20X140	4	98,3	97,6	99%
99P2	1S-2D-C-B4	CAMPUS FISCIANO PT ONLYPIEZO	0x434BF704	M20X140	4	98,3	97,4	99%
Node 1S-2D-C								
C02	1S-2C-D-B3	CAMPUS FISCIANO PT	0x7C26FD9C	M20X140	4	98,3	101,8	104%
100P2	1S-2C-D-B1	CAMPUS FISCIANO PT ONLYPIEZO	0x424BF704	M20X140	4	98,3	99,1	101%
101P2	1S-2C-D-B2	CAMPUS FISCIANO PT ONLYPIEZO	0x474BF784	M20X140	4	98,3	96,3	98%
102P2	1S-2C-D-B4	CAMPUS FISCIANO PT ONLYPIEZO	0x494BF704	M20X140	4	98,3	100,1	102%
Node 1S-2C-B								
C03	1S-2C-B-B1	CAMPUS FISCIANO PT	0x63027E07	M20X140	4	98,3	94,5	96%
103P2	1S-2C-B-B2	CAMPUS FISCIANO PT ONLYPIEZO	0x464BF704	M20X140	4	98,3	96,3	98%
104P2	1S-2C-B-B3	CAMPUS FISCIANO PT ONLYPIEZO	0x434BF784	M20X140	4	98,3	97,4	99%
105P2	1S-2C-B-B4	CAMPUS FISCIANO PT ONLYPIEZO	0x494BF7C4	M20X140	4	98,3	98,1	100%
Node 1S-2B-C								
C04	1S-2B-C-B3	CAMPUS FISCIANO PT	0x6473FBE5	M20X140	4	98,3	96,3	98%
106P2	1S-2B-C-B1	CAMPUS FISCIANO PT ONLYPIEZO	0x4B4BF704	M20X140	4	98,3	97,7	99%
107P2	1S-2B-C-B2	CAMPUS FISCIANO PT ONLYPIEZO	0x4A4BF704	M20X140	4	98,3	98,9	101%
108P2	1S-2B-C-B4	CAMPUS FISCIANO PT ONLYPIEZO	0x484BF744	M20X140	4	98,3	100,1	102%
Node 1S-6B-C								
C05	1S-6B-C-B1	CAMPUS FISCIANO PT	0x2D550FF6	M20X140	4	98,3	98,5	100%
109P2	1S-6B-C-B2	CAMPUS FISCIANO PT ONLYPIEZO	0x454BF7C4	M20X140	4	98,3	95,4	97%
110P2	1S-6B-C-B3	CAMPUS FISCIANO PT ONLYPIEZO	0x1D8ED580	M20X140	4	98,3	96,5	98%
111P2	1S-6B-C-B4	CAMPUS FISCIANO PT ONLYPIEZO	0x444BF784	M20X140	4	98,3	95,8	97%
Node 1S-6C-B								
C06	1S-6C-B-B3	CAMPUS FISCIANO PT	0xFDB61F45	M20X140	4	98,3	95,9	98%
112P2	1S-6C-B-B1	CAMPUS FISCIANO PT ONLYPIEZO	0x464BF7C4	M20X140	4	98,3	97,3	99%
113P2	1S-6C-B-B2	CAMPUS FISCIANO PT ONLYPIEZO	0x414BF7C4	M20X140	4	98,3	98,2	100%
114P2	1S-6C-B-B4	CAMPUS FISCIANO PT ONLYPIEZO	0x474BF7C4	M20X140	4	98,3	98,8	101%
Node 1S-6C-D								
C07	1S-6C-D-B1	CAMPUS FISCIANO PT	0xA58612CD	M20X140	4	98,3	98,2	100%
115P2	1S-6C-D-B2	CAMPUS FISCIANO PT ONLYPIEZO	0x4A4BF744	M20X140	4	98,3	97,7	99%
116P2	1S-6C-D-B3	CAMPUS FISCIANO PT ONLYPIEZO	0x424BF784	M20X140	4	98,3	98,5	100%
117P2	1S-6C-D-B4	CAMPUS FISCIANO PT ONLYPIEZO	0x444BF704	M20X140	4	98,3	96,5	98%
Node 1S-6D-C								
C08	1S-6D-C-B3	CAMPUS FISCIANO PT	0x8F1B3952	M20X140	4	98,3	93,1	95%
118P2	1S-6D-C-B1	CAMPUS FISCIANO PT ONLYPIEZO	0x444BF7C4	M20X140	4	98,3	96,4	98%
119P2	1S-6D-C-B2	CAMPUS FISCIANO PT ONLYPIEZO	0x4A4BF7C4	M20X140	4	98,3	99,5	101%
120P2	1S-6D-C-B4	CAMPUS FISCIANO PT ONLYPIEZO	0xD94AF744	M20X140	4	98,3	98,9	101%

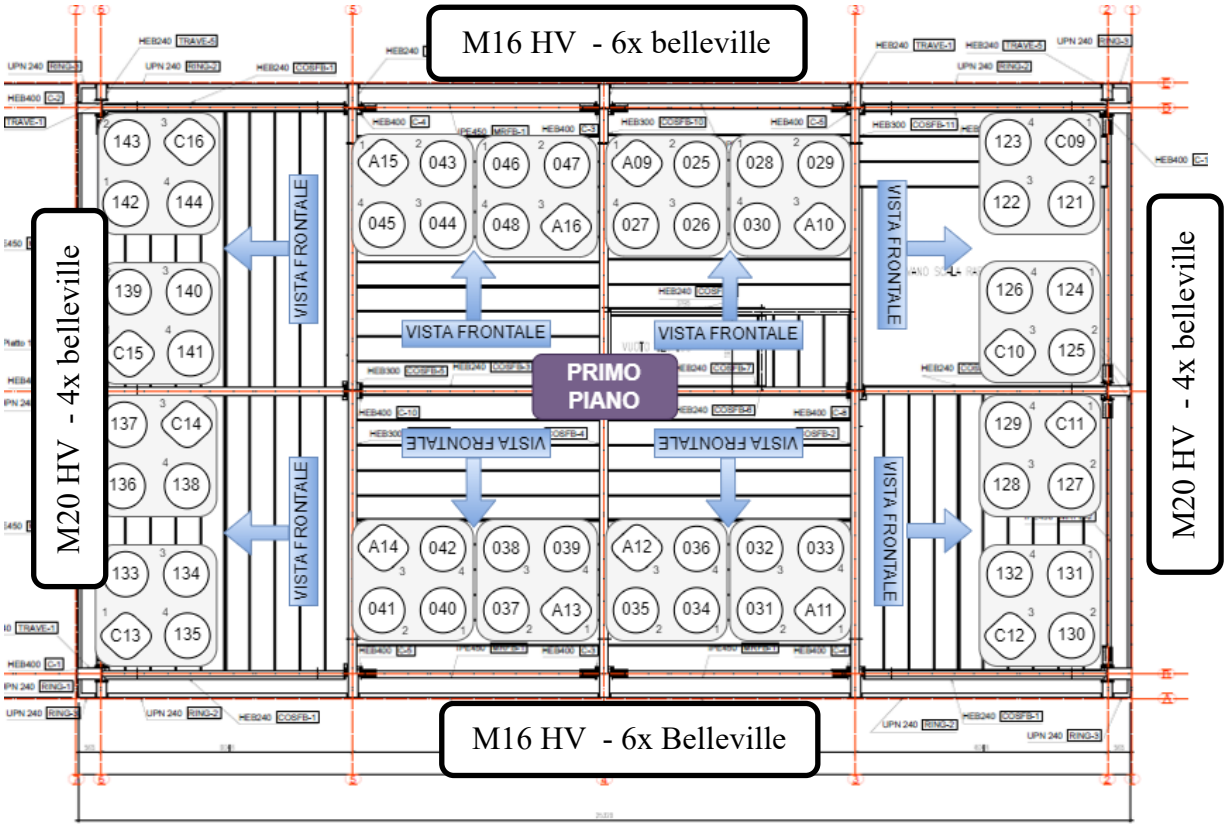

Figure 7.17: *First Floor – sensor ID*

Position	Node	Infrastructure	MAC DEF	Bolt Size	Nr belleville washers	F target	F0 [kN]	F0/ F target [%]
Node 2S-D4-3								
A09	2S-D4-3-B1	CAMPUS FISCIANO P1	0x52E13234	M16X130	6	83,3	83,1	100%
25PT	2S-D4-3-B2	CAMPUS FISCIANO P1 ONLYPIEZO	0xA081D580	M16X125	6	83,3	82,7	99%
26PT	2S-D4-3-B3	CAMPUS FISCIANO P1 ONLYPIEZO	0xA070D540	M16X125	6	83,3	84,1	101%
27PT	2S-D4-3-B4	CAMPUS FISCIANO P1 ONLYPIEZO	0xA0A5D540	M16X125	6	83,3	82	98%
Node 2S-D3-4								
A10	2S-D3-4-B3	CAMPUS FISCIANO P1	0x3AA24186	M16X130	6	83,3	79,8	96%
28PT	2S-D3-4-B1	CAMPUS FISCIANO P1 ONLYPIEZO	0xA042D540	M16X125	6	83,3	85,5	103%
29PT	2S-D3-4-B2	CAMPUS FISCIANO P1 ONLYPIEZO	0x203AD540	M16X125	6	83,3	84,3	101%
30PT	2S-D3-4-B4	CAMPUS FISCIANO P1 ONLYPIEZO	0x2094D580	M16X125	6	83,3	83,5	100%
Node 2S-B3-4								
A11	2S-B3-4-B1	CAMPUS FISCIANO P1	0xB671484B	M16X130	6	83,3	83,6	100%
31PT	2S-B3-4-B2	CAMPUS FISCIANO P1 ONLYPIEZO	0xA090D540	M16X125	6	83,3	81,6	98%
32PT	2S-B3-4-B3	CAMPUS FISCIANO P1 ONLYPIEZO	0xA092D580	M16X125	6	83,3	83,2	100%
33PT	2S-B3-4-B4	CAMPUS FISCIANO P1 ONLYPIEZO	0x209BD540	M16X125	6	83,3	79,9	96%
Node 2S-B4-3								
A12	2S-B4-3-B3	CAMPUS FISCIANO P1	0x6651EB46	M16X130	6	83,3	81,6	98%

34PT	2S-B4-3-B1	CAMPUS FISCIANO P1 ONLYPIEZO	0xA094D580	M16X125	6	83,3	82,9	100%
35PT	2S-B4-3-B2	CAMPUS FISCIANO P1 ONLYPIEZO	0x9DADD580	M16X125	6	83,3	83,1	100%
36PT	2S-B4-3-B4	CAMPUS FISCIANO P1 ONLYPIEZO	0x20A7D540	M16X125	6	83,3	84,4	101%
Node 2S-B4-5								
A13	2S-B4-5-B1	CAMPUS FISCIANO P1	0x2662F6F6	M16X130	6	83,3	80,5	97%
37PT	2S-B4-5-B2	CAMPUS FISCIANO P1 ONLYPIEZO	0xA074D540	M16X125	6	83,3	82,8	99%
38PT	2S-B4-5-B3	CAMPUS FISCIANO P1 ONLYPIEZO	0x1D85D580	M16X125	6	83,3	83,5	100%
39PT	2S-B4-5-B4	CAMPUS FISCIANO P1 ONLYPIEZO	0xA04DD540	M16X125	6	83,3	87,2	105%
Node 2S-B5-4								
A14	2S-B5-4-B3	CAMPUS FISCIANO P1	0x2F08D5E9	M16X130	6	83,3	79,2	95%
40PT	2S-B5-4-B1	CAMPUS FISCIANO P1 ONLYPIEZO	0xA091D580	M16X125	6	83,3	81,6	98%
41PT	2S-B5-4-B2	CAMPUS FISCIANO P1 ONLYPIEZO	0xA088D540	M16X125	6	83,3	84,1	101%
42PT	2S-B5-4-B4	CAMPUS FISCIANO P1 ONLYPIEZO	0xA0B2D580	M16X125	6	83,3	80,5	97%
Node 2S-D5-4								
A15	2S-D5-4-B1	CAMPUS FISCIANO P1	0x9BFC9739	M16X130	6	83,3	79,8	96%
43PT	2S-D5-4-B2	CAMPUS FISCIANO P1 ONLYPIEZO	0xA079D580	M16X125	6	83,3	79,6	96%
44PT	2S-D5-4-B3	CAMPUS FISCIANO P1 ONLYPIEZO	0x20B2D580	M16X125	6	83,3	83,1	100%
45PT	2S-D5-4-B4	CAMPUS FISCIANO P1 ONLYPIEZO	0x5455DEC0	M16X125	6	83,3	81,4	98%
Node 2S-D4-5								
A16	2S-D4-5-B3	CAMPUS FISCIANO P1	0x7161A8FB	M16X130	6	83,3	82,8	99%
46PT	2S-D4-5-B1	CAMPUS FISCIANO P1 ONLYPIEZO	0xA09ED580	M16X125	6	83,3	86,3	104%
47PT	2S-D4-5-B2	CAMPUS FISCIANO P1 ONLYPIEZO	0xA0A2D540	M16X125	6	83,3	80,8	97%
48PT	2S-D4-5-B4	CAMPUS FISCIANO P1 ONLYPIEZO	0xA083D540	M16X125	6	83,3	84,5	101%
Node 2S-2D-C								
C09	2S-2D-C-B1	CAMPUS FISCIANO P1	0x890763B	M20X140	4	98,3	101,2	103%
121P2	2S-2D-C-B2	CAMPUS FISCIANO P1 ONLYPIEZO	0x584BF784	M20X140	4	98,3	97,8	99%
122P2	2S-2D-C-B3	CAMPUS FISCIANO P1 ONLYPIEZO	0xD94AF7C4	M20X140	4	98,3	96,8	98%
123P2	2S-2D-C-B4	CAMPUS FISCIANO P1 ONLYPIEZO	0x574BF744	M20X140	4	98,3	98,3	100%
Node 2S-2C-D								
C10	2S-2C-D-B3	CAMPUS FISCIANO P1	0x6126FA79	M20X140	4	98,3	107	109%
124P2	2S-2C-D-B1	CAMPUS FISCIANO P1 ONLYPIEZO	0x574BF7C4	M20X140	4	98,3	100,9	103%
125P2	2S-2C-D-B2	CAMPUS FISCIANO P1 ONLYPIEZO	0x554BF784	M20X140	4	98,3	96,9	99%
126P2	2S-2C-D-B4	CAMPUS FISCIANO P1 ONLYPIEZO	0xDA4AF7C4	M20X140	4	98,3	98,6	100%
Node 2S-2C-B								
C11	2S-2C-B-B1	CAMPUS FISCIANO P1	0x4CFC6DF7	M20X140	4	98,3	96,3	98%
127P2	2S-2C-B-B2	CAMPUS FISCIANO P1 ONLYPIEZO	0x594BF704	M20X140	4	98,3	96,5	98%
128P2	2S-2C-B-B3	CAMPUS FISCIANO P1 ONLYPIEZO	0xDA4AF784	M20X140	4	98,3	100,5	102%
129P2	2S-2C-B-B4	CAMPUS FISCIANO P1 ONLYPIEZO	0xDA4AF704	M20X140	4	98,3	98,1	100%
Node 2S-2B-C								
C12	2S-2B-C-B3	CAMPUS FISCIANO P1	0xF13038B5	M20X140	4	98,3	99,1	101%
130P2	2S-2B-C-B1	CAMPUS FISCIANO P1 ONLYPIEZO	0x5B4BF7C4	M20X140	4	98,3	99,7	101%
131P2	2S-2B-C-B2	CAMPUS FISCIANO P1 ONLYPIEZO	0x594BF784	M20X140	4	98,3	99,7	101%
132P2	2S-2B-C-B4	CAMPUS FISCIANO P1 ONLYPIEZO	0x564BF744	M20X140	4	98,3	97,9	100%

Node 2S-6B-C								
C13	2S-6B-C-B1	CAMPUS FISCIANO P1	0xF221DF24	M20X140	4	98,3	96,1	98%
133P2	2S-6B-C-B2	CAMPUS FISCIANO P1 ONLYPIEZO	0x594BF744	M20X140	4	98,3	98,5	100%
134P2	2S-6B-C-B3	CAMPUS FISCIANO P1 ONLYPIEZO	0xDC4AF704	M20X140	4	98,3	95	97%

135P2	2S-6B-C-B4	CAMPUS FISCIANO P1 ONLYPIEZO	0x5B4BF784	M20X140	4	98,3	97,3	99%
Node 2S-6C-B								
C14	2S-6C-B-B3	CAMPUS FISCIANO P1	0x46349CDF	M20X140	4	98,3	94,4	96%
136P2	2S-6C-B-B1	CAMPUS FISCIANO P1 ONLYPIEZO	0x5C4BF704	M20X140	4	98,3	96,8	98%
137P2	2S-6C-B-B2	CAMPUS FISCIANO P1 ONLYPIEZO	0x584BF744	M20X140	4	98,3	100,2	102%
138P2	2S-6C-B-B4	CAMPUS FISCIANO P1 ONLYPIEZO	0x564BF784	M20X140	4	98,3	93,5	95%
Node 2S-6C-D								
C15	2S-6C-D-B1	CAMPUS FISCIANO P1	0xBEAD4B2	M20X140	4	98,3	96	98%
139P2	2S-6C-D-B2	CAMPUS FISCIANO P1 ONLYPIEZO	0x554BF7C4	M20X140	4	98,3	102,1	104%
140P2	2S-6C-D-B3	CAMPUS FISCIANO P1 ONLYPIEZO	0x584BF704	M20X140	4	98,3	97,8	99%
141P2	2S-6C-D-B4	CAMPUS FISCIANO P1 ONLYPIEZO	0xDB4AF744	M20X140	4	98,3	96,3	98%
Node 2S-6D-C								
C16	2S-6D-C-B3	CAMPUS FISCIANO P1	0x77399007	M20X140	4	98,3	94,3	96%
142P2	2S-6D-C-B1	CAMPUS FISCIANO P1 ONLYPIEZO	0x5A4BF744	M20X140	4	98,3	99,1	101%
143P2	2S-6D-C-B2	CAMPUS FISCIANO P1 ONLYPIEZO	0x574BF784	M20X140	4	98,3	97,3	99%
144P2	2S-6D-C-B4	CAMPUS FISCIANO P1 ONLYPIEZO	0x594BF7C4	M20X140	4	98,3	95,2	97%

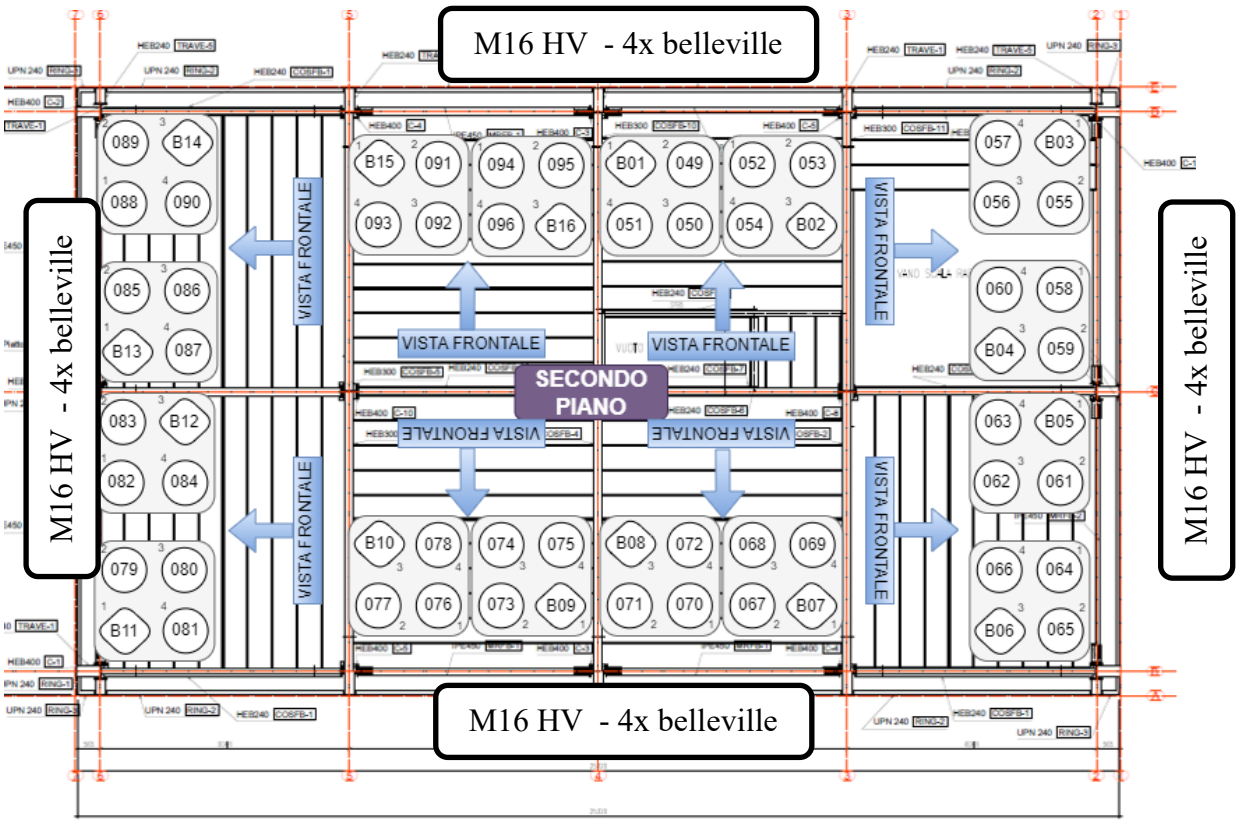

Figure 7.18: *Second Floor – sensor ID*

Position	Node	Infrastructure	MAC DEF	Bolt Size	Nr belleville washers	F target	F0 [kN]	F0/ F target [%]
Node 3S-D4-3								
B01	3S-D4-3-B1	CAMPUS FISCIANO P2	0x44AEEBAD	M16X120	4	69,5	68	98%
49P1	3S-D4-3-B2	CAMPUS FISCIANO P2 ONLYPIEZO	0x209FD580	M16X120	4	69,5	72,5	104%
50P1	3S-D4-3-B3	CAMPUS FISCIANO P2 ONLYPIEZO	0xA087D580	M16X120	4	69,5	69,3	100%
51P1	3S-D4-3-B4	CAMPUS FISCIANO P2 ONLYPIEZO	0xA09FD580	M16X120	4	69,5	65,8	95%
Node 3S-D3-4								
B02	3S-D3-4-B3	CAMPUS FISCIANO P2	0x667DF78E	M16X120	4	69,5	67,9	98%
52P1	3S-D3-4-B1	CAMPUS FISCIANO P2 ONLYPIEZO	0xA073D540	M16X120	4	69,5	70,4	101%
53P1	3S-D3-4-B2	CAMPUS FISCIANO P2 ONLYPIEZO	0xA091D540	M16X120	4	69,5	67,6	97%
54P1	3S-D3-4-B4	CAMPUS FISCIANO P2 ONLYPIEZO	0x2078D540	M16X120	4	69,5	68,5	99%
Node 3S-2D-C								
B03	3S-2D-C-B1	CAMPUS FISCIANO P2	0x84F76B9B	M16X120	4	69,5	66,7	96%
55P1	3S-2D-C-B2	CAMPUS FISCIANO P2 ONLYPIEZO	0x209AD540	M16X120	4	69,5	70,7	102%
56P1	3S-2D-C-B3	CAMPUS FISCIANO P2 ONLYPIEZO	0x207BD580	M16X120	4	69,5	69,3	100%
57P1	3S-2D-C-B4	CAMPUS FISCIANO P2 ONLYPIEZO	0x20A0D580	M16X120	4	69,5	70,6	102%
Node 3S-2C-D								
B04	3S-2C-D-B3	CAMPUS FISCIANO P2	0x666E5AE8	M16X120	4	69,5	66,6	96%
58P1	3S-2C-D-B1	CAMPUS FISCIANO P2 ONLYPIEZO	0xA0B2D540	M16X120	4	69,5	67,4	97%
59P1	3S-2C-D-B2	CAMPUS FISCIANO P2 ONLYPIEZO	0x2095D580	M16X120	4	69,5	68,7	99%

60P1	3S-2C-D-B4	CAMPUS FISCIANO P2 ONLYPIEZO	0x203BD540	M16X120	4	69,5	68,4	98%
Node 3S-2C-B								
B05	3S-2C-B-B1	CAMPUS FISCIANO P2	0xEC27B1C4	M16X120	4	69,5	68,8	99%
61P1	3S-2C-B-B2	CAMPUS FISCIANO P2 ONLYPIEZO	0x2076D540	M16X120	4	69,5	66,6	96%
62P1	3S-2C-B-B3	CAMPUS FISCIANO P2 ONLYPIEZO	0xA0A2D580	M16X120	4	69,5	67,1	97%
63P1	3S-2C-B-B4	CAMPUS FISCIANO P2 ONLYPIEZO	0xA069D540	M16X120	4	69,5	68,8	99%
Node 3S-2B-C								
B06	3S-2B-C-B3	CAMPUS FISCIANO P2	0x9C2DBE2E	M16X120	4	69,5	64,3	93%
64P1	3S-2B-C-B1	CAMPUS FISCIANO P2 ONLYPIEZO	0x2086D580	M16X120	4	69,5	66,9	96%
65P1	3S-2B-C-B2	CAMPUS FISCIANO P2 ONLYPIEZO	0x20A4D540	M16X120	4	69,5	69,4	100%
66P1	3S-2B-C-B4	CAMPUS FISCIANO P2 ONLYPIEZO	0xA09BD580	M16X120	4	69,5	68,6	99%
Node 3S-B3-4								
B07	3S-B3-4-B1	CAMPUS FISCIANO P2	0x201FA18B	M16X120	4	69,5	65,4	94%
67P1	3S-B3-4-B2	CAMPUS FISCIANO P2 ONLYPIEZO	0x20A9D580	M16X120	4	69,5	67,8	98%
68P1	3S-B3-4-B3	CAMPUS FISCIANO P2 ONLYPIEZO	0x20A6D580	M16X120	4	69,5	67,3	97%
69P1	3S-B3-4-B4	CAMPUS FISCIANO P2 ONLYPIEZO	0xA099D540	M16X120	4	69,5	68,8	99%
Node 3S-B4-3								
B08	3S-B4-3-B3	CAMPUS FISCIANO P2	0x3A51E77F	M16X120	4	69,5	66,2	95%
70P1	3S-B4-3-B1	CAMPUS FISCIANO P2 ONLYPIEZO	0xA074D580	M16X120	4	69,5	67,5	97%
71P1	3S-B4-3-B2	CAMPUS FISCIANO P2 ONLYPIEZO	0xA0A0D540	M16X120	4	69,5	67,4	97%
72P1	3S-B4-3-B4	CAMPUS FISCIANO P2 ONLYPIEZO	0x1D9CD580	M16X120	4	69,5	66	95%
Node 3S-B4-5								
B09	3S-B4-5-B1	CAMPUS FISCIANO P2	0x3B5BA1F5	M16X120	4	69,5	66,5	96%
73P1	3S-B4-5-B2	CAMPUS FISCIANO P2 ONLYPIEZO	0xA0B7D580	M16X120	4	69,5	71,9	103%
74P1	3S-B4-5-B3	CAMPUS FISCIANO P2 ONLYPIEZO	0x1DACD580	M16X120	4	69,5	68,3	98%
75P1	3S-B4-5-B4	CAMPUS FISCIANO P2 ONLYPIEZO	0xA04CD540	M16X120	4	69,5	66,8	96%
Node 3S-B5-4								
B10	3S-B5-4-B3	CAMPUS FISCIANO P2	0x4861C215	M16X120	4	69,5	61,8	89%
76P1	3S-B5-4-B1	CAMPUS FISCIANO P2 ONLYPIEZO	0x2077D580	M16X120	4	69,5	68	98%
77P1	3S-B5-4-B2	CAMPUS FISCIANO P2 ONLYPIEZO	0xA08AD580	M16X120	4	69,5	65,9	95%
78P1	3S-B5-4-B4	CAMPUS FISCIANO P2 ONLYPIEZO	0x208DD540	M16X120	4	69,5	68,3	98%
Node 3S-6B-C								
B11	3S-6B-C-B1	CAMPUS FISCIANO P2	0x3BE3A714	M16X120	4	69,5	68,5	99%
79P1	3S-6B-C-B2	CAMPUS FISCIANO P2 ONLYPIEZO	0xA099D580	M16X120	4	69,5	72,3	104%
80P1	3S-6B-C-B3	CAMPUS FISCIANO P2 ONLYPIEZO	0x203CD540	M16X120	4	69,5	69,7	100%
81P1	3S-6B-C-B4	CAMPUS FISCIANO P2 ONLYPIEZO	0x20B6D580	M16X120	4	69,5	70,9	102%
Node 3S-6C-B								
B12	3S-6C-B-B3	CAMPUS FISCIANO P2	0xAD3412B6	M16X120	4	69,5	65	94%
82P1	3S-6C-B-B1	CAMPUS FISCIANO P2 ONLYPIEZO	0xA0A0D580	M16X120	4	69,5	68,2	98%
83P1	3S-6C-B-B2	CAMPUS FISCIANO P2 ONLYPIEZO	0x207BD540	M16X120	4	69,5	69	99%
84P1	3S-6C-B-B4	CAMPUS FISCIANO P2 ONLYPIEZO	0xA0B6D540	M16X120	4	69,5	70,2	101%

Node 3S-6C-D								
B13	3S-6C-D-B1	CAMPUS FISCIANO P2	0xDA915898	M16X120	4	69,5	69,3	100%
85P1	3S-6C-D-B2	CAMPUS FISCIANO P2 ONLYPIEZO	0xA087D540	M16X120	4	69,5	70	101%
86P1	3S-6C-D-B3	CAMPUS FISCIANO P2 ONLYPIEZO	0xA0B0D580	M16X120	4	69,5	71,1	102%
87P1	3S-6C-D-B4	CAMPUS FISCIANO P2 ONLYPIEZO	0xA09DD580	M16X120	4	69,5	71,2	102%
Node 3S-6D-C								

B14	3S-6D-C-B3	CAMPUS FISCIANO P2	0x6EC83961	M16X120	4	69,5	70,8	102%
88P1	3S-6D-C-B1	CAMPUS FISCIANO P2 ONLYPIEZO	0x208BD540	M16X120	4	69,5	69,5	100%
89P1	3S-6D-C-B2	CAMPUS FISCIANO P2 ONLYPIEZO	0x2079D540	M16X120	4	69,5	70,9	102%
90P1	3S-6D-C-B4	CAMPUS FISCIANO P2 ONLYPIEZO	0x204CD540	M16X120	4	69,5	69	99%
Node 3S-D5-4								
B15	3S-D5-4-B1	CAMPUS FISCIANO P2	0x794FF57	M16X120	4	69,5	68,8	99%
91P1	3S-D5-4-B2	CAMPUS FISCIANO P2 ONLYPIEZO	0x204BD540	M16X120	4	69,5	67,5	97%
92P1	3S-D5-4-B3	CAMPUS FISCIANO P2 ONLYPIEZO	0x4F4BF7C4	M16X120	4	69,5	67,9	98%
93P1	3S-D5-4-B4	CAMPUS FISCIANO P2 ONLYPIEZO	0xD44FDEC0	M16X120	4	69,5	65,9	95%
Node 3S-D4-5								
B16	3S-D4-5-B3	CAMPUS FISCIANO P2	0x28DC3D9	M16X120	4	69,5	67,7	97%
94P1	3S-D4-5-B1	CAMPUS FISCIANO P2 ONLYPIEZO	0x484BF784	M16X120	4	69,5	68,5	99%
95P1	3S-D4-5-B2	CAMPUS FISCIANO P2 ONLYPIEZO	0x5445DEC0	M16X120	4	69,5	68	98%
96P1	3S-D4-5-B4	CAMPUS FISCIANO P2 ONLYPIEZO	0x1DAAD580	M16X120	4	69,5	69,1	99%

It has to be reported that during the installation activities and after 12 hours of the tightening operations, it has been assessed a relaxation phenomenon with magnitude 6%-12% of M16 HV bolted joints (+4 Belleville washers) of storey 2: a clamp force controlled recovery has been applied with manual torque wrench tightening.

The mean values of clamping force resulted by the installation activities for the single joint type on the single storey, are summarized in the below table.

It can be assessed the effectiveness of the applied Tokbo technology and the installation strategy, with final clamping force values that are in the range of ±2% of the target.

Storey	**Bolt size + nr Belleville washer**	**F_{target} [kN]**	**F_0 [kN] mean value**	**F_0 / F_{target} [%]**
1S – ground floor	M16 HV + 6x belleville	83,3	84,1	101
	M20 HV + 4x belleville	98,3	97,5	99
2S – first floor	M16 HV + 6x belleville	83,3	82,2	99
	M20 HV + 4x belleville	98,3	98,0	100
3S – second floor	M16 HV + 4x belleville	69,5	68,3	98

Since its activation, the Tokbo monitoring system has performed in line with expectations. The first weeks of operation were focused on validating the communication infrastructure, verifying data quality, and setting initial alert thresholds.

At the time of writing the current report, preliminary data confirm that the clamping forces remain stable, and no significant drift or degradation has been detected. Seasonal temperature variations have been logged and show no negative impact on sensor performance. Inertial data collected during minor events—such as heavy vehicle passage or wind loads—have been useful in validating the dynamic response models of the structure.

One of the most valuable contributions of the system is the creation of a baseline structural fingerprint, against which all future changes will be measured. This capability becomes especially important in the event of seismic activity, as it allows for rapid post-event assessments based on deviations from the baseline.

The monitoring activity carried out under Task 5.3 will continue throughout the operational life of the DREAMERS building. Over time, it is expected that the data collected will support:

- Empirical validation of FREEDAM behavior under real seismic excitations
- Assessment of long-term performance and maintenance needs
- Development of digital twin models for real-time structural diagnostics
- Contribution to the drafting of new design guidelines and Eurocode updates

More broadly, the DREAMERS monitoring system stands as a prototype for future intelligent buildings, where structural components are not only resistant but also self-aware and connected. The integration of cloud computing, sensor networks, and AI into the structural core of buildings marks a turning point in how civil infrastructures will be designed, managed, and maintained in the coming decades.

CHAPTER 8

Life Cycle Assessment of the DREAMERS Building

8.1 INTRODUCTION

This chapter presents the Life Cycle Assessment (LCA) of the building constructed as part of the European pilot project DREAMERS (RFCS-2020-101034015) on the campus of the University of Salerno, Italy.

The LCA has been conducted in accordance with the general framework outlined in ISO 14040:2006 and ISO 14044:2006, as well as the specific guidelines for construction materials, products and buildings provided by EN 15804:2012+A2:2019 and EN 15978:2011, respectively. The assessment focuses on environmental indicators defined in EN 15804:2012+A2:2019, covering environmental impacts, resource use, and waste flows.

The chapter is structured as follows: following this introductory section, the next section presents the background of the adopted LCA model. The subsequent section details the building under study and presents the LCA results, including all relevant assumptions and scenarios. Finally, the chapter concludes with a summary of key findings.

8.2 MODEL FOR LIFE CYCLE ASSESSMENT (LCA)

The LCA is carried out according to the rules for materials, products and buildings provided by EN 15804:2012+A2:2019 and EN 15978:2011, respectively, and the LCA model developed by Gervásio and Dimova (2018), which will be briefly described in the following sections.

8.2.1 Goals and boundaries of LCA

The goal of the LCA is to assess the environmental performance of a building over the respective life cycle. The declared unit for the LCA is simply the building with a respective typology (in this case, an office building), and a reference timespan. However, when the total area of the building is available, the results of the indicators are normalized by such area to allow an easier comparison with other buildings of the same typology and with the same functional unit.

For the scope of the analysis, the LCA model considers the modular concept introduced by CEN TC350 standards for defining the system boundaries of the LCA, which is illustrated in Table

8.1:. All modules are considered, except Modules B1 to B7 due to lack of data. Although the use stage of the building is not considered, a reference period of 50 years is assumed for the LCA.

Table 8.1: *Scope of the LCA*

Product stage			Const. stage		Use stage							End-of-life stage				
A1	A2	A3	A4	A5	B1	B2	B3	B4	B5	B6	B7	C1	C2	C3	C4	D
Raw material supply	Transport	Manufacturing	Transport	Construction	Use	Maintenance	Repair	Replacement	Refurbishment	Operational energy use	Operational water use	Deconstruction	Transport	Waste processing	Disposal	Reuse-recycling-recover
√	√	√	√	√	n.a.	n.a.	n.a.	n.a.	n.a.	n.a.	n.a.	√	√	√	√	√

The information contained in each module of Table 8.1: is the following:

- Modules A1 to A3 – Include the production the building materials and products until the gate of the factory. Data for these modules is usually provided from the Bill of Materials (BoM) of the building;
- Module A4 - Transportation of the materials needed for the foundations and structure of the building, from the production place to the construction site. This information may be based on best guesses or scenarios taking into account the location of the building;
- Module A5 – Use of equipment and machinery for the construction of the foundations and erection of the structure; in this case, the analysis considered the use of excavation equipment and the pumping of concrete at the construction site. It is noted that waste produced during the construction stage was not taken into account;
- Module C1 – C4 – These modules include all relevant data from the decommission of the structural system of the building to the stage in which the end-of-waste state is reached by all the structural materials. This includes the use of equipment and machinery for the deconstruction of the building structure, sorting of materials and transport of the resulting materials to their final destination (further information about the end-of-life stage is provided in section 2.3);
- Module D – This module allocates net benefits and burdens due to the reuse, recycling and recovery of materials. Data for this module should be based on scenarios taking into account the average available technology, current practices and current rates of recycling, reuse and

recovery of materials (likewise, further information about the end-of-life stage is provided in section 2.3).

8.2.2 Environmental indicators

The life cycle assessment of the building entails the core environmental indicators, indicators describing resource use and indicators describing waste categories, which are listed in Table 8.2:, Table 8.3: and Table 8.4:, respectively.

Table 8.2: *Core environmental impact indicators (EN 15804:2012+A2:2019)*

Impact category	Indicator	Unit
Climate Change - total	Global Warming Potential total (GWPt)	kg CO2 eq.
Climate Change, fossil	Global Warming Potential fossil fuels (GWPf)	kg CO2 eq.
Climate Change, biogenic	Global Warming Potential biogenic (GWPb)	kg CO2 eq.
Climate Change, land use and land use change	Global Warming Potential land use and land use change (GWPl	kg CO2 eq.
Ozone depletion	Depletion potential of the stratospheric ozone layer (ODP)	kg CFC-11 eq.
Acidification	Acidification potential, Accumulated Exceedance (AP)	Mole of H+ eq.
Eutrophication, freshwater	Eutrophication potential, fraction of nutrients reaching freshwater end compartment (EPf)	kg P eq.
Eutrophication, marine	Eutrophication potential, fraction of nutrients reaching marine end compartment (EPm)	kg N eq.]
Eutrophication, terrestrial	Eutrophication potential, Accumulated Exceedance (EPt)	[Mole of N eq.
Photochemical ozone formation	Formation potential of tropospheric ozone (POCP)	[kg NMVOC eq.
Depletion of abiotic resources, mineral and metals	Abiotic depletion potential for non-fossil resources (ADPe)	kg Sb eq.
Depletion of abiotic resources, fossils	Abiotic depletion for fossil resources potential (ADPf)	MJ, net calorific value
Water use	Water (user) deprivation potential, deprivation-weighted water consumption (WDP)	m^3 world eq. deprived

Table 8.3: *Indicators describing resource use (EN 15804:2012+A2:2019)*

Indicator	Unit
Use of renewable primary energy excluding renewable primary energy resources used as raw materials	MJ
Use of renewable primary energy resources used as raw materials	MJ
Total use of renewable primary energy resources	MJ
Use of non-renewable primary energy excluding non-renewable primary energy resources used as raw materials	MJ
Use of non-renewable primary energy resources used as raw materials	MJ
Total use of non-renewable primary energy resources	MJ
Net use of fresh water	m^3

Table 8.4: *Environmental information describing waste categories (EN 15804:2012+A2:2019)*

Indicator	Unit
Hazardous waste disposed (HWD)	kg
Non-hazardous waste disposed (NHWD)	kg

Radioactive waste disposed (RWD)	kg

8.2.3 End-of-life stage of buildings

Modules C1-C4 and D

The end-of-life stage includes Modules C1-C4 and D in Table 8.1:. Module C1 includes all processes and activities used on-site for the deconstruction of the building frame. This shall ideally include the use of equipment, supply of fuel and the quantification of other emissions due to the activities performed on-site. When precise data is not available, the values provided in Table 8.5: may be used. These values include the demolition/deconstruction of the foundations for each type of frame. However, in the analysis provided in this report, this stage was not taken into account.

Table 8.5: *Diesel used (in MJ/kg) for the demolition/deconstruction of different structural frames in buildings (Gervásio and Dimova, 2018)*

	Frame to be recycled (in MJ/kg)	Frame to be reuse (in MJ/kg)
Steel frame	0.239	0.432
Concrete frame	0.070	0.061
Wood frame	0.323	0.176

Module C2 includes the transport of the materials resulting from the disassembling of the structure to final disposal or until the end-of-waste state is reached.

Module C3 includes all the processes until the end-of-waste state is reached. Hence, appropriate scenarios should be considered for each material, taking into account additional processes (if applicable) that are needed to further process the materials, until they reach the end-of-waste state.

It is noted that, according to EN 15804, the end-of-life state is reached when:

- ✓ *the recovered material, product or construction element is commonly used for specific purposes;*
- ✓ *a market or demand, identified e.g. by a positive economic value, exists for such a recovered material, product or construction element;*
- ✓ *the recovered material, product or construction element fulfils the technical requirements for the specific purposes and meets the existing legislation and standards applicable to products;*
- ✓ *the use of the recovered material, product or construction element will not lead to overall adverse environmental or human health impacts.*

Module C4, scenarios should be considered which include all the necessary processes or activities that are needed before disposal and the disposal of materials itself.

Finally, Module D allocates net benefits and burdens due to the substitution of primary materials. Hence, scenarios should be considered for each material to enable the quantification of the net benefits. These scenarios should be based on average available technology, current practices and current rates of recycling, reuse and recovering of materials.

The end-of-life formulae in Module D considered for the net impact assessment of materials to be recycled (emissions and resources), is provided from Annex D of EN15804:2012+A2:2019:

$$e_{module\ D1} = \sum_{i} (M_{MR\ out\ i} - M_{MR\ int\ i}) \cdot \left(E_{MR\ after\ EoW\ out\ i} - E_{VMSub\ out\ i} \cdot \left(\frac{Q_{R\ out}}{Q_{sub}} \right)_i \right) \quad (8.1)$$

where;

- $e_{module\ D1}$ – are the net impacts (loads and benefits) related to the export of secondary materials;
- $M_{MR\ out\ i}$ - amount of material exiting the system that will be recovered (recycled and reused) in a subsequent system;
- $M_{MR\ in\ i}$ - amount of input material to the product system that has been recovered (recycled or reused) from a previous system (determined at the system boundary);
- $E_{VM\ sub\ out\ i}$ - specific emissions and resources consumed per unit of analysis arising from acquisition and pre-processing of the primary material, or average input material if primary material is not used, from the cradle to the point of functional equivalence where it would substitute secondary material that would be used in a subsequent system;
- $E_{MR\ after\ EoW\ out\ i}$ - specific emissions and resources consumed per unit of analysis arising from material recovery (recycling and reusing) processes of the previous system after the end-of-waste state;
- $Q_{R\ out\ i}$ - quality of the outgoing recovered material (recycled and reused), i.e. quality of the recycled material at the point of substitution;
- $Q_{sub\ i}$ - quality of the substituted material, i.e. quality of primary material or quality of the average input material if primary material is not used.

The above formulae is adopted to model the End-of-Life (EoL) scenario of steel and concrete, as described in the following sub-sections.

LCA model for recycling and reuse of steel products

When a steel product reaches the end-of-life (EoL) stage, it may be recycled, reused or both. According to the methodology proposed by Worldsteel (2024), the LCI for a steel product that

contains new and refurbished (reuse) components, and that after use may either be recycled or reused, is given by:

$$LCI = \{(1 - R_{u1}Z)X_m + (R_{u1}Z)X_{refurb}\} - \{[(R_2 - R_1 + (R_{u2} - R_{u1}).(R_2^* - R_1^*))X_{sc}] + [(R_{u2} - R_{u1})(X_{inc\_recycling} - X_{refurb})Z]\} \quad (8.2)$$

where, the first part represents the manufacture of the steel product, the second part the net benefit of EoL recycling, and the third part the net benefit of EoL reuse. The terminology used in expression (2) is provided in Table 8.1:.

Table 8.6: *Terminology according to Worldsteel (2024)*

Symbol	Description
X_m	LCI for the manufacture of the original product, which contains primary and secondary steel
X_{re}	LCI for 100% secondary steel production from scrap in the EAF, assuming 100% scrap input
X_{pr}	LCI for theoretical 100% primary steel production, from the BOF route, assuming 0% scrap input
X_{sc}	LCI of scrap either as an input or an output
X_{refurb}	LCI for 100% refurbishment for reuse or remanufacture of a steel product
$X_{inc\ recycling}$	Cradle-to-gate LCI, including the end-of-life impacts of recycling, for a product which is suitable for reuse or remanufacture.
Y	The process yield of the EAF process.
Z	The yield of the refurbishment process relating to reuse or remanufacture.
R_1	The amount of scrap used in the steelmaking process to make a specific product (defined as S in Fig 8.1).
R_2	The fraction of steel recovered as scrap after the lifetime of a steel product (defined as RR in Fig 8.1).
R_{u1}	The amount of a previously used product that is taken as an input to the reused or remanufactured product
R_{u2}	The fraction of steel recovered during the lifetime of a steel product, including end-of-life, that is either reused or remanufactured rather than recycled
R^*_1	The amount of scrap, used in the steelmaking process, which is used in the manufacture of the product which is reused or remanufactured.
R^*_2	The fraction of steel recovered as scrap after the product is no longer suitable for reuse or remanufacture. This includes any scrap that is generated during the refurbishment or remanufacturing process.

In expression (8.2), $X_{inc\_recycling}$ is given by:

$$X_{inc\_recycling} = X_m - (R_2^* - R_1^*)X_{sc} \quad (8.3)$$

Hence, replacing expression (8.3) in (8.2), leads to the following simplified expression:

$$LCI = \{(1 - R_{u1}Z)X_m + (R_{u1}Z)X_{refurb}\} - \{[(R_2 - R_1)X_{sc}] + [(R_{u2} - R_{u1})(X_m - X_{refurb})Z]\} \quad (8.4)$$

It is noted that the recycling credit (X_{sc}) is given by

$$X_{sc} = (X_{pr} - X_{re})Y \quad (8.5)$$

Expression (8.4) is adopted in the LCA model described in the following paragraphs, which applies to all types of steel products, and includes all processes indicated in Fig. 8.1, except the construction and use stage.

In this model, it is assumed that after the demolition process, steel scrap (RR) is recycled and/or reused (R_2), and the resulting steel is used in the construction of steel structures. Thus, credits are considered for the production of new steel. It is observed that expression (8.2) is consistent with expression (8.1), where only net credits are allocated to Module D. Furthermore, the allocation procedure in Module D, described by expression (8.1), considers a quality ratio between outgoing recovered material (recycled and reused) and the substituted material ($\frac{Q_{R\,out}}{Q_{sub}}$). In this case, this ratio was considered as 1 for both cases. In addition, yield factors (Y and Z) are introduced in Module D, representing the efficiency of the recycling and reuse processes, respectively. Likewise, in the following calculation, it is assumed that both factors are 1.

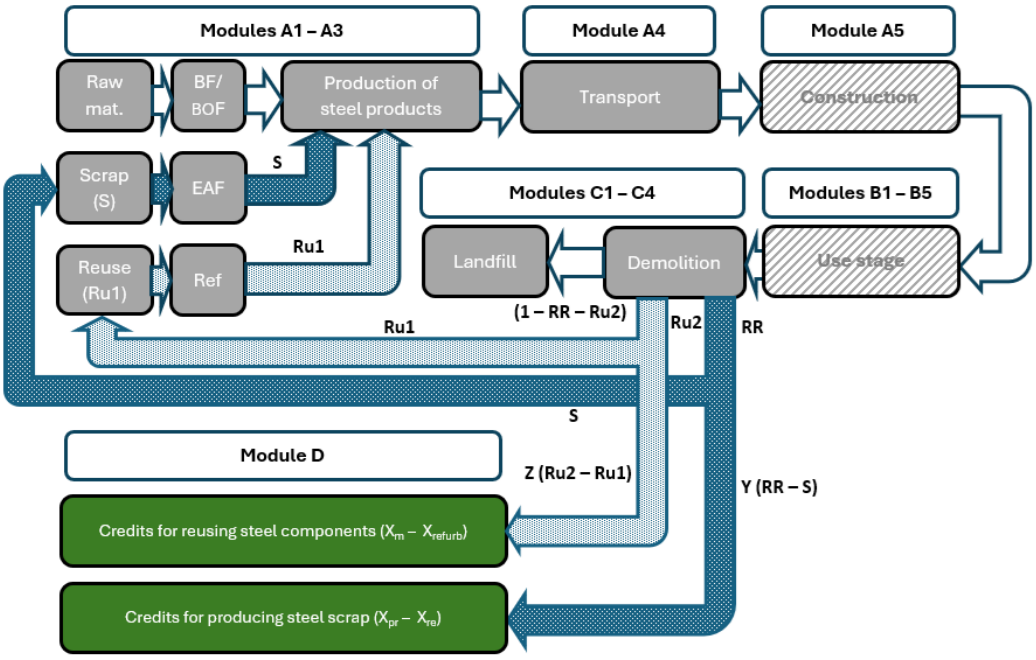

***Figure 8.1**. Model for the LCA of steel products.*

LCA model for recycling of concrete

A base scenario is also defined for the life cycle analysis of concrete. The life cycle model includes all processes indicated in Fig. 8.2, except the process of construction and all processes in the use stage.

In this case, it is assumed that, at the end-of-life stage, concrete is downcycled and the resulting recycled aggregates are used for road construction or backfilling. Thus, credits are considered for the avoided extraction of natural materials typically used for backfilling. The value-corrected values to represent the different between the two functional equivalents, the ratio $\frac{Q_{R\ out}}{Q_{sub}}$, takes this downcycling into consideration. The default parameters considered for this scenario are indicated in Table 8.7.

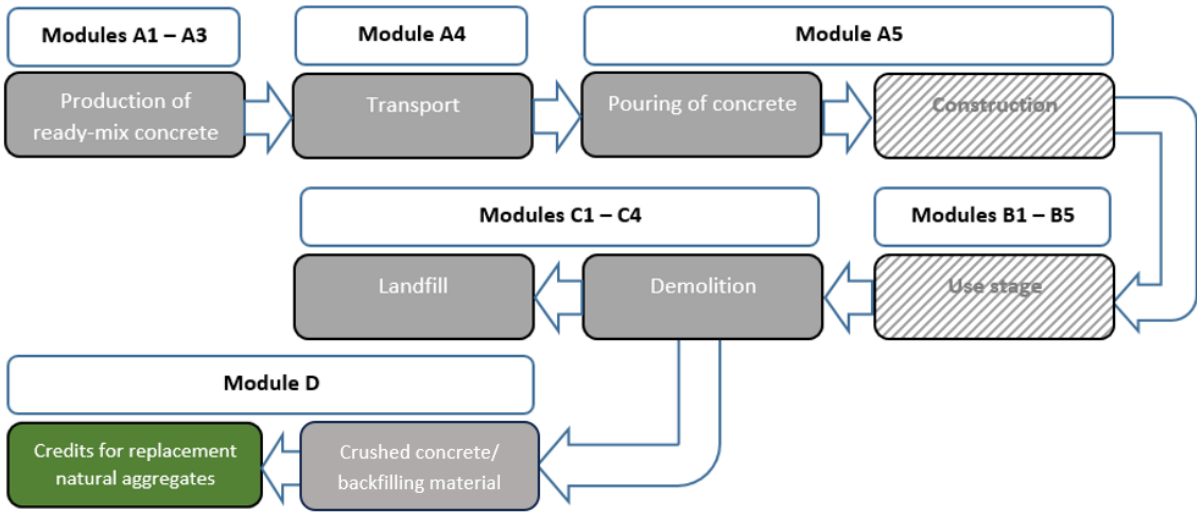

Figure 8.2. *Model for the LCA of concrete products*

Table 8.7: *Reference values of the basic parameters*

Parameter	Basic value
Distances in C2	50 km
Recycling rate (RR)	70%
Value-corrected ratio ($Q_{R\ out}/Q_{Sub}$)	0.50

8.3 LCA OF DREAMERS' BUILDING

8.3.1 Description of the building

The pilot building is situated on the campus of the University of Salerno, in Italy. Designed to accommodate offices and classrooms, it comprises two above-ground floors and a basement level designated for parking. The structure features a rectangular footprint measuring about 14.8 m by 25.4 m, with an overall height of approximately 11.9 m, as shown in Fig. 8.3. Each floor covers a surface area of roughly 376 m^2.

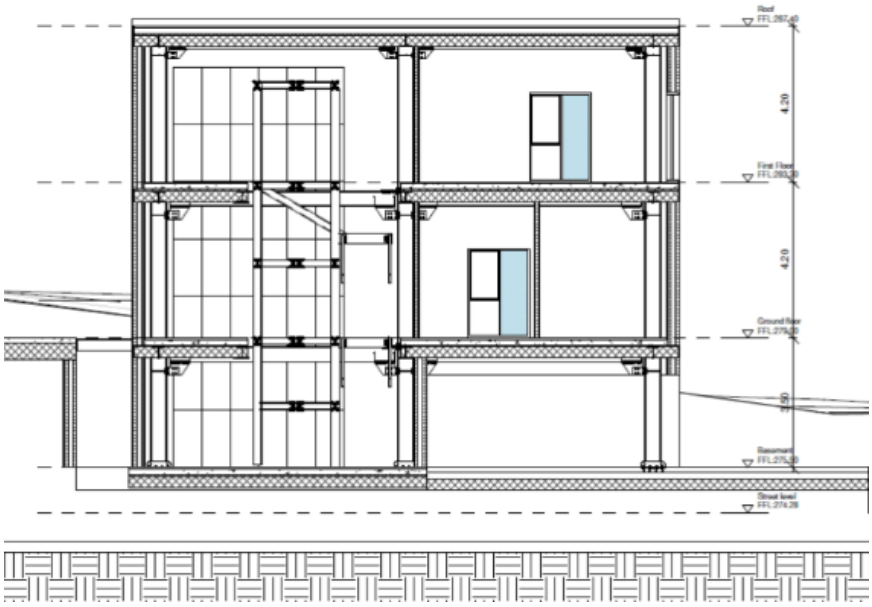

***Figure 8.3**: Cross-view of the building.*

The ground floor, illustrated in Fig. 8.4, will be used for a car park and for the technical plants equipments.

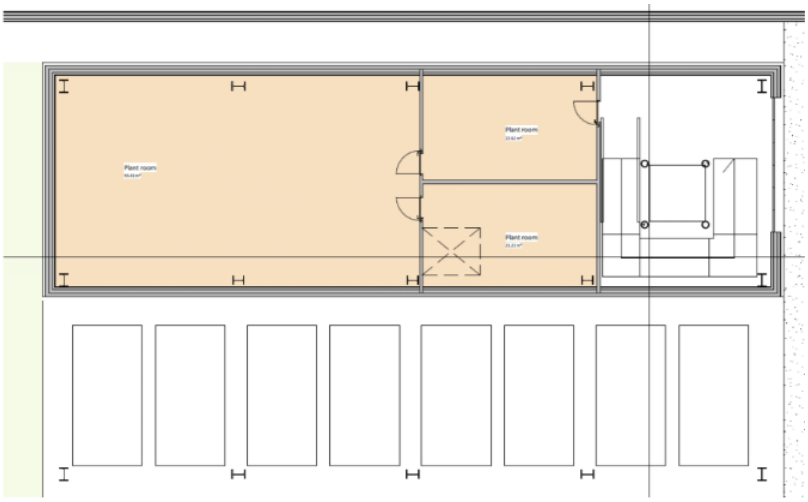

***Figure 8.4:** Ground floor*

The building has wide internal spaces that allow flexible use of the areas as lecture rooms or open space offices (Fig. 8.5 and 8.6).

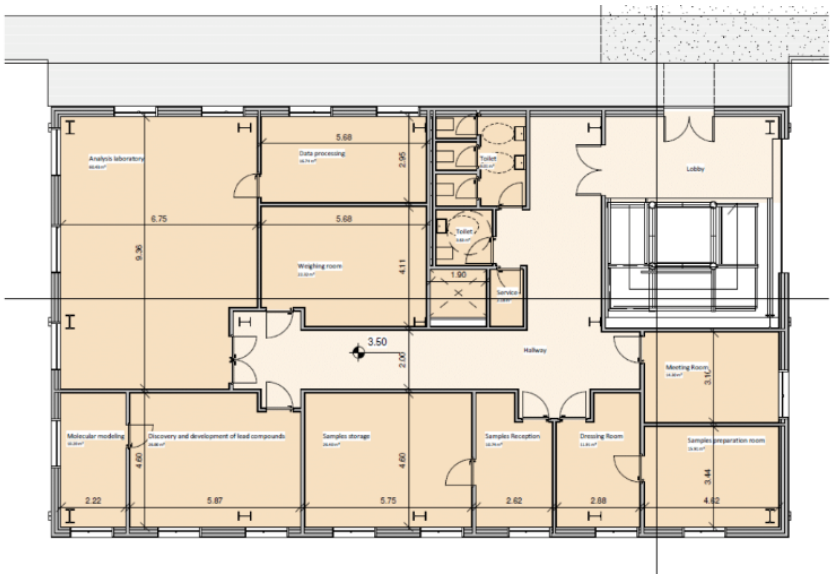

Figure 8.5: *Plan of the first floor*

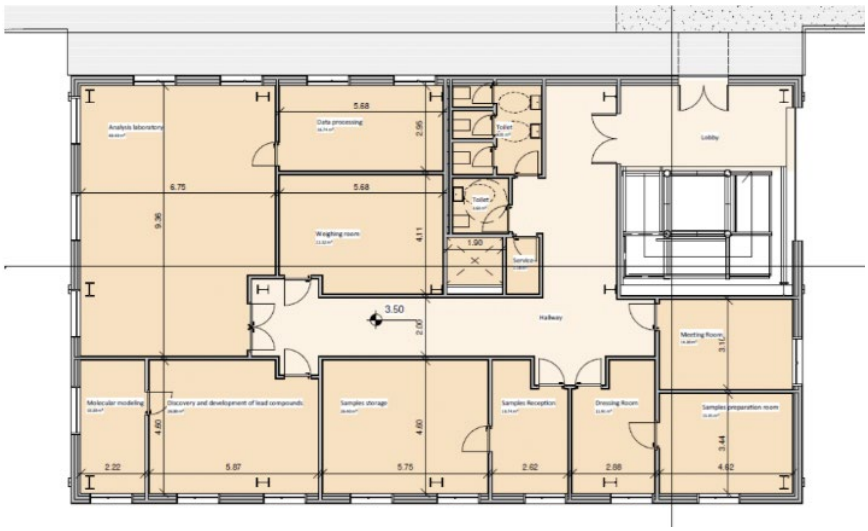

Figure 8.6. *Plan of the second floor*

The load-bearing structure is composed of hot rolled steel sections (HEB profiles) and slim composite floors belonging to the system commercialized by Arcelor Mittal (COFRADAL). This type of floor provides several technical advantages, and it is particularly suitable for medium-long spans, such as those adopted in the building. In addition, this floor system is compact, thus allowing for the maximization of the internal spaces of the building. The seismic-resistant part of the structure will be constructed, adopting three moment resisting frames (MRFs) bays in the -x direction and five MRFs bays in the -y direction, as illustrated in Fig. 8.4 – 8.6. The overall weight of the load-bearing steel structure is about 98 tons.

The LCA of the building is focused on the structure of the building, including foundations, the envelope of the building and internal walls. The Bill of Materials (BoM) considered in the LCA is indicated in Table 8.8:.

Table 8.8: *BoM of the office building*

Item	Unit	Quantity
Structural Work		
Excavation of earth	m^3	8816
Transport of earth (10 km)	m^3	5313.14
Foundations		
Concrete C20/25	m^3	144.61
Concrete C25/30	m^3	435.8
Reinforcement steel	kg	41818.85
Formwork for concrete structures	m^2	1055.74
Main structure		
Structural Steel sections (IPE, HEB,….)	kg	94706.78
Structural Hollow Steel sections	kg	2354.77
Concrete C32/40	m^3	146.35
Reinforcement steel	kg	2242.17
Formwork for concrete structures	m^2	255.01
COFRADAL deck	m^2	1076.47
Architecture		
External walls (AQUAPANEL), KNAUF	m^2	491.95
Rock wool (external walls)	m^2	619.42
Steel profiles (U – 90 x 30 x 0.55) – internal walls	kg	355.43
Steel profiles (U – 90 x 40 x 0.60) – internal walls	kg	1255.55
Rock wool (internal walls)	m^2	988.16
Plasterboard	m^2	784.03
Cement screed (2 cm)	m^2	375.92
Expanded polystyre	m^3	63.91
Primer coat	m^2	375.92
Vapour barrier in polyethylene (0.4 mm)	m^2	400
Vapour barrier in polyethylene (0.4 mm)	m^2	472.4
Membrane with polyester	m^2	848.32
Synthetic waterproofing membrane	m^2	472.4

8.3.2 Data and assumptions for the LCA

Environmental data

The environmental data considered for the analysis were taken from the generic database of 'LCA for Experts (GaBi)' software (version 10.7.1.28), except for the external walls. In this case, an EPD (EPD-KNQ-20240283-IBB1-EN) was considered for the AQUAPANEL system adopted in the building.

The environmental generic datasets considered for steel products are described in Table 8.9:.

Table 8.9: *Environmental datasets from GaBi for steel products.*

Item	Description	Observations
Reinforcement steel for concrete	Steel rebar [worldsteel 2022]	
IPE, HEB and other profiles	Steel sections [worldsteel 2022]	
Light gauge steel framing	Steel hot-dip galvanized (worldsteel)	Cold rolled coil with a molten zinc bath

Sensitivity analysis: end-of-life and low carbon emission steel

Three different scenarios are adopted for the LCA of the building, as illustrated in Fig. 8.7 and indicated in Table 8.10:. The first and second scenarios focus on the end-of-life stage, while the third scenario focuses on the production stage. Moreover, the differences between the three scenarios focused on steel products; the scenarios for all other materials remain unchanged. In addition, the distances considered in modules A4 and C2 were assumed as 100 km and 50 km, respectively, for steel products.

In the first scenario, the recycling rates (RR) and reuse rates (R_2) considered for steel products depend on the application of the material and ease of access. The rates considered in the LCA of each steel product, except steel rebars, are indicated in Table 8.11:, according to Annex H (default rates of reuse, recycling and losses) of prEN17662:2021.

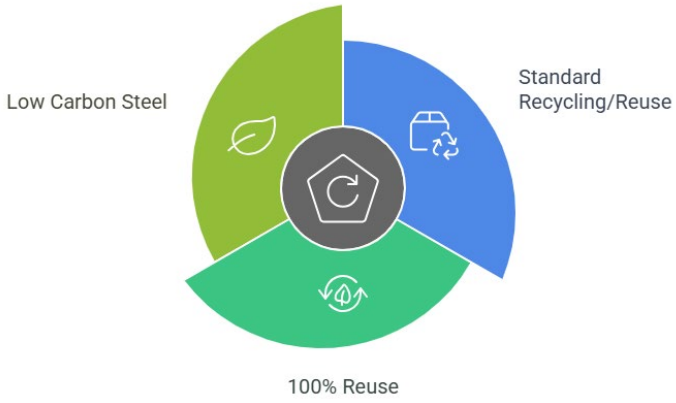

Figure 8.7: *End-of-life scenarios for the building.*

The second scenario considers the 100% reuse of the steel load-bearing structure, while for the other steel products, the recycling/reuse rates from scenario 1 remain unchanged.

Table 8.10: *End-of-life scenarios*

Scenario		Reuse	Recycling	Landfill
1 (base scenario)	Steel products	From Table 8.11:	From Table 8.11:	From Table 8.11:
	Concrete	0 %	70%	30%

2	Steel profiles (IPE, HEB, …)	100 %	0 %	0 %
	Other steel products	From Table 8.11:	From Table 8.11:	From Table 8.11:
	Concrete	0 %	70%	30%
3	Steel products (considering low carbon emission steels)	From Table 8.12:	From Table 8.12:	From Table 8.12:
	Concrete	0 %	70%	30%

The third scenario involves the use of low-carbon emission steels for all types of steel products—this approach was, in fact, implemented in the DREAMERS building. In this case, Environmental Product Declarations (EPDs) were used for all steel products, with the end-of-life scenarios defined according to the specifications provided in each EPD. It is important to note that the original environmental product declaration for hot rolled steel sections and steel rebars aligns with EN15804+A1. The LCA model for these EPDs was reassessed using the EN15804+A2 life cycle impact assessment method (EF 3.1) to ensure compatibility between the environmental indicators and characterization factors used.

The EPDs considered for each steel product are indicated in Table 8.12:, together with the EoL scenarios.

Table 8.11: *Default rates of reuse, recycling and losses according to prEN 17662:2021 – Annex H*

Product	Reuse	Recycling	Landfill
Structural sections/tubes	7 %	93 %	0 %
Light structural steel	5 %	93 %	2 %
Metal floor decking	6 %	79 %	15 %
Profile steel cladding	10 %	89 %	1 %
Rebar (in concrete superstructures)	0 %	70 % (*)	30 %
Rebar (in concrete sub-structure or foundations)	0 %	70 % (*)	30 %

(*) For steel rebars, a recycling rate of 70% was assumed

Table 8.12: *EPDs considered for steel products*

Steel products	EPD	EoL scenario
Structural steel sections	EPD-ARC-20210132-CBB1-EN - XCarb	Recycling – 88%, Reuse – 11%
Sutructural Hollow sections	S-P-09773	Recycling – 93%, Reuse – 7%
Rebar	EPD-ARC-20210245-CBA1-EN - XCarb	Recycling – 90%, Landfilling – 10%
Cold formed sections	S-P-11266	Recycling – 98%, Landfilling – 2%

The end-of-life scenarios considered for other materials, rather than steel products, are indicated in Table 8.13:. In addition, the distances considered in modules A4 and C2 were assumed as 40 km and 30 km, respectively, for all other materials.

Table 8.13: *Scenarios considered for the other materials at the end-of-life cycle stage.*

	Scenarios
Plaster boards	Incineration with an incineration rate of 80%
Insulation materials	Incineration with an incineration rate of 80%
Other materials	Disposal

8.4 RESULTS OF THE LCA

Scenario 1

Taking the above data and assumptions, the results of the life cycle impact assessment (LCIA) results are provided in Table 8.14:.

Table 8.14: *Indicators describing environmental problems of the mid-rise building (scenario 1).*

	A1-A3	A4-A5	C1	C2	C3	C4	D1.1	D1.2
Climate Change - total [kg CO2 eq.]	5.12E+05	1.80E+04	4.88E+00	7.56E+03	3.79E+03	1.03E+04	-7.57E+04	-2.33E+04
Climate Change, fossil [kg CO2 eq.]	5.38E+05	1.80E+04	4.84E+00	7.60E+03	3.80E+03	1.06E+04	-7.60E+04	-2.34E+04
Climate Change, biogenic [kg CO2 eq.]	-2.63E+04	-1.44E+02	-7.77E-03	-1.12E+02	-3.93E+01	-3.58E+02	2.16E+02	4.75E+01
Climate Change, land use & land change [kg CO2 eq.]	1.86E+02	1.31E+02	4.37E-02	7.04E+01	2.91E+01	3.38E+01	1.39E+01	-2.84E+00
Ozone depletion [kg CFC-11 eq.]	6.07E-07	1.07E-08	7.38E-13	6.76E-10	6.47E-09	2.75E-08	3.20E-08	-2.96E-09
Acidification [Mole of H+ eq.]	1.36E+03	9.63E+01	2.47E-02	2.61E+01	2.02E+01	7.65E+01	-1.80E+02	-5.25E+01
Eutrophication, freshwater [kg P eq.]	4.25E-01	5.28E-02	1.73E-05	2.76E-02	1.32E-02	2.16E-02	-1.53E-02	-7.81E-03
Eutrophication, marine [kg N eq.]	2.92E+02	4.63E+01	1.17E-02	1.21E+01	9.26E+00	1.98E+01	-2.93E+01	-1.01E+01
Eutrophication, terrestrial [Mole of N eq.]	3.72E+03	5.12E+02	1.28E-01	1.35E+02	1.02E+02	2.18E+02	-2.77E+02	-1.02E+02
Photochemical ozone formation, human health [kg NMVOC eq.]	9.53E+02	1.09E+02	3.24E-02	2.36E+01	2.51E+01	5.97E+01	-1.19E+02	-3.91E+01
Resource use, mineral and metals [kg Sb eq.]	-6.34E-01	1.27E-03	3.18E-07	4.93E-04	4.14E-03	5.03E-04	-2.87E-01	-1.32E-02
Resource use, fossils [MJ]	4.91E+06	2.47E+05	6.49E+01	1.03E+05	7.61E+04	1.44E+05	-9.70E+05	-2.54E+05
Water use [m³ world equiv.]	8.69E+04	2.40E+02	5.95E-02	8.70E+01	7.52E+02	1.18E+03	-9.73E+03	-3.11E+03

The results of the indicator ‘Climate change - total’, in kg CO_2 eq., are illustrated in Fig. 8.8, per stage. In addition, considering the normalization of the above values by total area of the building (A = 1128 m^2), the results are provided in Fig. 8.9.

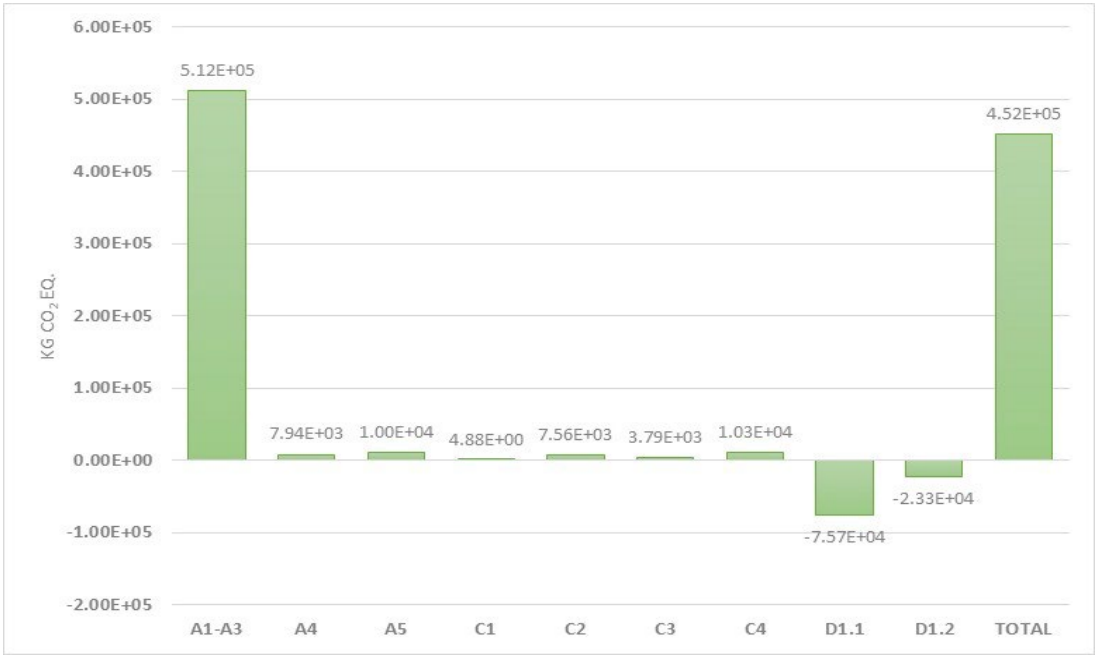

Figure 8.8: *Climate change (total) of the office building (scenario 1).*

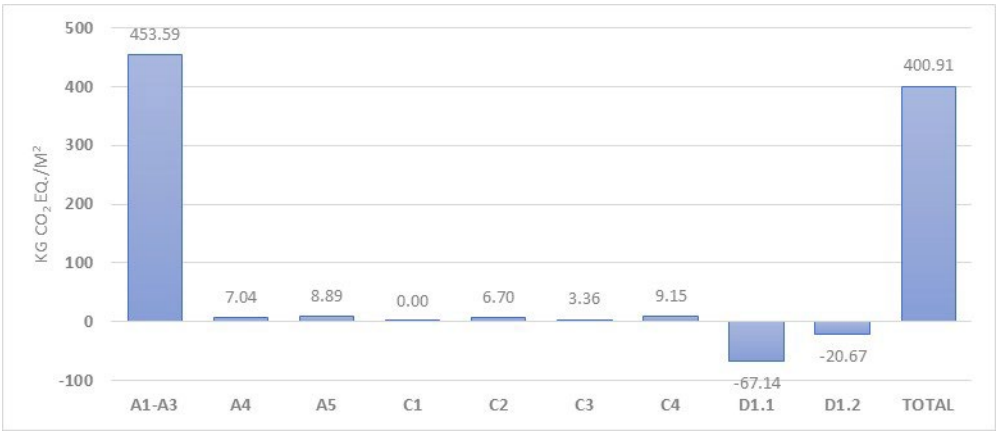

Figure 8.9: *Climate change of the mid-rise building, per area of the building (scenario 1).*

The LCIA results for the indicators describing resource use and waste categories are provided in Table 8.15:.

Table 8.15: *Indicators describing resource use and waste categories (scenario 1).*

	A1-A3	A4-A5	C1	C2	C3	C4	D1.1	D1.2
Total use of renewable primary energy resources (PERT) [MJ]	8.59E+05	2.17E+04	4.74E+00	7.31E+03	7.08E+03	2.35E+04	-6.28E+03	-6.99E+03
Total use of non-renewable primary energy resources (PENRT) [MJ]	4.91E+06	2.47E+05	6.54E+01	1.03E+05	7.63E+04	1.44E+05	-9.70E+05	-2.54E+05
Use of net fresh water (FW) [m3]	1.87E+04	2.07E+01	1.65E-02	7.94E+00	2.17E+01	3.63E+01	-6.78E+03	-1.65E+03
Hazardous waste disposed (HWD) [kg]	-1.01E-02	9.93E-08	3.35E-10	4.24E-07	-1.98E-07	3.84E-06	-3.51E-03	-1.53E-04
Non-hazardous waste disposed (NHWD) [kg]	8.50E+04	4.14E+01	1.01E-02	1.49E+01	2.01E+01	7.19E+05	7.27E+03	1.11E+03
Radioactive waste disposed (RWD) [kg]	5.98E+01	1.77E+00	1.27E-04	1.35E-01	1.02E+00	1.64E+00	-4.60E+00	9.95E-03

The LCIA results for the total use of non-renewable primary energy resources, in MJ/m², are provided in Fig. 8.10.

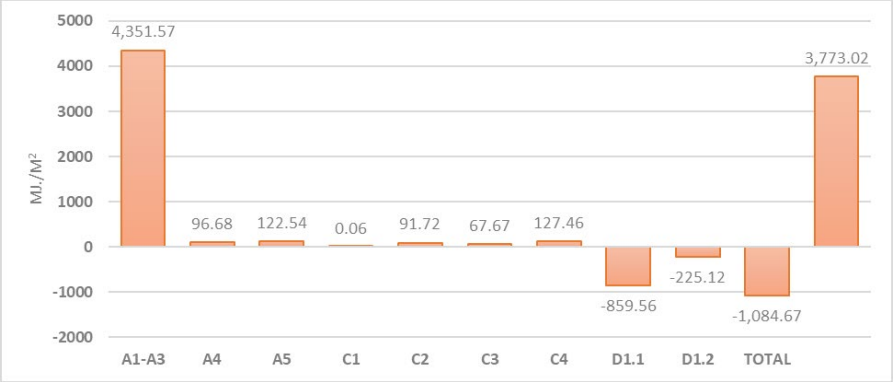

Figure 8.10: *Total use of non-renewable primary energy resources, per area of the building (scenario 1).*

Scenario 2

The results of the LCIA are provided in Table 8.16: for scenario 2.

Table 8.16: *Indicators describing environmental problems of the office building (scenario 2).*

	A1-A3	A4-A5	C1	C2	C3	C4	D1.1	D1.2
Climate Change - total [kg CO2 eq.]	5.12E+05	1.80E+04	4.88E+00	7.56E+03	3.79E+03	1.03E+04	8.01E+04	-2.84E+05
Climate Change, fossil [kg CO2 eq.]	5.38E+05	1.80E+04	4.84E+00	7.60E+03	3.80E+03	1.06E+04	8.08E+04	-2.84E+05
Climate Change, biogenic [kg CO2 eq.]	-2.63E+04	-1.44E+02	-7.77E-03	-1.12E+02	-3.93E+01	-3.58E+02	-7.08E+02	6.47E+02
Climate Change, land use & land change [kg CO2 eq.]	1.86E+02	1.31E+02	4.37E-02	7.04E+01	2.91E+01	3.38E+01	3.48E+01	-3.30E+01
Ozone depletion [kg CFC-11 eq.]	6.07E-07	1.07E-08	7.38E-13	6.76E-10	6.47E-09	2.75E-08	-1.78E-07	-5.16E-08
Acidification [Mole of H+ eq.]	1.36E+03	9.63E+01	2.47E-02	2.61E+01	2.02E+01	7.65E+01	2.04E+02	-6.33E+02
Eutrophication, freshwater [kg P eq.]	4.25E-01	5.28E-02	1.73E-05	2.76E-02	1.32E-02	2.16E-02	2.12E-02	-9.28E-02
Eutrophication, marine [kg N eq.]	2.92E+02	4.63E+01	1.17E-02	1.21E+01	9.26E+00	1.98E+01	3.23E+01	-1.20E+02
Eutrophication, terrestrial [Mole of N eq.]	3.72E+03	5.12E+02	1.28E-01	1.35E+02	1.02E+02	2.18E+02	2.75E+02	-1.20E+03
Photochemical ozone formation, human health [kg NMVOC eq.]	9.53E+02	1.09E+02	3.24E-02	2.36E+01	2.51E+01	5.97E+01	1.31E+02	-4.63E+02
Resource use, mineral and metals [kg Sb eq.]	-6.34E-01	1.27E-03	3.18E-07	4.93E-04	4.14E-03	5.03E-04	6.01E-01	-1.42E-01
Resource use, fossils [MJ]	4.91E+06	2.47E+05	6.49E+01	1.03E+05	7.61E+04	1.44E+05	5.89E+05	-3.07E+06
Water use [m³ world equiv.]	8.69E+04	2.40E+02	5.95E-02	8.70E+01	7.52E+02	1.18E+03	8.52E+02	-4.54E+04

The results of the indicator 'Climate change - total', in kg CO_2 eq., are illustrated in Fig. 8.11, per stage.

Figure 8.11: *Climate change (total) of the office building (scenario 2).*

In addition, considering the total area of the building (A = 1128 m^2), the results are provided in Fig. 8.12.

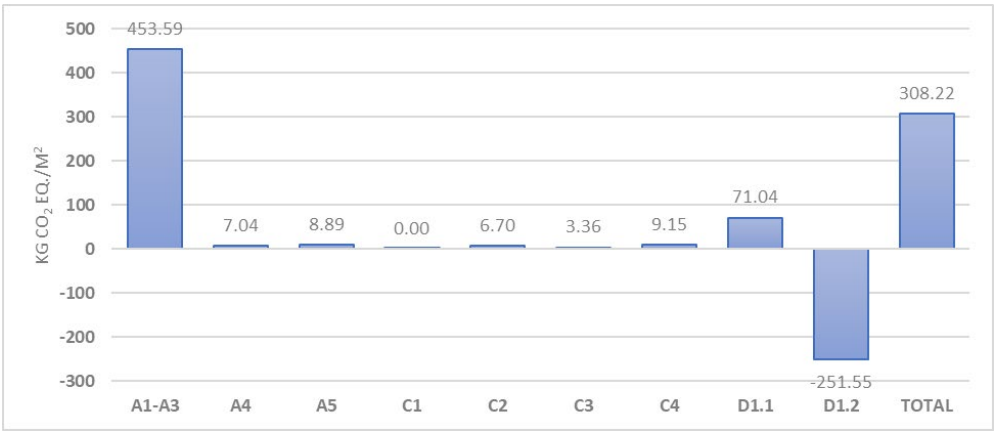

Figure 8.12: *Climate change of the mid-rise building, per area of the building (scenario 2).*

The LCIA results for the indicators describing resource use and waste categories are provided in Table 8.15:.

Table 8.17: *Indicators describing resource use and waste categories (scenario 1).*

	A1-A3	A4-A5	C1	C2	C3	C4	D1.1	D1.2
Total use of renewable primary energy resources (PERT) [MJ]	8.59E+05	2.17E+04	4.74E+00	7.31E+03	7.08E+03	2.35E+04	-6.78E+04	-9.47E+04
Total use of non-renewable primary energy resources (PENRT) [MJ]	4.91E+06	2.47E+05	6.54E+01	1.03E+05	7.63E+04	1.44E+05	5.89E+05	-3.07E+06
Use of net fresh water (FW) [m3]	1.87E+04	2.07E+01	1.65E-02	7.94E+00	2.17E+01	3.63E+01	9.07E+03	-2.30E+04
Hazardous waste disposed (HWD) [kg]	-1.01E-02	9.93E-08	3.35E-10	4.24E-07	-1.98E-07	3.84E-06	8.15E-03	-1.70E-03

Non-hazardous waste disposed (NHWD) [kg]	8.50E+04	4.14E+01	1.01E-02	1.49E+01	2.01E+01	7.19E+05	-1.16E+04	1.53E+04
Radioactive waste disposed (RWD) [kg]	5.98E+01	1.77E+00	1.27E-04	1.35E-01	1.02E+00	1.64E+00	-4.77E+00	1.35E-01

The LCIA results for the total use of non-renewable primary energy resources, in MJ/m^2, are provided in Fig. 8.13 for scenario 2.

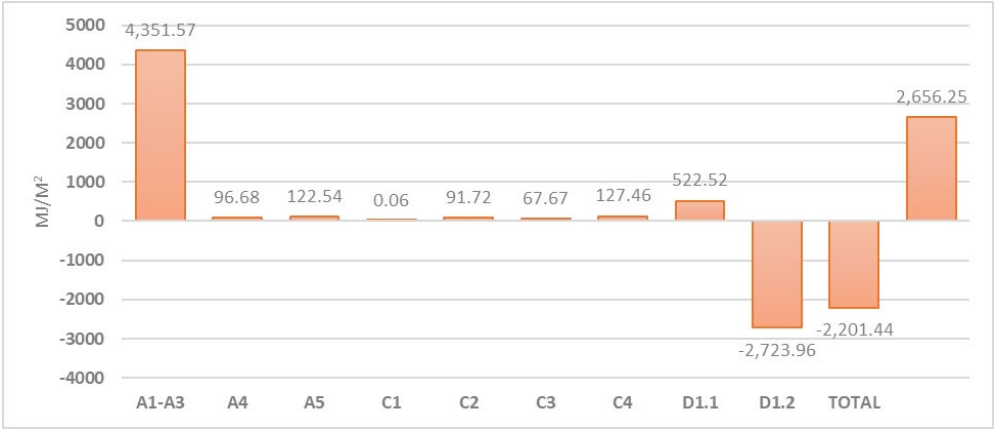

Figure 8.13: *Total use of non-renewable primary energy resources, per area of the building (scenario 2).*

Scenario 3

In case of scenario 3, the results of the LCA are provided in Table 8.18:.

Table 8.18: *Indicators describing environmental problems of the office building (scenario 3).*

	A1-A3	A4-A5	C1	C2	C3	C4	D1.1	D1.2
Climate Change - total [kg CO2 eq.]	3.26E+05	1.78E+04	1.72E+02	7.59E+03	4.00E+03	1.02E+04	-2.72E+04	-3.32E+03
Climate Change, fossil [kg CO2 eq.]	3.49E+05	1.78E+04	4.54E+00	7.53E+03	4.00E+03	1.05E+04	-2.72E+04	-3.32E+03
Climate Change, biogenic [kg CO2 eq.]	-2.63E+04	-1.40E+02	1.47E+00	-1.10E+02	-3.81E+01	-3.58E+02	9.87E+00	2.13E+00
Climate Change, land use & land change [kg CO2 eq.]	2.98E+03	1.30E+02	1.68E+02	1.74E+02	3.46E+01	3.36E+01	2.15E+01	-5.09E-01
Ozone depletion [kg CFC-11 eq.]	7.53E-05	1.07E-08	6.18E-11	6.77E-10	9.60E-09	2.71E-08	-3.63E-09	6.24E-10
Acidification [Mole of H+ eq.]	9.61E+02	9.61E+01	1.08E+00	2.68E+01	2.07E+01	7.54E+01	-5.50E+01	-7.87E+00
Eutrophication, freshwater [kg P eq.]	1.13E+00	5.24E-02	6.12E-04	2.78E-02	1.39E-02	2.14E-02	-1.59E-03	-1.26E-03
Eutrophication, marine [kg N eq.]	2.19E+02	4.62E+01	5.25E-01	1.24E+01	9.41E+00	1.95E+01	-8.64E+00	-1.63E+00
Eutrophication, terrestrial [Mole of N eq.]	2.95E+03	5.11E+02	5.83E+00	1.39E+02	1.04E+02	2.14E+02	-8.07E+01	-1.73E+01
Photochemical ozone formation, human health [kg NMVOC eq.]	6.64E+02	1.09E+02	1.03E+00	2.42E+01	2.55E+01	5.88E+01	-3.90E+01	-6.43E+00
Resource use, mineral and metals [kg Sb eq.]	4.59E-01	1.26E-03	1.13E-05	4.96E-04	4.18E-03	4.95E-04	-1.00E-01	-3.11E-03
Resource use, fossils [MJ]	2.70E+06	2.45E+05	2.37E+03	1.04E+05	8.01E+04	1.42E+05	-4.48E+05	-3.73E+04
Water use [m^3 world equiv.]	3.67E+04	2.39E+02	2.53E+00	8.79E+01	7.94E+02	1.17E+03	-3.15E+03	-5.97E+01

Fig. 8.14 illustrates the results of the indicator 'Climate change - total', in kg CO_2 eq., per stage.

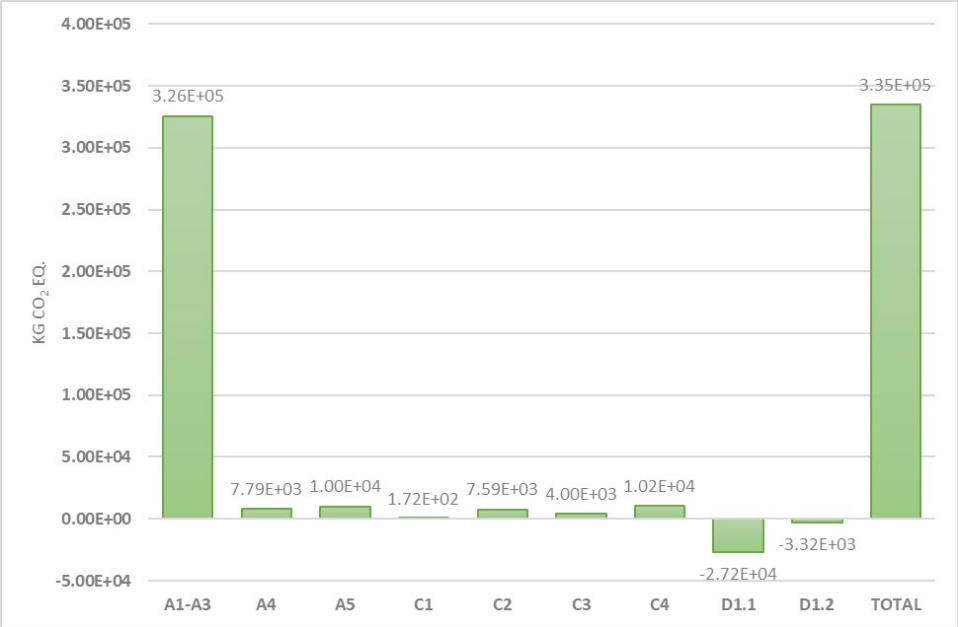

Figure 8.14: *Climate change (total) of the office building (scenario 3).*

In addition, considering the total area of the building (A = 1128 m^2), the results are provided in Fig. 8.15.

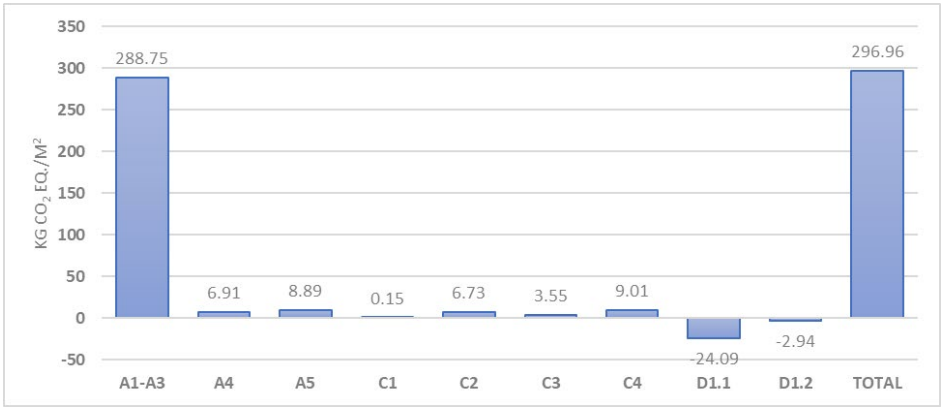

Figure 8.15: *Climate change of the mid-rise building, per area of the building (scenario 3).*

The LCA results for the indicators describing resource use and waste categories are provided in Table 8.19:.

Table 8.19: *Indicators describing resource use and waste categories (scenario 3).*

	A1-A3	A4-A5	C1	C2	C3	C4	D1.1	D1.2
Total use of renewable primary energy resources (PERT) [MJ]	1.73E+06	2.15E+04	1.90E+02	7.34E+03	8.83E+03	2.32E+04	-1.03E+04	-3.42E+02
Total use of non-renewable primary energy resources (PENRT) [MJ]	2.66E+06	2.45E+05	2.38E+03	1.04E+05	8.03E+04	1.42E+05	-4.48E+05	-3.73E+04

Use of net fresh water (FW) [m3]	2.16E+03	2.07E+01	2.13E-01	8.02E+00	2.34E+01	3.59E+01	-2.12E+03	-4.21E+01
Hazardous waste disposed (HWD) [kg]	-5.82E-05	2.47E-08	4.11E-09	3.91E-07	7.66E-07	3.37E-06	-1.30E-03	-3.27E-05
Non-hazardous waste disposed (NHWD) [kg]	8.55E+04	4.12E+01	3.94E-01	1.50E+01	2.28E+01	7.11E+05	3.12E+03	3.89E+01
Radioactive waste disposed (RWD) [kg]	6.69E+01	1.77E+00	1.15E-02	1.36E-01	1.58E+00	1.62E+00	-4.63E+00	4.55E-04

The LCA results for the total use of non-renewable primary energy resources, in MJ/m^2, are provided in Fig. 8.16 for scenario 3.

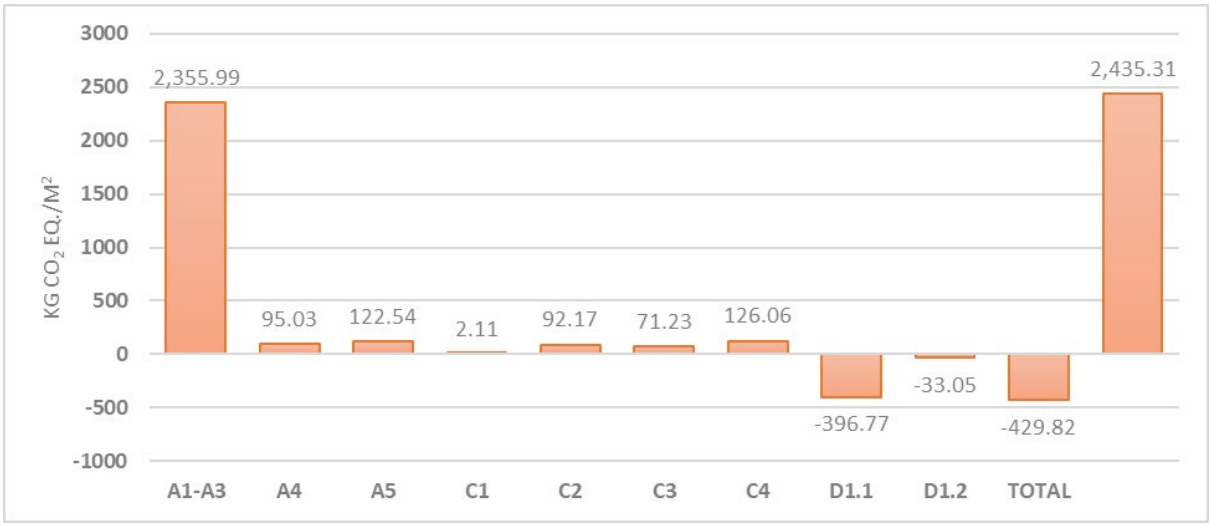

Figure 8.16: *Total use of non-renewable primary energy resources per area of the building (scenario* 3**).**

Comparison of different scenarios

The comparison between the different scenarios is provided in Fig. 8.17, for the impact category of Climate change – total (GWPt), per m^2.

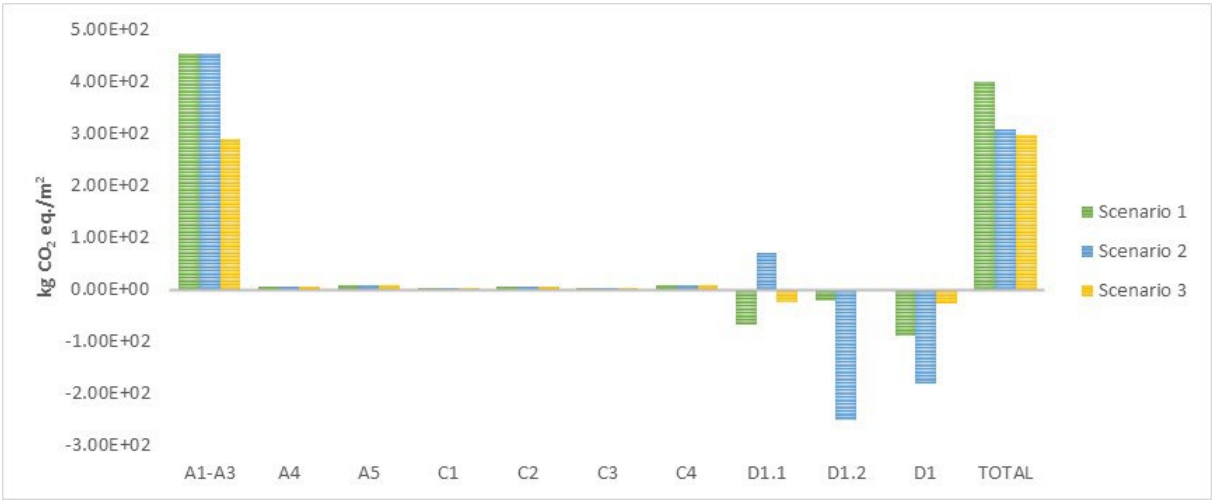

Figure 8.17: *Comparison of the different scenarios for GWPt (in kgCO_2 eq./m^2).*

In Scenario 2, the aggregated value (shown in the last column of the graph) decreases by approximately 23% compared to Scenario 1. This reduction is made possible by the reuse of the steel structure, which results in a higher value for module D1.2 that offsets the positive contribution of module D1.1. In Scenario 3, the aggregated value drops by about 26% relative to Scenario 1. In this case, the reduction is primarily due to a significantly lower value in modules A1–A3—a decrease of 36% compared to the other scenarios.

Similar conclusions can be drawn for the impact category of total non-renewable primary energy resource use (PENRT), as shown in Fig. 8.18. Compared to Scenario 1, the total aggregated value is reduced by 30% in Scenario 2 and by 35% in Scenario 3.

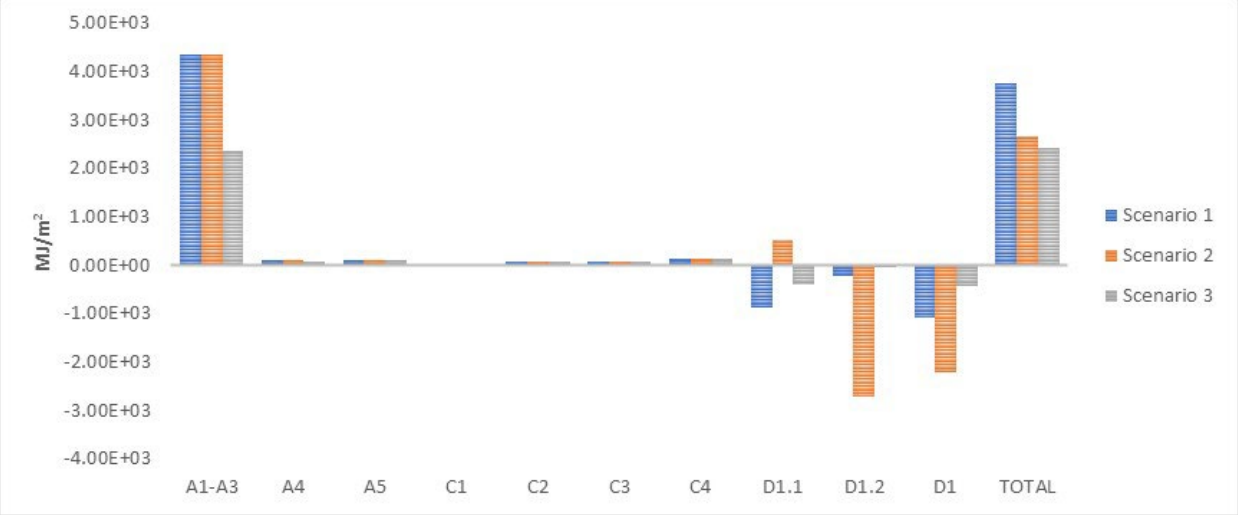

Figure 8.18: *Comparison of the different scenarios for PENRT (in MJ/m²).*

These results highlight the benefits of reusing steel at the end-of-life stage (Scenario 2) and using low-carbon emission steel (Scenario 3), which contribute to reducing impacts at the end-of-life phase and during the production stage, respectively.

8.5 CONCLUSIONS

To support sustainable construction and circular economy objectives, the DREAMERS building scenarios illustrate two particularly effective strategies: **reusing steel at the end-of-life stage** and **utilizing low-carbon emission steel during production**. These approaches can significantly reduce environmental impacts without compromising the structural integrity or safety of the building.

Reusing steel components at the end of a building's service life offers several environmental benefits. It avoids the need for new steel production, conserving non-renewable resources; reduces construction and demolition waste by keeping structural elements in use; and preserves

the embodied carbon of the original material, thereby improving the overall life cycle performance.

In parallel, selecting low-carbon emission steel—produced using renewable electricity and containing up to 100% recycled content (steel scrap)—greatly reduces CO_2eq. emissions during the production stage compared to conventional steel. This choice also facilitates compliance with increasingly stringent environmental standards and green building certifications.

The DREAMERS building was constructed using low-carbon emission steel, as described by scenario 3, demonstrating a clear environmental advantage over traditional steel options. Furthermore, when the building eventually reaches its end-of-life stage, the potential reuse of its steel frame and other structural elements provides an opportunity to further enhance its life cycle performance.

8.6 REFERENCES

[1] EN 15804:2012+A2:2019. Sustainability of construction works - Environmental product declarations - Core rules for the product category of construction products, CEN-CENELEC, Brussels.

[2] EN 15978:2011. Sustainability of construction works - Assessment of environmental performance of buildings - Calculation method, CEN-CENELEC, Brussels.

[3] Gervasio, H. and Dimova, S. (2018). Model for Life Cycle Assessment (LCA) of buildings, EUR 29123 EN, Publications Office of the European Union, ISBN 978-92-79-79974-7 (print),978-92-79-79973-0 (pdf), doi:10.2760/10016 (online),10.2760/789069 (print), JRC110082.

[4] ISO 14040:2006. Environmental management — Life cycle assessment — Principles and framework, ISO, Geneva.

[5] ISO 14044:2006Environmental management — Life cycle assessment — Requirements and guidelines, ISO, Geneva.

[6] prEN17662:2021. Execution of steel structures and aluminium structures - Environmental Product Declarations - Product category rules complementary to EN 15804 for Steel, Iron and Aluminium structural products for use in construction works, CEN-CENELEC, Brussels.

[7] Sphera (2024). LCA for Experts Software System and Database for Life Cycle Engineering. Version 10.7.1.28, Sphera Solutions GmbH, Leinfelden-Echterdingen.

[8] Wordsteel (2024). Guidance on methodologies for modelling reuse and remanufacture in LCA studies. Worldsteel Association, Task force on Reuse and Remanufacture, LCA expert Group, Brussels.

[9] EPDs:

[10] EPD-ARC-20210132-CBB1-EN - XCarb™ Recycled and renewably produced - Structural steel sections and merchant bars, ArcelorMittal Europe (valid until 18/07/2026).

[11] EPD-ARC-20210245-CBA1-EN - XCarb® Recycled and renewably produced - Reinforcing steel in bars, ArcelorMittal Europe (valid until 28/10/2026).

[12] EPD-KNQ-20240283-IBB1-EN - AQUAPANEL® Cement Board Outdoor- Plant Iserlohn, Knauf AQUAPANEL GmbH & Co. KG (valid until 14/10/2029).

[13] S-P-09773 - Structural Hollow Sections made of XCarb® recycled and renewably produced steel, ArcelorMittal Europe (valid until 16/10/2028).

[14] S-P-11266 - XCarb® recycled and renewably produced Cold Rolled Coils, ArcelorMittal Europe (valid until 14/12/2028).